

Scaling Behavior of Heavy Fermion Metals

V.R. Shaginyan^{a,b,*}, M.Ya. Amusia^{c,d}, A.Z. Msezane^b, K.G. Popov^e

^aPetersburg Nuclear Physics Institute, RAS, Gatchina, 188300, Russia

^bCTSPS, Clark Atlanta University, Atlanta, Georgia 30314, USA

^cRacah Institute of Physics, Hebrew University, Jerusalem 91904, Israel

^dIoffe Physical Technical Institute, RAS, St. Petersburg 194021, Russia

^eKomi Science Center, Ural Division, RAS, 3a, Chernova str. Syktyvkar, 167982, Russia

Abstract

Strongly correlated Fermi systems are fundamental systems in physics that are best studied experimentally, which until very recently have lacked theoretical explanations. This review discusses the construction of a theory and the analysis of phenomena occurring in strongly correlated Fermi systems such as heavy-fermion (HF) metals and two-dimensional (2D) Fermi systems. It is shown that the basic properties and the scaling behavior of HF metals can be described within the framework of a fermion condensation quantum phase transition (FCQPT) and extended quasiparticle paradigm that allow us to explain the non-Fermi liquid behavior observed in strongly correlated Fermi systems. In contrast to the Landau paradigm stating that the quasiparticle effective mass is a constant, the effective mass of new quasiparticles strongly depends on temperature, magnetic field, pressure, and other parameters. Having analyzed collected facts on strongly correlated Fermi systems with quite different microscopic nature, we find these to exhibit the same non-Fermi liquid behavior at FCQPT. We show both analytically and using arguments based entirely on the experimental grounds that the data collected on very different strongly correlated Fermi systems have a universal scaling behavior, and materials with strongly correlated fermions can unexpectedly be uniform in their diversity. Our analysis of strongly correlated systems such as HF metals and 2D Fermi systems is in the context of salient experimental results. Our calculations of the non-Fermi liquid behavior, the scales and thermodynamic, relaxation and transport properties are in good agreement with experimental facts.

Keywords: Quantum phase transitions; Heavy fermions; Non-Fermi liquid behavior; Scaling behavior; Entropy; Asymmetrical conductivity; Tricritical points; Topological phase transitions
PACS: 71.27.+a, 71.10.Hf, 73.43.Nq, 75.30.Kz, 74.20.Fg, 65.40.-b, 03.65.Vf

Contents

1 Introduction	3
1.1 Quantum phase transitions and the non-Fermi liquid behavior of correlated Fermi systems	3
1.2 Limits and goals of the review	6
2 Landau theory of Fermi liquids	7
3 Equation for the effective mass and the scaling behavior	9
4 Fermion condensation quantum phase transition	11
4.1 The order parameter of FCQPT	13
4.2 Quantum protectorate related to FCQPT	13

*Corresponding author at: Petersburg Nuclear Physics Institute, RAS, Gatchina, 188300, Russia; Phones: (office) 7-813-714-6096, (fax) 7-813-713-1963

Email address: vrshag@thd.pnpi.spb.ru (V.R. Shaginyan)

4.3	The influence of FCQPT at finite temperatures	14
4.4	Phase diagram of Fermi system with FCQPT	16
5	The superconducting state with FC	17
5.1	The superconducting state at $T = 0$	17
5.2	Green's function of the superconducting state with FC at $T = 0$	18
5.3	The superconducting state at finite temperatures	19
5.4	Bogoliubov quasiparticles	20
5.5	The pseudogap	21
5.6	Dependence of the critical temperature T_c of the superconducting phase transition on doping	23
5.7	The gap and heat capacity near T_c	23
6	The dispersion law and lineshape of single-particle excitations	25
7	Electron liquid with FC in magnetic fields	26
7.1	Phase diagram of electron liquid in magnetic field	26
7.2	Dependence of effective mass on magnetic fields in HF metals and high- T_c superconductors	29
7.2.1	Common QCP in the high- T_c $Tl_2Ba_2CuO_{6+x}$ and the HF metal $YbRh_2Si_2$	30
8	Appearance of FCQPT in Fermi systems	32
9	A highly correlated Fermi liquid in HF metals	34
9.1	Dependence of the effective mass M^* on magnetic field	34
9.2	Dependence of the effective mass M^* on temperature and the damping of quasiparticles	36
9.3	Scaling behavior of the effective mass	38
9.3.1	Schematic phase diagram of HF metal	39
9.4	Non-Fermi liquid behavior in $YbRh_2Si_2$	41
9.4.1	Heat capacity and the Sommerfeld coefficient	42
9.4.2	Magnetization	42
9.4.3	Longitudinal magnetoresistance	44
9.4.4	Magnetic entropy	44
9.4.5	Energy scales	46
9.5	Electric resistivity of HF metals	46
9.6	Magnetic susceptibility and magnetization measured on $CeRu_2Si_2$	47
9.7	Transverse magnetoresistance in the HF metal $CeCoIn_5$	48
9.8	Magnetic-field-induced reentrance of Fermi-liquid behavior and spin-lattice relaxation rates in $YbCu_{5-x}Au_x$	52
9.9	Relationships between critical magnetic fields B_{c0} and B_{c2} in HF metals and high- T_c superconductors	54
9.10	Scaling behavior of the HF $CePd_{1-x}Rh_x$ ferromagnet	56
10	Metals with a strongly correlated electron liquid	61
10.1	Entropy, linear expansion, and Grüneisen's law	62
10.2	The $T - B$ phase diagram of $YbRh_2Si_2$, Hall coefficient and magnetization	63
10.3	Heavy-fermion metals in the immediate vicinity of QCP	65
11	Scaling behavior of heavy fermion systems	68
11.1	Quantum criticality in 2D 3He	68
11.2	Kinks in the thermodynamic functions	72
11.3	Heavy-fermion metals at metamagnetic phase transitions	73
12	Asymmetric conductivity in HF metals and high-T_c superconductors	74
12.1	Normal state	74
12.1.1	Suppression of the asymmetrical differential resistance in $YbCu_{5-x}Al_x$ in magnetic fields	78
12.2	Superconducting state	80

13 Violation of the Wiedemann-Franz law in HF metals	83
14 The impact of FCQPT on ordinary continuous phase transitions in HF metals	84
14.1 $T - B$ phase diagram for YbRh_2Si_2 versus one for CeCoIn_5	85
14.2 The tricritical point in the $B - T$ phase diagram of YbRh_2Si_2	86
14.3 Entropy in YbRh_2Si_2 at low temperatures	87
15 Topological phase transitions related to FCQPT	88
16 Conclusions	94

1. Introduction

Strongly correlated Fermi systems, such as heavy fermion (HF) metals, high- T_c superconductors, and two-dimensional (2D) Fermi liquids, are among the most intriguing and best experimentally studied fundamental systems in physics. However until very recently lacked theoretical explanations. The properties of these materials differ dramatically from those of ordinary Fermi systems [1, 2, 3, 4, 5, 6, 7, 8, 9, 10, 11, 12]. For instance, in the case of metals with heavy fermions, the strong correlation of electrons leads to a renormalization of the effective mass of quasiparticles, which may exceed the ordinary, "bare", mass by several orders of magnitude or even become infinitely large. The effective mass strongly depends on the temperature, pressure, or applied magnetic field. Such metals exhibit NFL behavior and unusual power laws of the temperature dependence of the thermodynamic properties at low temperatures. Ideas based on quantum and thermal fluctuations taking place at a quantum critical point (QCP) have been put forward and the fascinating behavior of these systems known as the non-Fermi liquid (NFL) behavior was attributed to the fluctuations [1, 3, 13, 14, 15, 16, 17]. Suggested to describe one property, the ideas failed to do the same with the others and there was a real crisis and a new quantum phase transition responsible for the observed behavior was required [7, 8, 9, 10, 11, 13, 18].

The Landau theory of the Fermi liquid has a long history and remarkable results in describing a multitude of properties of the electron liquid in ordinary metals and Fermi liquids of the ^3He type [19, 20, 21]. The theory is based on the assumption that elementary excitations determine the physics at low temperatures. These excitations behave as quasiparticles, have a certain effective mass, and, judging by their basic properties, belong to the class of quasiparticles of a weakly interacting Fermi gas. Hence, the effective mass M^* is independent of the temperature, pressure, and magnetic field strength and is a parameter of the theory.

The Landau Fermi liquid (LFL) theory fails to explain the results of experimental observations related to the dependence of M^* on the temperature T , magnetic field B , pressure, etc.; this has led to the conclusion that quasiparticles do not survive in strongly correlated Fermi systems and that the heavy electron does not retain its identity as a quasiparticle excitation [7, 8, 9, 10, 11, 12, 13, 18].

1.1. Quantum phase transitions and the non-Fermi liquid behavior of correlated Fermi systems

The unusual properties and NFL behavior observed in high- T_c superconductors, HF metals and 2D Fermi systems are assumed to be determined by various magnetic quantum phase transitions [1, 2, 3, 4, 5, 6, 7, 8, 9, 11, 12, 13, 14]. Since a quantum phase transition occurs at the temperature $T = 0$, the control parameters are the composition, electron (hole) number density x , pressure, magnetic field strength B , etc. A quantum phase transition occurs at a quantum critical point, which separates the ordered phase that emerges as a result of quantum phase transition from the disordered phase. It is usually assumed that magnetic (e.g., ferromagnetic and antiferromagnetic) quantum phase transitions are responsible for the NFL behavior. The critical point of such a phase transition can be shifted to absolute zero by varying the above parameters.

Universal behavior can be expected only if the system under consideration is very close to a quantum critical point, e.g., when the correlation length is much longer than the microscopic length scale, and critical quantum and thermal fluctuations determine the anomalous contribution to the thermodynamic functions of the metal. Quantum phase transitions of this type are so widespread [2, 3, 4, 9, 10, 11, 12, 13] that we call them ordinary quantum phase transitions [22]. In this case, the physics of the phenomenon is determined by thermal and quantum fluctuations of the critical state, while quasiparticle excitations are destroyed by these fluctuations. Conventional arguments that quasiparticles in strongly correlated Fermi liquids "get heavy and die" at a quantum critical point commonly employ the well-known formula based on the

assumptions that the z -factor (the quasiparticle weight in the single-particle state) vanishes at the points of second-order phase transitions [18]. However, it has been shown that this scenario is problematic [23, 24].

The fluctuations in the order parameter developing an infinite correlation and the absence of quasiparticle excitations is considered the main reason for the NFL behavior of heavy-fermion metals, 2D fermion systems and high- T_c superconductors [3, 4, 9, 12, 13, 25]. This approach faces certain difficulties, however. Critical behavior in experiments with metals containing heavy fermions is observed at high temperatures comparable to the effective Fermi temperature T_k . For instance, the thermal expansion coefficient $\alpha(T)$, which is a linear function of temperature for normal LFL, $\alpha(T) \propto T$, demonstrates the \sqrt{T} temperature dependence in measurements involving CeNi₂Ge₂ as the temperature varies by two orders of magnitude (as it decreases from 6 K to at least 50 mK) [14]. Such behavior can hardly be explained within the framework of the critical point fluctuation theory. Obviously, such a situation is possible only as $T \rightarrow 0$, when the critical fluctuations make the leading contribution to the entropy and when the correlation length is much longer than the microscopic length scale. At a certain temperature T_k , this macroscopically large correlation length must be destroyed by ordinary thermal fluctuations and the corresponding universal behavior must disappear.

Another difficulty is in explaining the restoration of the LFL behavior under the application of magnetic field B , as observed in HF metals and in high- T_c superconductors [1, 15, 26]. For the LFL state as $T \rightarrow 0$, the electric resistivity $\rho(T) = \rho_0 + AT^2$, the heat capacity $C(T) = \gamma_0 T$, and the magnetic susceptibility $\chi = \text{const}$. It turns out that the coefficient $A(B)$, the Sommerfeld coefficient $\gamma_0(B) \propto M^*$, and the magnetic susceptibility $\chi(B)$ depend on the magnetic field strength B such that $A(B) \propto \gamma_0^2(B)$ and $A(B) \propto \chi^2(B)$, which implies that the Kadowaki-Woods relation $K = A(B)/\gamma_0^2(B)$ [27] is B -independent and is preserved [15]. Such universal behavior, quite natural when quasiparticles with the effective mass M^* playing the main role, can hardly be explained within the framework of the approach that presupposes the absence of quasiparticles, which is characteristic of ordinary quantum phase transitions in the vicinity of QCP. Indeed, there is no reason to expect that γ_0 , χ and A are affected by the fluctuations in a correlated fashion.

For instance, the Kadowaki-Woods relation does not agree with the spin density wave scenario [15] and with the results of research in quantum criticality based on the renormalization-group approach [28]. Moreover, measurements of charge and heat transfer have shown that the Wiedemann-Franz law holds in some high- T_c superconductors [26, 29] and HF metals [30, 31, 32, 33]. All this suggests that quasiparticles do exist in such metals, and this conclusion is also corroborated by photoemission spectroscopy results [34, 35].

The inability to explain the behavior of heavy-fermion metals while staying within the framework of theories based on ordinary quantum phase transitions implies that another important concept introduced by Landau, the order parameter, also ceases to operate (e.g., see Refs [9, 11, 18, 13]). Thus, we are left without the most fundamental principles of many-body quantum physics [19, 20, 21], and many interesting phenomena associated with the NFL behavior of strongly correlated Fermi systems remain unexplained.

NFL behavior manifests itself in the power-law behavior of the physical quantities of strongly correlated Fermi systems located close to their QCPs, with exponents different from those of a Fermi liquid [36, 37]. It is common belief that the main output of theory is the explanation of these exponents which are at least depended on the magnetic character of QCP and dimensionality of the system. On the other hand, the NFL behavior cannot be captured by these exponents as seen from Fig. 1. Indeed, the specific heat C/T exhibits a behavior that is to be described as a function of both temperature T and magnetic B field rather than by a single exponent. One can see that at low temperatures C/T demonstrates the LFL behavior which is changed by the transition regime at which C/T reaches its maximum and finally C/T decays into NFL behavior as a function of T at fixed B . It is clearly seen from Fig. 1 that, in particularly in the transition regime, these exponents may have little physical significance.

In order to show that the behavior of C/T displayed in Fig. 1 is of generic character, we remember that in the vicinity of QCP it is helpful to use "internal" scales to measure the effective mass $M^* \propto C/T$ and temperature T [38, 39]. As seen from Fig. 1, a maximum structure in $C/T \propto M_M^*$ at temperature T_M appears under the application of magnetic field B and T_M shifts to higher T as B is increased. The value of the Sommerfeld coefficient $C/T = \gamma_0$ is saturated towards lower temperatures decreasing at elevated magnetic field. To obtain the normalized effective mass M_N^* , we use M_M^* and T_M as "internal" scales: The maximum structure in C/T was used to normalize C/T , and T was normalized by T_M . In Fig. 2 the obtained $M_N^* = M^*/M_M^*$ as a function of normalized temperature $T_N = T/T_M$ is shown by geometrical figures. Note that we have excluded the experimental data taken in magnetic field $B = 0.06$ T. In that case, as will be shown in Subsections 9.3 and 9.4.5, $T_M \rightarrow 0$ and the corresponding T_M and M_M^* are unavailable. It is seen that the LFL state and NFL one are separated by the transition regime at which M_N^* reaches its maximum value. Figure 2 reveals the scaling behavior of the normalized experimental curves - the curves at different magnetic fields B merge into a single

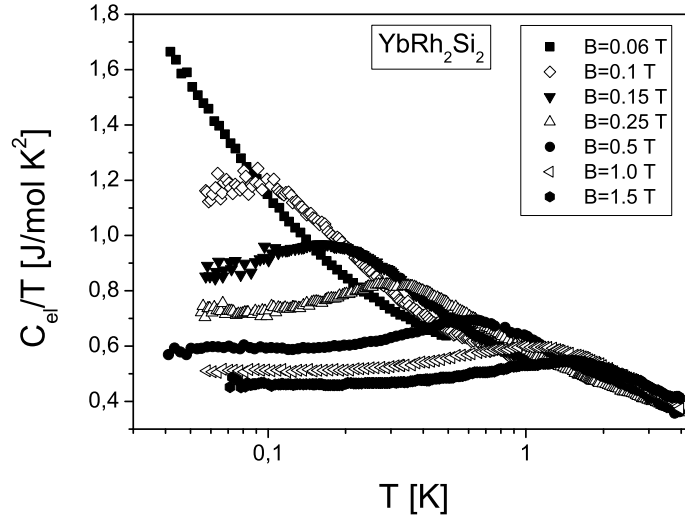


Figure 1: Electronic specific heat of YbRh_2Si_2 , C/T , versus temperature T as a function of magnetic field B [36] shown in the legend.

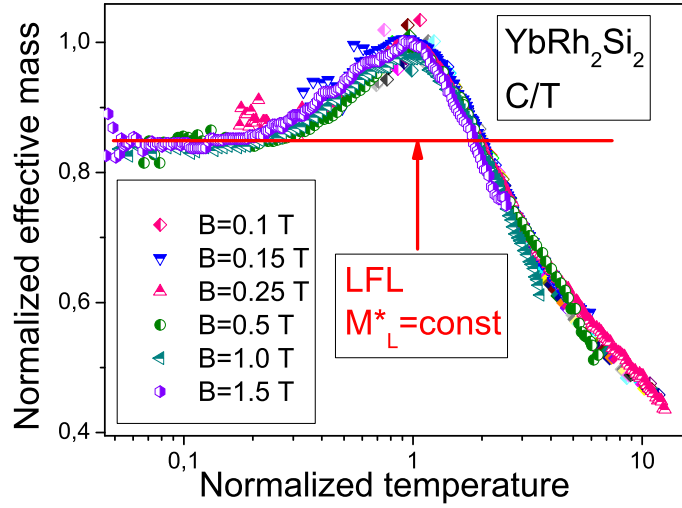


Figure 2: The normalized effective mass M_N^* versus normalized temperature T_N . M_N^* is extracted from the measurements of the specific heat C/T on YbRh_2Si_2 in magnetic fields B [36] listed in the legend. Constant effective mass M_L^* inherent in normal Landau Fermi liquids is depicted by the solid line.

one in terms of the normalized variable $y = T/T_M$. As seen from Fig. 2, the normalized effective mass $M_N^*(y)$ extracted from the measurements is not a constant, as would be for a LFL, and shows the scaling behavior over three decades in normalized temperature y . It is seen from Figs. 1 and 2 that the NFL behavior and the associated scaling extend at least to temperatures up to few Kelvins. Scenario where fluctuations in the order parameter of an infinite (or sufficiently large) correlation length and an infinite correlation time (or sufficiently large) develop the NFL behavior can hardly match up such high temperatures.

Thus, we conclude that a challenging problem for theories considering the critical behavior of the HF metals is to explain the scaling behavior of $M_N^*(y)$. While the theories calculating only the exponents that characterize $M_N^*(y)$ at $y \gg 1$

deal with a part of the observed facts related to the problem and overlook, for example, consideration of the transition regime. Another part of the problem is the remarkably large temperature ranges over which the NFL behavior is observed.

As we will see below, the large temperature ranges are precursors of new quasiparticles, and it is the scaling behavior of the normalized effective mass that allows us to explain the thermodynamic, transport and relaxation properties of HF metals at the transition and NFL regimes.

Taking into account the simple behavior shown in Fig. 2, we ask the question: what theoretical concepts can replace the Fermi-liquid paradigm with the notion of the effective mass in cases where Fermi-liquid theory breaks down? To date such a concept is not available [3]. Therefore, in our review we focus on a concept of fermion condensation quantum phase transition (FCQPT) preserving quasiparticles and intimately related to the unlimited growth of M^* . We shall show that it is capable revealing the scaling behavior of the effective mass and delivering an adequate theoretical explanation of a vast majority of experimental results in different HF metals. In contrast to the Landau paradigm based on the assumption that M^* is a constant as shown by the solid line in Fig. 2, in FCQPT approach the effective mass M^* of new quasiparticles strongly depends on T , x , B etc. Therefore, in accord with numerous experimental facts the extended quasiparticles paradigm is to be introduced. The main point here is that the well-defined quasiparticles determine as before the thermodynamic, relaxation and transport properties of strongly correlated Fermi-systems in large temperature ranges (see Section 9 and Subsection 9.4), while M^* becomes a function of T , x , B etc. The FCQPT approach had been already successfully applied to describe the thermodynamic properties of such different strongly correlated systems as ^3He on the one hand and complicated heavy-fermion (HF) compounds on the other [6, 23, 40].

1.2. Limits and goals of the review

The purpose of this review is to show that diverse strongly correlated Fermi systems such three dimensional (3D) and 2D compounds as HF metals and 2D strongly correlated Fermi liquids exhibit a scaling behavior, which can be described within a single approach based on FCQPT theory [6, 41, 42]. We discuss the construction of the theory and show that it delivers theoretical explanations of the vast majority of experimental results in strongly correlated systems such as HF metals and 2D systems. Our analysis is in the context of salient experimental results. Our calculations of the non-Fermi liquid behavior, the scales and thermodynamic, relaxation and transport properties are in good agreement with experimental facts. We shall also focus on the scaling behavior of the thermodynamic, transport and relaxation properties that can be revealed from experimental facts and theoretical analysis. As a result, we do not discuss the specific features of strongly correlated systems in full; instead, we focus on the universal behavior of such systems. For instance, we ignore the physics of Fermi systems such as neutron stars, atomic clusters and nuclei, quark plasma, and ultra-cold gases in traps, in which we believe fermion condensate (FC) induced by FCQPT can exist [43, 44, 45, 46, 47, 48]. Ultra-cold gases in traps are interesting because their easy tuning allows selecting the values of the parameters required for observations of quantum critical point and FC. We do not discuss also microscopic mechanisms of quantum criticality related to FCQPT. Such mechanisms can be developed within FC theory. For example, the mechanism of quantum criticality as observed in f-electron materials can take place in systems when the centers of merged single-particle levels "get stuck" at the Fermi surface. One observes that this could provide a simple mechanism for pinning narrow bands in solids to the Fermi surface [48]. On the other hand, we consider high- T_c superconductors within a coarse-grained model based on the FCQPT theory in order to illuminate their generic relationships with HF metals.

Experimental studies of the properties of quantum phase transitions and their critical points are very important for understanding the physical nature of high- T_c superconductivity and HF metals. The experimental data that refer to different strongly correlated Fermi systems complement each other. In the case of high- T_c superconductors, only few experiments dealing with their QCPs have been conducted, because the respective QCPs are in the superconductivity range at low temperatures and the physical properties of the respective quantum phase transition are altered by the superconductivity. As a result, high magnetic fields are needed to destroy the superconducting state. But such experiments can be conducted for HF metals. Experimental research has provided data on the behavior of HF metals, shedding light on the nature of critical points and phase transitions (e.g., see Refs [15, 26, 29, 31, 32, 34, 35]). Hence, a key issue is the simultaneous study of high- T_c superconductors and the NFL behavior of HF metals.

Since we are concentrated on properties that are non-sensitive to the detailed structure of the system we avoid difficulties associated with the anisotropy generated by the crystal lattice of solids, its special features, defects, etc., We study the universal behavior of high- T_c superconductors, HF metals, and 2D Fermi systems at low temperatures using the model of a homogeneous HF liquid [38, 39]. The model is quite meaningful because we consider the scaling behavior exhibited by these materials at low temperatures, a behavior related to the scaling of quantities such as the effective mass, the heat

capacity, the thermal expansion, etc. The scaling properties of the normalized effective mass that characterizes them, are determined by momentum transfers that are small compared to momenta of the order of the reciprocal lattice length. The high momentum contributions can therefore be ignored by substituting the lattice for the jelly model. While the values of the scales like the maximum M_M^* of the effective mass and T_M at which M_M^* takes place are determined by a wide range of momenta and thus these scales are controlled by the specific properties of the system.

We analyze the universal properties of strongly correlated Fermi systems using the FCQPT theory [6, 41, 42, 49], because the behavior of heavy-fermion metals already suggests that their unusual properties can be associated with the quantum phase transition related to the unlimited increase in the effective mass at the critical point. Moreover, we shall see that the scaling behavior displayed in Fig. 2 can be quite naturally captured within the framework of the quasiparticle extended paradigm supported by FCQPT which gives explanations of the NFL behavior observed in strongly correlated Fermi systems.

2. Landau theory of Fermi liquids

One of the most complex problems of modern condensed matter physics is the problem of the structure and properties of Fermi systems with large inter particle coupling constants. Theory of Fermi liquids, later called "normal", was first proposed by Landau as a means for solving such problems by introducing the concept of quasiparticles and amplitudes that characterize the effective quasiparticle interaction [19, 20]. The Landau theory can be regarded as an effective low-energy theory with the high-energy degrees of freedom eliminated by introducing amplitudes that determine the quasiparticle interaction instead of the strong inter particle interaction. The stability of the ground state of the Landau Fermi liquid is determined by the Pomeranchuk stability conditions: stability is violated when at least one Landau amplitude becomes negative and reaches its critical value [20, 50]. We note that the new phase in which stability is restored can also be described, in principle, by the LFL theory.

We begin by recalling the main ideas of the LFL theory [19, 20, 21]. The theory is based on the quasiparticle paradigm, which states that quasiparticles are elementary weakly excited states of Fermi liquids and are therefore specific excitations that determine the low-temperature thermodynamic and transport properties of Fermi liquids. In the case of the electron liquid, the quasiparticles are characterized by the electron quantum numbers and the effective mass M^* . The ground state energy of the system is a functional of the quasiparticle occupation numbers (or the quasiparticle distribution function) $n(\mathbf{p}, T)$, and the same is true of the free energy $F(n(\mathbf{p}, T))$, the entropy $S(n(\mathbf{p}, T))$, and other thermodynamic functions. We can find the distribution function from the minimum condition for the free energy $F = E - TS$ (here and in what follows $k_B = \hbar = 1$)

$$\frac{\delta(F - \mu N)}{\delta n(\mathbf{p}, T)} = \varepsilon(\mathbf{p}, T) - \mu(T) - T \ln \frac{1 - n(\mathbf{p}, T)}{n(\mathbf{p}, T)} = 0. \quad (1)$$

Here μ is the chemical potential fixing the number density

$$x = \int n(\mathbf{p}, T) \frac{d\mathbf{p}}{(2\pi)^3}, \quad (2)$$

and

$$\varepsilon(\mathbf{p}, T) = \frac{\delta E(n(\mathbf{p}, T))}{\delta n(\mathbf{p}, T)} \quad (3)$$

is the quasiparticle energy. This energy is a functional of $n(\mathbf{p}, T)$, in the same way as the energy E is: $\varepsilon(\mathbf{p}, T, n)$. The entropy $S(n(\mathbf{p}, T))$ related to quasiparticles is given by the well-known expression [19, 20]

$$\begin{aligned} S(n(\mathbf{p}, T)) &= -2 \int [n(\mathbf{p}, T) \ln(n(\mathbf{p}, T)) + (1 - n(\mathbf{p}, T)) \\ &\times \ln(1 - n(\mathbf{p}, T))] \frac{d\mathbf{p}}{(2\pi)^3}, \end{aligned} \quad (4)$$

which follows from combinatorial reasoning. Equation (1) is usually written in the standard form of the Fermi-Dirac distribution,

$$n(\mathbf{p}, T) = \left\{ 1 + \exp \left[\frac{(\varepsilon(\mathbf{p}, T) - \mu)}{T} \right] \right\}^{-1}. \quad (5)$$

At $T \rightarrow 0$, (1) and (5) have the standard solution $n(p, T \rightarrow 0) \rightarrow \theta(p_F - p)$ if the derivative $\partial\varepsilon(p \simeq p_F)/\partial p$ is finite and positive. Here p_F is the Fermi momentum and $\theta(p_F - p)$ is the step function. The single particle energy can be approximated as $\varepsilon(p \simeq p_F) - \mu \simeq p_F(p - p_F)/M_L^*$, and M_L^* inversely proportional to the derivative is the effective mass of the Landau quasiparticle,

$$\frac{1}{M_L^*} = \frac{1}{p} \left. \frac{d\varepsilon(p, T=0)}{dp} \right|_{p=p_F}. \quad (6)$$

In turn, the effective mass M_L^* is related to the bare electron mass m by the well-known Landau equation [19, 20, 21]

$$\begin{aligned} \frac{1}{M_L^*} &= \frac{1}{m} + \sum_{\sigma_1} \int \frac{\mathbf{p}_F \mathbf{p}_1}{p_F^3} F_{\sigma, \sigma_1}(\mathbf{p}_F, \mathbf{p}_1) \\ &\times \frac{\partial n_{\sigma_1}(\mathbf{p}_1, T)}{\partial p_1} \frac{d\mathbf{p}_1}{(2\pi)^3}. \end{aligned} \quad (7)$$

where $F_{\sigma, \sigma_1}(\mathbf{p}_F, \mathbf{p}_1)$ is the Landau amplitude, which depends on the momenta \mathbf{p}_F and \mathbf{p} and the spins σ . For simplicity, we ignore the spin dependence of the effective mass, because M_L^* is almost completely spin-independent in the case of a homogeneous liquid and weak magnetic fields. The Landau amplitude F is given by

$$F_{\sigma, \sigma_1}(\mathbf{p}, \mathbf{p}_1, n) = \frac{\delta^2 E(n)}{\delta n_{\sigma}(\mathbf{p}) \delta n_{\sigma_1}(\mathbf{p}_1)}. \quad (8)$$

The stability of the ground state of LFL is determined by the Pomeranchuk stability conditions: stability is violated when at least one Landau amplitude becomes negative and reaches its critical value [20, 21, 50]

$$F_L^{a,s} = -(2L + 1). \quad (9)$$

Here F_L^a and F_L^s are the dimensionless spin-symmetric and spin-antisymmetric Landau amplitudes, L is the angular momentum related to the corresponding Legendre polynomials P_L ,

$$F(\mathbf{p}\sigma, \mathbf{p}_1\sigma_1) = \frac{1}{N} \sum_{L=0}^{\infty} P_L(\Theta) [F_L^a \sigma, \sigma_1 + F_L^s]. \quad (10)$$

Here Θ is the angle between momenta \mathbf{p} and \mathbf{p}_1 and the density of states $N = M_L^* p_F / (2\pi^2)$. It follows from Eq. (7) that

$$\frac{M_L^*}{m} = 1 + \frac{F_1^s}{3}. \quad (11)$$

In accordance with the Pomeranchuk stability conditions it is seen from Eq. (11) that $F_1^s > -3$, otherwise the effective mass becomes negative leading to unstable state when it is energetically favorable to excite quasiparticles near the Fermi surface. In what follows, we shall omit the spin indices σ for simplicity.

To deal with the transport properties of Fermi systems, one needs a transport equation describing slowly varying disturbances of the quasiparticle distribution function $n_{\mathbf{p}}(\mathbf{r}, t)$ which depends on position \mathbf{r} and time t . As long as the transferred energy ω and momentum q of the quanta of external field are much smaller than the energy and momentum of the quasiparticles, $qp_F / (TM_L^*) \ll 1$ and $\omega/T \ll 1$, the quasiparticle distribution function $n(\mathbf{q}, \omega)$ satisfies the transport equation [19, 20, 21]

$$\frac{\partial n_{\mathbf{p}}}{\partial t} + \nabla_{\mathbf{p}} \varepsilon_{\mathbf{p}} \nabla_{\mathbf{r}} n_{\mathbf{p}} - \nabla_{\mathbf{r}} \varepsilon_{\mathbf{p}} \nabla_{\mathbf{p}} n_{\mathbf{p}} = I[n_{\mathbf{p}}]. \quad (12)$$

The left-hand side of Eq. (12) describes the dissipationless dynamic of quasiparticles in phase space. The quasiparticle energy $\varepsilon_{\mathbf{p}}(\mathbf{r}, t)$ now depends on its position and time, and the collision integral $I[n_{\mathbf{p}}]$ measures the rate of change of the distribution function due to collisions. The transport equation (12) allows one to derive all the transport properties and collective excitations of a Fermi system.

It is common belief that the equations of this subsection are phenomenological and inapplicable to describe Fermi systems characterized by the effective mass M^* strongly dependent on temperature, external magnetic fields B , pressure P etc. On the other hand, facts collected on HF metals demonstrate the specific behavior when the effective mass strongly

depends on temperature T , doping (or the number density) x and applied magnetic fields B , while the effective mass M^* itself can reach very high values or even diverge, see e.g. [3, 4]. As we have seen in Section 1 such a behavior is so unusual that the traditional Landau quasiparticles paradigm fails to describe it. Therefore, in accord with numerous experimental facts the extended quasiparticles paradigm is to be introduced with the well-defined quasiparticles determining as before the thermodynamic and transport properties of strongly correlated Fermi-systems, M^* becomes a function of T , x , B , while the dependence of the effective mass on T , x , B gives rise to the NFL behavior [6, 23, 38, 51, 52, 53].

As we shall see in the following Section 3, Eq. (7) can be derived microscopically and it becomes compatible with the extended paradigm.

3. Equation for the effective mass and the scaling behavior

To derive the equation determining the effective mass, we consider the model of a homogeneous HF liquid and employ the density functional theory for superconductors (SCDFT) [54] which allows us to consider E as a functional of the occupations numbers $n(\mathbf{p})$ [38, 55, 56, 57]. As a result, the ground state energy of the normal state E becomes the functional of the occupation numbers and the function of the number density x , $E = E(n(\mathbf{p}), x)$, while Eq. (3) gives the single-particle spectrum. Upon differentiating both sides of Eq. (3) with respect to \mathbf{p} and after some algebra and integration by parts, we obtain [23, 38, 55, 56]

$$\frac{\partial \varepsilon(\mathbf{p})}{\partial \mathbf{p}} = \frac{\mathbf{p}}{m} + \int F(\mathbf{p}, \mathbf{p}_1, n) \frac{\partial n(\mathbf{p}_1)}{\partial \mathbf{p}_1} \frac{d\mathbf{p}_1}{(2\pi)^3}. \quad (13)$$

To calculate the derivative $\partial \varepsilon(\mathbf{p})/\partial \mathbf{p}$, we employ the functional representation

$$\begin{aligned} E(n) &= \int \frac{p^2}{2m} n(\mathbf{p}) \frac{d\mathbf{p}}{(2\pi)^3} \\ &+ \frac{1}{2} \int F(\mathbf{p}, \mathbf{p}_1, n)_{n=0} n(\mathbf{p}) n(\mathbf{p}_1) \frac{d\mathbf{p} d\mathbf{p}_1}{(2\pi)^6} + \dots \end{aligned} \quad (14)$$

It is seen directly from Eq. (13) that the effective mass is given by the well-known Landau equation

$$\frac{1}{M^*} = \frac{1}{m} + \int \frac{\mathbf{p}_F \mathbf{p}_1}{p_F^3} F(\mathbf{p}_F, \mathbf{p}_1, n) \frac{\partial n(p_1)}{\partial p_1} \frac{d\mathbf{p}_1}{(2\pi)^3}. \quad (15)$$

For simplicity, we ignore the spin dependencies. To calculate M^* as a function of T , we construct the free energy $F = E - TS$, where the entropy S is given by Eq. (4). Minimizing F with respect to $n(\mathbf{p})$, we arrive at the Fermi-Dirac distribution, Eq. (5). Due to the above derivation, we conclude that Eqs. (13) and (15) are exact ones and allow us to calculate the behavior of both $\partial \varepsilon(\mathbf{p})/\partial \mathbf{p}$ and M^* which now is a function of temperature T , external magnetic field B , number density x and pressure P rather than a constant. As we will see it is this feature of M^* that forms both the scaling and the NFL behavior observed in measurements on HF metals.

In LFL theory it is assumed that M_L^* is positive, finite and constant. As a result, the temperature-dependent corrections to M_L^* , the quasiparticle energy $\varepsilon(\mathbf{p})$ and other quantities begin with the term proportional to T^2 in 3D systems and with the term proportional to T in 2D one [58]. The effective mass is given by Eq. (7), and the specific heat C is [19]

$$C = \frac{2\pi^2 NT}{3} = \gamma_0 T = T \frac{\partial S}{\partial T}, \quad (16)$$

and the spin susceptibility

$$\chi = \frac{3\gamma_0 \mu_B^2}{\pi^2 (1 + F_0^a)}, \quad (17)$$

where μ_B is the Bohr magneton and $\gamma_0 \propto M_L^*$. In the case of LFL, upon using the transport Eq. (12) one finds for the electrical resistivity at low T [21]

$$\rho(T) = \rho_0 + AT^{\alpha_R}, \quad (18)$$

where ρ_0 is the residual resistivity, the exponent $\alpha_R = 2$ and A is the coefficient determining the charge transport. The coefficient is proportional to the quasiparticle-quasiparticle scattering cross-section. Equation (18) symbolizes and defines the LFL behavior observed in normal metals.

Equation (15) at $T = 0$, combined with the fact that $n(\mathbf{p}, T = 0)$ becomes $\theta(p_F - p)$, yields the well-known result [59, 60, 61]

$$\frac{M^*}{m} = \frac{1}{1 - F^1/3},$$

where $F^1 = N_0 f^1$, $N_0 = mp_F/(2\pi^2)$ is the density of states of a free Fermi gas and $f^1(p_F, p_F)$ is the p -wave component of the Landau interaction amplitude. Because $x = p_F^3/3\pi^2$ in the Landau Fermi-liquid theory, the Landau interaction amplitude can be written as $F^1(p_F, p_F) = F^1(x)$. Provided that at a certain critical point x_{FC} , the denominator $(1 - F^1(x)/3)$ tends to zero, i.e., $(1 - F^1(x)/3) \propto (x - x_{FC}) + a(x - x_{FC})^2 + \dots \rightarrow 0$, we find that [62, 63]

$$\frac{M^*(x)}{m} \simeq a_1 + \frac{a_2}{x - x_{FC}} \propto \frac{1}{r}. \quad (19)$$

where a_1 and a_2 are constants and $r = (x - x_{FC})/x_{FC}$ is the “distance” from QCP x_{FC} at which $M^*(x \rightarrow x_{FC}) \rightarrow \infty$. We note that the divergence of the effective mass given by Eq. (19) does preserve the Pomeranchuk stability conditions for F^1 positive, see Eq. (9). Equations (11) and (19) seem to be different but it is not the case since $F^1 \propto m$, while $F_1^s \propto M^*$ and Eq. (11) represents an implicit formula for the effective mass.

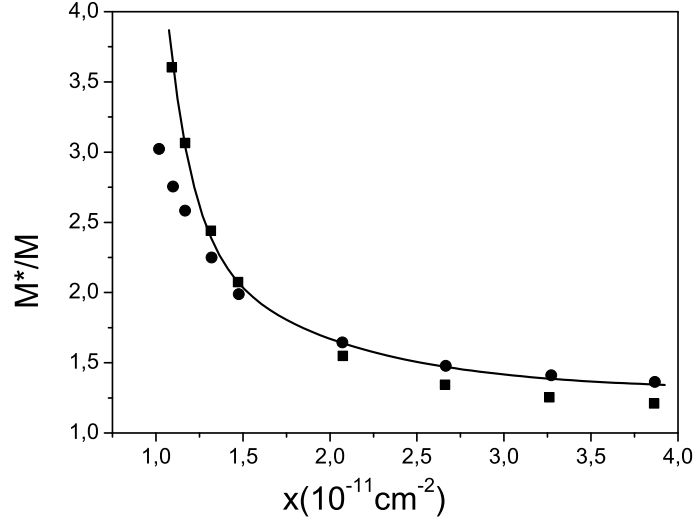


Figure 3: The ratio M^*/M in a silicon MOSFET as a function of the electron number density x . The black squares mark the experimental data on the Shubnikov-de Haas oscillations. The data obtained by applying a parallel magnetic field are marked by black circles [65, 66, 71]. The solid line represents the function (86).

The behavior of $M^*(x)$ described by formula (19) is in good agreement with the results of experiments [64, 65, 66] and calculations [67, 68, 69]. In the case of electron systems, Eq. (19) holds for $x > x_{FC}$, while for 2D ^3He we have $x < x_{FC}$ so that always $r > 0$ [42, 70] (see also Section 8). Such behavior of the effective mass is observed in HF metals, which have a fairly flat and narrow conductivity band corresponding to a large effective mass, with a strong correlation and the effective Fermi temperature $T_k \sim p_F^2/M^*(x)$ of the order of several dozen degrees kelvin or even lower (e.g., see Ref. [1]).

The effective mass as a function of the electron density x in a silicon MOSFET (Metal Oxide Semiconductor Field Effect Transistor), approximated by Eq. (19), is shown in Fig. 3. The parameters a_1 , a_2 and x_{FC} are taken as fitting. We see that Eq. (19) provides a good description of the experimental results.

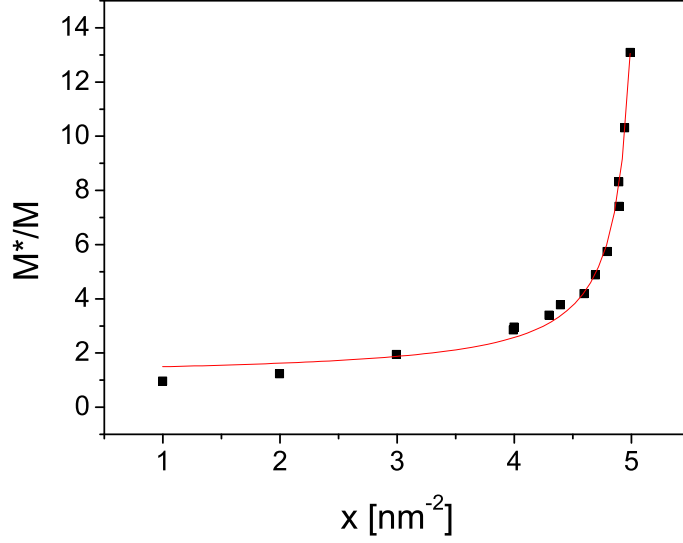


Figure 4: The ratio M^*/M in 2D ^3He as a function of the density x of the liquid, obtained from heat capacity and magnetization measurements. The experimental data are marked by black squares [64, 72], and the solid line represents the function given by Eq. (19), where $a_1=1.09$, $a_2 = 1.68 \text{ nm}^{-2}$, and $x_{FC} = 5.11 \text{ nm}^{-2}$.

The divergence of the effective mass $M^*(x)$ discovered in measurements involving 2D ^3He [64, 72] is illustrated in Fig. 4. Figures 3 and 4 show that the description provided by Eq. (19) does not depend on elementary Fermi particles constituting the system and is in good agreement with the experimental data.

It is instructive to briefly explore the scaling behavior of M^* in order to illustrate the ability of the quasiparticle extended paradigm to capture the scaling behavior, while more detailed consideration is reserved for Section 9. Let us write the quasiparticle distribution function as $n_1(\mathbf{p}) = n(\mathbf{p}, T) - n(\mathbf{p})$, with $n(\mathbf{p})$ being the step function, and Eq. (15) then becomes

$$\frac{1}{M^*(T)} = \frac{1}{M^*} + \int \frac{\mathbf{p}_F \mathbf{p}_1}{p_F^3} F(\mathbf{p}_F, \mathbf{p}_1) \frac{\partial n_1(p_1, T)}{\partial p_1} \frac{d\mathbf{p}_1}{(2\pi)^3}. \quad (20)$$

At QCP $x \rightarrow x_{FC}$, the effective mass $M^*(x)$ diverges and Eq. (20) becomes homogeneous determining M^* as a function of temperature while the system exhibits the NFL behavior. If the system is located before QCP, M^* is finite, at low temperatures the integral on the right hand side of Eq. (20) represents a small correction to $1/M^*$ and the system demonstrates the LFL behavior seen in Figs. 1 and 2. The LFL behavior assumes that the effective mass is independent of temperature, $M^*(T) \simeq \text{const}$, as shown by the horizontal line in Fig. 2. Obviously, the LFL behavior takes place only if the second term on the right hand side of Eq. (20) is small in comparison with the first one. Then, as temperature rises the system enters the transition regime: M^* grows, reaching its maximum M_M^* at $T = T_M$, with subsequent diminishing. As seen from Fig. 2, near temperatures $T \geq T_M$ the last "traces" of LFL regime disappear, the second term starts to dominate, and again Eq. (20) becomes homogeneous, and the NFL behavior is restored, manifesting itself in decreasing M^* as a function of T .

4. Fermion condensation quantum phase transition

As shown in Section 3, the Pomeranchuk stability conditions do not encompass all possible types of instabilities and that at least one related to the divergence of the effective mass given by Eq. (19) was overlooked [41]. This type of instability corresponds to a situation where the effective mass, the most important characteristic of quasiparticles, can become infinitely large. As a result, the quasiparticle kinetic energy is infinitely small near the Fermi surface and the quasiparticle distribution function $n(\mathbf{p})$ minimizing $E(n(\mathbf{p}))$ is determined by the potential energy. This leads to the

formation of a new class of strongly correlated Fermi liquids with FC [41, 42, 48, 73], separated from the normal Fermi liquid by FCQPT [22, 74, 75].

It follows from (19) that at $T = 0$ and as $r \rightarrow 0$ the effective mass diverges, $M^*(r) \rightarrow \infty$. Beyond the critical point x_{FC} , the distance r becomes negative and, correspondingly, so does the effective mass. To avoid an unstable and physically meaningless state with a negative effective mass, the system must undergo a quantum phase transition at the critical point $x = x_{FC}$, which, as we will see shortly, is FCQPT [74, 75, 22]. Because the kinetic energy of quasiparticles that are near the Fermi surface is proportional to the inverse effective mass, the potential energy of the quasiparticles near the Fermi surface determines the ground-state energy as $x \rightarrow x_{FC}$. Hence, a phase transition reduces the energy of the system and transforms the quasiparticle distribution function. Beyond QCP $x = x_{FC}$, the quasiparticle distribution is determined by the ordinary equation for a minimum of the energy functional [41]:

$$\frac{\delta E(n(\mathbf{p}))}{\delta n(\mathbf{p}, T = 0)} = \varepsilon(\mathbf{p}) = \mu; p_i \leq p \leq p_f. \quad (21)$$

Equation (21) yields the quasiparticle distribution function $n_0(\mathbf{p})$ that minimizes the ground-state energy E . This function found from Eq. (21) differs from the step function in the interval from p_i to p_f , where $0 < n_0(\mathbf{p}) < 1$, and coincides with the step function outside this interval. In fact, Eq. (21) coincides with Eq. (3) provided that the Fermi surface at $p = p_F$ transforms into the Fermi volume at $p_i \leq p \leq p_f$ suggesting that the single-particle spectrum is absolutely “flat” within this interval. A possible solution $n_0(\mathbf{p})$ of Eq. (21) and the corresponding single-particle spectrum $\varepsilon(\mathbf{p})$ are depicted in Fig. 5. Quasiparticles with momenta within the interval $(p_f - p_i)$ have the same single-particle energies equal to the chemical potential μ and form FC, while the distribution $n_0(\mathbf{p})$ describes the new state of the Fermi liquid with FC [41, 42, 73]. In contrast to the Landau, marginal, or Luttinger Fermi liquids [2, 76, 77], which exhibit the

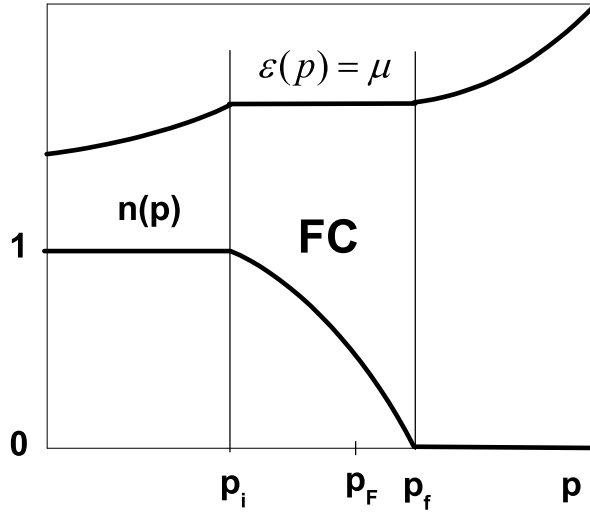


Figure 5: The single-particle spectrum $\varepsilon(p)$ and the quasiparticle distribution function $n_0(p)$. Because $n_0(p)$ is a solution of Eq. (21), we have $n_0(p < p_i) = 1$, $0 < n_0(p_i < p < p_f) < 1$, and $n_0(p > p_f) = 0$, while $\varepsilon(p_i < p < p_f) = \mu$. The Fermi momentum p_F satisfies the condition $p_i < p_F < p_f$.

same topological structure of the Green’s function, in systems with FC, where the Fermi surface spreads into a strip, the Green’s function belongs to a different topological class. The topological class of the Fermi liquid is characterized by the invariant [46, 47, 73]

$$N = \text{tr} \oint_C \frac{dl}{2\pi i} G(i\omega, \mathbf{p}) \partial_l G^{-1}(i\omega, \mathbf{p}), \quad (22)$$

where “tr” denotes the trace over the spin indices of the Green’s function and the integral is taken along an arbitrary contour C encircling the singularity of the Green’s function. The invariant N in (22) takes integer values even when the singularity is not of the pole type, cannot vary continuously, and is conserved in a transition from the Landau Fermi liquid to marginal liquids and under small perturbations of the Green’s function. As shown by Volovik [46, 47, 73], the situation is quite different for systems with FC, where the invariant N becomes a half-integer and the system with FC transforms into an entirely new class of Fermi liquids with its own topological structure.

4.1. The order parameter of FCQPT

We start with visualizing the main properties of FCQPT. To this end, again consider SCDFT. SCDFT states that the thermodynamic potential Φ is a universal functional of the number density $n(\mathbf{r})$ and the anomalous density (or the order parameter) $\kappa(\mathbf{r}, \mathbf{r}_1)$, providing a variational principle to determine the densities. At the superconducting transition temperature T_c a superconducting state undergoes the second order phase transition. Our goal now is to construct a quantum phase transition which evolves from the superconducting one.

Let us assume that the coupling constant λ_0 of the BCS-like pairing interaction [78] vanishes, with $\lambda_0 \rightarrow 0$ making vanish the superconducting gap at any finite temperature. In that case, $T_c \rightarrow 0$ and the superconducting state takes place at $T = 0$ while at finite temperatures there is a normal state. This means that at $T = 0$ the anomalous density

$$\kappa(\mathbf{r}, \mathbf{r}_1) = \langle \Psi \uparrow(\mathbf{r}) \Psi \downarrow(\mathbf{r}_1) \rangle \quad (23)$$

is finite, while the superconducting gap

$$\Delta(\mathbf{r}) = \lambda_0 \int \kappa(\mathbf{r}, \mathbf{r}_1) d\mathbf{r}_1 \quad (24)$$

is infinitely small [6, 63]. In Eq. (23), the field operator $\Psi_\sigma(\mathbf{r})$ annihilates an electron of spin σ , $\sigma = \uparrow, \downarrow$ at the position \mathbf{r} . For the sake of simplicity, we consider the model of homogeneous HF liquid [6]. Then at $T = 0$, the thermodynamic potential Φ reduces to the ground state energy E which turns out to be a functional of the occupation number $n(\mathbf{p})$ since in that case the order parameter $\kappa(\mathbf{p}) = v(\mathbf{p})u(\mathbf{p}) = \sqrt{n(\mathbf{p})(1-n(\mathbf{p}))}$. Indeed,

$$n(\mathbf{p}) = v^2(\mathbf{p}); \quad \kappa(\mathbf{p}) = v(\mathbf{p})u(\mathbf{p}), \quad (25)$$

where $u(\mathbf{p})$ and $v(\mathbf{p})$ are normalized parameters such that $v^2(\mathbf{p}) + u^2(\mathbf{p}) = 1$ and $\kappa(\mathbf{p}) = \sqrt{n(\mathbf{p})(1-n(\mathbf{p}))}$, see e.g. [20].

Upon minimizing E with respect to $n(\mathbf{p})$, we obtain Eq. (21). As soon as Eq. (21) has nontrivial solution $n_0(\mathbf{p})$ then instead of the Fermi step, we have $0 < n_0(\mathbf{p}) < 1$ in certain range of momenta $p_i \leq p \leq p_f$ with $\kappa(\mathbf{p}) = \sqrt{n_0(\mathbf{p})(1-n_0(\mathbf{p}))}$ being finite in this range, while the single particle spectrum $\varepsilon(\mathbf{p})$ is flat. Thus, the step-like Fermi filling inevitably undergoes restructuring and forms FC when Eq. (21) possesses for the first time the nontrivial solution at $x = x_c$ which is QCP of FCQPT. In that case, the range vanishes, $p_i \rightarrow p_f \rightarrow p_F$, and the effective mass M^* diverges at QCP [6, 23, 41]

$$\frac{1}{M^*(x \rightarrow x_c)} = \frac{1}{p_F} \frac{\partial \varepsilon(\mathbf{p})}{\partial \mathbf{p}} \Big|_{p \rightarrow p_F; x \rightarrow x_c} \rightarrow 0. \quad (26)$$

At any small but finite temperature the anomalous density κ (or the order parameter) decays and this state undergoes the first order phase transition and converts into a normal state characterized by the thermodynamic potential Φ_0 . Indeed, at $T \rightarrow 0$, the entropy $S = -\partial \Phi_0 / \partial T$ of the normal state is given by Eq. (4). It is seen from Eq. (4) that the normal state is characterized by the temperature-independent entropy S_0 [6, 23, 79]. Since the entropy of the superconducting ground state is zero, we conclude that the entropy is discontinuous at the phase transition point, with its discontinuity $\delta S = S_0$. Thus, the system undergoes the first order phase transition. The heat q of transition from the asymmetrical to the symmetrical phase is $q = T_c S_0 = 0$ since $T_c = 0$. Because of the stability condition at the point of the first order phase transition, we have $\Phi_0(n(\mathbf{p})) = \Phi(\kappa(\mathbf{p}))$. Obviously the condition is satisfied since $q = 0$.

4.2. Quantum protectorate related to FCQPT

With FCQPT (as well as with other phase transitions), we have to deal with strong particle interaction, and there is no way in which a theoretical investigation based on first principles can provide an absolutely reliable solution. Hence, the only way to verify that FC exists is to study this state by exactly solvable models and to examine the experimental facts that could be interpreted as direct confirmation of the existence of FC. Exactly solvable models unambiguously suggest

that Fermi systems with FC exist (e.g., see Refs [80, 81, 82, 83]). Taking the results of topological investigations into account, we can state that the new class of Fermi liquids with FC is nonempty, actually exists, and represents an extended family of new states of Fermi systems [46, 47, 73].

We note that the solutions $n_0(\mathbf{p})$ of Eq. (21) are new solutions of the well-known equations of the Landau Fermi-liquid theory. Indeed, at $T = 0$, the standard solution given by a step function, $n(\mathbf{p}, T \rightarrow 0) \rightarrow \theta(p_F - p)$, is not the only possible one. Anomalous solutions $\varepsilon(\mathbf{p}) = \mu$ of Eq. (1) can exist if the logarithmic expression on its right-hand side is finite. This is possible if $0 < n_0(\mathbf{p}) < 1$ within a certain interval ($p_i \leq p \leq p_f$). Then, this logarithmic expression remains finite within this interval as $T \rightarrow 0$, the product $T \ln[(1 - n_0(\mathbf{p}))/n_0(\mathbf{p})]_{T \rightarrow 0} \rightarrow 0$, and we again arrive at Eq. (21).

Thus, as $T \rightarrow 0$, the quasiparticle distribution function $n_0(\mathbf{p})$, which is a solution of Eq. (21), does not tend to the step function $\theta(p_F - p)$ and, correspondingly, in accordance with Eq. (4), the entropy $S(T)$ of this state tends to a finite value S_0 as $T \rightarrow 0$:

$$S(T \rightarrow 0) \rightarrow S_0. \quad (27)$$

As the density $x \rightarrow x_{FC}$ (or as the interaction force increases), the system reaches QCP at which FC is formed. This means that $p_i \rightarrow p_f \rightarrow p_F$ and that the deviation $\delta n(\mathbf{p})$ from the step function is small. Expanding the function $E(n(\mathbf{p}))$ in Taylor series in $\delta n(\mathbf{p})$ and keeping only the leading terms, we can use Eq. (21) to obtain the following relation that is valid within the interval $p_i \leq p \leq p_f$:

$$\mu = \varepsilon(\mathbf{p}) = \varepsilon_0(\mathbf{p}) + \int F(\mathbf{p}, \mathbf{p}_1) \delta n(\mathbf{p}_1) \frac{d\mathbf{p}_1}{(2\pi)^2}. \quad (28)$$

Both quantities, the Landau amplitude $F(\mathbf{p}, \mathbf{p}_1)$ and the single-particle energy $\varepsilon_0(\mathbf{p})$, are calculated at $n(\mathbf{p}) = \theta(p_F - p)$. Equation (28) has nontrivial solutions for densities $x \leq x_{FC}$ if the corresponding Landau amplitude, which is density-dependent, is positive and sufficiently large for the potential energy to be higher than the kinetic energy. For instance, such a state is realized in a low-density electron liquid. The transformation of the Fermi step function $n(\mathbf{p}) = \theta(p_F - p)$ into a smooth function determined by Eq. (28) then becomes possible [41, 42, 70].

It follows from Eq. (28) that the quasiparticles of FC form a collective state, because their state is determined by the macroscopic number of quasiparticles with momenta $p_i < p < p_f$. The shape of the single-particle spectrum related to FC is independent of the Landau interaction, which is in general determined by the properties of the system as a whole, including the collective states, irregularities of structure, the presence of impurities, and composition. The length of the interval from p_i to p_f where FC exists is the only characteristic determined by the Landau interaction; of course, the interaction must be strong enough for FCQPT to occur. Therefore, we conclude that spectra related to FC have a universal shape. In Sections 4.3 and 5.1 we show that these spectra are dependent on the temperature and the superconducting gap and that this dependence is also universal. The existence of such spectra can be considered a characteristic feature of a "quantum protectorate", in which the properties of the material, including the thermodynamic properties, are determined by a certain fundamental principle [84, 85]. In our case, the state of matter with FC is also a quantum protectorate, since the new type of quasiparticles of this state determines the special universal thermodynamic and transport properties of Fermi liquids with FC.

4.3. The influence of FCQPT at finite temperatures

According to Eq. (1), the single-particle energy $\varepsilon(\mathbf{p}, T)$ is linear in T for $T \ll T_f$ within the interval $(p_f - p_i)$ [86]. Expanding $\ln((1 - n(\mathbf{p}))/n(\mathbf{p}))$ in a series in $n(\mathbf{p})$ at $p \approx p_F$, we can write the expression

$$\frac{\varepsilon(\mathbf{p}, T) - \mu(T)}{T} = \ln \frac{1 - n(\mathbf{p})}{n(\mathbf{p})} \simeq \frac{1 - 2n(\mathbf{p})}{n(\mathbf{p})} \Big|_{p \approx p_F}. \quad (29)$$

where T_f is the temperature above which the effect of FC is insignificant [51]:

$$\frac{T_f}{\varepsilon_F} \sim \frac{p_f^2 - p_i^2}{2M\varepsilon_F} \sim \frac{\Omega_{FC}}{\Omega_F}. \quad (30)$$

with Ω_{FC} being the volume occupied by FC, ε_F being the Fermi energy, and Ω_F being the volume of the Fermi sphere. We note that for $T \ll T_f$, the occupation numbers $n(\mathbf{p})$ obtained from Eq. (21) are almost perfectly independent of T [51, 52, 86]. At finite temperatures, according to Eq. (29), the dispersionless plateau $\varepsilon(\mathbf{p}) = \mu$ shown in Fig. 5 is

slightly rotated counterclockwise in relation to μ . As a result, the plateau is slightly tilted and rounded off at its end points. According to Eqs. (6) and (29), the effective mass M_{FC}^* that refers to the FC quasiparticles is given by

$$M_{FC}^* \simeq p_F \frac{p_f - p_i}{4T}. \quad (31)$$

In deriving (31), we approximated the derivative as $dn(p)/dp \simeq -1/(p_f - p_i)$. Equation (31) clearly shows that for $0 < T \ll T_f$, the electron liquid with FC behaves as if it were placed at a quantum critical point, since the electron effective mass diverges as $T \rightarrow 0$. Actually, as we shall see in Subsection 4.4 the system is at a quantum critical line, because critical behavior is observed behind QCP with $x = x_{FC}$ of FCQPT as $T \rightarrow 0$. In Sections 7 and 10, we show that the behavior of such a system differs dramatically from that of a system at a quantum critical point.

Upon using Eqs. (30) and (31), we estimate the effective mass M_{FC}^* as

$$\frac{M_{FC}^*}{M} \sim \frac{N(0)}{N_0(0)} \sim \frac{T_f}{T}, \quad (32)$$

where $N_0(0)$ is the density of states of a noninteracting electron gas and $N(0)$ is the density of states on the Fermi surface. Equations (31) and (32) yield the temperature dependence of M_{FC}^* .

Multiplying both sides of Eq. (31) by $(p_f - p_i)$, we obtain an expression for the characteristic energy,

$$E_0 \simeq 4T, \quad (33)$$

which determines the momentum interval $(p_f - p_i)$ with the low-energy quasiparticles characterized by the energy $|\varepsilon(\mathbf{p}) - \mu| \leq E_0/2$ and the effective mass M_{FC}^* . The quasiparticles that do not belong to this momentum interval have an energy $|\varepsilon(\mathbf{p}) - \mu| > E_0/2$ and an effective mass M_L^* that is weakly temperature-dependent [74, 75, 87]. Equation (33) shows that E_0 is independent of the condensate volume. We conclude from Eqs. (31) and (33) that for $T \ll T_f$, the single-electron spectrum of FC quasiparticles has a universal shape and has the features of a quantum protectorate.

Thus, a system with FC is characterized by two effective masses, M_{FC}^* and M_L^* . This fact manifests itself in a break or an abrupt change in the quasiparticle dispersion law, which for quasiparticles with energies $\varepsilon(\mathbf{p}) \leq \mu$ can be approximated by two straight lines intersecting at $E_0/2 \simeq 2T$. Figure 5 shows that at $T = 0$, the straight lines intersect at $p = p_i$. This break also occurs when the system is in its superconducting state at temperatures $T_c \leq T \ll T_f$, where T_c is the critical temperature of the superconducting phase transition, which agrees with the experimental data in [88] and, as we will see in Section 5, this behavior agrees with the experimental data at $T \leq T_c$. At $T > T_c$, the quasiparticles are well-defined, because their width γ is small compared to their energy and is proportional to the temperature, $\gamma \sim T$ [34, 51]. The quasiparticle excitation curve (see Section 6) can be approximately described by a simple Lorentzian [87], which also agrees with the experimental data [88, 89, 90, 91].

We estimate the density x_{FC} at which FCQPT occurs. We show in Section 8 that an unlimited increase in the effective mass precedes the appearance of a density wave or a charge density wave formed in electron systems at $r_s = r_{cdw}$, where $r_s = r_0/a_B$, r_0 is the average distance between electrons, and a_B is the Bohr radius. Hence, FCQPT certainly occurs at $T = 0$ when r_s reaches its critical value r_{FC} corresponding to x_{FC} , with $r_{FC} < r_{cdw}$ [70]. We note that the increase in the effective mass as the electron number density decreases was observed in experiments, see Figs. 3 and 4.

Thus, the formation of FC can be considered a general property of different strongly correlated systems rather than an exotic phenomenon corresponding to the anomalous solution of Eq. (21). Beyond FCQPT, the condensate volume is proportional to $(r_s - r_{FC})$, with $T_f/\varepsilon_F \sim (r_s - r_{FC})/r_{FC}$, at least when $(r_s - r_{FC})/r_{FC} \ll 1$. This implies that [6]

$$\frac{r_s - r_{FC}}{r_{FC}} \sim \frac{p_f - p_i}{p_F} \sim \frac{x_{FC} - x}{x_{FC}}. \quad (34)$$

Because a state of a system with FC is highly degenerate, FCQPT serves as a stimulator of phase transitions that could lift the degeneracy of the spectrum. For instance, FC can stimulate the formation of spin density waves, antiferromagnetic state and ferromagnetic state etc., thus strongly stimulating the competition between phase transitions eliminating the degeneracy. The presence of FC strongly facilitates a transition to the superconducting state, because both phases have the same order parameter.

4.4. Phase diagram of Fermi system with FCQPT

At $T = 0$, a quantum phase transition is driven by a nonthermal control parameter, e.g. the number density x . As we have seen, at QCP, $x = x_{FC}$, the effective mass diverges. It follows from Eq. (19) that beyond QCP, the effective mass becomes negative. To avoid an unstable and physically meaningless state with a negative effective mass, the system undergoes FCQPT leading to the formation of FC.

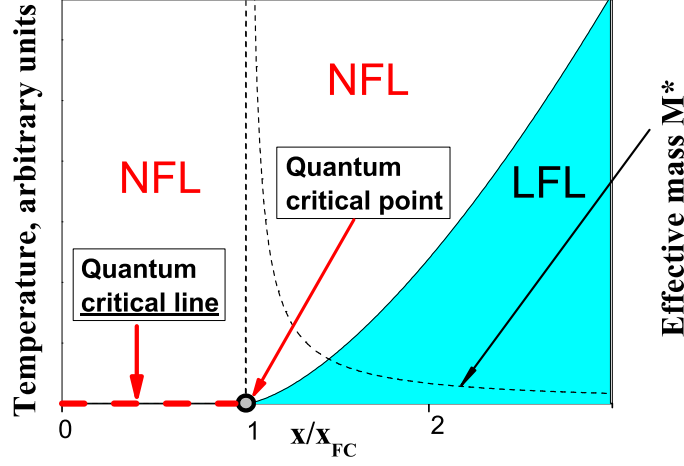


Figure 6: Schematic phase diagram of system with FC. The number density x is taken as the control parameter and depicted as x/x_{FC} . The dashed line shows $M^*(x/x_{FC})$ as the system approaches QCP, $x/x_{FC} = 1$, of FCQPT which is denoted by the arrow. At $x/x_{FC} > 1$ and sufficiently low temperatures, the system is in the LFL state as shown by the shadow area. At $T = 0$ and beyond the critical point, $x/x_{FC} < 1$, the system is at the quantum critical line depicted by the dashed line and shown by the vertical arrow. The critical line is characterized by the FC state with finite superconducting order parameter κ . At any finite low temperature $T > T_c = 0$, κ is destroyed, the system undergoes the first order phase transition, possesses finite entropy S_0 and exhibits the NFL behavior at any finite temperatures $T < T_f$.

A schematic phase diagram of the system which is driven to the FC state by variation of x is reported in Fig. 6. Upon approaching the critical density x_{FC} the system remains in the LFL region at sufficiently low temperatures as it is shown by the shadow area. The temperature range of the shadow area shrinks as the system approaches QCP, and $M^*(x/x_{FC})$ diverges as shown by the dashed line and Eq. (19). At QCP x_{FC} shown by the arrow in Fig. 6, the system demonstrates the NFL behavior down to the lowest temperatures. Beyond the critical point at finite temperatures the behavior remains the NFL and is determined by the temperature-independent entropy S_0 [6, 79]. In that case at $T \rightarrow 0$, the system is approaching a quantum critical line (shown by the vertical arrow and the dashed line in Fig. 6) rather than a quantum critical point. Upon reaching the quantum critical line from the above at $T \rightarrow 0$ the system undergoes the first order quantum phase transition, which is FCQPT taking place at $T_c = 0$. While at diminishing temperatures, the systems located before QCP do not undergo a phase transition and their behavior transits from NFL to LFL.

It is seen from Fig. 6 that at finite temperatures there is no boundary (or phase transition) between the states of systems located before or behind QCP shown by the arrow. Therefore, at elevated temperatures the properties of systems with $x/x_{FC} < 1$ or with $x/x_{FC} > 1$ become indistinguishable. On the other hand, at $T > 0$ the NFL state above the critical line and in the vicinity of QCP is strongly degenerate, therefore the degeneracy stimulates the emergence of different phase transitions lifting it and the NFL state can be captured by the other states such as superconducting (for example, by the superconducting state (SC) in CeCoIn₅ [63, 79]) or by antiferromagnetic (AF) state (e.g. AF one in YbRh₂Si₂ [38]) etc. The diversity of phase transitions occurring at low temperatures is one of the most spectacular features of the physics of many HF metals. Within the scenario of ordinary quantum phase transitions, it is hard to understand why these transitions are so different from one another and their critical temperatures are so extremely small. However, such diversity is endemic to systems with a FC [23].

Upon using nonthermal tuning parameters like the number density, pressure or magnetic field, the NFL behavior is destroyed and the LFL one is restored as we shall see in Sections 9 and 10. For example, the application of magnetic field $B > B_{c0}$ drives a system to QCP and destroys the AF state restoring the LFL behavior. Here, B_{c0} is a critical magnetic field, such that at $B > B_{c0}$ the system is driven towards its LFL state. In some cases as in the HF metal CeRu₂Si₂, $B_{c0} = 0$,

see e.g. [92], while in YbRh₂Si₂, $B_{c0} \simeq 0.06$ T [15].

5. The superconducting state with FC

In this section we discuss the superconducting state of a 2D liquid of heavy electrons, since high- T_c superconductors are represented mainly by 2D structures. On the other hand, our study can easily be generalized to the 3D case. To show that there is no fundamental difference between the 2D and 3D cases, we derive Green's functions for the 3D case in Section 5.2.

5.1. The superconducting state at $T = 0$

As we have seen in Subsection 4.1, the ground-state energy $E_{gs}(\kappa(\mathbf{p}), n(\mathbf{p}))$ of a 2D electron liquid is a functional of the superconducting state order parameter $\kappa(\mathbf{p})$ and of the quasiparticle occupation numbers $n(\mathbf{p})$. This energy is determined by the well-known Bardeen-Cooper-Schrieffer (BCS) equations and in the weak-coupling superconductivity theory is given by [54, 78, 93]

$$E_{gs}(\kappa(\mathbf{p}), n(\mathbf{p})) = E(n(\mathbf{p})) + \lambda_0 \int V(\mathbf{p}_1, \mathbf{p}_2) \times \kappa(\mathbf{p}_1) \kappa^*(\mathbf{p}_2) \frac{d\mathbf{p}_1 d\mathbf{p}_2}{(2\pi)^4}. \quad (35)$$

It is assumed that the constant λ_0 , which determines the magnitude of the pairing interaction $\lambda_0 V(\mathbf{p}_1, \mathbf{p}_2)$, is small. We define the superconducting gap as

$$\Delta(\mathbf{p}) = -\lambda_0 \int V(\mathbf{p}, \mathbf{p}_1) \kappa(\mathbf{p}_1) \frac{d\mathbf{p}_1}{4\pi^2}. \quad (36)$$

Minimizing E_{gs} in $v(\mathbf{p})$ and using (36), we arrive at equations that relate the single-particle energy $\varepsilon(\mathbf{p})$ to $\Delta(\mathbf{p})$ and $E(\mathbf{p})$

$$\varepsilon(\mathbf{p}) - \mu = \Delta(\mathbf{p}) \frac{1 - 2v^2(\mathbf{p})}{2\kappa(\mathbf{p})}, \quad \frac{\Delta(\mathbf{p})}{E(\mathbf{p})} = 2\kappa(\mathbf{p}). \quad (37)$$

Here the single-particle energy $\varepsilon(\mathbf{p})$ is determined by Eq. (3), and

$$E(\mathbf{p}) = \sqrt{\xi^2(\mathbf{p}) + \Delta^2(\mathbf{p})}, \quad (38)$$

with $\xi(\mathbf{p}) = \varepsilon(\mathbf{p}) - \mu$. Substituting the expression for $\kappa(\mathbf{p})$ from (37) in Eq. (36), we obtain the well-known equation of the BCS theory for $\Delta(\mathbf{p})$

$$\Delta(\mathbf{p}) = -\frac{\lambda_0}{2} \int V(\mathbf{p}, \mathbf{p}_1) \frac{\Delta(\mathbf{p}_1)}{E(\mathbf{p}_1)} \frac{d\mathbf{p}_1}{4\pi^2}. \quad (39)$$

As $\lambda_0 \rightarrow 0$, the maximum value of Δ_1 of the superconducting gap $\Delta(\mathbf{p})$ tends to zero and each equation in (37) reduces to Eq. (21)

$$\frac{\delta E(n(\mathbf{p}))}{\delta n(\mathbf{p})} = \varepsilon(\mathbf{p}) - \mu = 0, \quad (40)$$

if $0 < n(\mathbf{p}) < 1$, or $\kappa(\mathbf{p}) \neq 0$, in the interval $p_i \leq p \leq p_f$. Equation (40) shows that the function $n_0(\mathbf{p})$ is determined from the solution to the standard problem of finding the minimum of the functional $E(n(\mathbf{p}))$ [41, 51, 52]. Equation (40) specifies the quasiparticle distribution function $n_0(\mathbf{p})$ that ensures the minimum of the ground-state energy $E(\kappa(\mathbf{p}), n(\mathbf{p}))$. We can now study the relation between the state specified by Eq. (40) or Eq. (21) and the superconducting state.

At $T = 0$, Eq. (40) determines the specific state of a Fermi liquid with FC, the state for which the absolute value of the order parameter $|\kappa(\mathbf{p})|$ is finite in the momentum interval $p_i \leq p \leq p_f$ as $\Delta_1 \rightarrow 0$. Such a state can be considered superconducting with an infinitely small value of Δ_1 . Hence, the entropy of this state at $T = 0$ is zero. Solutions $n_0(\mathbf{p})$ of Eq. (40) constitute a new class of solutions of both the BCS equations and the Landau Fermi-liquid equations. In contrast to the ordinary solutions of the BCS equations [78], the new solutions are characterized by an infinitely small superconducting gap $\Delta_1 \rightarrow 0$, with the order parameter $\kappa(\mathbf{p})$ remaining finite. On the other hand, in contrast to the standard solution of the Landau Fermi-liquid theory, the new solutions $n_0(\mathbf{p})$ determine the state of a heavy-electron liquid with a

finite entropy S_0 as $T \rightarrow 0$ (see Eq. (27)). We arrive at an important conclusion that the solutions of Eq. (40) can be interpreted as the general solutions of the BCS equations and the Landau Fermi-liquid theory equations, while Eq. (40) itself can be derived either from the BCS theory or from the Landau Fermi-liquid theory. Thus, as shown in Subsection 4.1 both states of the system coexist as $T \rightarrow 0$. As the system passes into a state with the order parameter $\kappa(\mathbf{p})$, the entropy suddenly vanishes, with the system undergoing the first-order transition near which the critical quantum and thermal fluctuations are suppressed and the quasiparticles are well-defined excitations (see also Section 10). It follows from Eq. (22) that FCQPT is related to a change in the topological structure of the Green's function and belongs to Lifshitz's topological phase transitions, which occur at absolute zero [73]. This fact establishes a relation between FCQPT and quantum phase transitions under which the Fermi sphere splits into a sequence of Fermi layers [94, 95] (see Sections 7 and 15). We note that in the state with the order parameter $\kappa(\mathbf{p})$, the system entropy $S = 0$ and the Nernst theorem holds in systems with FC.

If $\lambda_0 \neq 0$, the gap Δ_1 becomes finite, leading to a finite value of the effective mass M_{FC}^* , which may be obtained from Eq. (37) by taking the derivative with respect to the momentum p of both sides and using Eq. (6) [74, 75, 87]:

$$M_{FC}^* \simeq p_F \frac{p_f - p_i}{2\Delta_1}. \quad (41)$$

It follows from Eq. (41) that in the superconducting state the effective mass is always finite. As regards the energy scale, it is determined by the parameter E_0 :

$$E_0 = \varepsilon(\mathbf{p}_f) - \varepsilon(\mathbf{p}_i) \simeq p_F \frac{(p_f - p_i)}{M_{FC}^*} \simeq 2\Delta_1. \quad (42)$$

5.2. Green's function of the superconducting state with FC at $T = 0$

We write two equations for the 3D case, the Gor'kov equations [96], which determine the Green's functions $F^+(\mathbf{p}, \omega)$ and $G(\mathbf{p}, \omega)$ of a superconductor (e.g., see Ref. [20]):

$$\begin{aligned} F^+ &= \frac{-\lambda_0 \Xi^*}{(\omega - E(\mathbf{p}) + i0)(\omega + E(\mathbf{p}) - i0)}; \\ G &= \frac{u^2(\mathbf{p})}{\omega - E(\mathbf{p}) + i0} + \frac{v^2(\mathbf{p})}{\omega + E(\mathbf{p}) - i0}. \end{aligned} \quad (43)$$

The gap Δ and the function Ξ are given by

$$\Delta = \lambda_0 |\Xi|, \quad i\Xi = \int \int_{-\infty}^{\infty} F^+(\mathbf{p}, \omega) \frac{d\omega d\mathbf{p}}{(2\pi)^4}. \quad (44)$$

We recall that the function $F^+(\mathbf{p}, \omega)$ has the meaning of the wave function of Cooper pairs and Ξ is the wave function of the motion of these pairs as a whole and is just a constant in a homogeneous system [20]. It follows from Eqs. (37) and (44) that

$$i\Xi = \int_{-\infty}^{\infty} F_0^+(\mathbf{p}, \omega) \frac{d\omega d\mathbf{p}}{(2\pi)^4} = i \int \kappa(\mathbf{p}) \frac{d\mathbf{p}}{(2\pi)^3}. \quad (45)$$

Taking Eqs. (44) and (37) into account, we can write Eqs. (43) as

$$\begin{aligned} F^+ &= -\frac{\kappa(\mathbf{p})}{\omega - E(\mathbf{p}) + i0} + \frac{\kappa(\mathbf{p})}{\omega + E(\mathbf{p}) - i0}; \\ G &= \frac{u^2(\mathbf{p})}{\omega - E(\mathbf{p}) + i0} + \frac{v^2(\mathbf{p})}{\omega + E(\mathbf{p}) - i0}. \end{aligned} \quad (46)$$

As $\lambda_0 \rightarrow 0$, the gap $\Delta \rightarrow 0$, but Ξ and $\kappa(\mathbf{p})$ remain finite if the spectrum becomes flat, $E(\mathbf{p}) = 0$, and Eqs. (46) become

$$\begin{aligned} F^+(\mathbf{p}, \omega) &= -\kappa(\mathbf{p}) \left[\frac{1}{\omega + i0} - \frac{1}{\omega - i0} \right]; \\ G(\mathbf{p}, \omega) &= \frac{u^2(\mathbf{p})}{\omega + i0} + \frac{v^2(\mathbf{p})}{\omega - i0}. \end{aligned} \quad (47)$$

in the interval $p_i \leq p \leq p_f$. The parameters $v(\mathbf{p})$ and $u(\mathbf{p})$ are determined by the condition that the spectrum be flat: $\varepsilon(\mathbf{p}) = \mu$. If we take the Landau equation (3) into account, this condition again reduces to Eqs. (21) and (40) for determining the minimum of the functional $E(n(\mathbf{p}))$.

We construct the functions $F^+(\mathbf{p}, \omega)$ and $G(\mathbf{p}, \omega)$ in the case where the constant λ_0 is finite but small, such that $v(\mathbf{p})$ and $\kappa(\mathbf{p})$ can be found on the basis of the FC solutions of Eq. (21). Then Ξ , $E(\mathbf{p})$ and Δ are given by Eqs. (45), (44), and (37) respectively. Substituting the functions constructed in this manner into (46), we obtain $F^+(\mathbf{p}, \omega)$ and $G(\mathbf{p}, \omega)$ [97]. We note that Eqs. (44) imply that the gap Δ is a linear function of λ_0 under the adopted conditions. As we shall see in Subsection 5.3, this gives rise to high- T_c at common values of the superconducting coupling constant

5.3. The superconducting state at finite temperatures

We assume that the region occupied by FC is small: $(p_f - p_i)/p_F \ll 1$ and $\Delta_1 \ll T_f$. Then, the order parameter $\kappa(\mathbf{p})$ is determined primarily by FC, i.e., the distribution function $n_0(\mathbf{p})$ [74, 75]. To be able to solve Eq. (39) analytically, we adopt the BCS approximation for the interaction [78]: $\lambda_0 V(\mathbf{p}, \mathbf{p}_1) = -\lambda_0$ if $|\varepsilon(\mathbf{p}) - \mu| \leq \omega_D$ and the interaction is zero outside this region, with ω_D being a certain characteristic energy. As a result, the superconducting gap depends only on the temperature, $\Delta(\mathbf{p}) = \Delta_1(T)$, and Eq. (39) becomes

$$1 = N_{FC} \lambda_0 \int_0^{E_0/2} \frac{d\xi}{\sqrt{\xi^2 + \Delta_1^2(0)}} + N_L \lambda_0 \int_{E_0/2}^{\omega_D} \frac{d\xi}{\sqrt{\xi^2 + \Delta_1^2(0)}}. \quad (48)$$

where we introduced the notation $\xi = \varepsilon(\mathbf{p}) - \mu$ and the density of states N_{FC} in the interval $(p_f - p_i)$ or in the E_0 -energy interval. It follows from Eq. (41) that $N_{FC} = (p_f - p_i)/p_F / (2\pi\Delta_1)$. Within the energy interval $(\omega_D - E_0/2)$, the density of states N_L has the standard form $N_L = M_L^*/2\pi$. As $E_0 \rightarrow 0$, Eq. (48) becomes the BCS equation. On the other hand, assuming that $E_0 \leq 2\omega_D$ and discarding the second integral on the right-hand side of Eq. (48), we obtain

$$\begin{aligned} \Delta_1(0) &= \frac{\lambda_0 p_F (p_f - p_i)}{2\pi} \ln(1 + \sqrt{2}) \\ &= 2\beta \varepsilon_F \frac{p_f - p_i}{p_F} \ln(1 + \sqrt{2}), \end{aligned} \quad (49)$$

where $\varepsilon_F = p_F^2/2M_L^*$ is the Fermi energy and $\beta = \lambda_0 M_L^*/2\pi$ is the dimensionless coupling constant. Using the standard value of β for ordinary superconductors, e.g., $\beta \simeq 0.3$, and assuming that $(p_f - p_i)/p_F \simeq 0.2$, we obtain a large value $\Delta_1(0) \sim 0.1\varepsilon_F$ from Eq. (49); for ordinary superconductors, this gap has a much smaller value: $\Delta_1(0) \sim 10^{-3}\varepsilon_F$. With the integral discarded earlier taken into account, we find that

$$\begin{aligned} \Delta_1(0) &\simeq 2\beta \varepsilon_F \frac{p_f - p_i}{p_F} \ln(1 + \sqrt{2}) \\ &+ \Delta_1(0) \beta \ln\left(\frac{2\omega_D}{\Delta_1(0)}\right). \end{aligned} \quad (50)$$

On the right-hand side of Eq. (50), the value of Δ_1 is given by (49). As $E_0 \rightarrow 0$ and $p_f \rightarrow p_F$, the first term on the right-hand side of Eq. (48) is zero, and we obtain the ordinary BCS result with $\Delta_1 \propto \exp(-1/\lambda_0)$. The correction related to the second integral in (48) is small because the second term on the right-hand side of Eq. (50) contains the additional factor β . In what follows, we show that $2T_c \simeq \Delta_1(0)$. The isotopic effect is small in this case, because T_c depends on ω_D logarithmically, but the effect is restored as $E_0 \rightarrow 0$.

At $T \simeq T_c$, Eqs. (41) and (42) are replaced by Eqs. (31) and (33), which also hold for $T_c \leq T \ll T_f$:

$$M_{FC}^* \simeq p_F \frac{p_f - p_i}{4T_c}, \quad E_0 \simeq 4T_c, \quad \text{if } T \simeq T_c; \quad (51)$$

$$M_{FC}^* \simeq p_F \frac{p_f - p_i}{4T}, \quad E_0 \simeq 4T, \quad \text{at } T < T_c. \quad (52)$$

Equation (48) is replaced by its standard generalization valid for finite temperatures:

$$1 = N_{FC} \lambda_0 \int_0^{E_0/2} \frac{d\xi}{\sqrt{\xi^2 + \Delta_1^2}} \tanh \frac{\sqrt{\xi^2 + \Delta_1^2}}{2T} + N_L \lambda_0 \int_{E_0/2}^{\omega_D} \frac{d\xi}{\sqrt{\xi^2 + \Delta_1^2}} \tanh \frac{\sqrt{\xi^2 + \Delta_1^2}}{2T}. \quad (53)$$

Because $\Delta_1(T \rightarrow T_c) \rightarrow 0$, Eq. (53) implies a relation that closely resembles the BCS result [5],

$$2T_c \simeq \Delta_1(0), \quad (54)$$

where $\Delta_1(T = 0)$ is found from Eq. (50). Comparing (41) and (42) with (51) and (52), we see that both M_{FC}^* and E_0 are temperature-independent for $T \leq T_c$.

5.4. Bogoliubov quasiparticles

Equation (39) shows that the superconducting gap depends on the single-particle spectrum $\varepsilon(\mathbf{p})$. On the other hand, it follows from Eq. (37) that $\varepsilon(\mathbf{p})$ depends on $\varepsilon(\mathbf{p})$ if Eq. (40) has a solution that determines the existence of FC as $\lambda_0 \rightarrow 0$. We assume that λ_0 is so small that the pairing interaction $\lambda_0 V(\mathbf{p}, \mathbf{p}_1)$ leads only to a small perturbation of the order parameter $\kappa(\mathbf{p})$. Equation (41) implies that the effective mass and the density of states $N(0) \propto M_{FC}^* \propto 1/\Delta_1$ are finite. Thus, in contrast to the spectrum in the standard superconductivity theory, the single-particle spectrum $\varepsilon(\mathbf{p})$ depends strongly on the superconducting gap, and Eqs. (3) and (39) must be solved by a self-consistent method.

We assume that Eqs. (3) and (39) have been solved and the effective mass M_{FC}^* has been found. This means that we can find the quasiparticle dispersion law $\varepsilon(\mathbf{p})$ by choosing the effective mass M^* equal to the obtained value of M_{FC}^* and then solve Eq. (39) without taking (3) into account, as is done in the standard BCS superconductivity theory [78]. Hence, the superconducting state with FC is characterized by Bogoliubov quasiparticles [98] with dispersion (38) and the normalization condition $v^2(\mathbf{p}) + u^2(\mathbf{p}) = 1$ for the coefficients $v(\mathbf{p})$ and $u(\mathbf{p})$. Moreover, quasiparticle excitations of the superconducting state in the presence of FC coincide with the Bogoliubov quasiparticles characteristic of the BCS theory, and superconductivity with FC resembling the BCS superconductivity, which points to the applicability of the BCS formalism to the description of the high- T_c superconducting state [99]. At the same time, the maximum value of the superconducting gap set by Eq. (50) and other exotic properties are determined by the presence of FC. These results are in good agreement with the experimental facts obtained for the high- T_c superconductor $\text{Bi}_2\text{Sr}_2\text{Ca}_2\text{Cu}_3\text{O}_{10+\delta}$ [100].

In constructing the superconducting state with FC, we returned to the foundations of the LFL theory, from which the high-energy degrees of freedom had been eliminated by the introduction of quasiparticles. The main difference between the LFL, which forms the basis for constructing the superconducting state, and the Fermi liquid with FC is that in the latter case we must increase the number of low-energy degrees of freedom by introducing the new type of quasiparticle with the effective mass M_{FC}^* and the characteristic energy E_0 given by Eq. (42). Hence, the dispersion law $\varepsilon(\mathbf{p})$ is characterized by two types of quasiparticles with the effective masses M_L^* and M_{FC}^* and the scale E_0 . The extended paradigm and new quasiparticles determine the properties of the superconductor, including the lineshape of quasiparticle excitations [74, 75, 101], while the dispersion of the Bogoliubov quasiparticles has the standard form.

We note that for $T < T_c$, the effective mass M_{FC}^* and the scale E_0 are temperature-independent [101]. For $T > T_c$, the effective mass M_{FC}^* and the scale E_0 are given by Eqs. (31) and (33). Obviously, we cannot directly relate these new quasiparticles (excitations) of the Fermi liquid with FC to excitations (quasiparticles) of an ideal Fermi gas, as is done in the standard LFL theory, because the system is beyond FCQPT. The properties and dynamics of quasiparticles are given by the extended paradigm and closely related to the properties of the superconducting state and are of a collective nature, formed by FCQPT and determined by the macroscopic number of FC quasiparticles with momenta in the interval $(p_f - p_i)$. Such a system cannot be perturbed by scattering on impurities and lattice defects and, therefore, has the features of a quantum protectorate and demonstrates universal behavior [74, 75, 84, 85].

Several remarks concerning the quantum protectorate and the universal behavior of superconductors with FC are in order. Similarly to the Landau Fermi liquid theory, the theory of high- T_c superconductivity based on FCQPT deals with quasiparticles that are elementary low-energy excitations. The theory provides a qualitative general description of the superconducting and the normal states of superconductors and HF metals. Of course, with phenomenological parameters (e.g., the pairing coupling constant) chosen, we can obtain a quantitative description of superconductivity, in the same way as this can be done in the Landau theory when describing a normal Fermi liquid, e.g., ^3He . Hence, any theory capable of describing FC and compatible with the BCS theory gives the same qualitative picture of the superconducting and normal states as the picture based on FCQPT. Obviously, both approaches may be coordinated on the level of numerical results by choosing the appropriate parameters. For instance, because the formation of FC is possible in the Hubbard model [83], it allows reproducing the results of the theory based on FCQPT. It is appropriate to note here that the corresponding description restricted to the case of $T = 0$ has been obtained within the framework of the Hubbard model [102, 103].

5.5. The pseudogap

We now discuss some features of the superconducting state with FC [57, 87, 104] considering two possible types of the superconducting gap $\Delta(\mathbf{p})$ determined by Eq. (39) and the interaction $\lambda_0 V(\mathbf{p}, \mathbf{p}_1)$. If the interaction is caused by attraction, occurring, for instance, as a result of an exchange of phonons or magnetic excitations, the solution of Eq. (39) with an s -wave or $s + d$ -mixed waves has the lowest energy. If the pairing interaction $\lambda_0 V(\mathbf{p}_1, \mathbf{p}_2)$ is a combination of an attractive interaction and a strongly repulsive interaction, d -wave superconductivity may occur (e.g., see Refs [105, 106]). However, both the s - and d -wave symmetries lead to approximately the same result for the size of the gap Δ_1 in Eq. (50). Hence, d -wave superconductivity is not a universal and necessary property of high- T_c superconductors. This conclusion agrees with the experimental evidence described in Refs. [107, 108, 109, 110, 111].

We can define the critical temperature T^* as the temperature at which $\Delta_1(T^*) \equiv 0$. For $T \geq T^*$, Eq. (53) has only the trivial solution $\Delta_1 \equiv 0$. On the other hand, the critical temperature T_c can be defined as the temperature at which superconductivity disappears and the gap occupies only a part of the Fermi surface. Thus, there are two different temperatures T_c and T^* , which may not coincide in the case of the d -wave symmetry of the gap. As shown in Refs [57, 87], in the presence of FC, Eq. (53) has nontrivial solutions at $T_c \leq T \leq T^*$, when the pairing interaction $\lambda_0 V(\mathbf{p}_1, \mathbf{p}_2)$ consists of attraction and strong repulsion, which leads to d -wave superconductivity. In this case, the gap $\Delta(\mathbf{p})$ as a function of the angle ϕ , or $\Delta(\mathbf{p}) = \Delta(p_F, \phi)$, has new nodes at $T > T_{node}$, as shown in Fig. 7 [87].

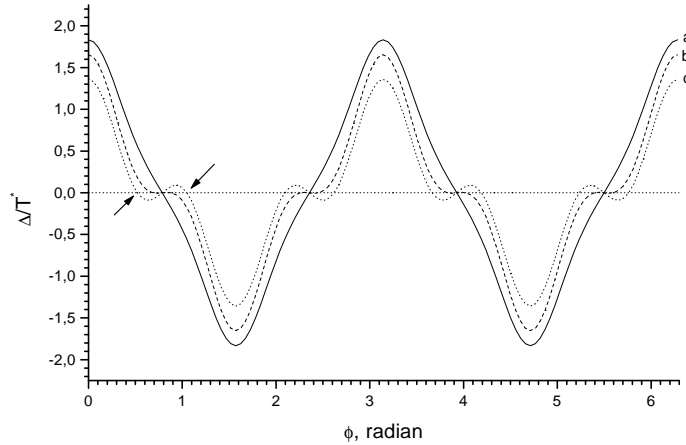


Figure 7: The gap $\Delta(p_F, \phi)$ as a function of ϕ calculated for three values of the temperature expressed in units of $T_{node} \approx T_c$. The solid curve (a) represents the function $\Delta(p_F, \phi)$ calculated for the temperature $0.9 T_{node}$. The dashed curves (b) represents the same function at $T = T_{node}$, and the dotted curve (c) depicts the function calculated at $1.2 T_{node}$. The arrows indicate the region θ_c limited by the two new zeros that emerge at $T > T_{node}$.

Figure 7 shows the ratio $\Delta(p_F, \phi)/T^*$ calculated for three temperatures: $0.9 T_{node}$, T_{node} and $1.2 T_{node}$. In contrast to

curve (a), curves (b) and (c) have flat sections. Clearly, the flattening occurs because of the two new zeros that emerge at $T = T_{node}$. As the temperature increases, the region θ_c between the zeros (indicated by arrows in Fig. 7) increases in size. It is also clear that the gap Δ is very small within the interval θ_c . It was found in [112, 113] that the magnetism and the superconductivity affect each other, which leads to suppression of the magnetism at temperatures below T_c . In view of this, we can expect suppression of superconductivity due to magnetism.

Thus, we may conclude that the gap in the vicinity of T_c can be destroyed by strong antiferromagnetic correlations (or spin density waves), impurities, and sizable inhomogeneities existing in high- T_c superconductors [114]. Because the superconducting gap is destroyed in a macroscopic region of the phase space, θ_c , superconductivity is also destroyed, and therefore $T_c \simeq T_{node}$. The exact value of T_c is determined by the competition between the antiferromagnetic state (or spin density waves) and the superconductivity in the interval θ_c . The behavior and the shape of the pseudogap closely resemble the similar characteristics of the superconducting gap, as Fig. 7 shows. The main difference is that the pseudogap disappears in the segment θ_c of the Fermi surface, while the gap disappears at isolated nodes of the d -wave. This result is in accord with observations [115]. Our estimates show that for small values of the angle ψ , the function $\theta_c(\psi)$ rapidly increases, $\theta_c(\psi) \simeq \sqrt{\psi}$. These estimates agree with the results of numerical calculations of the function $\theta_c([T - T_c]/T_c)$, (Fig. 8). Hence, we may conclude that T_c is close to T_{node} . Thus, the pseudogap state appears at $T \geq T_c \simeq T_{node}$ and

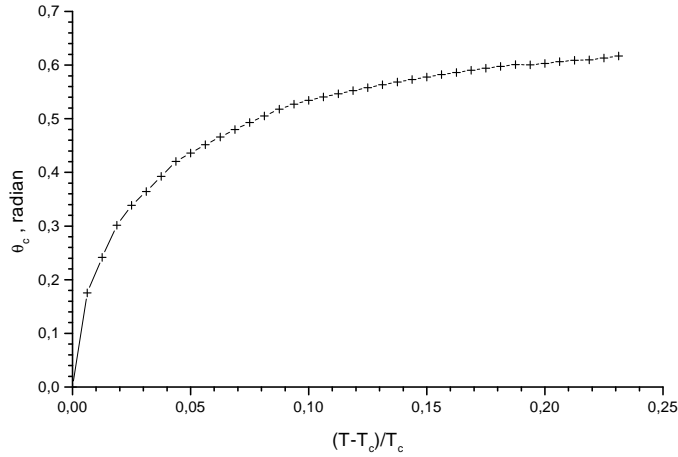


Figure 8: . The result of a numerical calculation of the angle θ_c separating two zeros as a function of $(T - T_c)/T_c$.

disappears at temperatures $T \geq T^*$ at which Eq. (53) has only the trivial solution $\Delta_1 \equiv 0$. Obviously, Δ_1 determines T^* and not T_c , with the result that Eq. (54) should be rewritten as

$$2T^* \simeq \Delta_1(0). \quad (55)$$

The temperature T^* has the physical meaning of the temperature of the BCS transition between the state with the order parameter $\kappa \neq 0$ and the normal state.

At temperatures below $T < T_c$, the quasiparticle excitations of the superconducting state are characterized by the presence of sharp peaks. When the temperature becomes high ($T > T_c$) and $\Delta(\theta) \equiv 0$ in the interval θ_c , normal quasiparticle excitations with a width γ appear in the segments θ_c of the Fermi surface. A pseudogap exists outside the segments θ_c , and the Fermi surface is occupied by excitations of the BCS type in this region. Excitations of both types have widths of the same order of magnitude, transferring their energy and momenta into excitations of normal quasiparticles. These results are in accord with strong indications of the pairing or the formation of preformed pairs in the pseudogap regime at temperatures above T_c [115, 116, 117, 118, 119, 120].

We now estimate the value of γ . If the entire Fermi surface were occupied by the normal state, the width γ would be $\gamma \approx N(0)^3 T^2 / \varepsilon_d(T)^2$ with the density of states $N(0) \sim M^*(T) \sim 1/T$ [see Eq. (31)]. The dielectric constant $\varepsilon_d(T) \sim N(0)$

and, hence, $\gamma \sim T$ [51, 52]. However, only a part of the Fermi surface within θ_c is occupied by normal excitations in our case. Therefore, the number of states accessible for quasiparticles and quasiholes is proportional to θ_c , and the factor T^2 is replaced by the factor $T^2\theta_c^2$. Taking all this into account yields $\gamma \sim \theta_c^2 T \sim T(T - T_c)/T_c \sim (T - T_c)$. Here, we ignored the small contribution provided by excitations of the BCS type. It is precisely for this reason that the width γ vanishes at $T = T_c$. Moreover, the resistivity of the normal state $\rho(T) \propto \gamma \propto (T - T_c)$, because $\gamma \sim (T - T_c)$. Obviously, at temperatures $T > T^*$, the relation $\rho(T) \propto \gamma \propto T$ remains valid up to $T \sim T_f$, and T_f may be as high as the Fermi energy if FC occupies a significant part of the Fermi volume.

The temperature T_{node} is determined mainly by the repulsive interaction, which is part of the pairing interaction $\lambda_0 V(\mathbf{p}_1, \mathbf{p}_2)$. The value of the repulsive interaction, in turn, may be determined by the properties of the materials, such as composition or doping. Because superconductivity is destroyed at $T_c \simeq T_{node}$, the ratio $2\Delta_1/T_c$ may vary within broad limits and strongly depends on the properties of the material [57, 87, 104]. For instance, in the case of $\text{Bi}_2\text{Sr}_2\text{CaCu}_2\text{O}_{6+\delta}$ it is assumed that superconductivity and the pseudogap are of common origin: $2\Delta_1/T_c \simeq 28$, while $2\Delta_1/T^* \simeq 4$, which agrees with the experimental data obtained in measurements involving other high- T_c superconductors [105].

We note that Eq. (55) also provides a good description of the maximum value of the gap Δ_1 in the case of d -wave superconductivity, because different regions with the maximum density of states may be considered unrelated [106]. We may also conclude that without a strong repulsion, with which s -wave pairing is possible, there can be no pseudogap. Thus, the transition from the superconducting gap to the pseudogap may proceed only in the case of d -wave pairing, when superconductivity is destroyed at $T_c \simeq T_{node}$ and the superconducting gap gradually transforms into a pseudogap, which closes at a certain temperature $T^* > T_c$ [57, 87, 104]. The fact that there is no pseudogap in the case of s -wave pairing agrees with the experimental data (e.g., see Ref. [111]).

5.6. Dependence of the critical temperature T_c of the superconducting phase transition on doping

We examine the maximum value of the superconducting gap Δ_1 as a function of the number density x of mobile charge carriers, which is proportional to the degree of doping. Using Eq. (34), we can rewrite Eq. (49) as

$$\frac{\Delta_1}{\varepsilon_F} \sim \beta \frac{(x_{FC} - x)x}{x_{FC}}. \quad (56)$$

where we took into account that the Fermi level $\varepsilon_F \propto p_F^2$ and that the number density $x \sim p_F^2/(2M^*)$, with the result that $\varepsilon_F \propto x$. It is realistic to assume that $T_c \propto \Delta_1$, because the curve $T_c(x)$ obtained in experiments with high- T_c superconductors [2] must be a smooth function of x . Hence, we can approximate $T_c(x)$ by a smooth bell-shape function [121]:

$$T_c(x) \propto \beta(x_{FC} - x)x. \quad (57)$$

To illustrate the application of the above analysis, we examine the main features of a superconductor that can hypothetically exist at room temperature. Such a superconductor must be a two-dimensional structure, just as high- T_c superconducting cuprates are. Equation (49) implies that $\Delta_1 \sim \beta\varepsilon_F \propto \beta/r_s^2$. Bearing in mind that FCQPT occurs at $r_s \sim 20$ in 3D systems and at $r_s \sim 8$ in 2D systems [70], we can expect that in 3D systems Δ_1 amounts to 10% of the maximum size of the superconducting gap in 2D systems, which in our case amounts to 60 mV for lightly doped cuprates with $T_c = 70$ K [122]. On the other hand, Eq. (49) implies that Δ_1 may be even larger, $\Delta_1 \sim 75$ mV. We can expect that $T_c \sim 300$ K in the case of s -wave pairing, as the simple relation $2T_c \simeq \Delta_1$ implies. Indeed, we can take $\varepsilon_F \sim 500$ mV, $\beta \sim 0.3$, and $(p_f - p_i)/p_F \sim 0.5$.

Thus, the hypothetical superconductor at room temperature must be an s -wave superconductor in order to eliminate the pseudogap effect, which dramatically decreases the temperature T_c at which superconductivity is destroyed. We note that the number density x of mobile charge carriers must satisfy the condition $x \leq x_{FC}$ and must be varied to reach the optimum degree of doping $x_{opt} \simeq x_{FC}/2$.

5.7. The gap and heat capacity near T_c

We now calculate the gap and heat capacity at temperatures $T \rightarrow T_c$. Our analysis is valid if $T^* \simeq T_c$, since otherwise the discontinuities in the heat capacity considered below are smeared over the temperature interval between T^* and T_c . To simplify matters, we calculate the leading contribution to the gap and heat capacity related to FC. We use Eq. (53) to

find the function $\Delta_1(T \rightarrow T_c)$ simply by expanding the first integral on its right-hand side in powers of Δ_1 and dropping the contribution from the second integral. This procedure leads to the equation [101]

$$\Delta_1(T) \simeq 3.4T_c \sqrt{1 - \frac{T}{T_c}}. \quad (58)$$

Therefore, the gap in the spectrum of single-particle excitations behaves in the ordinary manner.

To calculate the heat capacity, we can use the standard expression for the entropy S [78]:

$$\begin{aligned} S(T) &= -2 \int [f(\mathbf{p}) \ln f(\mathbf{p}) + (1 - f(\mathbf{p})) \\ &\times \ln(1 - f(\mathbf{p}))] \frac{d\mathbf{p}}{(2\pi)^2}, \end{aligned} \quad (59)$$

where

$$\begin{aligned} f(\mathbf{p}) &= (1 + \exp[E(\mathbf{p})/T])^{-1}, \\ E(\mathbf{p}) &= \sqrt{(\varepsilon(\mathbf{p}) - \mu)^2 + \Delta_1^2(T)}. \end{aligned} \quad (60)$$

The heat capacity C is given by

$$\begin{aligned} C(T) &= T \frac{dS}{dT} \simeq 4 \frac{N_{FC}}{T^2} \int_0^{E_0} f(E)(1 - f(E)) \\ &\times \left[E^2 + T \Delta_1(T) \frac{d\Delta_1(T)}{dT} \right] d\xi \\ &+ 4 \frac{N_L}{T^2} \int_{E_0}^{\omega_D} f(E)(1 - f(E)) \\ &\times \left[E^2 + T \Delta_1(T) \frac{d\Delta_1(T)}{dT} \right] d\xi. \end{aligned} \quad (61)$$

In deriving Eq. (61), we again used the variable ξ , the above notation for the density of states, N_{FC} and N_L , and the notation $E = \sqrt{\xi^2 + \Delta_1^2(T)}$. Equation (61) describes a jump in heat capacity, $\delta C(T) = C_s(T) - C_n(T)$, where $C_s(T)$ and $C_n(T)$ are respectively the heat capacities of the superconducting and normal states at T_c ; the jump is determined by the last two terms in the square brackets on the right-hand side of this equation. Using Eq. (58) to calculate the first term on the right-hand side of Eq. (61), we find [101]

$$\delta C(T_c) \simeq \frac{3}{2\pi^2} (p_f - p_i) p_F^n. \quad (62)$$

where $n = 1$ in the 2D case and $n = 2$ in the 3D case. This result differs from the ordinary BCS result, according to which the discontinuity in the heat capacity is a linear function of T_c . The jump $\delta C(T_c)$ is independent of T_c because, as Eq. (52) shows, the density of state varies in inverse proportion to T_c . We note that in deriving Eq. (62) we took the leading contribution coming from FC into account. This contribution disappears as $E_0 \rightarrow 0$, and the second integral on the right-hand side of Eq. (61) yields the standard result.

As we will show in Section 10 [see Eq. (134)], the heat capacity of a system with FC behaves as $C_n(T) \propto \sqrt{T/T_f}$. The jump in the heat capacity given by Eq. (62) is temperature-independent. As a result, we find that

$$\frac{\delta C(T_c)}{C_n(T_c)} \sim \sqrt{\frac{T_f}{T_c}} \frac{(p_f - p_i)}{p_F}. \quad (63)$$

In contrast to the case of normal superconductors, in which $\delta C(T_c)/C_n(T_c) = 1.43$ [20], in our case Eq. (63) implies that the ratio $\delta C(T_c)/C_n(T_c)$ is not constant and may be very large when $T_f/T_c \gg 1$ [79, 101]. It is instructive to apply this analysis to CeCoIn₅, where $T_c = 2.3$ K [79]. In this material [123], $\delta C/C_n \simeq 4.5$ is substantially higher than the BCS value, in agreement with Eq. (63).

6. The dispersion law and lineshape of single-particle excitations

The recently discovered break in the dispersion of quasiparticles at energies between 40 and 70 mV, resulting in a change in the quasiparticle speed at this energy [88, 89, 90, 91], can hardly be explained by the marginal Fermi-liquid theory, because this theory contains no additional energy scales or parameters that would allow taking the break into account [76, 77]. We could assume that the break, which leads to a new energy scale, occurs because of the interaction of electrons and collective excitations, but then we would have to discard the idea of a quantum protectorate, which would contradict the experimental data [84, 85].

As shown in Sections 4 and 5, a system with FC has two effective masses: M_{FC}^* , which determines the single-particle spectrum at low energies, and M_L^* , which determines the spectrum at high energies. The fact that there are two effective masses manifests itself in the form of a break in the quasiparticle dispersion law. The dispersion law can be approximated by two straight lines intersecting at a binding energy $E_0/2$ [see Eqs. (33) and (42)]. The break in the dispersion law occurs at temperatures much lower than $T \ll T_f$, when the system is in the superconducting or normal state. Such behavior is in good agreement with the experimental data [88]. It is pertinent to note that at temperatures below $T < T_c$, the effective mass M_{FC}^* is independent of the momenta p_F , p_f , and p_i , as shown by Eqs. (41) and (49):

$$M_{FC}^* \sim \frac{2\pi}{\lambda_0}. \quad (64)$$

This formula implies that M_{FC}^* is only weakly dependent on x if a dependence of λ_0 on x is allowed. This result is in good agreement with the experimental facts [124, 125, 126]. The same is true of the dependence of the Fermi velocity $v_F = p_F/M_{FC}^*$ on x because the Fermi momentum $p_F \sim \sqrt{n}$ is weakly dependent on the electron number density $n = n_0(1 - x)$ [124, 125]; here, n_0 is the single-particle electron number density at half-filling.

Because λ_0 is the coupling constant that determines the magnitude of the pairing interaction, e.g., the electron-phonon interaction, we can expect the break in the quasiparticle dispersion law to be caused by the electron-phonon interaction. The phonon scenario could explain the constancy of the break at $T > T_c$ because phonons are temperature independent. On the other hand, it was found that the quasiparticle dispersion law distorted by the interaction with phonons has a tendency to restore itself to the ordinary single particle dispersion law when the quasiparticle energy becomes higher than the phonon energy [127]. However, there is no experimental evidence that such restoration of the dispersion law actually takes place [88].

The quasiparticle excitation curve $L(q, \omega)$ is a function of two variables. Measurements at a constant energy $\omega = \omega_0$, where ω_0 is the single particle excitation energy, determine the curve $L(q, \omega = \omega_0)$ as a function of the momentum q . We established above that M_{FC}^* is finite and constant at temperatures not exceeding T_c . Hence, at excitation energies $\omega < E_0$, the system behaves as an ordinary superconducting Fermi liquid with the effective mass determined by Eq. (41) [74, 75, 87]. At $T_c \leq T$, the effective mass M_{FC}^* is also finite and is given by Eq. (31). In other words, at $\omega < E_0$, the system behaves as a Fermi liquid whose single-particle spectrum is well defined and the width of the single-particle excitations is of the order of T [74, 75, 51]. Such behavior has been observed in experiments in measuring the quasiparticle excitation curve at a fixed energy [34, 90, 128].

The quasiparticle excitation curve can also be described as a function of ω , at a constant momentum $q = q_0$. For small values of ω , the behavior of this function is similar to that described above, with $L(q = q_0, \omega)$ having a characteristic maximum and width. For $\omega \geq E_0$, the contribution provided by quasiparticles of mass M_L^* becomes significant and leads to an increase in the function $L(q = q_0, \omega)$. Thus, $L(q = q_0, \omega)$ has a certain structure of maxima and minima [129] directly determined by the existence of two effective masses, M_{FC}^* and M_L^* [74, 75, 87]. We conclude that, in contrast to Landau quasiparticles, these quasiparticles have a more complicated spectral lineshape.

We use the Kramers-Kronig transformation to calculate the imaginary part $\text{Im}\Sigma(\mathbf{p}, \varepsilon)$ of the self-energy part $\Sigma(\mathbf{p}, \varepsilon)$. But we begin with the real part $\text{Re}\Sigma(\mathbf{p}, \varepsilon)$, which determines the effective mass M^* [130],

$$\frac{1}{M^*} = \left(\frac{1}{m} + \frac{1}{p_F} \frac{\partial \text{Re}\Sigma}{\partial p} \right) \left(1 - \frac{\partial \text{Re}\Sigma}{\partial \varepsilon} \right). \quad (65)$$

The corresponding momenta p and energies ε satisfy the inequalities $|p - p_F|/p_F \ll 1$, and $\varepsilon/\varepsilon_F \ll 1$. We take $\text{Re}\Sigma(\mathbf{p}, \varepsilon)$

in the simplest form possible that ensures the variation of the effective mass at the energy $E_0/2$,

$$\begin{aligned} \text{Re}\Sigma(\mathbf{p}, \varepsilon) &= -\varepsilon \frac{M_{FC}^*}{m} + \left(\varepsilon - \frac{E_0}{2}\right) \frac{M_{FC}^* - M_L^*}{m} \\ &\times \left[\theta\left(\varepsilon - \frac{E_0}{2}\right) + \theta\left(-\varepsilon - \frac{E_0}{2}\right) \right], \end{aligned} \quad (66)$$

where $\theta(\varepsilon)$ is the step function. To ensure a smooth transition from the single-particle spectrum characterized by M_{FC}^* to the spectrum characterized by M_L^* , we must replace the step function with a smoother function. Substituting Eq. (66) in Eq. (65), we see that $M^* \simeq M_{FC}^*$ within the interval $(-E_0/2, E_0/2)$, while $M^* \simeq M_L^*$ outside this interval. Applying the Kramers-Kronig transformation to $\text{Re}\Sigma(\mathbf{p}, \varepsilon)$, we express the imaginary part of the self-energy as [101]

$$\begin{aligned} \text{Im}\Sigma(\mathbf{p}, \varepsilon) &\sim \varepsilon^2 \frac{M_{FC}^*}{\varepsilon_F m} + \frac{M_{FC}^* - M_L^*}{m} \\ &\times \left[\varepsilon \ln \left| \frac{2\varepsilon + E_0}{2\varepsilon - E_0} \right| + \frac{E_0}{2} \ln \left| \frac{4\varepsilon^2 - E_0^2}{E_0^2} \right| \right]. \end{aligned} \quad (67)$$

Clearly, with $\varepsilon/E_0 \ll 1$, the imaginary part is proportional to ε^2 ; at $2\varepsilon/E_0 \simeq 1$, we have $\text{Im}\Sigma \sim \varepsilon$, and for $E_0/\varepsilon \ll 1$, the main contribution to the imaginary part is approximately constant.

It follows from Eq. (67) that as $E_0 \rightarrow 0$, the second term on its right-hand side tends to zero and the single-particle excitations become well-defined, which resembles the situation with a normal Fermi liquid, while the pattern of minima and maxima eventually disappears. Now the quasiparticle renormalization factor $z(\mathbf{p})$ is given by the equation [130]

$$\frac{1}{z(\mathbf{p})} = 1 - \frac{\partial \text{Re}\Sigma(\mathbf{p}, \varepsilon)}{\partial \varepsilon}. \quad (68)$$

Consequently, from Eqs. (67) and (68) for $T \leq T_c$, the amplitude of a quasiparticle on the Fermi surface increases as the characteristic energy E_0 decreases. Equations (42) and (57) imply that $E_0 \sim (x_{FC} - x)/x_{FC}$. When $T > T_c$, it follows from (66) and (68) that the quasiparticle amplitude increases as the effective mass M_{FC}^* decreases. So, from Eqs. (31) and (34) $M_{FC}^* \sim (p_f - p_i)/p_F \sim (x_{FC} - x)/x_{FC}$. As a result, we conclude that the amplitude increases with the doping level and the single-particle excitations are better defined in heavily doped samples. As $x \rightarrow x_{FC}$, the characteristic energy $E_0 \rightarrow 0$ and the quasiparticles become normal excitations of LFL. We note that such behavior has been observed in experiments with heavily doped Bi2212, which demonstrates high- T_c superconductivity with a gap of about 10 mV [131]. The size of the gap suggests that the region occupied by FC is small because $E_0/2 \simeq \Delta_1$. For $x > x_{FC}$ and low temperatures, the HF liquid behaves as LFL (see Fig. 6 and Section 9). Experimental data show that, as expected, the LFL state exists in super-heavily doped nonsuperconducting $\text{La}_{1.7}\text{Sr}_{0.3}\text{CuO}_4$ [132, 133].

7. Electron liquid with FC in magnetic fields

In this Section, we discuss the behavior of HF liquid with FC in magnetic field. We assume that the coupling constant is nonzero, $\lambda_0 \neq 0$, but is infinitely small. We found in Section 5 that at $T = 0$ the superconducting order parameter $\kappa(\mathbf{p})$ is finite in the region occupied by FC and that the maximum value of the superconducting gap $\Delta_1 \propto \lambda_0$ is infinitely small. Hence, any weak magnetic field $B \neq 0$ is critical and destroys $\kappa(\mathbf{p})$ and FC. Simple energy arguments suffice to determine the type of rearrangement of the FC state. On the one hand, because the FC state is destroyed, the gain in energy $\Delta E_B \propto B^2$ tends to zero as $B \rightarrow 0$. On the other hand, the function $n_0(\mathbf{p})$, which occupies the finite interval $(p_f - p_i)$ in the momentum space and is specified by Eq. (21) or (42), leads to a finite gain in the ground-state energy compared to the ground-state energy of a normal Fermi liquid [41]. Thus, the distribution function is to be reconstructed so that the order parameter is to vanish while a new distribution function is to deliver the same ground state energy.

7.1. Phase diagram of electron liquid in magnetic field

Thus, in weak magnetic fields, the new ground state without FC must have almost the same energy as the state with FC. As shown in Section 15, such a state is formed by multiply connected Fermi spheres resembling an onion, in which

a smooth distribution function of quasiparticles, $n_0(\mathbf{p})$, is replaced in the interval $(p_f - p_i)$ with the distribution function [94, 134]

$$v(\mathbf{p}) = \sum_{k=1}^n \theta(p - p_{2k-1})\theta(p_{2k} - p). \quad (69)$$

where the parameters $p_i \leq p_1 < p_2 < \dots < p_{2n} \leq p_f$ are chosen such that they satisfy the normalization condition and the condition needed for the conservation of the number of particles:

$$\int_{p_{2k-1}}^{p_{2k+3}} v(\mathbf{p}) \frac{d\mathbf{p}}{(2\pi)^3} = \int_{p_{2k-1}}^{p_{2k+3}} n_0(\mathbf{p}) \frac{d\mathbf{p}}{(2\pi)^3}.$$

Figure 9 shows the corresponding multiply connected distribution. For definiteness, we present the most interesting case of a three-dimensional system. The two-dimensional case can be examined similarly. We note that the possibility of the existence of multiply connected Fermi spheres was studied in e.g. [23, 135, 136, 137].

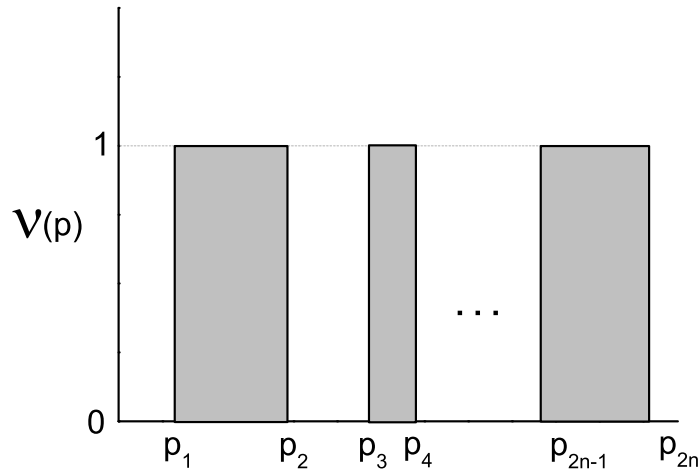


Figure 9: The function $v(\mathbf{p})$ for the multiply connected distribution that replaces the function $n_0(\mathbf{p})$ in the region $(p_f - p_i)$ occupied by FC. The momenta satisfy the inequalities $p_i < p_F < p_f$. The outer Fermi surface at $p \approx p_{2n} \approx p_f$ has the shape of a Fermi step, and therefore the system behaves like LFL at sufficiently low temperatures.

We assume that the thickness of each inner slice of the Fermi sphere, $\delta p \approx p_{2k+1} - p_{2k}$, is determined by the magnetic field B . Using the well-known rule for estimating errors in calculating integrals, we find that the minimum loss of the ground-state energy due to slice formation is approximately $(\delta p)^4$. This becomes especially clear if we account for the fact that the continuous FC functions $n_0(\mathbf{p})$ ensure the minimum value of the energy functional $E[n(\mathbf{p})]$, while the approximation of $v(\mathbf{p})$ by steps of width δp leads to a minimal error of the order of $(\delta p)^4$. Recalling that the gain due to the magnetic field is proportional to B^2 and equating the two contributions, we obtain

$$\delta p \propto \sqrt{B}. \quad (70)$$

Therefore, as $T \rightarrow 0$, with $B \rightarrow 0$, the slice thickness δp also tends to zero and the behavior of a Fermi liquid with FC is replaced with that of LFL with the Fermi momentum p_f . Equation (40) implies that $p_f > p_F$ and the electron number density x remains constant, with the Fermi momentum of the multiply connected Fermi sphere $p_{2n} \approx p_f > p_F$ (see Fig. 9). We see in what follows that these observations play an important role in studying the behavior of the Hall coefficients $R_H(B)$ as a function of B in heavy-fermion metals at low temperatures.

To calculate the effective mass $M^*(B)$ as a function of the applied magnetic field B , we first note that at $T = 0$ the field B splits the FC state into Landau levels, suppresses the superconducting order parameter $\kappa(\mathbf{p})$, and destroys FC,

which leads to restoration of LFL [49, 138]. The Landau levels near the Fermi surface can be approximated by separate slices whose thickness in momentum space is δp . Approximating the quasiparticle dispersion law within a single slice, $\varepsilon(p) - \mu \sim (p - p_f + \delta p)(p - p_f)/M^*$, we find the effective mass $M^*(B) \sim M^*/(\delta p/p_f)$. The energy increment ΔE_{FC} caused by the transformation of the FC state can be estimated based on the Landau formula [20]

$$\Delta E_{FC} = \int (\varepsilon(\mathbf{p}) - \mu) \delta n(\mathbf{p}) \frac{d\mathbf{p}^3}{(2\pi)^3}. \quad (71)$$

The region occupied by the variation $\delta n(\mathbf{p})$ has the thickness δp , with $(\varepsilon(\mathbf{p}) - \mu) \sim (p - p_f)p_f/M^*(B) \sim \delta p p_f/M^*(B)$. As a result, we find that $\Delta E_{FC} \sim p_f^3 \delta p^2/M^*(B)$. On the other hand, there is the addition $\Delta E_B \sim (B\mu_B)^2 M^*(B) p_f$ caused by the applied magnetic field, which decreases the energy and is related to the Zeeman splitting. Equating ΔE_B and ΔE_{FC} and recalling that $M^*(B) \propto 1/\delta p$ in this case, we obtain the chain of relations

$$\frac{\delta p^2}{M^*(B)} \propto \frac{1}{(M^*(B))^3} \propto B^2 M^*(B), \quad (72)$$

which implies that the effective mass $M^*(B)$ diverges as

$$M^*(B) \propto \frac{1}{\sqrt{B - B_{c0}}}, \quad (73)$$

where B_{c0} is the critical magnetic field, which places HF metal at the magnetic-field-tuned quantum critical point and nullifies the respective Néel temperature, $T_{NL}(B_{c0}) = 0$ [49]. In our simple model of HF liquid, the quantity B_{c0} is a parameter determined by the properties of the specific metal with heavy fermions. We note that in some cases $B_{c0} = 0$, e.g., the HF metal CeRu_2Si_2 has no magnetic order, exhibits no superconductivity, and does not behave like a Landau Fermi liquid even at the lowest reached temperatures [92].

Formula (73) and Fig. 9 show that the application of a magnetic field $B > B_{c0}$ brings the FC system back to the LFL state with the effective mass $M^*(B)$ that depends on the magnetic field. This means that the following characteristic of LFL are restored: $C/T = \gamma_0(B) \propto M^*(B)$ for the heat capacity and $\chi_0(B) \propto M^*(B)$ for the magnetic susceptibility. The coefficient $A(B)$ determines the temperature-dependent part of the resistivity, $\rho(T) = \rho_0 + \Delta\rho$, where ρ_0 is the residual resistivity and $\Delta\rho = A(B)T^2$. Because this coefficient is directly determined by the effective mass, $A(B) \propto (M^*(B))^2$ [139], Eq. (73) yields

$$A(B) \propto \frac{1}{B - B_{c0}}. \quad (74)$$

Thus, the empirical Kadowaki-Woods relation [27] $K = A/\gamma_0^2 \simeq \text{const}$ is valid in our case [139]. Furthermore, K may depend on the degree of degeneracy of the quasiparticles. With this degeneration, the Kadowaki-Woods relation provides a good description of the experimental data for a broad class of HF metals [140, 141]. In the simplest case, where HF liquid is formed by spin-1/2 quasiparticles with the degeneracy degree 2, the value of K turns out to be close to the empirical value [139] known as the Kadowaki-Woods ratio [27]. Hence, under a magnetic field, the system returns to the state of LFL and the constancy of the Kadowaki-Woods relation holds.

At finite temperatures, the system remains in the LFL state, but when $T > T^*(B)$, the NFL behavior is restored. As regards finding the function $T^*(B)$, we note that the effective mass M^* characterizing the single-particle spectrum cannot change at $T^*(B)$ because no phase transition occurs at this temperature. To calculate $M^*(T)$, we equate the effective mass $M^*(T)$ in Eq. (31) to $M^*(B)$ in (73), $M^*(T) \sim M^*(B)$,

$$\frac{1}{M^*(T)} \propto T^*(B) \propto \frac{1}{M^*(B)} \propto \sqrt{B - B_{c0}}, \quad (75)$$

whence

$$T^*(B) \propto \sqrt{B - B_{c0}}. \quad (76)$$

At temperatures $T \geq T^*(B)$, the system returns to the NFL behavior and the effective mass M^* specified by Eq. (31). Thus, expression (76) determines the line in the $T - B$ phase diagram that separates the region where the effective mass depends on B and the heavy Fermi liquid behaves like a Landau Fermi liquid from the region where the effective mass

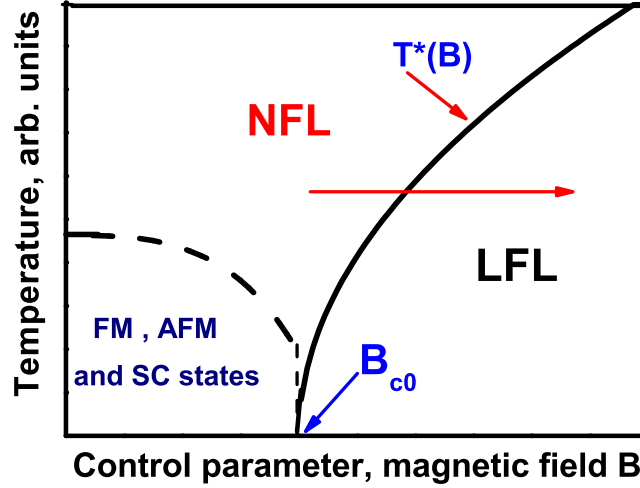


Figure 10: Schematic $T - B$ phase diagram of heavy electron liquid. B_{c0} denotes the magnetic field at which the effective mass diverges as given by (73). The horizontal arrow illustrates the system moving in the NFL-LFL direction along B at fixed temperature. As shown by the dashed curve, at $B < B_{c0}$ the system can be in its ferromagnetic (FM), antiferromagnetic (AFM) or superconducting (SC) states. The NFL state is characterized by the entropy S_0 given by Eq. (27). The solid curve $T^*(B)$ separates the NFL state and the weakly polarized LFL one and represents the transition regime.

is temperature-dependent. At $T^*(B)$, the temperature dependence of the resistivity ceases to be quadratic and becomes linear.

A schematic $T - B$ phase diagram of HF liquid with FC in magnetic field is shown in Fig. 10. At magnetic field $B < B_{c0}$ the FC state can be captured by ferromagnetic (FM), antiferromagnetic (AFM) and superconducting (SC) states lifting the degeneracy of the FC state. It follows from (76) that at a certain temperature $T^*(B) \ll T_f$, the heavy-electron liquid transits from its NFL state to LFL one acquiring the properties of LFL at $(B - B_{c0}) \propto (T^*(B))^2$. At temperatures below $T^*(B)$, as shown by the horizontal arrow in Fig. 10, the heavy-electron liquid demonstrates an increasingly metallic behavior as the magnetic field B increases, because the effective mass decreases [see Eq. (73)]. Such behavior of the effective mass can be observed, for instance, in measurements of the heat capacity, magnetic susceptibility, resistivity, and Shubnikov-de Haas oscillations. From the $T - B$ phase diagram shown in Fig. 10 and constructed in this manner, it follows that a unique possibility emerges where a magnetic field can be used to control the variations in the physical nature and type of behavior of the electron liquid with FC.

We briefly discuss the case where the system is extremely close to FCQPT on the ordered side of this transition, and hence $\delta p_{FC} = (p_f - p_i)/p_F \ll 1$. Because $\delta p \propto M^*(B)$, it follows from Eqs. (70) and (73) that

$$\frac{\delta p}{p_F} \sim a_c \sqrt{\frac{B - B_{c0}}{B_{c0}}}, \quad (77)$$

where a_c is a constant of the order of unity, $a_c \sim 1$. As the magnetic field B increases, $\delta p/p_F$ becomes comparable to δp_{FC} , and the distribution function $\nu(\mathbf{p})$ disappears, being absorbed by the ordinary Zeeman splitting. As a result, we are dealing with HF liquid located on the disordered side of FCQPT. We show in Section 10 that the behavior of such a system differs markedly from that of a system with FC. Equation (77) implies that the relatively weak magnetic field B_{cr} ,

$$B_{red} \equiv \frac{B - B_{c0}}{B_{c0}} = (\delta p_{FC})^2 \sim B_{cr}, \quad (78)$$

where B_{red} is the reduced field, takes the system from the ordered side of the phase transition to the disordered if $\delta p_{FC} \ll 1$.

7.2. Dependence of effective mass on magnetic fields in HF metals and high- T_c superconductors

Observations have shown that in the normal state obtained by applying a magnetic field whose strength is higher than the maximum critical field B_{c2} that destroys superconductivity, the heavily doped cuprate ($Tl_2Ba_2CuO_{6+\delta}$) [26] and

the optimally doped cuprate ($\text{Bi}_2\text{Sr}_2\text{CuO}_{6+\delta}$) [29] exhibit no significant violations of the Wiedemann-Franz law. Studies of the electron-doped superconductor $\text{Pr}_{0.91}\text{LaCe}_{0.09}\text{CuO}_{4-y}$ ($T_c=24$ K), revealed that when a magnetic field destroyed superconductivity in this material, the spin-lattice relaxation constant $1/T_1$ obeyed the relation $T_1T = \text{const}$, known as the Korringa law, down to temperatures about $T \simeq 0.2$ K [142, 143]. At higher temperatures and in magnetic fields up to 15.3 T perpendicular to the CuO_2 plane, the ratio $1/T_1T$ remains constant as a function of T for $T \leq 55$ K. In the temperature range from 50 to 300 K, the ratio $1/T_1T$ decreases as the temperature increases [143]. Measurements involving the heavily doped nonsuperconducting material $\text{La}_{1.7}\text{Sr}_{0.3}\text{CuO}_4$ have shown that the resistivity ρ varies with T as T^2 and that the Wiedemann-Franz law holds [132, 133].

Because the Korringa and Wiedemann-Franz laws strongly indicate the presence of the LFL state, experiments show that the observed elementary excitations cannot be distinguished from Landau quasiparticles in high- T_c superconductors. This places severe restrictions on models describing hole- or electron-doped high- T_c superconductors. For instance, for a Luttinger liquid [144, 145], for spin-charge separation [8], and in some $t-J$ models [146], a violation of the Wiedemann-Franz law was predicted, which contradicts experimental evidence and points to the limited applicability of these models.

If the constant λ_0 is finite, then a HF liquid with FC is in the superconducting state. We examine the behavior of the system in magnetic fields $B > B_{c2}$. In this case, the system becomes LFL induced by the magnetic field, and the elementary excitations become quasiparticles that cannot be distinguished from Landau quasiparticles, with the effective mass $M^*(B)$ given by Eq. (73). As a result, the Wiedemann-Franz law holds as $T \rightarrow 0$, which agrees with the experimental facts [26, 29]. The low-temperature properties of the system depend on the effective mass; in particular, the resistivity $\rho(T)$ behaves as given by Eq. (18), with $A(B) \propto (M^*(B))^2$. Assuming that the critical field $B = B_{c0}$ in the case of high- T_c superconductors, we deduce from Eq. (73) that

$$\gamma_0 \sqrt{B - B_{c0}} = \text{const}. \quad (79)$$

Taking Eqs. (74) and (79) into account, we find that

$$\gamma_0 \sim A(B) \sqrt{B - B_{c0}}. \quad (80)$$

At finite temperatures, the system remains LFL, but for $T > T^*(B)$ the effective mass becomes temperature-dependent, $M^* \propto 1/T$, and the resistivity becomes a linear function of the temperature, $\rho(T) \propto T$ [147]. Such behavior of the resistivity has been observed in the high- T_c superconductor $\text{Tl}_2\text{Ba}_2\text{CuO}_{6+\delta}$ ($T_c < 15$ K) [148]. At $B < 10$ T, the resistivity is a linear function of the temperature in the range from 120 mK to 1.2 K, and at $B = 10$ T the temperature dependence of the resistivity can be written in the form $\rho(T) \propto AT^2$ in the same temperature range [148, 149], clearly demonstrating that the LFL state is restored under the application of magnetic fields.

In LFL, the spin-lattice relaxation parameter $1/T_1$ is determined by the quasiparticles near the Fermi level, whose population is proportional to M^*T , whence $1/T_1T \propto M^*$, and is a constant quantity [142, 143]. When the superconducting state disappears as a magnetic field is applied, the ground state can be regarded as a field-induced LFL with the field-dependent effective mass. As a result, $T_1T = \text{const}$, which implies that the Korringa law holds. According to Eq. (73), the ratio $1/T_1T \propto M^*(B)$ decreases as the magnetic field increases at $T < T^*(B)$, whereas in the case of a Landau Fermi liquid it remains constant, as noted above. On the other hand, at $T > T^*(B)$, the ratio $1/T_1T$ is a decreasing function of the temperature, $1/T_1T \propto M^*(T)$. These results are in good agreement with the experimental facts [143]. Because $T^*(B)$ is an increasing function of the magnetic field [see Eq. (76)], the Korringa law remains valid even at higher temperatures and in stronger magnetic fields. Hence, at $T_0 \leq T^*(B_0)$ and high magnetic fields $B > B_0$, the system demonstrates distinct metallic behavior, because the effective mass decreases as B increases, see Eq. (73).

The existence of FCQPT can also be verified in experiments, because at number densities $x > x_{FC}$ or beyond the FCQPT point, the system must become LFL at sufficiently low temperatures [138]. Experiments have shown that such a liquid indeed exists in the heavily doped non-superconducting compound $\text{La}_{1.7}\text{Sr}_{0.3}\text{CuO}_4$ [132, 133]. It is remarkable that for $T < 55$ K, the resistivity exhibits a T^2 -behavior without an additional linear term and the Wiedemann-Franz law holds [132, 133]. At temperatures above 55 K, experimenters have observed significant deviations from the LFL behavior. Observations [6, 134] are in accord with these experimental findings showing that the system can again be returned to the LFL state by applying sufficiently strong magnetic fields (also see Section 9).

7.2.1. Common QCP in the high- T_c $\text{Tl}_2\text{Ba}_2\text{CuO}_{6+x}$ and the HF metal YbRh_2Si_2

Under the application of magnetic fields $B > B_{c2} > B_{c0}$ and at $T < T^*(B)$, a high- T_c superconductor or HF metal can be driven to the LFL state with its resistivity given by Eq. (18). In that case measurements of the coefficient A produce

information on its dependence on the applied field. We note that relationships between critical magnetic fields B_{c2} and B_{c0} are clarified in Subsection 9.9.

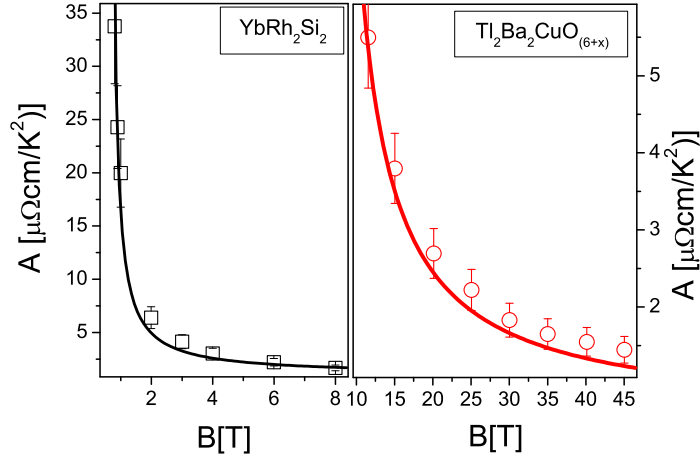


Figure 11: The charge transport coefficient $A(B)$ as a function of magnetic field B obtained in measurements on YbRh_2Si_2 [15] and $\text{Tl}_2\text{Ba}_2\text{CuO}_{6+x}$ [150]. The different field scales are clearly seen. The solid curves represent our fit by using Eq. (81)

Precise measurements of the coefficient $A(B)$ on high- T_c $\text{Tl}_2\text{Ba}_2\text{CuO}_{6+x}$ [150] allow us to establish relationships between the physics of both high- T_c superconductors and HF metals and clarify the role of the extended quasiparticle paradigm. The $A(B)$ coefficient, being proportional to the quasiparticle–quasiparticle scattering cross-section, is found to be $A \propto (M^*(B))^2$ [15, 139]. With respect to Eq. (73), this implies that

$$A(B) \simeq A_0 + \frac{D}{B - B_{c0}}, \quad (81)$$

where A_0 and D are fitting parameters.

Figure 11 reports the fit of our theoretical dependence (81) to the experimental data for the measurements of the coefficient $A(B)$ for two different classes of substances: HF metal YbRh_2Si_2 (with $B_{c0} = 0.06$ T, left panel) [15] and high- T_c $\text{Tl}_2\text{Ba}_2\text{CuO}_{6+x}$ (with $B_{c0} = 5.8$ T, right panel) [150]. In Fig. 11, left panel, $A(B)$ is shown as a function of magnetic field B , applied both along and perpendicular to the c axis. For the latter the B values have been multiplied by a factor of 11 [15]. The different scales of field B_{c0} are clearly seen and demonstrate that B_{c0} has to be taken as an input parameter. Indeed, the critical field of $\text{Tl}_2\text{Ba}_2\text{CuO}_{6+x}$ with $B_{c0} = 5.8$ T is 2 orders of magnitude larger than that of YbRh_2Si_2 with $B_{c0} = 0.06$ T.

Figure 11 displays good coincidence of the theoretical dependence (74) with the experimental facts [150, 151]. This means that the physics underlying the field-induced reentrance of LFL behavior, is the same for both classes of substances. To further corroborate this point, we rewrite Eq. (81) in the reduced variables A/A_0 and B/B_{c0} . Such rewriting immediately reveals the scaling nature of the behavior of these two substances - both of them are driven to common QCP related to FCQPT and induced by the application of magnetic field. As a result, Eq. (81) takes the form

$$\frac{A(B)}{A_0} \simeq 1 + \frac{D_N}{B/B_{c0} - 1}, \quad (82)$$

where $D_N = D/(A_0 B_{c0})$ is a constant. From Eq. (82) it is seen that upon applying the scaling to both coefficients $A(B)$ for $\text{Tl}_2\text{Ba}_2\text{CuO}_{6+x}$ and $A(B)$ for YbRh_2Si_2 they are reduced to a function depending on the single variable B/B_{c0} thus demonstrating universal behavior. To support Eq. (82), we replot both dependencies in reduced variables A/A_0 and B/B_{c0} in Fig. 12. Such replotting immediately reveals the universal scaling nature of the behavior of these two substances. It is seen from Fig. 12 that close to the magnetic induced QCP there are no "external" physical scales revealing the scaling.

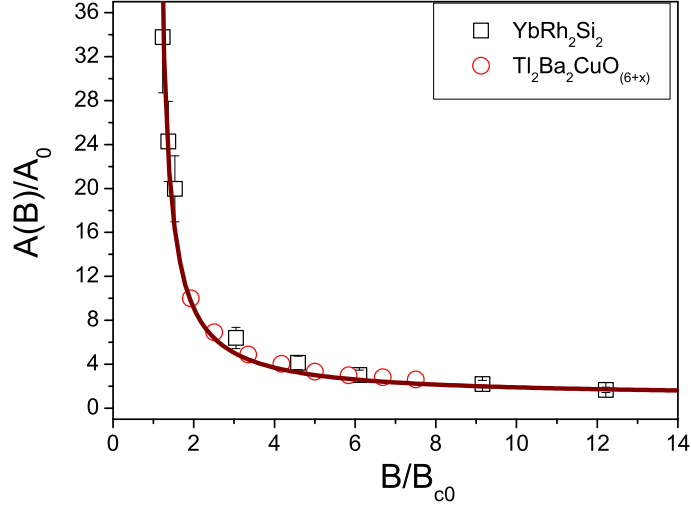


Figure 12: Normalized coefficient $A(B)/A_0 \simeq 1 + D_N/(y - 1)$ given by Eq. (82) as a function of normalized magnetic field $y = B/B_{c0}$ shown by squares for YbRh_2Si_2 and by circles for high- T_c $\text{Tl}_2\text{Ba}_2\text{CuO}_{6+x}$. D_N is the only fitting parameter.

Therefore the normalization by the scales A_0 and B_{c0} immediately reveals the common physical nature of these substances, allowing us to get rid of the specific properties of the system that define the values of A_0 and B_{c0} .

Based on the above analysis of the A coefficients, we conclude that there is at least one quantum phase transition inside the superconducting dome of high- T_c superconductors, and this transition is FCQPT [120].

8. Appearance of FCQPT in Fermi systems

We say that Fermi systems that approach QCP from a disordered state are highly correlated systems in order to distinguish them from strongly correlated systems (or liquids) that are already beyond FCQPT placed at the quantum critical line as shown in Fig. 6. A detailed description of the properties of highly correlated systems are given in Section 9, and the properties of strongly correlated systems are discussed in Section 10. In the present section, we discuss the behavior of the effective mass M^* as a function of the density x of the system as $x \rightarrow x_{FC}$.

The experimental facts for high-density 2D ^3He [64, 72, 152, 153] show that the effective mass becomes divergent when the value of the density at which the 2D liquid ^3He begins to solidify is reached [72]. Also observed was a sharp increase in the effective mass in the metallic 2D electron system as the density x decreases and tends to the critical density of the metal-insulator transition [65]. We note that there is no ferromagnetic instability in the Fermi systems under consideration and the corresponding Landau amplitude $F_0^a > -1$ [65, 72], which agrees with the model of nearly localized fermions [59, 60, 61].

We examine the divergence of the effective mass in 2D and 3D highly correlated Fermi liquids at $T = 0$ as the density $x \rightarrow x_{FC}$ approaching FCQPT from the disordered phase. We begin by calculating M^* as a function of the difference $(x - x_{FC})$ for a 2D Fermi liquid. For this, we use the equation for M^* derived in [70], where the divergence of M^* related to the generation of density wave in various Fermi liquids was predicted. As $x \rightarrow x_{FC}$, the effective mass M^* can be approximately written as

$$\frac{1}{M^*} \simeq \frac{1}{m} + \frac{1}{4\pi^2} \int_{-1}^1 \int_0^{g_0} \frac{ydydg}{\sqrt{1-y^2}} \times \frac{v(q(y))}{[1 - R(q(y), g)\chi_0(q(y))]^2}. \quad (83)$$

Here we use the notation $p_F \sqrt{2(1-y)} = q(y)$, where $q(y)$ is the momentum transfer, $v(y)$ is the pair interaction, the integral with respect to the coupling constant g is taken from zero to the actual value g_0 , $\chi_0(q, \omega)$ is the linear response function for the noninteracting Fermi liquid, and $R(q, \omega)$ is the effective interaction, with both functions taken at $\omega = 0$. The quantities R and χ_0 determine the response function for the system,

$$\chi(q, \omega, g) = \frac{\chi_0(q, \omega)}{1 - R(q, \omega)\chi_0(q, \omega)}. \quad (84)$$

Near the instability related to the generation of density wave at the density x_{cdw} , the singular part of the response function χ has the well-known form, see e.g. [2]

$$\chi^{-1}(q, \omega, g) \simeq a(x_{cdw} - x) + b(q - q_c)^2 + c(g_0 - g), \quad (85)$$

where a , b , and c are constants and $q_c \simeq 2p_F$ is the density-wave momentum. Substituting Eq. (85) in (83) and integrating, we can represent the equation for the effective mass M^* as

$$\frac{1}{M^*(x)} = \frac{1}{m} - \frac{c}{\sqrt{x - x_{cdw}}}, \quad (86)$$

where c is a positive constant. It follows from Eq. (86) that $M^*(x)$ diverges as a function of the difference $(x - x_{FC})$ and $M^*(x) \rightarrow \infty$ as $x \rightarrow x_{FC}$ [62, 63]

$$\frac{M^*(x)}{m} \simeq a_1 + \frac{a_2}{x - x_{FC}}, \quad (87)$$

where a_1 and a_2 are constants. We note that Eqs. (86) and (87) do not explicitly contain the interaction $v(q)$, although $v(q)$ affects a_1 , a_2 and x_{FC} . This result agrees with Eq. (19), which determines the same universal type of divergence (i.e., a divergence that is independent of the interaction). Hence, both Eqs. (19) and (87) can be applied to 2D ^3He , the electron liquid, and other Fermi liquids. We also see that FCQPT precedes the formation of density waves (or charge-density waves) in Fermi systems.

We note that the difference $(x - x_{FC})$ must be positive in both cases, since the density x approaches x_{FC} when the system is on the disordered side of FCQPT with the finite effective mass $M^*(x) > 0$. In the case of ^3He , FCQPT occurs as the density increases, when the potential energy begins to dominate the ground-state energy due to the strong repulsive short ranged part of the inter-particle interaction. Thus, for the 2D ^3He liquid, the difference $(x - x_{FC})$ on the right hand side of Eq. (87) must be replaced with $(x_{FC} - x)$. Experiments have shown that the effective mass indeed diverges at high densities in the case of 2D ^3He and at low densities in the case of 2D electron systems [65, 72].

In Fig. 13, we report the experimental values of the effective mass $M^*(z)$ obtained by the measurements on ^3He monolayer [72]. These measurements, in coincidence with those from Ref. [153, 154], show the divergence of the effective mass at $x = x_{FC}$. To show, that our FCQPT approach is able to describe the above data, we represent the fit of $M^*(z)$ by the fractional expression $M^*(z)/M \propto b_1 + b_2/(1 - z)$ and the reciprocal effective mass by the linear fit $m/M^*(z) \propto b_3 z$. We note here, that the linear fit has been used to describe the experimental data for bilayer ^3He [153, 155] and we use this function here for the sake of illustration. It is seen from Fig. 13 that the data of Ref. [153] (^3He bilayer) can be equally well approximated by both linear and fractional functions, while the data in Ref. [72] cannot. For instance, both fitting functions give for the critical density in bilayer $x_{FC} \approx 9.8 \text{ nm}^{-2}$, while for monolayer [72] these values are different - $x_{FC} = 5.56 \text{ nm}^{-2}$ for linear fit and $x_{FC} = 5.15 \text{ nm}^{-2}$ for fractional fit. It is seen from Fig. 13, that linear fit is unable to properly describe the experiment [72] at small $1 - z$ (i.e. near $x = x_{FC}$), while the fractional fit describes the experiment very well. This means that more detailed measurements are necessary in the vicinity $x = x_{FC}$ [40].

The effective mass as a function of the electron density x in a silicon MOSFET is shown in Fig. 3. We see that Eq. (86) provides a good description of the experimental results. The divergence of the effective mass $M^*(x)$ discovered in measurements involving 2D ^3He [64, 72, 153] is illustrated by Figs. 4 and 13. Figures 3, 4 and 13 show that the description provided by Eqs. (19), (86) and (87) is in good agreement with the experimental data.

In the case of 3D systems, as $x \rightarrow x_{FC}$, the effective mass is given by the expression [70]

$$\frac{1}{M^*} \simeq \frac{1}{m} + \frac{p_F}{4\pi^2} \int_{-1}^1 \int_0^{g_0} \frac{v(q(y))ydydg}{[1 - R(q(y), g)\chi_0(q(y))]^2}. \quad (88)$$

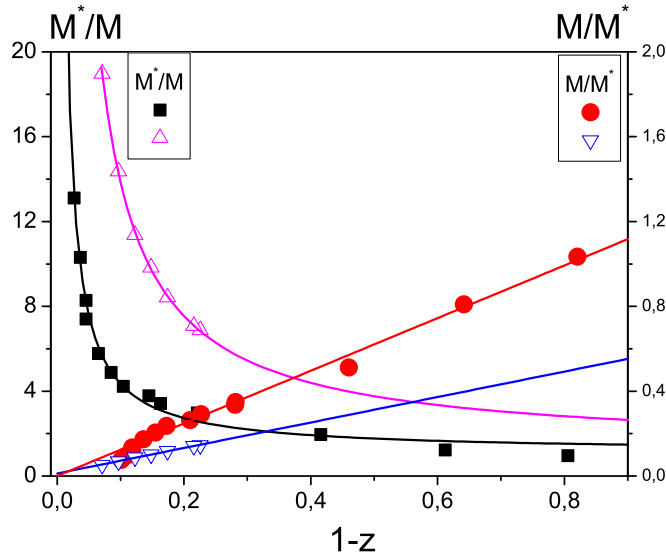


Figure 13: The dependence of the effective mass $M^*(z)$ on dimensionless density $1-z = 1-x/x_{FC}$. Experimental data from Ref. [72] are shown by circles and squares and those from Ref. [153] are shown by triangles. The effective mass is fitted as $M^*(z)/m \propto b_1 + b_2/(1-z)$ (also see Eq. (19)), while the reciprocal one as $m/M^*(z) \propto b_3 z$, where b_1, b_2 and b_3 are constants.

Comparison of Eqs. (83) and (88) shows that there is no essential difference between them, although they describe different cases, 2D and 3D. In the 3D case, we can derive equations similar to (86) and (87) just as we did in the 2D case, but the numerical coefficients are different, because they depend on the number of dimensions. The only difference between 2D and 3D electron systems is that FCQPT occurs in 3D systems at densities much lower than those corresponding to 2D systems. No such transition occurs in massive 3D ^3He because the transition is absorbed by the first-order liquid-solid phase transition [64, 72].

9. A highly correlated Fermi liquid in HF metals

As noted in the Introduction, the challenge for the theories is to explain the scaling behavior of the normalized effective mass $M_N^*(y)$ displayed in Fig. 2; the theories analyzing only the critical exponents that characterize $M_N^*(y)$ at $y \gg 1$ consider a part of the problem. In this Section we analyze and derive the scaling behavior of the normalized effective mass near QCP as depicted in Fig. 2 and show that numerous facts collected in measurements of the thermodynamic, transport and relaxation properties carried out at the transition regime on HF metals can be explained within the framework of the extended quasiparticle paradigm describing the scaling behavior.

9.1. Dependence of the effective mass M^* on magnetic field

When the system approaches FCQPT from the disordered side, at sufficiently low temperatures as shown in Fig. 6, it remains LFL with the effective mass M^* that strongly depends on the distance $r = (x-x_{FC})/x_{FC}$ and magnetic field B . This state of the system with M^* that strongly depends on r and B resembles the state of strongly correlated liquid described in Sections 4 and 10. But in contrast to a strongly correlated liquid, the system in question involves no temperature independent entropy S_0 specified by Eq. (27) and at low temperatures becomes LFL with effective mass $M^* \propto 1/r$ [see Eqs. (19) and (87)]. Such a liquid can be called a highly correlated liquid; as we see shortly, its effective mass exhibits the scaling behavior. We study this behavior when the system transits from its LFL to NFL states.

We use the Landau equation to study the behavior of the effective mass $M^*(T, B)$ as a function of the temperature and the magnetic field. For the model of homogeneous HF liquid at finite temperatures and magnetic fields, this equation

acquires the form [20]

$$\begin{aligned} \frac{1}{M^*(T, B)} &= \frac{1}{m} + \sum_{\sigma_1} \int \frac{\mathbf{p}_F \mathbf{p}}{p_F^3} F_{\sigma, \sigma_1}(\mathbf{p}_F, \mathbf{p}) \\ &\times \frac{\partial n_{\sigma_1}(\mathbf{p}, T, B)}{\partial p} \frac{d\mathbf{p}}{(2\pi)^3}. \end{aligned} \quad (89)$$

where $F_{\sigma, \sigma_1}(\mathbf{p}_F, \mathbf{p})$ is the Landau amplitude dependent on momenta p_F , p and spin σ . For the sake of definiteness, we assume that the HF liquid is 3D liquid. As seen in Section 8, the scaling behavior calculated within the model of HF liquid does not depend on dimensionality and on the inter-particle interaction, while the values of scales like M_M^* and T_M do depend. To simplify matters, we ignore the spin dependence of the effective mass, because $M^*(T, B)$ is nearly independent of the spin in weak fields. The quasiparticle distribution function can be expressed as

$$n_{\sigma}(\mathbf{p}, T) = \left\{ 1 + \exp \left[\frac{(\varepsilon(\mathbf{p}, T) - \mu_{\sigma})}{T} \right] \right\}^{-1}, \quad (90)$$

where $\varepsilon(\mathbf{p}, T)$ is determined by (3). In our case, the single-particle spectrum depends on the spin only weakly, but the chemical potential may depend on the spin due to the Zeeman splitting. When this is important, we specifically indicate the spin dependence of physical quantities. We write the quasiparticle distribution function as $n_{\sigma}(\mathbf{p}, T, B) \equiv \delta n_{\sigma}(\mathbf{p}, T, B) + n_{\sigma}(\mathbf{p}, T = 0, B = 0)$. Equation (89) then becomes

$$\begin{aligned} \frac{m}{M^*(T, B)} &= \frac{m}{M^*(x)} + \frac{m}{p_F^2} \sum_{\sigma_1} \int \frac{\mathbf{p}_F \mathbf{p}_1}{p_F} \\ &\times F_{\sigma, \sigma_1}(\mathbf{p}_F, \mathbf{p}_1) \frac{\partial \delta n_{\sigma_1}(\mathbf{p}_1, T, B)}{\partial p_1} \frac{d\mathbf{p}_1}{(2\pi)^3}. \end{aligned} \quad (91)$$

We assume that the highly correlated HF liquid is close to FCQPT and the distance $r \rightarrow 0$, and therefore $M/M^*(x) \rightarrow 0$, as follows from Eq. (19). For normal metals, where the electron liquid behaves like LFL with the effective mass of several bare electron masses $M^*/m \sim 1$, at temperatures even near 1000 K, the second term on the right hand side of Eq. (91) is of the order of T^2/μ^2 and is much smaller than the first term. The same is true, as can be verified, when a magnetic field $B \sim 100$ T is applied. Thus, the system behaves like LFL with the effective mass that is actually independent of the temperature or magnetic field, while $\rho(T) \propto AT^2$. This means that the corrections to the effective mass determined by the second term on the right-hand side of Eq. (91) are proportional to $(T/\mu)^2$ or $(\mu_B B/\mu)^2$.

Near QCP x_{FC} , with $m/M^*(x \rightarrow x_{FC}) \rightarrow 0$, the behavior of the effective mass changes dramatically because the first term on the right-hand side of Eq. (91) vanishes, the second term becomes dominant, and the effective mass is determined by the homogeneous version of Eq. (91) as a function of B and T . As a result, the LFL state vanishes and the system demonstrates the NFL behavior down to lowest temperatures.

We now qualitatively analyze the solutions of Eq. (91) at $x \simeq x_{FC}$ and $T = 0$. Application of magnetic field leads to Zeeman splitting of the Fermi surface, and the distance δp between the Fermi surfaces with spin up and spin down becomes $\delta p = p_F^{\uparrow} - p_F^{\downarrow} \sim \mu_B B M^*(B)/p_F$. We note that the second term on the right-hand side of Eq. (91) is proportional to $(\delta p)^2 \propto (\mu_B B M^*(B)/p_F)^2$, and therefore Eq. (91) reduces to [49, 53, 138]

$$\frac{m}{M^*(B)} = \frac{m}{M^*(x)} + c \frac{(\mu_B B M^*(B))^2}{p_F^4}, \quad (92)$$

where c is a constant. We also note that $M^*(B)$ depends on x and that this dependence disappears at $x = x_{FC}$. At this point, the term $m/M^*(x)$ vanishes and Eq. (92) becomes homogeneous and can be solved analytically [53, 63, 138]:

$$M^*(B) \propto \frac{1}{(B - B_{c0})^{2/3}}. \quad (93)$$

where B_{c0} is the critical magnetic field, regarded as a parameter (see remarks to Fig. 11).

Equation (93) specifies the universal power-law behavior of the effective mass, irrespective of the interaction type and is valid in 3D and 2D cases. For densities $x > x_{FC}$, the effective mass $M^*(x)$ is finite and we deal with the LFL state if the magnetic field is so weak that

$$\frac{M^*(x)}{M^*(B)} \ll 1, \quad (94)$$

with $M^*(B)$ given by Eq. (93). The second term on the right-hand side of Eq. (92), which is proportional to $(BM^*(x))^2$, is only a small correction. In the opposite case, at $T/T^*(B) \ll 1$, where

$$\frac{M^*(x)}{M^*(B)} \gg 1, \quad (95)$$

the electron liquid behaves as if it were at the quantum critical point. In the LFL state, the main thermodynamic and transport properties of the system are determined by the effective mass. It therefore follows from Eq. (93) that we have the unique possibility of controlling the magnetoresistance, resistivity, heat capacity, magnetization, thermal bulk expansion, etc by varying the magnetic field B . It must be noted that a large effective mass leads to a high density of states, which causes the emergence of a large number of competing states and phase transitions. We believe that such states can be suppressed by applying an external magnetic field, and we examine the thermodynamic properties of the system without considering such competition.

9.2. Dependence of the effective mass M^* on temperature and the damping of quasiparticles

For a qualitative examination of the behavior of $M^*(T, B, x)$ as the temperature increases, we simplify Eq. (91) by dropping the variable B and by imitating the effect of an external magnetic field by a finite effective mass in the denominator of the first term on the right hand side of Eq. (91). Then the effective mass becomes a function of the distance r , $M^*(r)$, determined also by both the magnitude of the magnetic field B and x . In a zero magnetic field, $r = (x - x_{FC})/x_{FC}$. We integrate the second term on the right-hand side of Eq. (91) with respect to the angular variables, then integrate by parts with respect to p , and replace p with $z = (\varepsilon(p) - \mu)/T$. In the case of a flat and narrow band, we can use the approximation where $(\varepsilon(p) - \mu) \simeq p_F(p - p_F)/M^*(T)$. The result is

$$\begin{aligned} \frac{M}{M^*(T)} &= \frac{m}{M^*(r)} - \alpha \int_0^\infty \frac{F(p_F, p_F(1 + \alpha z)) dz}{1 + e^z} \\ &+ \alpha \int_0^{1/\alpha} F(p_F, p_F(1 - \alpha z)) \frac{dz}{1 + e^z}. \end{aligned} \quad (96)$$

where we use the notation

$$F \sim m \frac{d(F^1 p^2)}{dp}, \alpha = \frac{TM^*(T)}{p_F^2} = \frac{TM^*(T)}{(T_k M^*(r))},$$

$T_k = p_F^2/M^*(r)$, and the Fermi momentum is defined by the condition $\varepsilon(p_F) = \mu$.

We first consider the case where $\alpha \ll 1$. Then, discarding terms of the order $\exp(-1/\alpha)$, we can set the upper limit in the second integral on the right hand side of Eq. (96) to infinity, with the result that the sum of the second and third terms is an even function of α . The resulting integrals are typical expressions involving the Fermi-Dirac function in the integrand and can be evaluated by a standard procedure (e.g., see Ref. [156]). Because we need only an estimate of the integrals, we write Eq. (96) as

$$\begin{aligned} \frac{m}{M^*(T)} &\simeq \frac{m}{M^*(r)} + a_1 \left(\frac{TM^*(T)}{T_k M^*(r)} \right)^2 \\ &+ a_2 \left(\frac{TM^*(T)}{T_k M^*(r)} \right)^4 + \dots, \end{aligned} \quad (97)$$

where a_1 and a_2 are constants of the order of unity.

Equation (97) is a typical equation of the LFL theory. The only exception is the effective mass $M^*(r)$, which depends strongly on the distance r and diverges as $r \rightarrow 0$. Nevertheless, Eq. (97) implies that as $T \rightarrow 0$, the corrections to $M^*(r)$ begin with terms of the order T^2 if

$$\frac{m}{M^*(r)} \gg \left(\frac{TM^*(T)}{T_k M^*(r)} \right)^2 \simeq \frac{T^2}{T_k^2}, \quad (98)$$

and the system behaves like LFL. Condition (98) implies that the behavior inherent in LFL disappears as $r \rightarrow 0$ and $M^*(r) \rightarrow \infty$. Then the free term on the right-hand side of Eq. (96) is negligible, $m/M^*(r) \rightarrow 0$, and Eq. (96) becomes homogeneous and determines the universal behavior of the effective mass $M^*(T)$. At a certain temperature $T^* \ll T_k$, the value of the sum on the right-hand side of Eq. (97) is determined by the second term and relation (98) becomes invalid. Keeping only the second term in Eq. (97), we arrive at an equation for determining $M^*(T)$ in the transition region [53, 157]:

$$M^*(T) \propto \frac{1}{T^{2/3}}. \quad (99)$$

As regards an estimate of the transition temperature $T^*(B)$ at which the effective mass becomes temperature-dependent, we note that the effective mass is a continuous function of the temperature and the magnetic field: $M^*(B) \sim M^*(T^*)$. With Eqs. (93) and (99), we obtain

$$T^*(B) \simeq \mu_B(B - B_{c0}). \quad (100)$$

As the temperature increases, the system transfers into another mode. The coefficient α is then of the order of unity, $\alpha \sim 1$, the upper limit in the second integral in Eq. (96) cannot be set to infinity, and odd terms begin to play a significant role. As a result, Eq. (97) breaks down and the sum of the first and second integrals on the right-hand side of Eq. (96) becomes proportional to $M^*(T)T$. Ignoring the first term $m/M^*(r)$ and approximating the sum of integrals by $M^*(T)T$, we obtain from (96) that

$$M^*(T) \propto \frac{1}{\sqrt{T}}. \quad (101)$$

We note that $M^*(T)$ is also given by Eq. (101) if the Landau amplitude $F(p)$ is determined by a nonanalytic function, that is the function cannot be expanded in Taylor series at $p \rightarrow 0$, see Section 15.

We therefore conclude that as the temperature increases and the condition $x \simeq x_{FC}$ is satisfied, the system demonstrates regimes of three types: (i) the behavior of the Landau Fermi liquid at $\alpha \ll 1$, when Eq. (98) is valid and the behavior of the effective mass is described by Eq. (93); (ii) the behavior defined by Eq. (99), when $M^*(T) \propto T^{-2/3}$ and $S(T) \propto M^*(T)T \propto T^{1/3}$; and (iii) the behavior at $\alpha \sim 1$, when Eq. (101) is valid, $M^*(T) \propto 1/\sqrt{T}$, the entropy $S(T) \propto M^*(T)T \propto \sqrt{T}$, and the heat capacity $C(T) = T(\partial S(T)/\partial T) \propto \sqrt{T}$.

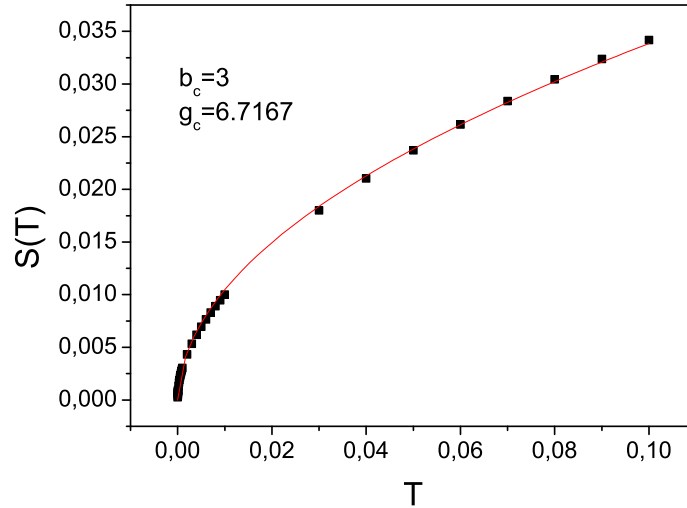


Figure 14: The entropy $S(T)$ of a highly correlated Fermi liquid at the critical point of FCQPT. The solid line represents the function $S(T) \propto \sqrt{T}$, and the squares mark the results of calculations.

We illustrate the behavior of $S(T)$ when Eq. (101) is valid using calculations based on the model Landau functional [42, 158]

$$E[n(p)] = \int \frac{\mathbf{p}^2}{2M} \frac{d\mathbf{p}}{(2\pi)^3} + \frac{1}{2} \int V(\mathbf{p}_1 - \mathbf{p}_2) \times n(\mathbf{p}_1)n(\mathbf{p}_2) \frac{d\mathbf{p}_1 d\mathbf{p}_2}{(2\pi)^6}, \quad (102)$$

with the nonanalytic Landau amplitude

$$V(\mathbf{p}) = g_0 \frac{\exp(-\beta_0|\mathbf{p}|)}{|\mathbf{p}|}. \quad (103)$$

We normalize the effective mass to m , i.e., $M^* = M^*/m$, and the temperature T_0 to the Fermi energy ε_F^0 , $T = T_0/\varepsilon_F^0$, and use the dimensionless coupling constant $g = (g_0 m)/(2\pi^2)$ and also $\beta = \beta_0 p_F$. FCQPT occurs when these parameters reach the critical values $\beta = b_c$ and $g = g_c$. On the other hand, a transition of this kind occurs as $M^* \rightarrow \infty$. This condition allows deriving a relation between b_c and g_c [42, 158]:

$$\frac{g_c}{b_c^3} (1 + b_c) \exp(-b_c) [b_c \cosh(b_c) - \sinh(b_c)] = 1. \quad (104)$$

This relation implies that the critical point of FCQPT can be reached by varying g_0 if β_0 and p_F are fixed, by varying p_F if β_0 and g_0 are fixed, etc. For definiteness, we vary g to reach FCQPT or to study the properties of the system beyond the critical point. Calculations of $M^*(T)$, $S(T)$, and $C(T)$ based on the model functional (102) with the parameters $g = g_c = 6.7167$ and $\beta = b_c = 3$ show that $M^*(T) \propto 1/\sqrt{T}$, $S(T) \propto \sqrt{T}$, and $C(T) \propto \sqrt{T}$. The temperature dependence of the entropy in this case is depicted in Fig. 14.

We now estimate the quasiparticle damping $\gamma(T)$. In the Landau Fermi-liquid theory, $\gamma(T)$ is given by [20]

$$\gamma \sim |\Gamma|^2 (M^*)^3 T^2, \quad (105)$$

where Γ is the particle-hole amplitude. In the case of highly correlated HF system with a high density of states caused by the enormous effective mass, Γ cannot be approximated by the "bare" interaction between particles but can be estimated within the "ladder" approximation, which yields $|\Gamma| \sim 1/(p_F M^*(T))$ [51, 52]. As a result, we find that $\gamma(T) \propto T^2$ in the Landau Fermi-liquid regime since M^* is temperature-independent. Then, $\gamma(T) \propto T^{4/3}$ in the $T^{-2/3}$ -regime, and $\gamma(T) \propto T^{3/2}$ in the $1/\sqrt{T}$ -regime. We note that in all these cases, the width is small compared to the characteristic quasiparticle energy, which is assumed to be of the order of T , and hence the quasiparticle concept is meaningful.

The conclusion that can be drawn here is that when the HF liquid is localized near QCP of FCQPT and is on the disordered side, its low-energy excitations are quasiparticles with the effective mass $M^*(B, T)$. We note that at FCQPT, the quasiparticle renormalization z -factor remains approximately constant and the divergence of the effective mass that follows from Eq. (19) is not related to the fact that $z \rightarrow 0$ [23, 24, 159]. Therefore, the quasiparticle concept remains valid and it is these quasiparticles that constitute the extended paradigm and determine the transport, relaxation and thermodynamic properties of HF liquid.

9.3. Scaling behavior of the effective mass

As was mentioned in the Introduction, to avoid difficulties associated with the anisotropy generated by the crystal lattice of HF metals, we study the universal behavior of HF metals using the model of the homogeneous HF (electron) liquid. The model is quite meaningful because we consider the scaling behavior exhibited by the effective mass at low temperatures. The scaling behavior of the effective mass is determined by energy and momentum transfers that are small compared to the Debye characteristic temperature and momenta of the order of the reciprocal lattice cell length a^{-1} . Therefore quasiparticles are influenced by the crystal lattice averaged over large distances compared to the length a . Thus, we can use the well-known jelly model. We note that the values of such scales as M_M^* , T_M , B_{c0} and B_{c2} etc depend on the properties of a HF metal, its lattice, composition etc. For example, the critical magnetic field B_{c0} depends even on its orientation with respect to the lattice.

To explore the scaling behavior of M^* , we start with qualitative analysis of Eq. (89). At FCQPT the effective mass M^* diverges and Eq. (89) becomes homogeneous determining M^* as a function of temperature as given by Eq. (99). If

the system is located before FCQPT, M^* is finite, and at low temperatures the system demonstrates the LFL behavior, that is $M^*(T) \simeq M^* + a_1 T^2$. As we have seen in Subsection 9.2, the LFL behavior takes place when the second term on the right hand side of Eq. (89) is small in comparison with the first one. Then, at increasing temperatures the system enters the transition regime: M^* grows, reaching its maximum M_M^* at $T = T_M$, with subsequent diminishing. Near temperatures $T \geq T_M$ the last "traces" of LFL regime disappear, the second term starts to dominate, and again Eq. (89) becomes homogeneous, and the NFL behavior restores, manifesting itself in decreasing of M^* as $T^{-2/3}$. When the system is near FCQPT, it turns out that the solution of Eq. (89) $M^*(T)$ can be well approximated by a simple universal interpolating function [160]. The interpolation occurs between the LFL ($M^* \simeq M^* + a_1 T^2$) and NFL ($M^* \propto T^{-2/3}$) regimes, thus describing the above crossover. Introducing the dimensionless variable $y = T_N = T/T_M$, we obtain the desired expression

$$M_N^*(y) \approx c_0 \frac{1 + c_1 y^2}{1 + c_2 y^{8/3}}. \quad (106)$$

Here $M_N^* = M^*/M_M^*$ is the normalized effective mass, $c_0 = (1 + c_2)/(1 + c_1)$, c_1 and c_2 are fitting parameters, parameterizing the Landau amplitude.

It follows from Eq. (93), that the application of magnetic field restores the LFL behavior, so that M_M^* depends on B as

$$M_M^* \propto (B - B_{c0})^{-2/3}, \quad (107)$$

while

$$T_M \propto \mu_B (B - B_{c0}). \quad (108)$$

Employing Eqs. (107) and (108) to calculate M_M^* and T_M , we conclude that Eq. (106) is valid to describe the normalized effective mass in external fixed magnetic fields with $y = T/(B - B_{c0})$. On the other hand, Eq. (106) is valid when the applied magnetic field becomes a variable, while temperature is fixed at $T = T_f$. In that case, it is convenient to represent the variable as $y = (B - B_{c0})/T_f$.

9.3.1. Schematic phase diagram of HF metal

The schematic phase diagram of HF metal is reported in Fig. 15, panel **a**. Magnetic field B is taken as the control parameter. In fact, the control parameter can be pressure P or doping (the number density) x etc as well. At $B = B_{c0}$, FCQPT takes place leading to a strongly degenerate state, where B_{c0} is a critical magnetic field, such that at $B > B_{c0}$ the system is driven towards the LFL state. We recall, that in our simple model B_{c0} is a parameter. The FC state is captured by the superconducting (SC), ferromagnetic (FM), antiferromagnetic (AFM) etc. states lifting the degeneracy. Below in Subsection 9.4 we consider the HF metal YbRh₂Si₂. In that case, $B_{c0} \simeq 0.06$ T ($B_{\perp c}$) and at $T = 0$ and $B < B_{c0}$ the AFM state takes place with temperature dependent resistivity $\rho(T) \propto T^2$ [15]. At elevated temperatures and fixed magnetic fields the NFL regime occurs, while rising B again drives the system from the NFL state to the LFL one as shown by the dash-dot horizontal arrow in Fig. 15. We consider the transition region when the system moves from the NFL state to LFL one along the horizontal arrow and also moves from LFL state to NFL one along the vertical arrow as shown in Fig. 15. The inset to Fig. 15 demonstrates the scaling behavior of the normalized effective mass $M_N^* = M^*/M_M^*$ versus normalized temperature $T_N = T/T_M$, where M_M^* is the maximum value that M^* reaches at $T = T_M$. The $T^{-2/3}$ regime is marked as NFL since the effective mass depends strongly on temperature. The temperature region $T \simeq T_M$ signifies the crossover (or the transition region) between the LFL state with almost constant effective mass and NFL behavior, given by $T^{-2/3}$ dependence. Thus temperatures $T \sim T_M$ can be regarded as the crossover region between the LFL and NFL states.

The transition (crossover) temperature $T^*(B)$ is not really the temperature of a phase transition. It is necessarily broad, very much depending on the criteria for determination of the point of such a crossover, as it is seen from the inset to Fig. 15 **a**, see e.g. Refs. [15, 150]. As usual, the temperature $T^*(B)$ is extracted from the field dependence of charge transport, for example from the resistivity $\rho(T)$ given by Eq. (18). The LFL state is characterized by the T^{α_R} dependence of the resistivity with $\alpha_R = 2$, see Subsection 9.5. The crossover (that is the transition regime shown by the hatched area both in the panel **a** of Fig. 15 and in its inset) takes place at temperatures where the resistance starts to deviate from the LFL behavior with $\alpha_R = 2$ so that the exponent becomes $1 < \alpha_R < 2$, see Subsection 9.5. As it will be shown in Subsection 9.5, in the NFL state $\alpha_R = 1$.

The panel **b** of Fig. 15 represents the experimental $T - B$ phase diagram of the exponent $\alpha_R(T, B)$ as a function of temperature T versus magnetic field B [7]. The evolution of $\alpha_R(T, B)$ is shown by the color: the yellow color corresponds

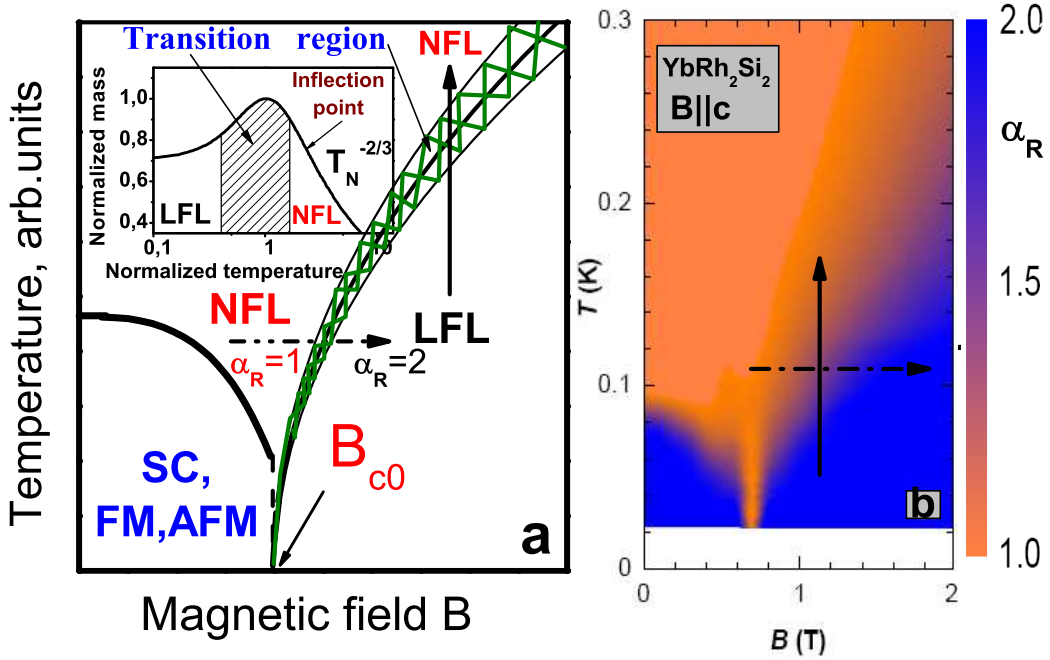


Figure 15: The panel **a** represents a schematic phase diagram of HF metals. B_{c0} is magnetic field at which the effective mass divergences. SC, FM, AFM denote the superconducting (SC), ferromagnetic (FM) and antiferromagnetic (AFM) states, respectively. At $B < B_{c0}$ the system can be in SC, FM or AFM states. The vertical arrow shows the transition from the LFL to the NFL state at fixed B along T with M^* depending on T . The dash-dot horizontal arrow illustrates the system moving from the NFL to LFL state along B at fixed T . The exponent α_R determines the temperature dependent part of the resistivity, see Eq. (18). In the LFL state the exponent $\alpha_R = 2$ and in the NFL $\alpha_R = 1$. In the transition regime the exponent evolves from its LFL value to the NFL one. The inset shows a schematic plot of the normalized effective mass versus the normalized temperature. Transition regime, where M_N^* reaches its maximum value M_M^* at $T = T_M$, is shown by the hatched area both in the panel **a** and in the inset. The arrows mark the position of inflection point in M_N^* and the transition region. The panel **b** shows the experimental $T - B$ phase diagram of the exponent $\alpha_R(T, B)$ as a function of temperature T versus magnetic field B [7]. The evolution of $\alpha_R(T, B)$ is shown by the color: the yellow color corresponds to $\alpha_R(T, B) = 1$ (the NFL state) and the blue color corresponds to $\alpha_R(T, B) = 2$ (the LFL state). The NFL behavior occurs at the lowest temperatures right at QCP tuned by magnetic field. At rising magnetic fields $B > B_{c0}$ and $T \sim T^*(B)$, the broad transition regime from the NFL state to the field-induced LFL state occurs. As in the panel **a**, the both transitions from the LFL to the NFL state and from the NFL to LFL state are shown by the corresponding arrows.

to $\alpha_R(T, B) = 1$ and the blue color corresponds to $\alpha_R(T, B) = 2$. It is seen from the panel that at the critical field $B_{c0} \approx 0.66$ T ($B \parallel c$) the NFL behavior occurs down to the lowest temperatures. While YbRh_2Si_2 transits from the NFL to LFL behavior under the application of magnetic field. It is worthy to note that the phase diagram displayed in Fig. 15 (the panel **a**) coincides with that of shown in the panel **b**.

A few remarks are in order here. As we shall see, the magnetic field dependence of the effective mass or of other observable like the longitudinal magnetoresistance do not have "peculiar points" like maxima. The normalization is to be performed in the other points like the inflection point at $T = T_{inf}$ (or at $B = B_{inf}$) shown in the inset to Fig. 15 by the arrow. Such a normalization is possible since it is established on the scales, $T_{inf} \propto T_M \propto (B - B_{c0})$. As a result, we obtain

$$\mu_B(B_{inf} - B_{c0}) \propto T_f. \quad (109)$$

It follows from Eq. (106) that in contrast to the Landau paradigm of quasiparticles the effective mass strongly depends on T and B . This dependence leads to the extended quasiparticle paradigm and forms the NFL behavior. Also from Eq. (106) the scaling behavior of M^* near QCP is revealed by the application of appropriate physical scales to measure the effective mass, magnetic field and temperature. At fixed magnetic fields, the characteristic scales of temperature and of the function $M^*(T, B)$ are defined by both T_M and M_M^* respectively. At fixed temperatures, the characteristic scales are $(B_M - B_{c0})$ and M_M^* . From Eqs. (107) and (108) it is seen that at fixed magnetic fields, $T_M \rightarrow 0$, and $M_M^* \rightarrow \infty$, and the width of the transition region shrinks to zero as $B \rightarrow B_{c0}$ when these are measured in "external" scales like T in K, magnetic field B in T etc. In the same way, it follows from Eqs. (99) and (109) that at fixed temperature T_f , $(B_{inf} - B_{c0}) \rightarrow 0$, and $M_M^* \rightarrow \infty$,

and the width of the transition region shrinks to zero as $T_f \rightarrow 0$. Thus, the application of the external scales obscure the scaling behavior of the effective mass and the thermodynamic and transport properties.

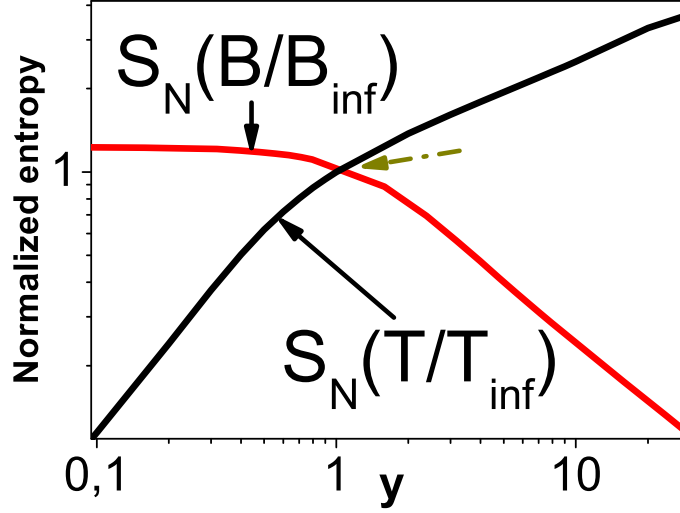


Figure 16: The normalized entropy $S_N(B/B_{inf})$ versus $y = B/B_{inf}$ and the normalized entropy $S_N(T/T_{inf})$ versus $y = T/T_{inf}$ calculated at fixed temperature and magnetic field, correspondingly, are represented by the solid lines and shown by the arrows. The inflection point is depicted by the dash-dot arrow.

In what follows, we compute the effective mass using Eq. (89) and employ Eq. (106) for estimations of the considered values. To compute the effective mass $M^*(T, B)$, we solve Eq. (89) with a quite general form of Landau interaction amplitude [53]. Choice of the amplitude is dictated by the fact that the system has to be at QCP, which means that the first two p -derivatives of the single-particle spectrum $\varepsilon(\mathbf{p})$ should equal zero. Since the first derivative is proportional to the reciprocal quasiparticle effective mass $1/M^*$, its zero just signifies QCP of FCQPT. The second derivative must vanish; otherwise $\varepsilon(p) - \mu$ has the same sign below and above the Fermi surface, and the Landau state becomes unstable before $r \rightarrow 0$ [23, 137]. Zeros of these two subsequent derivatives mean that the spectrum $\varepsilon(\mathbf{p})$ has an inflection point at p_F so that the lowest term of its Taylor expansion is proportional to $(p - p_F)^3$. After solution of Eq. (89), the obtained spectrum has been used to calculate the entropy $S(B, T)$, which, in turn, has been used to recalculate the effective mass $M^*(T, B)$ by virtue of the well-known LFL relation $M^*(T, B) = S(T, B)/T$. Our calculations of the normalized entropy as a function of the normalized magnetic field $B/B_{inf} = y$ and as a function of the normalized temperature $y = T/T_{inf}$ are reported in Fig. 16. Here T_{inf} and B_{inf} are the corresponding inflection points in the function S . We normalize the entropy by its value at the inflection point $S_N(y) = S(y)/S(1)$. As seen from Fig. 16, our calculations corroborate the scaling behavior of the normalized entropy, that is the curves at different temperatures and magnetic fields merge into a single one in terms of the variable y . The inflection point T_{inf} in $S(T)$ makes $M^*(T, B)$ have its maximum as a function of T , while $M^*(T, B)$ versus B has no maximum. We note that our calculations of the entropy confirm the validity of Eq. (106) and the scaling behavior of the normalized effective mass shown in Fig. 15.

9.4. Non-Fermi liquid behavior in YbRh_2Si_2

In this Subsection, we analyze the transition regime and the NFL behavior of the HF metal YbRh_2Si_2 . We demonstrate that the NFL behavior observed in the thermodynamic and transport properties of YbRh_2Si_2 can be described in terms of the scaling behavior of the normalized effective mass. This allows us to construct the scaled thermodynamic and transport properties extracted from experimental facts in a wide range of the variation of scaled variable and conclude that the extended quasiparticles paradigm is strongly valid. We show that "peculiar points" of the normalized effective mass give rise to the energy scales observed in the thermodynamic and transport properties of HF metals. Our calculations of the thermodynamic and transport properties are in good agreement with the heat capacity, magnetization, longitudinal magnetoresistance and magnetic entropy obtained in remarkable measurements on the heavy fermion metal YbRh_2Si_2 [15, 17, 36, 37]. For YbRh_2Si_2 the constructed thermodynamic and transport functions extracted from experimental facts show the scaling over three decades in the variable. The energy scales in these functions are also explained [38].

9.4.1. Heat capacity and the Sommerfeld coefficient

Exciting measurements of $C/T \propto M^*$ on samples of the new generation of YbRh_2Si_2 in different magnetic fields B up to 1.5 T [36] allow us to identify the scaling behavior of the effective mass M^* and observe the different regimes of M^* behavior such as the LFL regime, transition region from LFL to NFL regimes, and the NFL regime itself. A maximum structure in $C/T \propto M^*$ at T_M appears under the application of magnetic field B and T_M shifts to higher T as B is increased. The value of $C/T = \gamma_0$ is saturated towards lower temperatures decreasing at elevated magnetic fields.

The transition region corresponds to the temperatures where the vertical arrow in the main panel **a** of Fig. 15 crosses the hatched area. The width of the region, being proportional to $T_M \propto (B - B_{c0})$ shrinks, T_M moves to zero temperature and $\gamma_0 \propto M^*$ increases as $B \rightarrow B_{c0}$. These observations are in accord with the experimental facts [36].

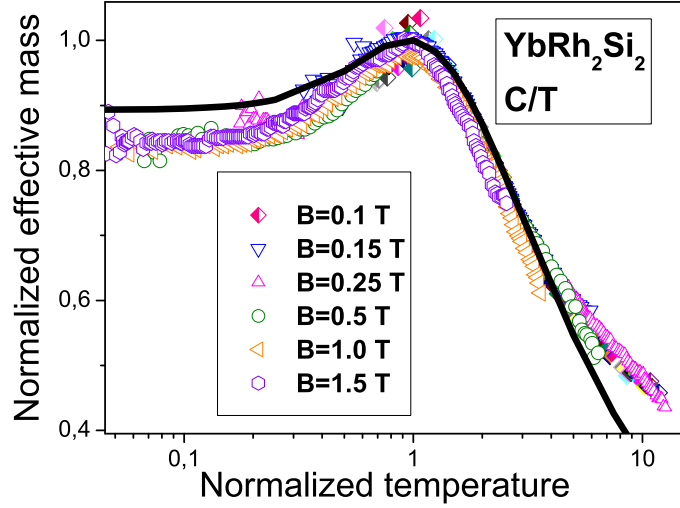


Figure 17: The normalized effective mass M_N^* extracted from the measurements of the specific heat C/T on YbRh_2Si_2 in magnetic fields B [36] listed in the legend. Our calculations are depicted by the solid curve tracing the scaling behavior of M_N^* .

To obtain the normalized effective mass M_N^* , the maximum structure in C/T was used to normalize C/T , and T was normalized by T_M . In Fig. 17 M_N^* as a function of normalized temperature T_N is shown by geometrical figures, our calculations are shown by the solid line. Figure 17 reveals the scaling behavior of the normalized experimental curves - the scaled curves at different magnetic fields B merge into a single one in terms of the normalized variable $y = T/T_M$. As seen, the normalized mass M_N^* extracted from the measurements is not a constant, as would be for LFL. The two regimes (the LFL regime and NFL one) separated by the transition region, as depicted by the hatched area in the inset to Fig. 15 **a**, are clearly seen in Fig. 17 displaying good agreement between the theory and experimental facts. It is worthy to note that the normalization procedure allows us to construct the scaled function C/T extracted from the experimental facts in wide range variation of the normalized temperature. Indeed, it integrates measurements of C/T taken at the application of different magnetic fields into unique function of the normalized temperature which demonstrates the scaling behavior over three decades in the normalized temperature as seen from Fig. 17. As seen from Figs. 1, the NFL behavior extends at least to temperatures up to few Kelvins. Thus, we conclude that the extended quasiparticle paradigm does take into account the remarkably large temperature ranges over which the NFL behavior is observed. We note that at these temperatures the contribution coming from phonons is still small.

9.4.2. Magnetization

Consider now the magnetization M as a function of magnetic field B at fixed temperature $T = T_f$

$$M(B, T) = \int_0^B \chi(b, T) db, \quad (110)$$

where the magnetic susceptibility χ is given by [20]

$$\chi(B, T) = \frac{\beta M^*(B, T)}{1 + F_0^a}. \quad (111)$$

Here, β is a constant and F_0^a is the Landau amplitude related to the exchange interaction. In the case of strongly correlated systems $F_0^a \geq -0.9$ [59, 60, 61]. Therefore, as seen from Eq. (111), due to the normalization the coefficients β and $(1 + F_0^a)$ drops out from the result, and $\chi \propto M^*$. One might assume that F_0^a can strongly depend on B . This is not the case [38, 39],

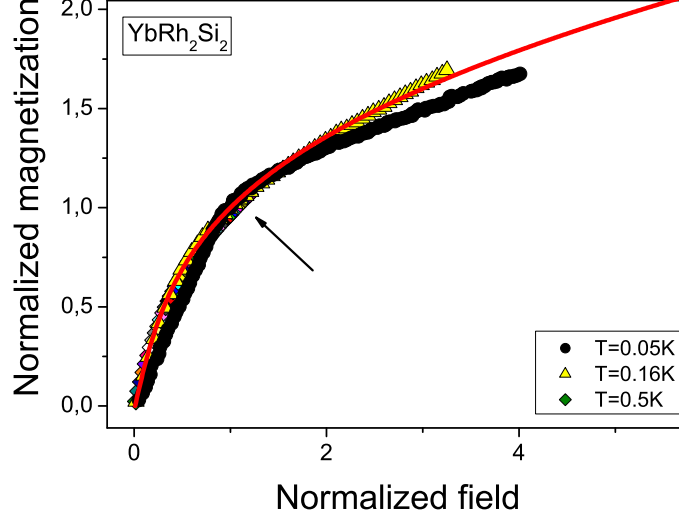


Figure 18: The field dependencies of the normalized magnetization M collected at different temperatures shown at right bottom corner are extracted from measurements collected on YbRu_2Si_2 [17, 37]. The kink (shown by the arrow) is clearly seen at the normalized field $B_N = B/B_k \simeq 1$. The solid curve represents our calculations.

since the Kadowaki-Woods ratio is conserved [14, 27, 141], $A(B)/\gamma_0^2(B) \propto A(B)/\chi^2(B) \propto \text{const}$, we have $\gamma_0 \propto M^* \propto \chi$. Note that the Sommerfeld coefficient does not depend on F_0^a .

Our calculations show that the magnetization exhibits a kink at some magnetic field $B = B_k$. The experimental magnetization demonstrates the same behavior [17, 37]. We use B_k and $M(B_k)$ to normalize B and M respectively. The normalized magnetization $M(B)/M(B_k)$ extracted from experimental facts depicted by the geometrical figures and calculated magnetization shown by the solid line are reported in Fig. 18. As seen, the scaled data at different T_f merge into a single one in terms of the normalized variable $y = B/T_k$. It is also seen, that these exhibit energy scales separated by kink at the normalized magnetic field $B_N = B/B_k = 1$. The kink is a crossover point from the fast to slow growth of M at rising magnetic field. Figure 18 shows that our calculations are in good agreement with the experimental facts, and all the data exhibit the kink (shown by the arrow) at $B_N \simeq 1$ taking place as soon as the system enters the transition region corresponding to the magnetic fields where the horizontal dash-dot arrow in the main panel **a** of Fig. 15 crosses the hatched area. Indeed, as seen from Fig. 18, at lower magnetic fields M is a linear function of B since M^* is approximately independent of B . Then, Eqs. (106) and (107) show that at elevated magnetic fields M^* becomes a diminishing function of B and generates the kink in $M(B)$ separating the energy scales discovered in Refs. [17, 37]. It is seen from Eq. (109) that the magnetic field B_k at which the kink appears, $B_k \simeq B_M \propto T_f$, shifts to lower B as T_f is decreased. This observation is in accord with experimental facts [17, 37].

Consider now an ‘‘average’’ magnetization $\underline{M} \equiv B\chi + M$ as a function of the magnetic field B at fixed temperature $T = T_f$ [17]. We again use B_k and $\underline{M}(B_k)$ to normalize B and \underline{M} respectively. The normalized \underline{M} vs the normalized field $B_N = B/B_k$ are shown in Fig. 19. Our calculations are depicted by the solid line. The stars trace out our calculations of \underline{M} with $M^*(y)$ extracted from the data C/T shown in Fig. 17. It is seen from Fig. 19 that our calculations are in good agreement with the experimental facts, and all the data exhibit the kink (shown by arrow) at $B_N \simeq 1$ taking place as soon as the system enters the transition region corresponding to the magnetic fields where the horizontal dash-dot arrow in the main panel **a** of Fig. 15 crosses the hatched area. Indeed, as seen from Fig. 19, at lower magnetic fields \underline{M} is a linear

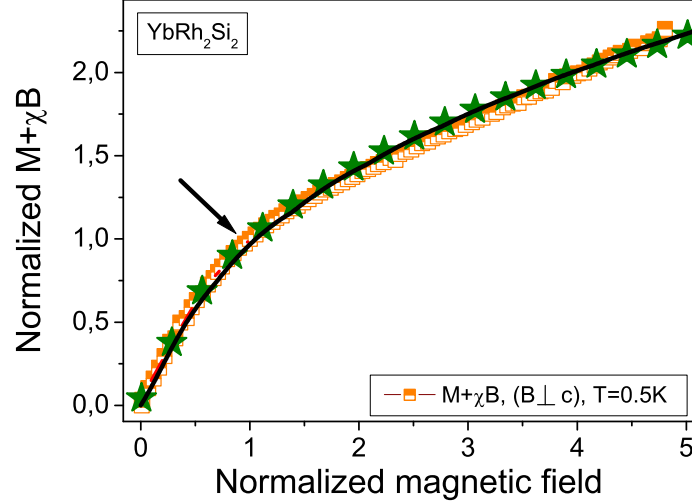


Figure 19: The field dependence of the normalized “average” magnetization $\underline{M} \equiv M + B\chi$ is shown by squares and has been extracted from measurements collected on YbRu_2Si_2 [17]. The kink (shown by the arrow) is clearly seen at the normalized field $B_N = B/B_k \approx 1$. The solid curve and stars (see text) represent our calculations.

function of B since M^* is approximately independent of B . It follows from Eq. (107) that at elevated magnetic fields M^* becomes a diminishing function of B and generates the kink in $\underline{M}(B)$ separating the energy scales discovered in Ref. [17]. Then, it is seen from Eq. (109) that the magnetic field $B_k \approx B_M$ at which the kink appears shifts to lower B as T_f is decreased.

9.4.3. Longitudinal magnetoresistance

Consider a longitudinal magnetoresistance (LMR) $\rho(B, T) = \rho_0 + AT^2$ as a function of B at fixed T_f . In that case, the classical contribution to LMR due to orbital motion of carriers induced by the Lorentz force is small, while the Kadowaki-Woods relation [14, 27, 139, 140, 141], $K = A/\gamma_0^2 \propto A/\chi^2 = \text{const}$, allows us to employ M^* to construct the coefficient A , since $\gamma_0 \propto \chi \propto M^*$. Omitting the classical contribution to LMR, we obtain that $\rho(B, T) - \rho_0 \propto (M^*)^2$. Fig. 20 reports the normalized magnetoresistance

$$\rho_N(y) \equiv \frac{\rho(y) - \rho_0}{\rho_{inf}} = (M_N^*(y))^2 \quad (112)$$

versus normalized magnetic field $y = B/B_{inf}$ at different temperatures, shown in the legend. Here ρ_{inf} and B_{inf} are LMR and magnetic field respectively taken at the inflection point marked by the arrow in Fig. 20. Both theoretical (shown by the solid line) and experimental (marked by the geometrical symbols) curves have been normalized by their inflection points, which also reveal the scaling behavior - the scaled curves at different temperatures merge into a single one as a function of the variable y and show the scaling behavior over three decades in the normalized magnetic field. The transition region at which LMR starts to decrease is shown in the inset to Fig. 15 a by the hatched area. Obviously, as seen from Eq. (109), the width of the transition region being proportional to $B_M \approx B_{inf} \propto T_f$ decreases as the temperature T_f is lowered. In the same way, the inflection point of LMR, generated by the inflection point of M^* shown in the inset to Fig. 15 by the arrow, shifts to lower B as T_f is decreased. All these observations are in good agreement with the experimental facts [17, 37].

9.4.4. Magnetic entropy

The evolution of the derivative of magnetic entropy $dS(B, T)/dB$ as a function of magnetic field B at fixed temperature T_f is of great importance since it allows us to study the scaling behavior of the derivative of the effective mass $TdM^*(B, T)/dB \propto dS(B, T)/dB$. While the scaling properties of the effective mass $M^*(B, T)$ can be analyzed via LMR, see Fig. 20. As seen from Eqs. (106) and (109), at $y \leq 1$ the derivative

$$-\frac{dM_N(y)}{dy} \propto y$$

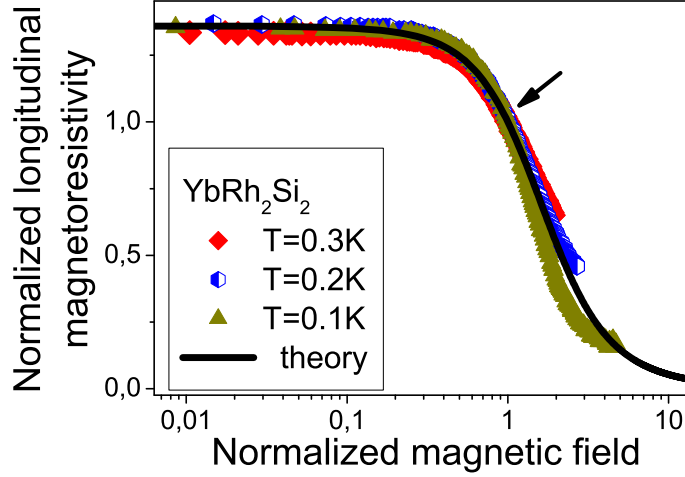


Figure 20: Magnetic field dependence of the normalized magnetoresistance ρ_N versus normalized magnetic field. ρ_N was extracted from LMR of YbRh_2Si_2 at different temperatures [17, 37] listed in the legend. The inflection point is shown by the arrow, and the solid line represents our calculations.

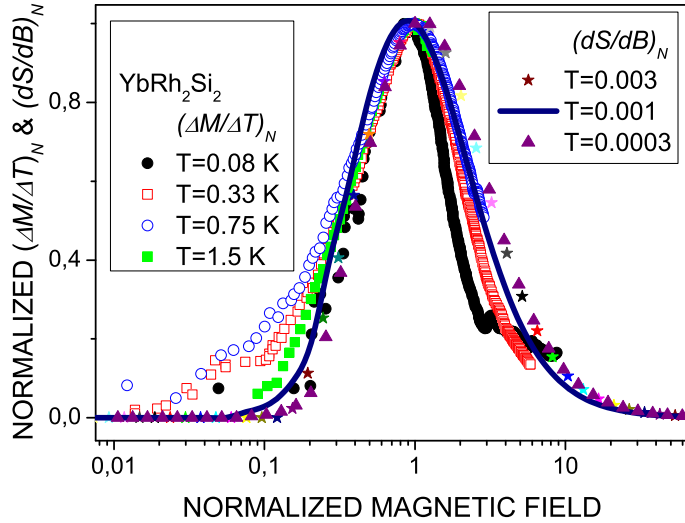


Figure 21: Normalized magnetization difference divided by temperature increment $(\Delta M/\Delta T)_N$ vs normalized magnetic field at fixed temperatures (listed in the legend in the upper left corner) is extracted from the facts collected on YbRh_2Si_2 [161]. Our calculations of the normalized derivative $(dS/dB)_N \simeq (\Delta M/\Delta T)_N$ vs normalized magnetic field are given at fixed dimensionless temperatures T/μ (listed in the legend in the upper right corner). All the data are shown by the geometrical figures depicted in the legend at the upper left corner.

with $y = (B - B_{c0})/(B_{inf} - B_{c0}) \propto (B - B_{c0})/T_f$. We note that the effective mass as a function of B does not have the maximum. At elevated y the derivative $-dM_N(y)/dy$ possesses a maximum at the inflection point and then becomes a diminishing function of y . Upon using the variable $y = (B - B_{c0})/T_f$, we conclude that at decreasing temperatures, the leading edge of the function $-dS/dB \propto -TdM^*/dB$ becomes steeper and its maximum at $(B_{inf} - B_{c0}) \propto T_f$ is higher. These observations are in quantitative agreement with striking measurements of the magnetization difference divided by temperature increment, $-\Delta M/\Delta T$, as a function of magnetic field at fixed temperatures T_f collected on YbRh_2Si_2 [161]. We note that according to the well-known thermodynamic equality $dM/dT = dS/dB$, and $\Delta M/\Delta T \simeq dS/dB$. To carry out a quantitative analysis of the scaling behavior of $-dM^*(B, T)/dB$, we calculate as described above the entropy $S(B, T)$ shown in Fig. 16 as a function of B at fixed dimensionless temperatures T_f/μ shown in the upper right corner of Fig. 21.

This figure reports the normalized $(dS/dB)_N$ as a function of the normalized magnetic field. The function $(dS/dB)_N$ is obtained by normalizing $(-dS/dB)$ by its maximum taking place at B_M , and the field B is scaled by B_M . The measurements of $-\Delta M/\Delta T$ are normalized in the same way and depicted in Fig. 21 as $(\Delta M/\Delta T)_N$ versus normalized field. It is seen from Fig. 21 that our calculations are in good agreement with the experimental facts and both the experimental functions $(\Delta M/\Delta T)_N$ and the calculated $(dS/dB)_N$ show the scaling behavior over three decades in the normalized magnetic field.

9.4.5. Energy scales

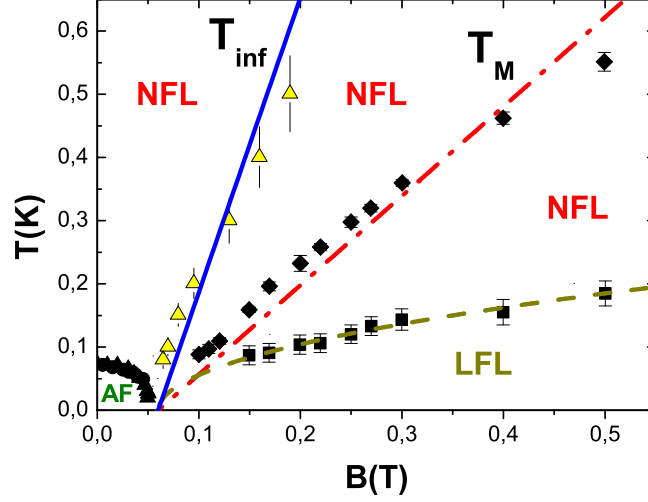


Figure 22: Temperature versus magnetic field $T - B$ phase diagram for YbRh_2Si_2 . Solid circles represent the boundary between AF and NFL states. The solid squares denote the boundary of the NFL and LFL regime [15, 17, 37] shown by the dashed line which is approximated by $\sqrt{B - B_{c0}}$ [6]. Diamonds mark the maximums T_M of C/T [189] shown in Fig. 17. The dash-dot line is approximated by $T_M \propto a(B - B_{c0})$, a is a fitting parameter, see Eq. (108). Triangles along the solid line denote T_{inf} in LMR [17, 37] shown in Fig. 21, and the solid line represents the function $T_{inf} \propto b(B - B_{c0})$, b is a fitting parameter, see Eq. (109).

Fig. 22 reports T_{inf} and T_M versus B depicted by the solid and dash-dotted lines, respectively. The boundary between the NFL and LFL regimes is shown by the dashed line, and AF marks the antiferromagnetic state. The corresponding data are taken from Ref. [17, 37, 161]. It is seen that our calculations are in good agreement with the experimental facts. In Fig. 22, the solid and dash-dotted lines corresponding to the functions T_{inf} and T_M , respectively, represent the positions of the kinks separating the energy scales in C and M reported in Ref. [17, 161]. Furthermore, our calculations are in accord with experimental facts, and we conclude that the energy scales are reproduced by Eqs. (108) and (109) and related to the peculiar points T_{inf} and T_M of the normalized effective mass M_N^* which are shown by the arrows in the inset to Fig. 15.

At $B \rightarrow B_{c0}$ both $T_{inf} \rightarrow 0$ and $T_M \rightarrow 0$, thus the LFL and the transition regimes of both C/T and M as well as those of LMR and the magnetic entropy are shifted to very low temperatures. Therefore due to experimental difficulties these regimes cannot often be observed in experiments on HF metals. As it is seen from Figs. 17, 18, 20, 21 and 22, the normalization allows us to construct the unique scaled thermodynamic and transport functions extracted from the experimental facts in a wide range of the variation of the scaled variable y . As seen from the mentioned Figures, the constructed normalized thermodynamic and transport functions show the scaling behavior over three decades in the normalized variable.

9.5. Electric resistivity of HF metals

The electric resistivity of strongly correlated Fermi systems, $\rho(T) = \rho_0 + \Delta\rho_1(B, T)$, is determined by the effective mass, because of the Kadowaki-Woods relation $\Delta\rho_1(B, T) = A(B, T)T^2 \propto (M^*(B, T)T)^2$, see Subsection 9.4.3 and Refs. [139, 140, 141], and therefore the temperature dependence of the effective mass discussed above can be observed in measurements of the resistivity of HF metals. At temperatures $T \ll T^*(B)$, the system is in the LFL state, the behavior of

the effective mass as $x \rightarrow x_{FC}$ is described by Eq. (93), and the coefficient $A(B)$ can be represented as

$$A(B) \propto \frac{1}{(B - B_{c0})^{4/3}}. \quad (113)$$

In this regime, the resistivity behaves as $\Delta\rho_1 = c_1 T^2 / (B - B_{c0})^{4/3} \propto T^2$. The second regime, a highly correlated Fermi liquid determined by Eq. (99), is characterized by the resistivity dependence $\Delta\rho_1 = c_2 T^2 / (T^{2/3})^2 \propto T^{2/3}$. The third regime at $T > T^*(B)$ is determined by Eq. (101). In that case we obtain $\Delta\rho_1 = c_3 T^2 / (T^{1/2})^2 \propto T$. If the system is above the quantum critical line as shown in Fig. 6, the dependence of the effective mass on temperature is given by Eq. (31), so we obtain from Eq. (105) that the quasiparticle damping $\gamma(T) \propto T$ [51]. As a result, we see that the resistivity dependence on temperature is $\Delta\rho_1 = c_4 T$ [147]. Here, c_1, c_2, c_3 and c_4 are constants. If the system at the transition regime, as shown by the arrows in Fig. 15, the dependence of the effective mass on temperature cannot be characterized by a single exponent as it is clearly seen from the inset to Fig. 15 a. So we have that $\Delta\rho_1 \propto T^{\alpha_R}$ with $1 < \alpha_R < 2$. We note that all temperature dependencies corresponding to these regimes have been observed in measurements involving the heavy-fermion metals CeCoIn₅, YbRh₂Si₂ and YbAgGe [15, 30, 31, 162, 163].

9.6. Magnetic susceptibility and magnetization measured on CeRu₂Si₂

Experimental investigations of the magnetic properties of CeRu₂Si₂ down to the lowest temperatures (down to 170 mK) and ultrasmall magnetic fields (down to 0.21 mT) have shown neither evidence of the magnetic ordering, superconductivity nor conventional LFL behavior [92]. These results imply a magnetic quantum critical point in CeRu₂Si₂ is absent and the critical field $B_{c0} = 0$. Even if the magnetic quantum critical point were there it should maintain the NFL behavior over four decades in temperature. Such a strong influence can hardly exist within the framework of conventional quantum phase transitions.

Temperature dependence on a logarithmic scale of the normalized AC susceptibility $\chi(B, T)$ is shown at different applied magnetic fields B as indicated in the left panel of Fig. 23 versus normalized temperature. The right panel of the Figure shows the normalized static magnetization $M_B(B, T)$ (DC susceptibility) in the same normalized temperature range. The temperature is normalized to T_M (the temperature at which the susceptibility reaches its peak value), the susceptibility is normalized to the peak value $\chi(B, T_M)$, and the magnetization is normalized to $M_B(B, T \rightarrow 0)$, for each value of the field [92]. If we use Eq. (110) and the definition of susceptibility (111), we conclude that the susceptibility and magnetization also demonstrate the scaling behavior and can be represented by the universal function (106) of the single variable y , if they are respectively normalized as discussed above. We see from Fig. 23 that at finite field strengths

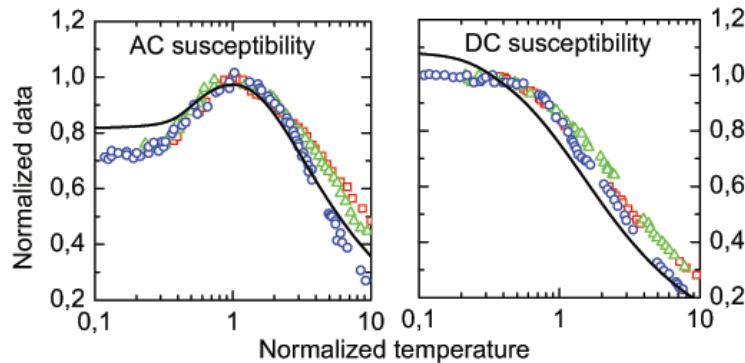


Figure 23: The normalized magnetic susceptibility $\chi(B, T)/\chi(B, T_M)$ (the left panel) and normalized magnetization $M_B(B, T)/M_B(B, T_M)$ (DC susceptibility, the right panel) for CeRu₂Si₂ in magnetic fields 0.20 mT (squares), 0.39 mT (triangles), and 0.94 mT (circles) as functions of the normalized temperature T/T_M [92]. The solid lines depict the calculated scaling behavior [53] as described in Subsection 9.3.1.

B , the curve describing $\chi(B, T)/\chi(B, T_M)$ has a peak at a certain temperature T_M , while $M_B(B, T)/M_B(B, T_M)$ has no such peak [49, 53, 157]. This behavior agrees well with the experimental results [49, 53, 157] obtained in measurements on CeRu₂Si₂ [92]. We note that such behavior of the susceptibility is not typical of ordinary metals and cannot be explained within the scope of theories that take only ordinary quantum phase transitions into account [92].

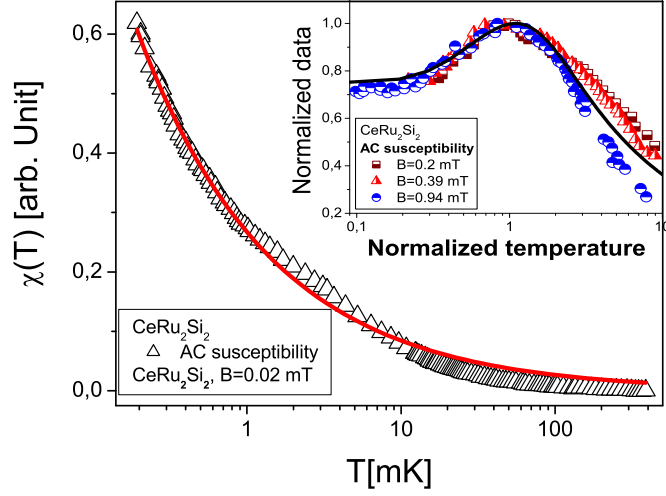


Figure 24: Temperature dependence of the AC susceptibility χ_{AC} for CeRu_2Si_2 . The solid curve is a fit for the data shown by the triangles at $B = 0.02$ mT [92] and represented by the function $\chi(T) = a/\sqrt{T}$ given by Eq. (101) with a being a fitting parameter. Inset shows the normalized effective mass versus normalized temperature T_N extracted from χ_{AC} measured at different fields as indicated in the inset [92]. The solid curve traces the universal behavior of $M_N^*(T_N)$ determined by Eq. (106). Parameters c_1 and c_2 are adjusted to fit the average behavior of the normalized effective mass M_N^* .

To verify Eq. (101) and illustrate the transition from LFL behavior to NFL one, we use measurements of $\chi_{AC}(T)$ in CeRu_2Si_2 at magnetic field $B = 0.02$ mT at which this HF metal demonstrates the NFL behavior down to lowest temperatures [92]. Indeed, in this case we expect that LFL regime to start to form at temperatures lower than $T_M \sim \mu_B B \sim 0.01$ mK as it follows from Eq. (108). It is seen from Fig. 24 that Eq. (101) gives good description of the experimental facts in the extremely wide range of temperatures: the susceptibility χ_{AC} as a function of T , is not a constant upon cooling, as would be for a Fermi liquid, but shows a $1/\sqrt{T}$ divergence over almost four decades in temperature. The inset of Fig. 24 exhibits a fit for M_N^* extracted from measurements of $\chi_{AC}(T)$ at different magnetic fields, clearly indicating the change from LFL behavior at $T_N < 1$ to NFL one at $T_N > 1$ when the system moves along the vertical arrow as shown in Fig. 15. It seen from Figs. 23 and 24 that the function given by Eq. (106) represents a good approximation for M_N^* within the extended paradigm. In Subsection 9.4 we have seen that the same is true in the case of YbRh_2Si_2 with the AF quantum critical point. We conclude that both alloys CeRu_2Si_2 and YbRh_2Si_2 demonstrate the universal NFL thermodynamic behavior, independent of the details of the HF metals such as their lattice structure, composition and magnetic ground state. This conclusion implies also that numerous QCPs related to conventional quantum phase transitions assumed to be responsible for the NFL behavior of different HF metals can be well reduced to a single QCP related to FCQPT and accounted for within the extended quasiparticle paradigm [164].

9.7. Transverse magnetoresistance in the HF metal CeCoIn_5

Our comprehensive theoretical study of both the longitudinal and transverse magnetoresistance (MR) shows that it is (similar to other thermodynamic characteristics like magnetic susceptibility, specific heat, etc) governed by the scaling behavior of the quasiparticle effective mass. The crossover from negative to positive MR occurs at elevated temperatures and fixed magnetic fields when the system transits from the LFL behavior to NFL one and can be well captured by this scaling behavior.

By definition, MR is given by

$$\rho_{mr}(B, T) = \frac{\rho(B, T) - \rho(0, T)}{\rho(0, T)}, \quad (114)$$

We apply Eq. (114) to study MR of strongly correlated electron liquid versus temperature T as a function of magnetic field B . The resistivity $\rho(B, T)$ is

$$\rho(B, T) = \rho_0 + \Delta\rho(B, T) + \Delta\rho_L(B, T), \quad (115)$$

where ρ_0 is a residual resistance, $\Delta\rho = c_1 A T^2$, c_1 is a constant. The classical contribution $\Delta\rho_L(B, T)$ to MR due to orbital motion of carriers induced by the Lorentz force obeys the Kohler's rule [165]. We note that $\Delta\rho_L(B) \ll \rho(0, T)$ as it is assumed in the weak-field approximation. To calculate A , we again use the quantities $\gamma_0 = C/T \propto M^*$ and/or $\chi \propto M^*$ as well as employ the fact that the Kadowaki-Woods ratio $K = A/\gamma_0^2 \propto A/\chi^2 = \text{const}$. As a result, we obtain $A \propto (M^*)^2$, so that $\Delta\rho(B, T) = c(M^*(B, T))^2 T^2$ and c is a constant. Suppose that the temperature is not very low, so that $\rho_0 \leq \Delta\rho(B=0, T)$, and $B \geq B_{c0}$. Substituting (115) into (114), we find that [166]

$$\rho_{mr} \simeq \frac{\rho_0 + \Delta\rho_L(B, T)}{\rho(0, T)} + cT^2 \frac{(M^*(B, T))^2 - (M^*(0, T))^2}{\rho(0, T)}. \quad (116)$$

Consider the qualitative behavior of MR described by Eq. (116) as a function of B at a certain temperature $T = T_0$. In weak magnetic fields, when the system exhibits NFL (see Fig. 15), the main contribution to MR is made by the term $\Delta\rho_L(B)$, because the effective mass is independent of the applied magnetic field. Hence, $|M^*(B, T) - M^*(0, T)|/M^*(0, T) \ll 1$ and the leading contribution is made by $\Delta\rho_L(B)$. As a result, MR is an increasing function of B . When B becomes so high that $T^*(B) \sim \mu_B(B - B_{c0}) \sim T_0$, the difference $(M^*(B, T) - M^*(0, T))$ becomes negative because $M^*(B, T)$ is now the diminishing function of B given by Eq. (107). Thus, MR as a function of B reaches its maximal value at $T^*(B) \sim T_N(B) \sim T_0$. At further increase of magnetic field, when $T_M(B) > T_0$, the effective mass $M^*(B, T)$ becomes a decreasing function of B . As B increases,

$$\frac{(M^*(B, T) - M^*(0, T))}{M^*(0, T)} \rightarrow -1, \quad (117)$$

and the magnetoresistance, being a decreasing function of B , can reach its negative values.

Now we study the behavior of MR as a function of T at fixed value B_0 of magnetic field. At low temperatures $T \ll T^*(B_0)$, it follows from Eqs. (106) and (93) that $M^*(B_0, T)/M^*(0, T) \ll 1$, and it is seen from Eq. (117) that $\rho_{mr}(B_0, T) \sim -1$, because $\Delta\rho_L(B_0, T)/\rho(0, T) \ll 1$. We note that B_0 must be relatively high to guarantee that $M^*(B_0, T)/M^*(0, T) \ll 1$. As the temperature increases, MR increases, remaining negative. At $T \simeq T^*(B_0)$, MR is approximately zero, because $\rho(B_0, T) \simeq \rho(0, T)$ at this point. This allows us to conclude that the change of the temperature dependence of resistivity $\rho(B_0, T)$ from quadratic to linear manifests itself in the transition from negative to positive MR. One can also say that the transition takes place when the system goes from the LFL behavior to the NFL one. At $T \geq T^*(B_0)$, the leading contribution to MR is made by $\Delta\rho_L(B_0, T)$ and MR reaches its maximum. At $T_M(B_0) \ll T$, MR is a decreasing function of the temperature, because

$$\frac{|M^*(B, T) - M^*(0, T)|}{M^*(0, T)} \ll 1, \quad (118)$$

and $\rho_{mr}(B_0, T) \ll 1$. Both transitions (from positive to negative MR with increasing B at fixed temperature T and from negative to positive MR with increasing T at fixed B value) have been detected in measurements of the resistivity of CeCoIn₅ in a magnetic field [30].

Let us turn to quantitative analysis of MR [166]. As it was mentioned above, we can safely assume that the classical contribution $\Delta\rho_L(B, T)$ to MR is small as compared to $\Delta\rho(B, T)$. Omission of $\Delta\rho_L(B, T)$ allows us to make our analysis and results transparent and simple while the behavior of $\Delta\rho_L(B_0, T)$ is not known in the case of HF metals. Consider the ratio $R^\rho = \rho(B, T)/\rho(0, T)$ and assume for a while that the residual resistance ρ_0 is small in comparison with the temperature dependent terms. Taking into account Eq. (115) and $\rho(0, T) \propto T$, we obtain from Eq. (116) that

$$R^\rho = \rho_{mr} + 1 = \frac{\rho(B, T)}{\rho(0, T)} \propto T(M^*(B, T))^2, \quad (119)$$

and consequently, from Eqs. (106) and (119) that the ratio R^ρ reaches its maximal value R_M^ρ at some temperature $T_{Rm} \sim T_M$. If the ratio is measured in units of its maximal value R_M^ρ and T is measured in units of $T_{Rm} \sim T_M$ then it is seen from Eqs. (106) and (119) that the normalized MR

$$R_N^\rho(y) = \frac{R^\rho(B, T)}{R_M^\rho(B)} \simeq y(M_N^*(y))^2 \quad (120)$$

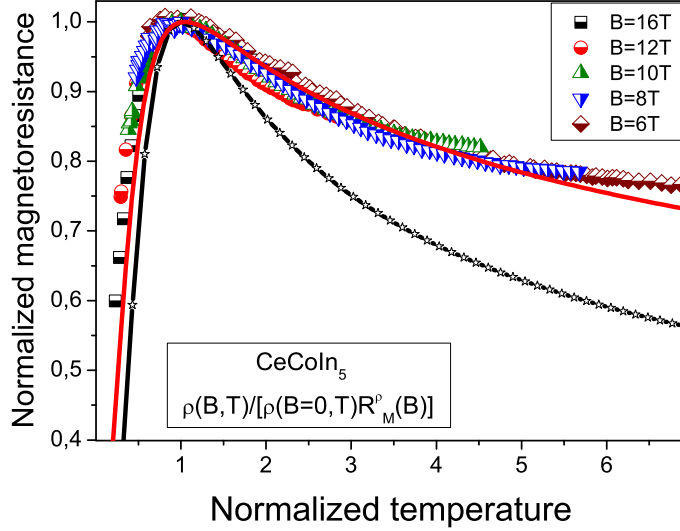


Figure 25: The normalized magnetoresistance $R_N^\rho(y)$ given by Eq. (120) versus normalized temperature $y = T/T_{Rm}$. $R_N^\rho(y)$ was extracted from MR shown in Fig. 27 and collected on CeCoIn₅ at fixed magnetic fields B [30] listed in the right upper corner. The starred line represents our calculations based on Eqs. (106) and (120) with the parameters extracted from AC susceptibility of CeRu₂Si₂ (see the caption to Fig. 24). The solid line displays our calculations based on Eqs. (121) and (120); only one parameter was used to fit the data, while the other were extracted from the AC susceptibility measured on CeRu₂Si₂.

becomes a function of the only variable $y = T/T_{Rm}$. To verify Eq. (120), we use MR obtained in measurements on CeCoIn₅, see Fig. 1(b) of Ref. [30]. The results of the normalization procedure of MR are reported in Fig. 25. It is clearly seen that the data collapse into the same curve, indicating that the normalized magnetoresistance R_N^ρ obeys the scaling behavior well given by Eq. (120). This scaling behavior obtained directly from the experimental facts is a vivid evidence that MR behavior is predominantly governed by the effective mass $M^*(B, T)$.

Now we are in position to calculate $R_N^\rho(y)$ given by Eq. (120). Using Eq. (106) to parameterize $M_N^*(y)$, we extract parameters c_1 and c_2 from measurements of the magnetic AC susceptibility χ on CeRu₂Si₂ [92] and apply Eq. (120) to calculate the normalized ratio. It is seen that the calculations shown by the starred line in Fig. 25 start to deviate from experimental points at elevated temperatures. To improve the coincidence, we employ Eq. (101) which describes the behavior of the effective mass at elevated temperatures and ensures that at these temperatures the resistance behaves as $\rho(T) \propto T$. To correct the behavior of $M_N^*(y)$ at rising temperatures $M^* \sim T^{-1/2}$, we add a term to Eq. (106) and obtain

$$M_N^*(y) \approx \frac{M^*(x)}{M_M^*} \left[\frac{1 + c_1 y^2}{1 + c_2 y^{8/3}} + c_3 \frac{\exp(-1/y)}{\sqrt{y}} \right], \quad (121)$$

where c_3 is a parameter. The last term on the right hand side of Eq. (121) makes M_N^* satisfy Eq. (101) at temperatures $T/T_M > 2$. In Fig. 25, the fit of $R_N^\rho(y)$ by Eq. (121) is shown by the solid line. Constant c_3 is taken as a fitting parameter, while the other were extracted from AC susceptibility of CeRu₂Si₂ as described in the caption to Fig. 24.

Before discussing the magnetoresistance $\rho_{mr}(B, T)$ given by Eq. (114), we consider the magnetic field dependence of both the MR peak value $R_{max}(B)$ and the corresponding peak temperature $T_{Rm}(B)$. It is possible to use Eq. (119) which relates the position and value of the peak with the function $M^*(B, T)$. Since $T_{Rm} \propto \mu_B(B - B_{c0})$, B enters Eq. (119) only as tuning parameter of QCP, as both $\Delta\rho_L$ and ρ_0 were omitted. At $B \rightarrow B_{c0}$ and $T \ll T_{Rm}(B)$, this omission is not correct since $\Delta\rho_L$ and ρ_0 become comparable with $\Delta\rho(B, T)$. Therefore, both $R_{max}(B)$ and $T_{Rm}(B)$ are not characterized by any critical field, being continuous functions at the quantum critical field B_{c0} , in contrast to $M^*(B, T)$ whose peak value diverges and the peak temperature tends to zero at B_{c0} as seen from Eqs. (107) and (108). Thus, we have to take into account $\Delta\rho_L(B, T)$ and ρ_0 which prevent $T_{Rm}(B)$ from vanishing and make $R_{max}(B)$ finite at $B \rightarrow B_{c0}$. As a result, we have to replace B_{c0} by some effective field $B_{eff} < B_{c0}$ and take B_{eff} as a parameter which imitates the contributions coming from both $\Delta\rho_L(B, T)$ and ρ_0 . Upon modifying Eq. (119) by taking into account $\Delta\rho_L(B, T)$ and ρ_0 , we obtain

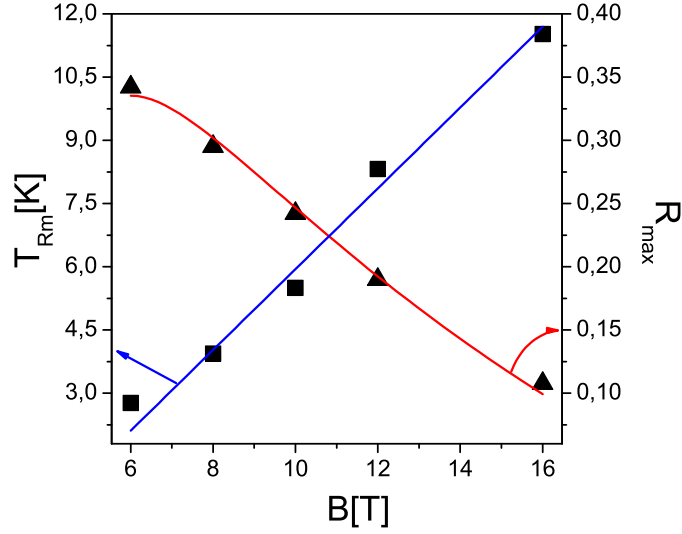


Figure 26: The peak temperatures T_{Rm} (squares) and the peak values R_{max} (triangles) versus magnetic field B extracted from measurements of MR [30]. The solid lines represent our calculations based on Eqs. (122) and (123).

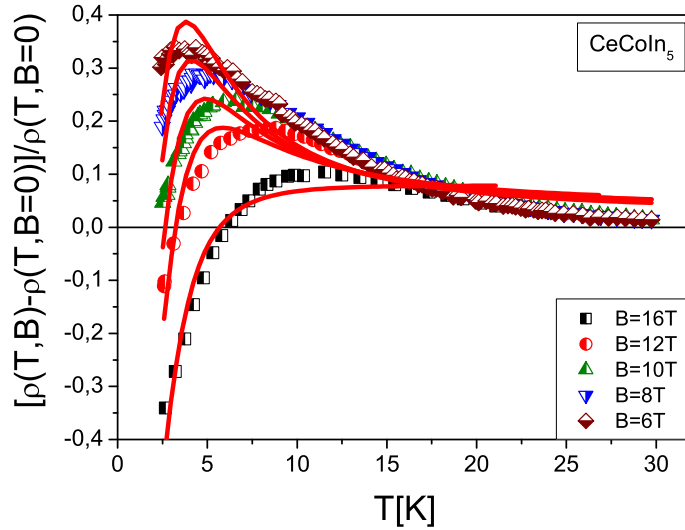


Figure 27: MR versus temperature T as a function of magnetic field B . The experimental data on MR were collected on $CeCoIn_5$ at fixed magnetic field B [30] shown in the right bottom corner of the Figure. The solid lines represent our calculations, Eq. (106) is used to fit the effective mass entering Eq. (120).

$$T_{Rm}(B) \simeq b_1(B - B_{eff}), \quad (122)$$

$$R_{max}(B) \simeq \frac{b_2(B - B_{eff})^{-1/3} - 1}{b_3(B - B_{eff})^{-1} + 1}. \quad (123)$$

Here b_1 , b_2 , b_3 and B_{eff} are the fitting parameters. It is pertinent to note that while deriving Eq. (123) we use Eq. (122) with substitution $(B - B_{eff})$ for T . Then, Eqs. (122) and (123) are not valid at $B \lesssim B_{c0}$. In Fig. 26, we show the field dependence of both T_{Rm} and R_{max} , extracted from measurements of MR [30]. Clearly both T_{Rm} and R_{max} are well described by Eqs. (122) and (123) with $B_{eff} = 3.8$ T. We note that this value of B_{eff} is in good agreement with observations obtained from the $T - B$ phase diagram of $CeCoIn_5$, see the position of the MR maximum shown by the filled circles in Fig. 3 of Ref. [30].

To calculate $\rho_{mr}(B, T)$, we apply Eq. (120) to describe its universal behavior, Eq. (106) for the effective mass along with Eqs. (122) and (123) for MR parameters. Figure 27 shows the calculated MR versus temperature as a function of magnetic field B together with the experimental points from Ref. [30]. We recall that the contributions coming from $\Delta\rho_L(B, T)$ and ρ_0 were omitted. As seen from Fig. 27, our description of the experiment is good.

9.8. Magnetic-field-induced reentrance of Fermi-liquid behavior and spin-lattice relaxation rates in $\text{YbCu}_{5-x}\text{Au}_x$

One of the most interesting and puzzling issues in the research on HF metals is their anomalous dynamic and relaxation properties. It is important to verify whether quasiparticles with effective mass M^* still exist and determine the physical properties of the muon and ^{63}Cu nuclear spin-lattice relaxation rates $1/T_1$ in HF metals throughout their temperature - magnetic field phase diagram, see Fig. 15. This phase diagram comprises both LFL and NFL regions as well as NFL-LFL transition or the crossover region, where magnetic-field-induced LFL reentrance occurs. Measurements of the muon and ^{63}Cu nuclear spin-lattice relaxation rates $1/T_1$ in $\text{YbCu}_{4.4}\text{Au}_{0.6}$ have shown that it differs substantially from ordinary Fermi liquids obeying the Korringa law [167]. Namely, it was reported that for $T \rightarrow 0$ reciprocal relaxation time diverges as $1/T_1 T \propto T^{-4/3}$ following the behavior predicted by the self-consistent renormalization (SCR) theory [168]. The static uniform susceptibility χ diverges as $\chi \propto T^{-2/3}$ so that $1/T_1 T$ scales with χ^2 . Latter result is at variance with SCR theory [167]. Moreover, the application of magnetic field B restores the LFL behavior from initial the NFL one, significantly reducing $1/T_1$. These experimental findings are hard to explain within both the conventional LFL approach and in terms of other approaches like SCR theory [167, 168].

In this Subsection we show that the above anomalies along with magnetic-field-induced reentrance of LFL properties are indeed determined by the dependence of the quasiparticle effective mass M^* on magnetic field B and temperature T and demonstrate that violations of the Korringa law also come from $M^*(B, T)$ dependence. Our theoretical analysis of experimental data on the base of FCQPT approach permits not only to explain the above two experimental facts in a unified manner, but to unveil their universal properties, relating the peculiar features of both longitudinal magnetoresistance and specific heat in YbRh_2Si_2 to the behavior of spin-lattice relaxation rates.

To discuss the deviations from the Korringa law in light of NFL properties of $\text{YbCu}_{4.4}\text{Au}_{0.6}$, we notice that in LFL theory the spin-lattice relaxation rate $1/T_1$ is determined by the quasiparticles near the Fermi level. The above relaxation rate is related to the decay amplitude of the quasiparticles, which in turn is proportional to the density of states at the Fermi level $N(E_F)$. Formally, the spin-lattice relaxation rate is determined by the imaginary part χ'' of the low-frequency dynamical magnetic susceptibility $\chi(\mathbf{q}, \omega \rightarrow 0)$, averaged over momentum \mathbf{q}

$$\frac{1}{T_1} = \frac{3T}{4\mu_B^2} \sum_{\mathbf{q}} A_{\mathbf{q}} A_{-\mathbf{q}} \frac{\chi''(\mathbf{q}, \omega)}{\omega}, \quad (124)$$

where $A_{\mathbf{q}}$ is the hyperfine coupling constant of the muon (or nuclei) with the spin excitations at wave vector \mathbf{q} [168]. If $A_{\mathbf{q}} \equiv A_0$ is independent of q , then standard LFL theory yields the relation

$$\frac{1}{T_1 T} = \pi A_0^2 N^2(E_F). \quad (125)$$

Equation (125) can be viewed as Korringa law. Since in our FCQPT approach the physical properties of the system under consideration are determined by the effective mass $M^*(T, B, x)$, we express $1/T_1 T$ in Eq. (125) via it. This is accomplished with the standard expression [20] $N(E_F) = M^* p_F / \pi^2$, rendering Eq. (125) to the form

$$\frac{1}{T_1 T} = \frac{A_0^2 p_F^2}{\pi^3} M^{*2} \equiv \eta [M^*(T, B, x)]^2, \quad (126)$$

where $\eta = (A_0^2 p_F^2) / \pi^3 = \text{const}$. The empirical expression

$$\frac{1}{T_1 T} \propto \chi^2(T), \quad (127)$$

extracted from experimental data in $\text{YbCu}_{5-x}\text{Au}_x$ [167], follows explicitly from Eq. (126) and well-known LFL relations $M^* \propto \chi \propto C/T$.

In what follows, we compute the effective mass as it was explained in Subsection 9.3.1 and employ Eq. (106) for estimations of obtained values [169]. The decay law given by Eq. (99) along with Eq. (126) permits to express the relaxation rate in this temperature range as

$$\frac{1}{T_1 T} = a_1 + a_2 T^{-4/3} \propto \chi^2(T), \quad (128)$$

where a_1 and a_2 are fitting parameters. The dependence (128) is reported in Fig. 28 along with experimental points for the muon and nuclear spin-lattice relaxation rates in $\text{YbCu}_{4.4}\text{Au}_{0.6}$ at zero magnetic field [167]. It is seen from Fig. 28 that Eq. (128) gives good description of the experiment in the extremely wide temperature range. This means that the extended paradigm is valid and quasiparticles survive in close vicinity of FCQPT, while the observed violation of Korringa law comes from the dependence of the effective mass on temperature.

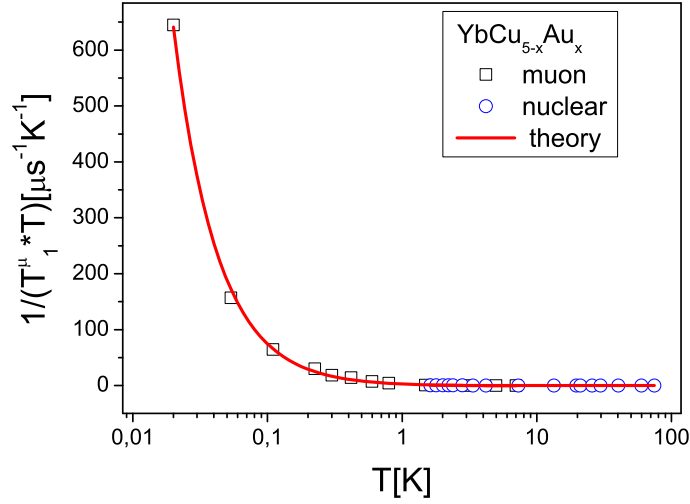


Figure 28: Temperature dependence of muon (squares) and nuclear (circles) spin-lattice relaxation rates (divided by temperature) for $\text{YbCu}_{4.4}\text{Au}_{0.6}$ at zero magnetic field [167]. The solid curve represents our calculations based on Eq. (128).

Figure 29 displays magnetic field dependence of normalized muon spin-lattice relaxation rate $1/T_{1N}^\mu$ in $\text{YbCu}_{5-x}\text{Au}_x$ ($x=0.6$) along with our theoretical B -dependence. To obtain the latter theoretical curve we (for fixed temperature and in magnetic field B) employ Eq. (126) and solve the Landau integral equation to calculate $M^*(T, B)$ as it was described in Subsection 9.3.1. We note that the normalized effective mass $M_N^*(y)$ was obtained by normalizing $M^*(T, B)$ at its inflection point shown in the inset to Fig. 15.

It is instructive to compare the LMR analyzed in Subsection 9.4.3 and $1/T_{1N}^\mu$. LMR $\rho(B, T) = \rho_0 + \rho_B + A(B, T)T^2$ is as a function of B at fixed T , where ρ_0 is the residual resistance, ρ_B is the contribution to LMR due to orbital motion of carriers induced by the Lorentz force, and A is the coefficient. As we see in Subsection 9.4.3, ρ_B is small and we omit this contribution. The Kadowaki-Woods relation allows us to employ M^* to calculate $A(B, T)$. As a result, $\rho(B, T) - \rho_0 \propto (M^*)^2$, and $1/T_{1N}^\mu \propto (M^*)^2$ as seen from Eq. (126). As a result, we see that that LMR and the magnetic field dependence of normalized muon spin-lattice relaxation rate $1/T_{1N}^\mu$ can be evaluated from the same equation

$$R_N^\rho(y) = \frac{\rho(y) - \rho_0}{\rho_{\text{inf}}} = \frac{1}{T_{1N}^\mu} = (M_N^*(y))^2. \quad (129)$$

Inset to Fig. 29 reports the normalized LMR vs normalized magnetic field $y = B/B_{\text{inf}}$ at different temperatures, shown in the legend. Here ρ_{inf} and B_{inf} are respectively LMR and magnetic field taken at the inflection point. The inflection points of both LMR and $1/T_{1N}^\mu$ are generated by the inflection point of M^* shown in the inset to Fig. 15 a by the arrow. The transition region where LMR starts to decrease is shown in the inset by the hatched area and takes place when the

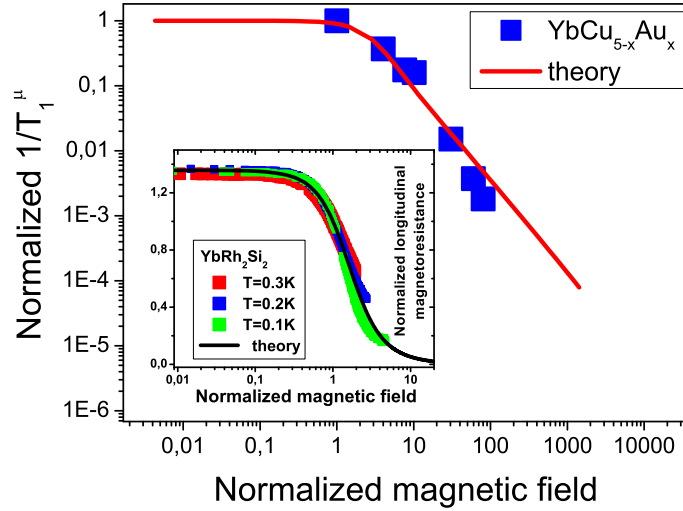


Figure 29: Magnetic field dependence of normalized at the inflection point muon spin-lattice relaxation rate $1/T_{1N}^{\mu}$ extracted from measurements [167] on $\text{YbCu}_{4.4}\text{Au}_{0.6}$ along with our calculations of B -dependence of the quasiparticle effective mass. Inset shows the normalized LMR $R_N^{\rho}(y)$ versus normalized magnetic field. $R_N^{\rho}(y)$ was extracted from LMR of YbRh_2Si_2 at different temperatures [17] listed in the legend. The solid curves represent our calculations.

system moves along the horizontal dash-dot arrow. We note that the same normalized effective mass has been used to calculate both $1/T_{1N}^{\mu}$ in $\text{YbCu}_{4.4}\text{Au}_{0.6}$ and the normalized LMR in YbRh_2Si_2 . Thus, Eq. (129) determines the close relationship between the quite different dynamic properties, showing the validity of the quasiparticle extended paradigm. In Fig. 29, both theoretical and experimental curves have been normalized by their inflection points, which also reveals the scaling behavior - the curves at different temperatures merge into a single one in terms of the scaled variable y . Figure 29 shows clearly that both normalized magnetoresistance R_N^{ρ} and reciprocal spin-lattice relaxation time obey well the scaling behavior given by Eq. (129). This fact obtained directly from the experimental findings is vivid evidence that the behavior of both the above quantities is predominantly governed by the field and temperature dependence of the effective mass.

We remark that the same normalized effective mass determines the behavior of the thermodynamic and transport properties in YbRh_2Si_2 , see Subsection 9.4. It is seen from the Figures presented in Subsection 9.4 that our calculations of the effective mass offer good descriptions of such different quantities as the relaxation rates ($1/T_1T$) and the transport (LMR) and thermodynamic properties in such different HF metals as $\text{YbCu}_{5-x}\text{Au}_x$ and YbRh_2Si_2 . It is pertinent to note that the obtained good description makes an impressive case in favor of the reliability of the quasiparticle extended paradigm.

9.9. Relationships between critical magnetic fields B_{c0} and B_{c2} in HF metals and high- T_c superconductors

Recently, in high- T_c superconductors, exciting measurements revealing their physics have been performed. One type of the measurements demonstrate the existence of Bogoliubov quasiparticles (BQ) in the superconducting state [100, 116, 117]. While in the pseudogap regime at temperatures above T_c when the superconductivity vanishes, a strong indication of the pairing of electrons or the formation of preformed pairs of electrons was observed, while the gap continues to follow the simple d-wave form [116, 117]. Another type of the measurement explored the normal state induced by the application of magnetic field, when the transition from the NFL behavior to LFL one occurs [150]. As we have mentioned in Subsection 7.2.1, there are the experimental relationships between the critical fields $B_{c2} \geq B_{c0}$, where B_{c2} is the field destroying the superconducting state, and B_{c0} is the critical field at which the magnetic field induced QCP takes place. Now we show that $B_{c2} \geq B_{c0}$. We note that to study the aforementioned transition experimentally in high- T_c superconductors, strong magnetic fields of $B \geq B_{c2}$ are required; earlier, such investigation was technically inaccessible. An attempt to study the transition experimentally had already been made [148].

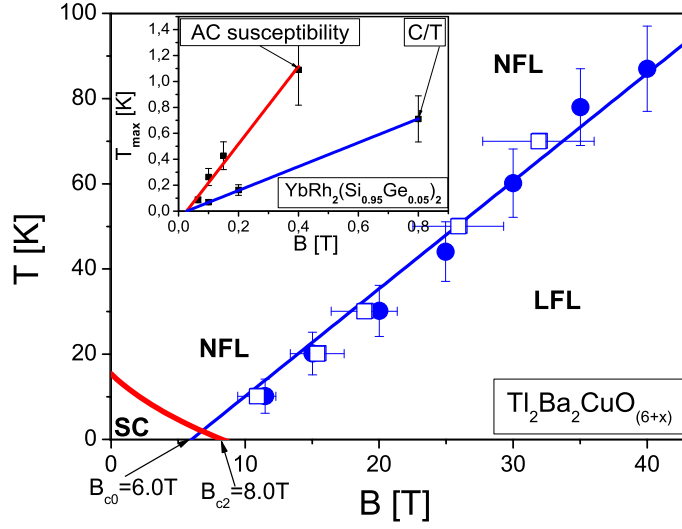


Figure 30: $T - B$ phase diagram of the superconductor $\text{Tl}_2\text{Ba}_2\text{CuO}_{6+x}$. The crossover (from LFL to NFL regime) line $T^*(B)$ is given by the Eq. (108). Open squares and solid circles are experimental values [150]. Thick line represents the boundary between the superconducting and normal phases. Arrows near the bottom left corner indicate the critical magnetic field B_{c2} destroying the superconductivity and the critical field B_{c0} . Inset displays the peak temperatures $T_{\max}(B)$, extracted from measurements of C/T and χ_{AC} on $\text{YbRh}_2(\text{Si}_{0.95}\text{Ge}_{0.05})_2$ [7, 170] and approximated by straight lines Eq. (108). The lines intersect at $B \approx 0.03$ T.

Let us now consider the $T - B$ phase diagram of the high- T_c superconductor $\text{Tl}_2\text{Ba}_2\text{CuO}_{6+x}$ shown in Fig. 30. The substance is a superconductor with T_c from 15 K to 93 K, being controlled by oxygen content [150]. In Fig. 30 open squares and solid circles show the experimental values of the crossover temperature from the LFL to NFL regimes [150]. The solid line given by Eq. (100) shows our fit with $B_{c0} = 6$ T that is in good agreement with $B_{c0} = 5.8$ T obtained from the field dependence of the charge transport [150].

As it is seen from Fig. 30, the linear behavior agrees well with the experimental data [150, 166]. The peak temperatures T_{\max} shown in the inset to Fig. 30, depict the maxima of $C(T)/T$ and $\chi_{AC}(T)$ measured on $\text{YbRh}_2(\text{Si}_{0.95}\text{Ge}_{0.05})_2$ [7, 170]. From Fig. 30, T_{\max} is seen to shift to higher values with increase of the applied magnetic field and both functions can be represented by straight lines intersecting at $B \approx 0.03$ T. This observation is in good agreement with experiments [7, 170]. Clearly from Fig. 30 the critical field $B_{c2} = 8$ T destroying the superconductivity is close to $B_{c0} = 6$ T. We now show that this is more than a simple coincidence, and $B_{c2} \gtrsim B_{c0}$. Indeed, at $B > B_{c0}$ and low temperatures $T < T^*(B)$, the system is in its LFL state. The superconductivity is then destroyed since the superconducting gap is exponentially small as we have seen in Subsection 5.3. At the same time, there is the FC state at $B < B_{c0}$ and this low-field phase has large prerequisites towards superconductivity as in this case the gap is a linear function of the superconducting coupling constant λ_0 as it was shown in Subsection 5.3. We note that this is exactly the case in CeCoIn_5 where $B_{c0} \approx B_{c2} \approx 5$ T [30] as seen from Fig. 31, while the application of pressure makes $B_{c2} > B_{c0}$ [33]. However, if the superconducting coupling constant is rather weak then antiferromagnetic order wins the competition. As a result, $B_{c2} = 0$, while B_{c0} can be finite as in YbRh_2Si_2 and $\text{YbRh}_2(\text{Si}_{0.95}\text{Ge}_{0.05})_2$ [15, 170].

Comparing the phase diagram of $\text{Tl}_2\text{Ba}_2\text{CuO}_{6+x}$ with that of CeCoIn_5 shown in Figs. 30 and 31 respectively, it is possible to conclude that they are similar in many respects. Further, we note that the superconducting boundary line $B_{c2}(T)$ at decreasing temperatures acquires a step, i.e. the corresponding phase transition becomes first order [97, 171]. This leads us to speculate that the same may be true for $\text{Tl}_2\text{Ba}_2\text{CuO}_{6+x}$. We expect that in the NFL state the tunneling conductivity is asymmetrical function of the applied voltage, while it becomes symmetrical at the application of increased magnetic fields when $\text{Tl}_2\text{Ba}_2\text{CuO}_{6+x}$ transits to the LFL behavior, as it predicted to be in CeCoIn_5 [172].

It follows from Eq. (81) that it is impossible to observe the relatively high values of $A(B)$ since in our case $B_{c2} > B_{c0}$.

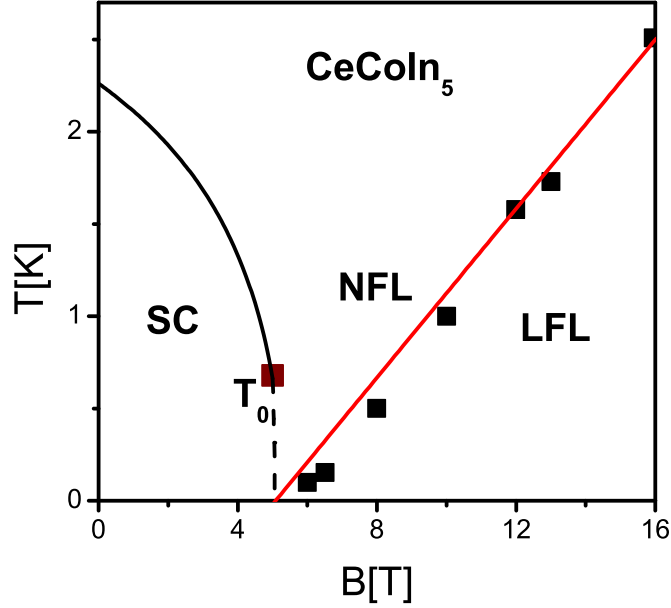


Figure 31: $T - B$ phase diagram of the CeCoIn_5 heavy fermion metal. The interface between the superconducting and normal phases is shown by the solid line to the square where the phase transition becomes a first-order phase transition [171]. At $T < T_0$, the phase transition is a first-order phase transition [171]. The interface between the superconducting and normal phases is shown by the dashed line. The solid straight line represented by Eq. (108) with the experimental points [31] shown by squares is the interface between the LFL and NFL states.

We note that Eq. (81) is valid when the superconductivity is destroyed by the application of magnetic field, otherwise the effective mass is also finite being given by Eq. (41). Therefore, as was mentioned above, in high- T_c QCP is poorly accessible to experimental observations being "hidden in superconductivity". Nonetheless, thanks to the experimental facts [150], we have seen in Subsection 7.2.1 that it is possible to study QCP of high- T_c [120]. As seen from Fig. 12, the facts give evidences that the physics underlying the field-induced reentrance of LFL behavior, is the same for both HF metals and high- T_c superconductors.

9.10. Scaling behavior of the HF $\text{CePd}_{1-x}\text{Rh}_x$ ferromagnet

QCP can arise by suppressing the transition temperature T_{NL} of a ferromagnetic (FM) (or antiferromagnetic (AFM)) phase to zero by tuning some control parameter ζ other than temperature, such as pressure P , magnetic field B , or doping x as it takes place in the HF ferromagnet $\text{CePd}_{1-x}\text{Rh}_x$ [173, 174] or the HF metal $\text{CeIn}_{3-x}\text{Sn}_x$ [175].

The HF metal $\text{CePd}_{1-x}\text{Rh}_x$ evolves from ferromagnetism at $x = 0$ to a non-magnetic state at some critical concentration x_{FC} . Utilizing the extended quasiparticle paradigm picture and the concept of FCQPT, we address the question about the NFL behavior of the ferromagnet $\text{CePd}_{1-x}\text{Rh}_x$ and show that it coincides with that of the antiferromagnets $\text{YbRh}_2(\text{Si}_{0.95}\text{Ge}_{0.05})_2$ and YbRh_2Si_2 , and paramagnets CeRu_2Si_2 and CeNi_2Ge_2 . We again conclude that the NFL behavior, being independent of the peculiarities of a specific alloy, is universal. Incidentally, numerous quantum critical points assumed to be responsible for the NFL behavior of different HF metals can be well reduced to the only quantum critical point related to FCQPT [176, 177].

As we have seen above, the effective mass $M^*(T, B)$ can be measured in experiments on HF metals. For example, $M^*(T, B) \propto C(T)/T \propto \alpha(T)/T$ and $M^*(T, B) \propto \chi_{AC}(T)$ where $\chi_{AC}(T)$ is ac magnetic susceptibility. If the corresponding measurements are carried out at fixed magnetic field B (or at fixed both the concentration x and B) then the effective mass reaches its maximum at some temperature T_M . Upon normalizing both the effective mass by its peak value at each field B and the temperature by T_M , we observe that all the curves merge into a single one, given by Eq. (106), thus demonstrating a scaling behavior.

It is seen from Fig. 32, that the behavior of the normalized ac susceptibility $\chi_{AC}^N(y) = \chi_{AC}(T/T_M, B)/\chi_{AC}(1, B) = M^*(T_N)$ obtained in measurements on the HF paramagnet CeRu_2Si_2 [92] agrees with both the approximation given by

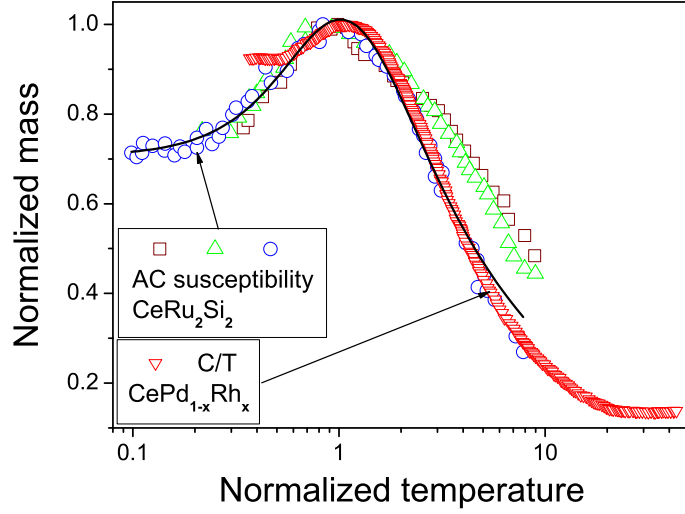


Figure 32: Normalized magnetic susceptibility $\chi_N(T_N, B) = \chi_{AC}(T/T_M, B)/\chi_{AC}(1, B) = M_N^*(T_N)$ for CeRu_2Si_2 in magnetic fields 0.20 mT (squares), 0.39 mT (upright triangles) and 0.94 mT (circles) versus normalized temperature $T_N = T/T_M$ [92]. The susceptibility reaches its maximum $\chi_{AC}(T_M, B)$ at $T = T_M$. The normalized specific heat $(C(T_N)/T_N)/C(1)$ of the HF ferromagnet $\text{CePd}_{1-x}\text{Rh}_x$ with $x = 0.8$ versus T_N is shown by downright triangles [174]. Here T_M is the temperature at the peak of $C(T)/T$. The solid curve traces the universal behavior of the normalized effective mass determined by Eq. (106). Parameters c_1 and c_2 are adjusted for $\chi_N(T_N, B)$ at $B = 0.94$ mT.

Eq. (106) and the normalized specific heat $(C(T_N)/T_N)/C(1) = M_N^*(T_N)$ obtained in measurements on $\text{CePd}_{1-x}\text{Rh}_x$ [174]. Also, from Fig. 32, we see that the curve given by Eq. (106) agrees perfectly with the measurements on CeRu_2Si_2 whose electronic system is placed at FCQPT [164].

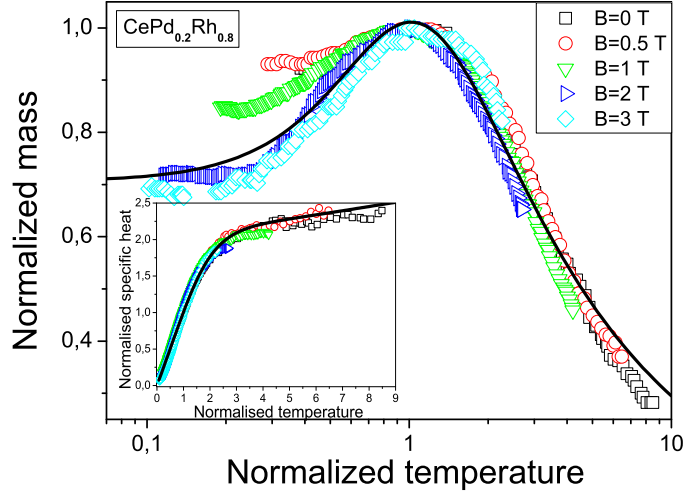


Figure 33: The normalized effective mass at elevated magnetic fields as a function of $y = T/T_M$. The mass taken from the specific heat C/T of the HF ferromagnet $\text{CePd}_{1-x}\text{Rh}_x$ with $x = 0.8$ (Ref. [174]) is shown at different magnetic fields B depicted at the right upper corner. At $B \geq 1$ T, $M_N^*(y)$ coincides with that of CeRu_2Si_2 (solid curve, see the caption to Fig. 32). The normalized specific heat $C(y)/C(T_M)$ of $\text{CePd}_{1-x}\text{Rh}_x$ at different magnetic fields B is shown in the inset. The kink in the specific heat is clearly seen at $y \approx 2$. The solid curve represents the function $yM_N^*(y)$ with parameters c_1 and c_2 adjusted for the magnetic susceptibility of CeRu_2Si_2 at $B = 0.94$ mT.

Now we consider the behavior of $M_N^*(T)$, extracted from measurements of the specific heat on $\text{CePd}_{1-x}\text{Rh}_x$ under the application of magnetic field [174] and shown in Fig. 33. It is seen from Fig. 33 that for $B \geq 1$ T M_N^* describes the normalized specific heat almost perfectly, coinciding with that of CeRu_2Si_2 and is in accord with the universal behavior of the normalized effective mass given by Eq. (106). Thus, we conclude that the thermodynamic properties of $\text{CePd}_{1-x}\text{Rh}_x$ with $x = 0.8$ are determined by quasiparticles rather than by the critical magnetic fluctuations. On the other hand, one could expect the growth of the critical fluctuations contribution as $x \rightarrow x_{FC}$ so that the behavior of the normalized effective mass would deviate from that given by Eq. (106). This is not the case as observed from Fig. 33. It is also seen that at increasing magnetic fields B all the curves corresponding to the normalized effective masses extracted from $\text{CePd}_{1-x}\text{Rh}_x$ with $x = 0.8$ merge into a single one, thus demonstrating a scaling behavior in accord with equation (106). We note that existing theories based on the quantum and thermal fluctuations predict that magnetic and thermal properties of the ferromagnet $\text{CePd}_{1-x}\text{Rh}_x$ differ from those of the paramagnet CeRu_2Si_2 , Refs. [3, 25, 174, 178, 179]. Clearly, from the inset of Fig. 33, there is the kink in the temperature dependence of the normalized specific heat $C(T_N)/C(T_M)$ of $\text{CePd}_{1-x}\text{Rh}_x$ appearing at $T_N \simeq 2$. In the inset, the solid line depicts the function $T_N M_N^*(T_N)$ with parameters c_1 and c_2 which are adjusted for the magnetic susceptibility at $B = 0.94$ mT. Since the function $T_N M_N^*(T_N)$ describes the normalized specific heat very well and its bend (or kink) comes from the crossover from the LFL regime to the NFL one, we safely conclude that the kink emerges at temperatures when the system transits from the LFL behavior to the NFL one. As shown in Subsection 9.7, the magnetoresistance changes from positive values to negative ones at the same temperatures. One may speculate that there is an energy scale which could make the kink coming from fluctuations of the order parameter [17]. In that case we must to concede that such different HF metals as $\text{CePd}_{1-x}\text{Rh}_x$, CeRu_2Si_2 and CeCoIn_5 with different magnetic ground states have the same fluctuations which exert coherent influence on the heat capacity, susceptibility and transport properties. Indeed, as we have seen above and will also see below in this Subsection, that Eq. (106) allows us to describe quantitatively all the mentioned quantities.

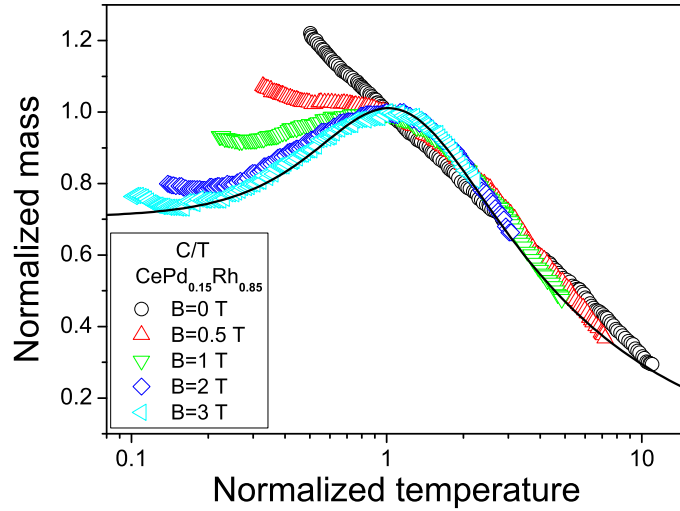


Figure 34: Same as in Fig. 33 but $x = 0.85$ [174]. At $B \geq 1$ T, $M_N^*(T_N)$ demonstrates the universal behavior (solid curve, see the caption to Fig. 32).

In Fig. 34, the effective mass $M_N^*(T_N)$ at fixed B 's is shown. Since the curve shown by circles and extracted from measurements at $B = 0$ does not exhibit any maximum down to 0.08 K [174], we conclude that in this case x is very close to x_{FC} and the maximum is shifted to very low temperatures. As seen from Fig. 34, the application of magnetic field restores the scaling behavior given by Eq. (106). Again, this permits us to conclude that the thermodynamic properties of $\text{CePd}_{1-x}\text{Rh}_x$ with $x = 0.85$ are determined by quasiparticles rather than by the critical magnetic fluctuations.

The thermal expansion coefficient $\alpha(T)$ is given by $\alpha(T) \simeq M^*T/(p_F^2 K)$ [156]. The compressibility $K(\rho)$ is not expected to be singular at FCQPT and is approximately constant [180]. Taking into account Eq. (101), we find that $\alpha(T) \propto \sqrt{T}$ and the specific heat $C(T) = TM^* \propto \sqrt{T}$. Measurements of the specific heat $C(T)$ on $\text{CePd}_{1-x}\text{Rh}_x$ with $x = 0.9$ show a power-law temperature dependence. It is described by the expression $C(T)/T = AT^{-q}$ with $q \simeq 0.5$ and

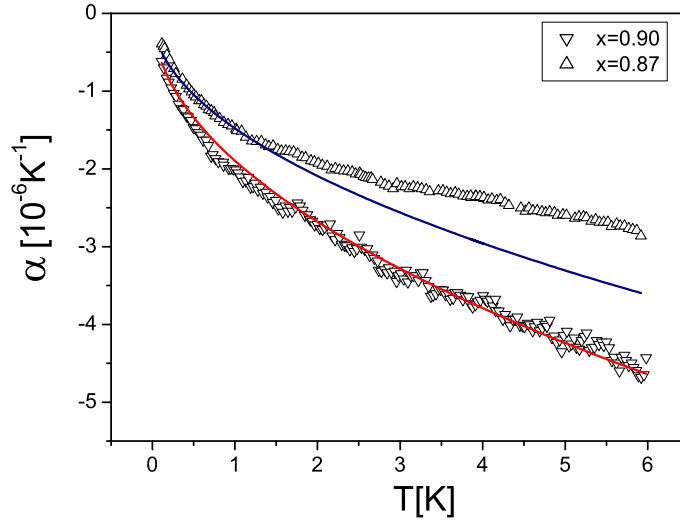


Figure 35: Thermal expansion coefficient $\alpha(T)$ as a function of temperature in the interval $0.1 \leq T \leq 6$ K. The experimental values for doping levels $x = 0.90, 0.87$ are taken from Ref. [173]. The solid lines represent approximations of the experimental values of $\alpha(T) = c_1 \sqrt{T}$, where c_1 is a fitting parameter.

$A = \text{const}$ [173].

Figure 35 shows that at the critical point $x = 0.90$ at which the critical temperature of the ferromagnetic phase transition vanishes, the thermal expansion coefficient is well approximated by the dependence $\alpha(T) \propto \sqrt{T}$ as the temperature varies by almost two orders of magnitude. However, even a small deviation of the system from the critical point destroys the correspondence between this approximation and the experimental data. We note that it is possible to describe the critical behavior of two entirely different heavy-fermion metals (one is a paramagnet and the other a ferromagnet) by the function $\alpha(T) = c_1 \sqrt{T}$ with only one fitting parameter c_1 . This fact vividly shows that fluctuations do not determine the behavior of $\alpha(T)$. Heat-capacity measurements for $\text{CePd}_{1-x}\text{Rh}_x$ with $x = 0.90$ have shown that $C(T) \propto \sqrt{T}$ [173]. Thus, the electron systems of both metals can be interpreted as being highly correlated electron liquids. Hence, we conclude that the behavior of the effective mass given by Eq. (101) agrees with experimental facts.

Measurements of $\alpha(T)/T$ on both $\text{CePd}_{1-x}\text{Rh}_x$ with $x = 0.9$ [173] and CeNi_2Ge_2 [14] are shown in Fig. 36. It is seen that the approximation $\alpha(T) = c_3 \sqrt{T}$ is in good agreement with the results of measurements of $\alpha(T)$ in $\text{CePd}_{1-x}\text{Rh}_x$ and CeNi_2Ge_2 over two decades in T_N . It is noted that measurements on $\text{CeIn}_{3-x}\text{Sn}_x$ with $x = 0.65$ [175] demonstrate the same behavior $\alpha(T) \propto \sqrt{T}$ (not shown in Fig. 36). As a result, we suggest that $\text{CeIn}_{3-x}\text{Sn}_x$ with $x = 0.65$, $\text{CePd}_{1-x}\text{Rh}_x$ with $x \approx 0.9$, and CeNi_2Ge_2 are located at FCQPT; recall that $\text{CePd}_{1-x}\text{Rh}_x$ is a three dimensional FM [173, 174], CeNi_2Ge_2 exhibits a paramagnetic ground state [14] and $\text{CeIn}_{3-x}\text{Sn}_x$ is AFM cubic metal [175].

The normalized effective mass $M_N^*(T_N)$ extracted from measurements on the HF metals $\text{YbRh}_2(\text{Si}_{0.95}\text{Ge}_{0.05})_2$, CeRu_2Si_2 , $\text{CePd}_{1-x}\text{Rh}_x$ and CeNi_2Ge_2 is reported in Fig. 37. Clearly, the scaling behavior of the effective mass given by Eq. (106) is in accord with the experimental facts and $M_N^*(T_N)$, shown by inverted triangles and collected on the AFM phase of $\text{YbRh}_2(\text{Si}_{0.95}\text{Ge}_{0.05})_2$ [170], coincides with that collected on the PM phase (shown by upright triangles) of $\text{YbRh}_2(\text{Si}_{0.95}\text{Ge}_{0.05})_2$ [170]. We note that in the case of LFL theory the corresponding normalized effective mass $M_{NL}^* \approx 1$ is independent of both T and B as shown in Fig. 2.

The peak temperatures T_{max} , where the maxima of $C(T)/T$, $\chi_{AC}(T)$ and $\alpha(T)/T$ occur, shift to higher values with increase of the applied magnetic field. In Fig. 38, $T_{\text{max}}(B)$ are shown for C/T and χ_{AC} , measured on $\text{YbRh}_2(\text{Si}_{0.95}\text{Ge}_{0.05})_2$. It is seen that both functions can be represented by straight lines intersecting at $B \approx 0.03$ T. This observation [161, 170] as well as the measurements on $\text{CePd}_{1-x}\text{Rh}_x$, CeNi_2Ge_2 and CeRu_2Si_2 demonstrate similar behavior [14, 92, 174] which is well described by Eq. (108).

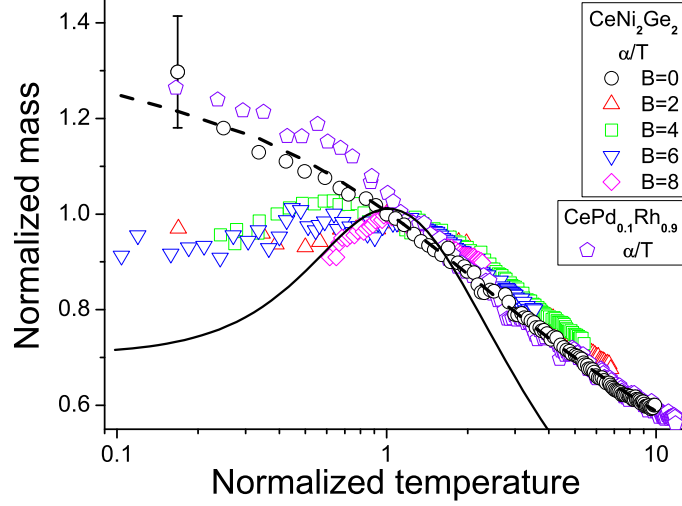


Figure 36: The normalized thermal expansion coefficient $(\alpha(T_N)/T_N)/\alpha(1) = M_N^*(T_N)$ for CeNi_2Ge_2 [14] and for $\text{CePd}_{1-x}\text{Rh}_x$ with $x = 0.90$ [174] versus $T_N = T/T_M$. Data obtained in measurements on $\text{CePd}_{1-x}\text{Rh}_x$ at $B = 0$ are multiplied by some factor to adjust them at one point to the data for CeNi_2Ge_2 . Dashed line is a fit to the data shown by the circles and pentagons at $B = 0$; it is represented by the function $\alpha(T) = c_3 \sqrt{T}$ with c_3 being a fitting parameter. The solid curve traces the universal behavior of the normalized effective mass determined by Eq. (106), see the caption to Fig. 32.

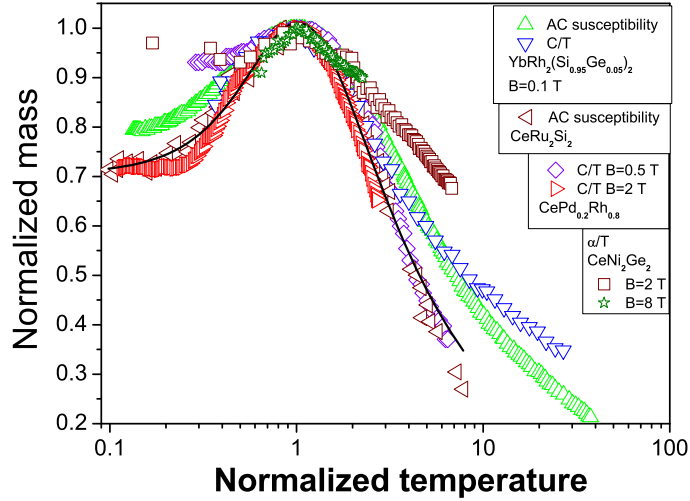


Figure 37: The universal behavior of $M_N^*(T_N)$, extracted from $\chi_{AC}(T, B)/\chi_{AC}(T_M, B)$ for both $\text{YbRh}_2(\text{Si}_{0.95}\text{Ge}_{0.05})_2$ and CeRu_2Si_2 [92, 170], $(C(T)/T)/(C(T_M)/T_M)$ for both $\text{YbRh}_2(\text{Si}_{0.95}\text{Ge}_{0.05})_2$ and $\text{CePd}_{1-x}\text{Rh}_x$ with $x = 0.80$ [174, 170], and $(\alpha(T)/T)/(\alpha(T_M)/T_M)$ for CeNi_2Ge_2 [14]. All the measurements were performed under the application of magnetic field as shown in the insets. The solid curve gives the universal behavior of M_N^* determined by Eq.(106), see the caption to Fig. 32.

We conclude, that subjecting the different experimental data (like $C(T)/T$, $\chi_{AC}(T)$, $\alpha(T)/T$ etc) collected in measurements on different HF metals ($\text{YbRh}_2(\text{Si}_{0.95}\text{Ge}_{0.05})_2$, CeRu_2Si_2 , $\text{CePd}_{1-x}\text{Rh}_x$, $\text{CeIn}_{3-x}\text{Sn}_x$ and CeNi_2Ge_2) to the above normalized form immediately reveals their universal scaling behavior [177]. This is because all the above experimental quantities are indeed proportional to the normalized effective mass exhibiting the scaling behavior. Since the effective mass determines the thermodynamic properties, we further conclude that the above HF metals demonstrate the same scaling behavior, independent of the details of HF metals such as their lattice structure, magnetic ground states, dimensionality etc [164, 177].

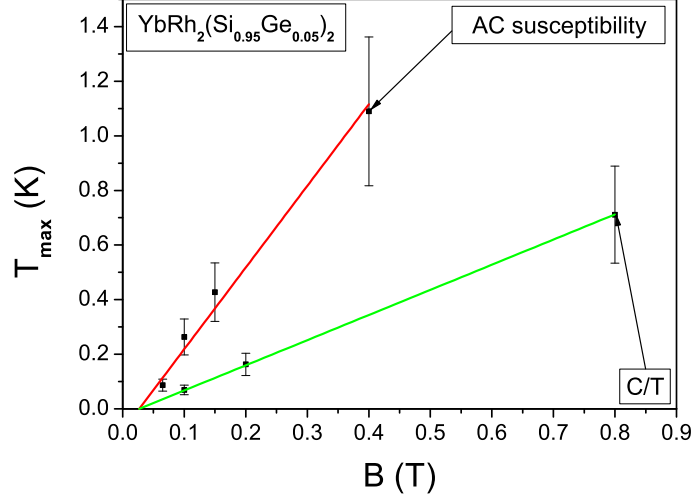


Figure 38: The peak temperatures $T_{\max}(B)$, extracted from measurements of χ_{AC} and C/T on $\text{YbRh}_2(\text{Si}_{0.95}\text{Ge}_{0.05})_2$ [161, 170] and approximated by straight lines given by Eq. (108). The lines intersect at $B \approx 0.03$ T.

10. Metals with a strongly correlated electron liquid

For $T \ll T_f$, the function $n_0(\mathbf{p})$ given by Eq. (21) determines the entropy $S_{NFL}(T)$ given by Eq. (4) of the HF liquid located above the quantum critical line shown in Fig. 6. From Eqs. (4) and (27), the entropy contains a temperature-independent contribution,

$$S_0 \sim \frac{p_f - p_i}{p_F} \sim |r|, \quad (130)$$

where $r = (x - x_{FC})/x_{FC}$. Another specific contribution is related to the spectrum $\varepsilon(\mathbf{p})$, which ensures a link between the dispersionless region ($p_f - p_i$) occupied by FC and the normal quasiparticles in the regions $p < p_i$ and $p > p_f$. This spectrum has the form $\varepsilon(\mathbf{p}) \propto (p - p_f)^2 \sim (p_i - p)^2$. Such a shape of the spectrum, corroborated by exactly solvable models for systems with FC, leads to a contribution to the heat capacity $C \sim \sqrt{T/T_f}$ [41]. Therefore, for $0 < T \ll T_f$, the entropy can be approximated by the function [181]

$$S_{NFL}(T) \simeq S_0 + a \sqrt{\frac{T}{T_f}} + b \frac{T}{T_f}, \quad (131)$$

where a and b are constants. The third term on the right-hand side of Eq. (131), which emerges because of the contribution of the temperature-independent part of the spectrum $\varepsilon(\mathbf{p})$, yields a relatively small addition to the entropy. As we will see shortly, the temperature-independent term S_0 determines the universal transport and thermodynamic properties of the heavy-electron liquid with FC, which we call a strongly correlated Fermi liquid. The properties of this liquid differ dramatically from those of highly correlated Fermi liquid that at $T \rightarrow 0$ becomes LFL liquid. As a result, we can think of QCP of FCQPT as the phase transition that separates highly correlated and strongly correlated Fermi liquids. Because the highly correlated liquid behaves like LFL as $T \rightarrow 0$, QCP separates LFL from a strongly correlated Fermi liquid. On the other hand, as was shown in Subsection 4.4, at elevated temperatures the properties of both liquids become indistinguishable. Thus, as shall be seen below, both systems can be discriminated at diminishing temperatures when the impact of both QCP and the quantum critical line on the properties become more vivid.

Figure 39 shows the temperature dependence of $S(T)$ calculated on the basis of the model functional (102). The calculations were done with $g = 7, 8, 12$ and $\beta = b_c = 3$. We recall that the critical value of g is $g_c = 6.7167$. We see in Fig. 39 that in accord with Eq. (130) S_0 increases as the system moves away from QCP along the quantum critical line, see Fig. 6. Obviously, the term S_0 on the right-hand side of Eq. (131), which is temperature-independent, contributes nothing to the heat capacity; the second term in (131) makes a contribution so that the heat capacity behaves as $C(T) \propto \sqrt{T}$.

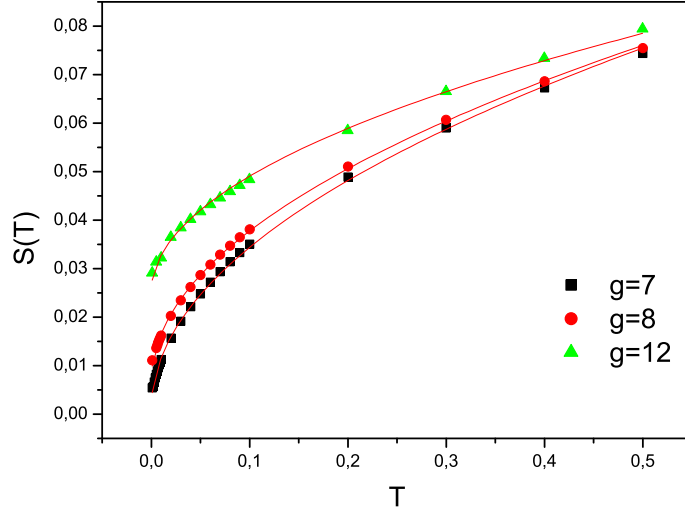


Figure 39: Entropy $S(T)$ as a function of temperature. The lines represent the approximation for $S(T)$ based on Eq. (131), the symbols mark the results of calculations based on (102).

10.1. Entropy, linear expansion, and Grüneisen's law

The unusual temperature dependence of the entropy of a strongly correlated electron liquid specified by Eq. (131) determines the unusual behavior of the liquid. The existence of a temperature-independent term S_0 can be illustrated by calculating the thermal expansion coefficient $\alpha(T)$ [181, 182], which is given by [20]

$$\alpha(T) = \frac{1}{3} \left(\frac{\partial(\log V)}{\partial T} \right)_P = -\frac{1}{3V} \left(\frac{\partial(S/x)}{\partial P} \right)_T, \quad (132)$$

where P is the pressure and V is the volume. We note that the compressibility $K = d\mu/d(Vx)$ does not develop a singularity at FCQPT and is approximately constant in systems with FC [180]. Substituting (131) in Eq. (132), we find that [181, 182]

$$\frac{\alpha_{FC}(T)}{T} \simeq \frac{a_0}{T} \sim \frac{M_{FC}^*}{p_F^2 K}, \quad (133)$$

where $a_0 \sim \partial S_0/\partial P$ is temperature-independent. In (133), we took only the leading contribution related to S_0 into account. We recall that

$$C(T) = T \frac{\partial S(T)}{\partial T} \simeq \frac{a}{2} \sqrt{\frac{T}{T_f}}, \quad (134)$$

and obtain from Eqs. (133) and (134) that the Grüneisen ratio $\Gamma(T)$ diverges as

$$\Gamma(T) = \frac{\alpha(T)}{C(T)} \simeq 2 \frac{a_0}{a} \sqrt{\frac{T_f}{T}}, \quad (135)$$

from which we conclude that Grüneisen's law does not hold in strongly correlated Fermi systems.

Measurements that have been conducted with $\text{YbRh}_2(\text{Si}_{0.95}\text{Ge}_{0.05})_2$ show that $\alpha/T \propto 1/T$ and that the Grüneisen ratio diverges as $\Gamma(T) \simeq T^{-q}$, $q \simeq 0.33$, which allows classifying the electron system of this compound as strongly correlated liquid [14]. Our estimate $q = 0.5$, which follows from Eq. (135), is in satisfactory agreement with this experimental value. The behavior of $\alpha(T)/T$ given by Eq. (133) contradicts the LFL theory, according to which the thermal expansion

coefficient $\alpha(T)/T = M^* = \text{const}$ as $T \rightarrow 0$. The $1/T$ -dependence of the ratio α/T predicted in Ref. [182] is in good agreement with facts collected on $\text{YbRh}_2(\text{Si}_{0.95}\text{Ge}_{0.05})_2$ [14].

Equation (31) implies that $M^*(T \rightarrow 0) \rightarrow \infty$ and that the strongly correlated electron system behaves as if it were placed at the quantum critical point. Actually, as we have seen in Subsection 4.4 the system is at the quantum critical line $x/x_{FC} \leq 1$, and critical behavior is observed for all $x \leq x_{FC}$ as $T \rightarrow 0$. It was shown in Section 5 that as $T \rightarrow 0$, the strongly correlated electron liquid undergoes the first-order quantum phase transition, because the entropy becomes a discontinuous function of the temperature: at finite temperatures, the entropy is given by Eq. (131), while $S(T = 0) = 0$. Hence, the entropy has a discontinuity $\delta S = S_0$ as $T \rightarrow 0$. This implies that, as a result of the first-order phase transition, all critical fluctuations are suppressed along the quantum critical curve and the respective divergences, e.g., the divergence of $\Gamma(T)$, are determined by quasiparticles and not critical fluctuations, as could be expected in the case of an ordinary quantum phase transition [4]. We note that according to the well-known inequality [156] $q \leq T\delta S$, in our case the heat q of the first order transition tends to zero as its critical temperature $T_{NL} \rightarrow 0$.

10.2. The $T - B$ phase diagram of YbRh_2Si_2 , Hall coefficient and magnetization

To study the $T - B$ phase diagram of strongly correlated electron liquid, we examine the case where NFL behavior emerges when the AF phase is suppressed by an external magnetic field B , as it is in the HF metals $\text{YbRh}_2(\text{Si}_{0.95}\text{Ge}_{0.05})_2$ and YbRh_2Si_2 [14, 15].

The antiferromagnetic phase is LFL with the entropy vanishing as $T \rightarrow 0$. For magnetic fields higher than the critical value B_{c0} at which the Néel temperature $T_{NL}(B \rightarrow B_{c0}) \rightarrow 0$, the antiferromagnetic phase transforms into a weakly polarized paramagnetic strongly correlated electron liquid [14, 15]. As shown in Section 7, a magnetic field applied to the system with $T = 0$ splits the FC state occupying the interval $(p_f - p_i)$ into Landau levels and suppresses the superconducting order parameter $\kappa(\mathbf{p})$. The new state is specified by a multiply connected Fermi sphere, on which a smooth quasiparticle distribution function $n_0(\mathbf{p})$ in the interval $(p_f - p_i)$ is replaced with a distribution $\nu(\mathbf{p})$ as seen from Fig. 9. Hence, the behavior of LFL is restored and characterized by quasiparticles with the effective mass $M^*(B)$ given by Eq. (73). When the temperature increases so high that $T > T^*(B)$ with $T^*(B)$ given by Eq. (76), the entropy of the electron liquid is determined by Eq. (131). The described behavior of the system is shown in the $T - B$ diagram in Fig. 40.

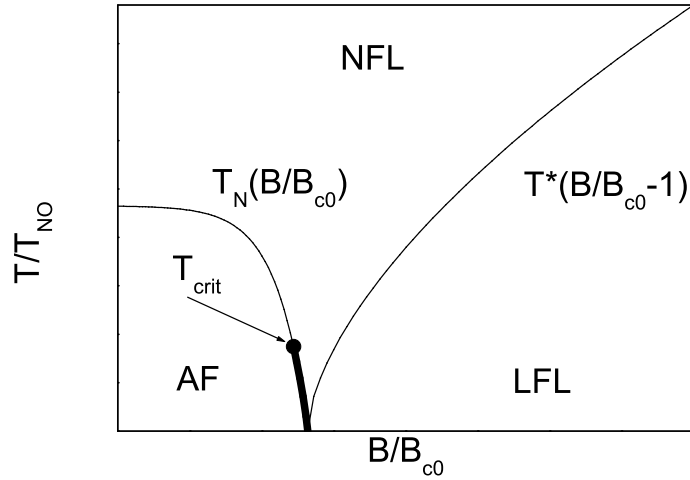


Figure 40: The $T - B$ phase diagram of a strongly correlated electron liquid. The line $T_N(B/B_{c0})$ represents the dependence of the Néel temperature on the field strength B . The black dot at $T = T_{crit}$ marks the critical temperature at which the second-order AF phase transition becomes a first-order one. For $T < T_{crit}$, the heavy solid line represents the function $T_N(B/B_{c0})$, when the AF phase transition becomes a first-order one. The strongly correlated liquid in the NFL region is characterized by the entropy S_{NFL} given by Eq. (131). The line separating the strongly correlated liquid (NFL) from the weakly polarized electron liquid, which behaves like the Landau Fermi liquid, is described by the function $T^*(B/B_{c0} - 1) \propto \sqrt{B/B_{c0} - 1}$ [see Eq. (76)].

In accordance with the experimental data, we assume that at relatively high temperatures, such that $T/T_{N0} \sim 1$, where T_{N0} is the Néel temperature in a zero magnetic field, the antiferromagnetic phase transition is a second-order one [15]. In this case, the entropy and other thermodynamic functions at the transition temperature T_{NL} are continuous. This means that the entropy S_{AF} of the antiferromagnetic phase coincides with the entropy S_{NFL} of the strongly correlated liquid given by Eq. (131):

$$S_{AF}(T \rightarrow T_{NL}(B)) = S_{NFL}(T \rightarrow T_{NL}(B)). \quad (136)$$

Since the antiferromagnetic phase behaves like LFL, with its entropy $S_{AF}(T \rightarrow 0) \rightarrow 0$, Eq. (136) cannot be satisfied at sufficiently low temperatures $T \leq T_{crit}$ because of the temperature-independent term S_0 . Hence, the second order antiferromagnetic phase transition becomes the first order one at $T = T_{crit}$ [183, 184] as shown by the arrow in Fig. 40. A detailed consideration of this item is given in Section 14.

At $T = 0$, the critical magnetic field B_{c0} in which the antiferromagnetic phase becomes LFL is determined by the condition that the ground-state energy of the antiferromagnetic phase be equal to the ground-state energy $E[n_0(\mathbf{p})]$ of the HF liquid with FC, since, as it was shown in Subsection 10.1, the heat of the transition $q = 0$. This means that the ground state of the antiferromagnetic phase is degenerate at $B = B_{c0}$. Hence, at $B \rightarrow B_{c0}$ the Néel temperature T_{NL} tends to zero and the behavior of the effective mass $M^*(B \geq B_{c0})$ is determined by Eq. (73), so that $M^*(B)$ diverges as $B \rightarrow B_{c0}$ from top. As a result, at $T = 0$, the phase transition separating the antiferromagnetic phase existing at $B \leq B_{c0}$ from LFL taking place at $B \geq B_{c0}$ is the first order quantum phase transition. The driving parameter of this phase transition is the magnetic field strength B . We note that the respective quantum and thermal critical fluctuations disappear at $T < T_{crit}$ because the first-order antiferromagnetic phase transition occurs at such temperatures.

We now examine the jump in the Hall coefficient detected in measurements involving YbRh_2Si_2 [185]. The Hall coefficient $R_H(B)$ as a function of B experiences a jump at $T \rightarrow 0$ when the applied magnetic field reaches its critical value $B = B_{c0}$, and then becomes even higher than the critical value at $B = B_{c0} + \delta B$, where δB is an infinitely small magnetic field strength [185]. As shown in Section 7, when $T = 0$, the application of the critical magnetic field B_{c0} , which suppresses the antiferromagnetic phase with the Fermi momentum p_F restores LFL with the Fermi momentum $p_f > p_F$. When $B < B_{c0}$, the ground-state energy of the antiferromagnetic phase is lower than that of the LFL state induced by the application of magnetic field, but for $B > B_{c0}$ we are confronted with the opposite case, where the LFL state has the lower energy. At $B = B_{c0}$ and $T = 0$, both phases have the same ground state energy and $T_{NL} = 0$, because the phases are degenerate, being separated by the first order phase transition as shown in Fig. 40.

Thus, at $T = 0$ and $B = B_{c0}$, an infinitely small increase δB in the magnetic field leads to a finite discontinuity in the Fermi momentum. This is because the distribution function becomes multiply connected (see Fig. 9) and the number of mobile electrons does not change. Thus, the antiferromagnetic ground state can be viewed as having a "small" Fermi surface characterized by the Fermi momentum p_F , correspondingly the paramagnetic ground state at $B > B_{c0}$ has a "large" Fermi surface with $p_f > p_F$. As a result, the Hall coefficient experiences a sharp jump because $R_H(B) \propto 1/p_F^3$ in the antiferromagnetic phase and $R_H(B) \propto 1/p_f^3$ in the paramagnetic phase. Assuming that $R_H(B)$ is a measure of the Fermi momentum [185] (as is the case with a simply connected Fermi volume), we obtain

$$\frac{R_H(B = B_{c0} - \delta)}{R_H(B = B_{c0} + \delta)} \simeq 1 + 3 \frac{p_f - p_F}{p_F} \simeq 1 + d \frac{S_0}{x_{FC}}, \quad (137)$$

where S_0/x_{FC} is the entropy per heavy electron and d is a constant $d \sim 5$. It follows from Eq. (137) that the discontinuity in the Hall coefficient is determined by the anomalous behavior of the entropy, which can be attributed to S_0 . Hence, the discontinuity tends to zero as $r \rightarrow 0$ and disappears when the system is on the disordered side of FCQPT, where the entropy has no temperature-independent term [183].

We now turn to the magnetization which is determined by Eq. (110). For $T \ll T^*(B)$, the effective mass is given by Eq. (73) and the static magnetization is

$$M(B) \simeq a_M \sqrt{B - B_{c0}}. \quad (138)$$

Figure 41 shows that the function $M(B)$ determined by Eq. (138) is in good agreement with the data obtained in measurements on $\text{YbRh}_2(\text{Si}_{0.95}\text{Ge}_{0.05})_2$ [7]. We note that $B_{c0} \simeq 0$ in this case.

We examine the experimental $T - B$ diagram of the heavy-fermion metal YbRh_2Si_2 [7, 15] shown in Fig. 42. In the LFL state, the behavior of the metal is characterized by the effective mass $M^*(B)$, which diverges as $1/\sqrt{B - B_{c0}}$ [15]. It is quite evident that Eq. (73) provides a good description of this experimental fact: $M^*(B)$ diverges as $B \rightarrow B_{c0}$ at $T_N(B = B_{c0}) = 0$ and, as Fig. 41 shows, the calculated behavior of the magnetization agrees with the experimental data.

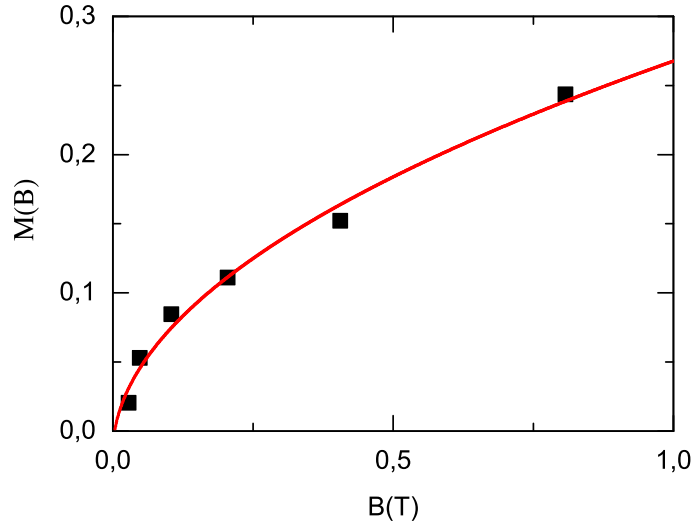


Figure 41: The values of magnetization $M(B)$ obtained in measurements involving $\text{YbRh}_2(\text{Si}_{0.95}\text{Ge}_{0.05})_2$ (black squares) [7]. The curve represents the field-dependent function $M(B) = a_M \sqrt{B}$ given by Eq. (138), where a_M is a fitting parameter.

The magnetic-field dependence of the coefficient $A(B)$ shown in the left panel of Fig. 11 is also in good agreement with experimental facts collected on YbRh_2Si_2 [15]. Figure 42 shows that in accordance with (76), the curve separating the LFL region from the NFL region can be approximated by the function $c \sqrt{B - B_{c0}}$ with a fitting parameter c . Bearing in mind that the behavior of YbRh_2Si_2 is like that of $\text{YbRh}_2(\text{Si}_{0.95}\text{Ge}_{0.05})_2$ [7, 14, 170, 186], we also conclude that the thermal expansion coefficient $\alpha(T)$ is temperature-independent and that the Grüneisen ratio diverges as a function of T in the NFL state [14]. We conclude that the entropy in the NFL state is determined by Eq. (131). Since the antiferromagnetic phase transition is the second order at relatively high temperatures [15], we can predict that as the temperature decreases, the phase transition becomes the first order. The above description of the behavior of the Hall coefficient $R_H(B)$ also agrees with the experimental facts [185].

Thus, we conclude that the $T - B$ phase diagram of the strongly correlated electron liquid shown in Fig. 40 agrees with the experimental $T - B$ diagram obtained from experiments involving the heavy-fermion metals YbRh_2Si_2 and $\text{YbRh}_2(\text{Si}_{0.95}\text{Ge}_{0.05})_2$ and shown in Fig. 42.

10.3. Heavy-fermion metals in the immediate vicinity of QCP

We now consider the case where $\delta p_{FC} = (p_f - p_i)/p_F \ll 1$ and the electron system of HF metal is in a state close to QCP while remaining on the ordered side that is at the quantum critical line, see Fig. 6. It follows from Eq. (78) that when the system is placed in a magnetic field $(B - B_{c0})/B_{c0} \geq B_{cr}$, the system passes from the ordered side of FCQPT to the disordered side, or the strongly correlated liquid transforms into the highly correlated one. As a result, when $T \leq T^*(B)$, the effective mass $M^*(B)$ is determined by Eqs. (93) and (99); thus both the Kadowaki-Woods relation and the Wiedemann-Franz law remain valid, and there are quasiparticles in the system. The resistivity then behaves as described in Subsection 9.5.

In magnetic field with $B \simeq B_{c0}$ and at temperatures $T_f \gg T > T^*(B)$, the system behaves like the strongly correlated Fermi liquid, the effective mass $M^*(T)$ is given by Eq. (31), and the entropy is determined by Eq. (131). The thermal expansion coefficient $\alpha(T)$ is temperature-independent [as follows from Eq. (133)], and the Grüneisen ratio diverges, as follows from Eq. (135). It follows from Eq. (31) that the width $\gamma(T) \propto T$ (see also Section 5.5). Hence, at $T_f \gg T \gg T^*(B)$, the temperature-dependent part of the resistivity behaves as $\Delta\rho(T) \propto \gamma(T) \propto T$ in either case, when the electron system is in the highly correlated state or in the strongly correlated state.

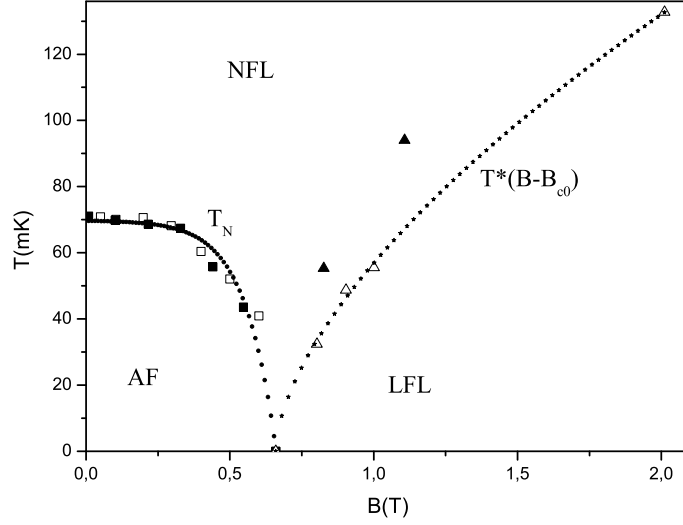


Figure 42: $T - B$ phase diagram for YbRh_2Si_2 ; the symbols denote the experimental data [7, 15]. The line T_N depicts the field dependence of the Néel temperature $T_{NL}(B)$. In the NFL region, the behavior of the strongly correlated liquid is characterized by the entropy S_{NFL} determined by Eq. (131). The line separating the NFL region from the LFL region is approximated by the function $T^*(B - B_{c0}) = c \sqrt{B - B_{c0}}$ given by Eq. (76) where c is a fitting parameter.

We assume that the system becomes superconducting at a certain temperature T_c . In contrast to the jump $\delta C(T_c)$ of the heat capacity at T_c in ordinary superconductors, which is a linear function of T_c , the value of $\delta C(T_c)$ is independent of T_c in our case. Equations (62) and (63) show that both $\delta C(T_c)$ and the ratio $\delta C(T_c)/C_n(T_c)$ can be very large compared to the corresponding quantities in the ordinary BCS case as it was observed in the HF metal CeCoIn_5 [79, 101, 187]. Experiments show that the electron system in CeCoIn_5 can be considered as a strongly correlated electron liquid. Indeed, for $T > T^*(B)$, the linear thermal expansion coefficient $\alpha(T) \propto \text{const}$ and the Grüneisen ratio diverges [189] [see Eqs. (133) and (135)], so we may assume that the entropy is given by (131).

A finite magnetic field takes the system to the disordered side of FCQPT; for $T < T^*(B)$, the system behaves like the highly correlated liquid with the effective mass given by Eq. (93). Estimates of δp_{FC} based on calculations of the magnetic susceptibility show that $\delta p_{FC} \simeq 0.044$ [79]. We conclude that $B_{cr} \sim 0.01$, as follows from Eq. (78), and the electron system of the heavy-fermion metal CeCoIn_5 passes, in relatively weak magnetic fields, to the disordered side of FCQPT and acquires the behavior characteristic of highly correlated liquid. We note that the estimated value of δp_{FC} provides an explanation for the relatively large jump $\delta C(T_c)$ [79] observed at $T_c = 2.3$ K in experiments with CeCoIn_5 [187].

As Fig. 43 shows, the behavior $A(B) \propto B_H(B) \propto M^*(B) \propto (B - B_{c0})^{-4/3}$ specified by Eq. (113) is in good agreement with the experimental results [30, 31]. The coefficient $B_H(B)$ determines the T^2 -dependence of the thermal resistance, and the ratio $A(B)/B_H(B)$ is field-independent, with $A/B_H \simeq 0.70$ [31, 30]. In the LFL state, the Kadowaki-Woods relation and the Wiedemann-Franz law hold, and the behavior of the system is determined by quasiparticles [30, 31, 188]. Thus, we conclude that our description is in good agreement with the experimental facts.

At low temperatures and in magnetic fields $B_{red} \sim B_{cr}$ [see Eq. (78)], the electron system is in its LFL state. As the temperature increases, the behavior of the strongly correlated liquid determined by the entropy S_0 is restored at $T^*(B)$, and the effective mass becomes temperature-dependent, according to Eq. (31). To calculate $T^*(B)$, we use the fact that the behavior of the effective mass is given by Eq. (93) for $T < T^*(B)$ and by Eq. (31) for $T > T^*(B)$. Since the effective mass cannot change at $T = T^*(B)$, we can estimate $T^*(B)$ by equating these two values of the effective mass. As a result, we obtain

$$T^*(B) \propto (B - B_{c0})^{2/3}. \quad (139)$$

The function $T^*(B)$ (139) is shown by the dotted line in Fig. 43. As the magnetic field becomes stronger, $B \gg B_{cr}$, the system becomes the highly correlated liquid in which the behavior of $M^*(T)$ is given by Eq. (99) and that of $M^*(B)$ by Eq. (93). Comparison of these two types of behavior yields Eq. (100). The function $T^*(B)$ given by Eq. (100) is depicted by the light solid line in Fig. 43. Clearly, both lines match the experimental results.

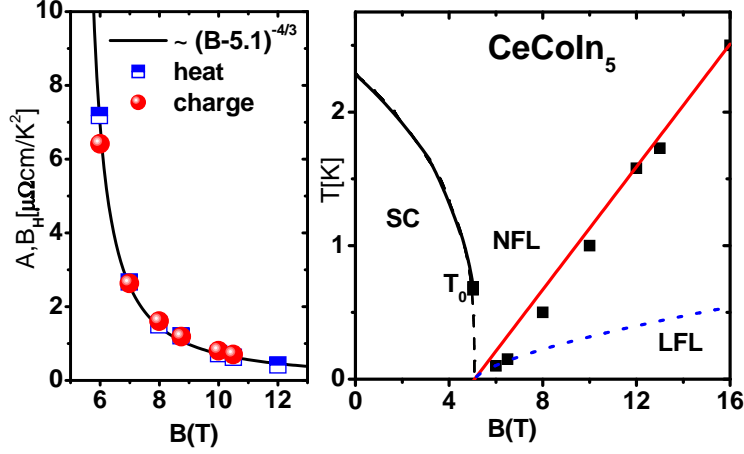


Figure 43: $T - B$ phase diagram for CeCoIn_5 . In the left panel, shown are $A(B)$ and $B_H(B)$ that determine the T^2 -dependence of the resistance and heat transfer in the LFL state induced by the magnetic field; the symbols mark the experimental data. The right panel depicts the curves of phase transitions in a magnetic field; the line separates the normal (NFL) state from the superconducting (SC) state [188]; the solid curve corresponds to the second-order phase transitions, the dashed curve corresponds to the first-order phase transitions, the black square (at T_0) is the point where second-order transitions become first-order transitions. The dotted line represents the function $T^*(B)$ calculated in accordance with (139) for the transition region between the LFL and NFL states. The light solid line represents the function $T^*(B)$ calculated according to Eq. (100) for the transition region (when $B > B_{cr}$) between the highly correlated and strongly correlated liquids; the black squares mark the experimental results obtained from resistivity measurements [30, 31].

Using Eq. (136) to study the superconducting phase transition, we can explain the main universal properties of the $T - B$ phase diagram of the HF metal CeCoIn_5 shown in Fig. 43. The latter substance is a d -wave superconductor with $T_c = 2.3$ K, while field tuned QCP with a critical field of $B_{c0} = 5.1$ T coincides with B_{c2} , the upper critical field where superconductivity vanishes [30, 31, 188]. Under the application of magnetic fields B_{c0} , CeCoIn_5 demonstrates the NFL behavior [189]. It also follows from the above consideration given in Subsection 9.9 that $B_{c2} \geq B_{c0}$. Therefore, the approximate equality $B_{c2} \approx B_{c0}$ observed in CeCoIn_5 is an accidental coincidence that has to disappear under the application of external factors. Indeed, B_{c2} is determined by λ_0 which in turn is given by the coupling of electrons with magnetic, phonon, etc excitations rather than by B_{c0} . As a result, under the application of pressure influencing differently the coupling constant λ_0 and B_{c0} , the above coincidence is lifted in complete agreement with experimental facts, so that $B_{c2} > B_{c0}$ [33] as has been shown in Subsection 9.9. At relatively high temperatures, the superconducting-normal phase transition in CeCoIn_5 shown by the solid line in the right panel of Fig. 43 is of the second order [171, 190] so that S and the other thermodynamic quantities are continuous at the transition temperature $T_c(B)$. Since $B_{c2} \approx B_{c0}$, upon the application of magnetic field, the HF metal transits to its NFL state down to lowest temperatures as it is seen from Fig. 43. As long as the phase transition is of the second order, the entropy of the superconducting phase $S_{SC}(T)$ coincides with the entropy $S_{NFL}(T)$ of the NFL state and Eq. (136) becomes

$$S_{SC}(T \rightarrow T_c(B)) = S_{NFL}(T \rightarrow T_c(B)). \quad (140)$$

Since $S_{SC}(T \rightarrow 0) \rightarrow 0$, Eq. (140) cannot be satisfied at sufficiently low temperatures due to the presence of the temperature independent term S_0 . Thus, in accordance with experimental results [171, 190], the second order phase transition converts to the first order one below some temperature $T_0(B)$ [97]. To estimate $T_0(B)$, we use the scaling idea

of Volovik (see Ref. [191] for details), who derived the interpolation formula for the entropy of a d -wave superconductor in a magnetic field B , while S_{NFL} has been estimated in [79]. As a result, we obtain $T_0(B)/T_c \simeq 0.3$. This point coincides well with the experimental value, shown on the Fig. 43. Note that the prediction that the superconducting phase transition may change its order had been made in the early 1960-s [192]. Since our consideration is based on purely thermodynamic reasoning, it is robust and can be generalized to the cases when the superconducting phase is replaced by another ordered state, e.g. ferromagnetic state or antiferromagnetic one.

Under constant entropy (adiabatic) conditions, there should be a temperature step as a magnetic field crosses the phase boundary due to the above thermodynamic inequality. Indeed, the entropy jump would release the heat, but since $S = const$ the heat q is absorbed, causing the temperature to decrease in order to keep the constant entropy of the NFL state. Note that the minimal jump is given by the temperature-independent term S_0 , and q can be quite large so that the corresponding HF metal can be used as an effective cooler at low temperatures.

11. Scaling behavior of heavy fermion systems

As we have seen in Section 2 and Subsection 9.1 the core of Landau Fermi liquid theory, the effective mass M_L^* practically does not depend on temperature T , magnetic field B etc, $M_L^*(T, B) = M_L^* = const$ [19]. The thermodynamic functions such as the entropy S , heat capacity C , magnetic susceptibility χ behave as in the case of noninteracting Fermi gas, namely low temperatures $S/T \propto C/T \propto \chi \propto M_L^*$. In other words, when the inter-particle interaction is switching on and its strength λ is increasing, a noninteracting Fermi gas continuously transforms into LFL with $S(\lambda)$, $M_L^*(\lambda)$ etc. becoming functions of λ , while the main scaling behavior of LFL, $S \propto M_L^*(\lambda)T$, remains untouched. This fact imposes strict conditions on the low temperature thermodynamic properties causing LFL exhibit the scaling behavior, which could be represented by some reference LFL with a normalized effective mass $M_{NL}^* = M_L^*(T, B)/M_L^* \simeq 1$. As seen from Fig. 2, in the case of HF metals the scaling behavior of M_N^* is different from that of M_L^* .

Here we show that despite of the very different microscopic nature of 2D ^3He and HF metals with various ground state magnetic properties their NFL behavior is universal and can be captured well within the framework of FCQPT [6, 41, 42, 47, 73, 164] that supports the extended quasiparticles paradigm. We concentrate on the NFL behavior observed when heavy fermion systems transit from their LFL to NFL states. This area is mostly puzzling and important because the behavior of the system in its transition state strongly depends on the scenario shaping the corresponding QCP. For example, if the transition region is described by theories based on quantum and thermal critical fluctuations there are no theoretical grounds to expect that these systems with different magnetic ground states could exhibit a universal scaling behavior [1, 3, 15, 13, 25].

There are many measurements of the heat capacity $C(T, B)$, thermal expansion coefficient $\alpha(T, B)$ and the magnetic AC susceptibility $\chi(T, B)$ on strongly correlated Fermi systems such as HF metals, high- T_c superconductors and 2D ^3He carried out at different temperatures T , fixed magnetic fields B and the number density (or doping) x . Many of these measurements allow to explore the systems at their transition from the LFL state to the NFL one. Due to the equation

$$C/T \propto S/T \propto \sqrt{A} \propto \chi \propto \alpha/T \propto M^*, \quad (141)$$

relating all the above quantities to the effective mass, these can be regarded as the effective mass $M^*(T, B, x)$ measurements producing information about the scaling behavior of the normalized effective mass M_N^* .

Experimental facts show that the effective mass extracted from numerous measurements on different strongly correlated Fermi systems upon using Eq. (141) depends on magnetic field, temperature, number density and composition. As we have seen and shall see, a 4D function describing the normalized effective mass is reduced to a function of a single variable. Indeed, the normalized effective mass depends (as the effective mass does) on magnetic field, temperature, number density and the composition of a strongly correlated Fermi system such as HF metals and 2D Fermi systems, and all these parameters can be merged into the single variable y by means of Eq. (106).

11.1. Quantum criticality in 2D ^3He

We now discuss how the scaling behavior of the normalized effective mass M_N^* given by Eq. (106) describes the quantum criticality observed in 2D ^3He [72, 152, 153]. This quantum criticality is extremely significant as it allows us to check the possibility of the scaling behavior in the 2D system formed by ^3He atoms which are essentially different from electrons. Namely, the neutral atoms of ^3He are fermions interacting with each other by Van der Waals forces with strong

hardcore repulsion and a weakly attractive tail. The different character of the inter-particle interaction along with the fact that the mass of the ^3He atom is 3 orders of magnitude larger than that of an electron, makes ^3He systems have drastically different properties than those of HF metals. Because of this difference nobody can be sure that the macroscopic physical properties of these systems will be more or less similar to each other at their QCP. The 2D ^3He has a very important feature: a change in the total density of ^3He film drives it towards QCP at which the quasiparticle effective mass M^* diverges [72, 152, 153] as seen from Figs. 4 and 13. This peculiarity permits to plot the experimental dependence of the normalized effective mass versus temperature as a function of the number density x , which can be directly compared with M_N^* given by Eq. (106). As a result, 2D ^3He , being an intrinsically isotropic Fermi-liquid with negligible spin-orbit interaction becomes an ideal system to test a theory describing the NFL behavior. Note that the bulk liquid ^3He is historically the first object to which the LFL theory had been applied [19]. One may speculate that at a sufficiently high pressure the liquid ^3He would exhibit the NFL behavior. Unfortunately, the application of pressure causes 3D ^3He to solidify.

Let us consider HF liquid at $T = 0$ characterized by the effective mass M^* . As it was shown in Section 8, at QCP $x = x_{FC}$ the effective mass diverges at $T = 0$ and the system undergoes FCQPT. The leading term of this divergence reads

$$\frac{M^*(x)}{m} = a_1 + \frac{a_2}{1-z}, \quad z = \frac{x}{x_{FC}}, \quad (142)$$

where m is the bare mass. Equation (142) is valid in both 3D and 2D cases, while the values of the factors a_1 and a_2 depend on dimensionality and inter-particle interaction [6]. At $x > x_{FC}$ (or $z > 1$) FCQPT takes place. Here we confine ourselves to the case $x < x_{FC}$. It is seen from Eq. (142) that FCQPT takes place in 2D ^3He at elevated densities due to Van der Waals forces with strong hardcore repulsion. This strong hardcore repulsion makes the potential energy produce the main contribution to the ground state energy resulting in strong rearrangement of the single-particle spectrum and FCQPT. We recall that in the heavy electron liquid FCQPT occurs at diminishing densities due to Coulomb interaction.

When the system approaches QCP, the dependence of quasiparticle effective mass on temperature and number density x is governed by Eq. (89). It follows from Fig. 15 that the effective mass $M^*(T)$ as a function of T at fixed x reveals three different regimes at growing temperature. At the lowest temperatures we have the LFL state. The effective mass grows, reaching its maximum $M_M^*(T, x)$ at some temperature $T_M(x)$ and subsequently diminishing as $T^{-2/3}$ as seen from Eq. (99). Moreover, the closer is the number density x to its threshold value x_c , the higher is the rate of the growth. The peak value M_M^* grows also, but the maximum temperature T_M diminishes. Near the T_M temperature the last "traces" of the LFL state disappear, manifesting themselves in substantial growth of $M^*(x)$. The temperature region beginning near $T_M(x)$ signifies the crossover between the LFL state with almost constant effective mass and the NFL behavior with the $T^{-2/3}$ dependence. Thus the T_M point can be regarded as crossover between the LFL and NFL states or regimes.

As we have seen, $M^*(T, x)$ in the T and x range can be well approximated by a simple universal interpolating function. The interpolation occurs between the LFL ($M^* \propto T^2$) and NFL ($M^* \propto T^{-2/3}$) states, thus describing the above crossover. Substituting T by the dimensionless variable $y = T/T_M$, we obtain the desired expression (106). It is possible to calculate T_M as a function of z . Equation (142) shows that $M_M^* \propto 1/(1-z)$ and it follows from (99) that $M_M^* \propto T^{-2/3}$. As a result, we obtain [40]

$$T_M \propto (1-z)^{3/2}. \quad (143)$$

Equation (141) demonstrates that $M^*(T)$ can be measured in experiments on strongly correlated Fermi systems. Upon normalizing both $M^*(T)$ by its peak value at each x and the temperature by T_M , we see from Eq. (106) that all the curves merge into a single one demonstrating a scaling behavior.

In Fig. 44, we show the phase diagram of 2D ^3He in the variables T and z (see Eq. (142)). For the sake of comparison, the plot of the effective mass versus z is shown by the dashed line. The part of the diagram where $z < 1$ corresponds to HF behavior and consists of LFL and NFL parts, separated by the line $T_M(z) \propto (1-z)^{3/2}$. We note here that our exponent $3/2 = 1.5$ is exact as compared to that from Ref. [153] 1.7 ± 0.1 . The good agreement between the theoretical and experimental exponents supports our FCQPT description of the NFL behavior of both 2D ^3He and HF metals; the former system is in great detail similar to the latter. The regime for $z > 1$ consists of a low-temperature LFL piece (shadowed region, beginning in the intervening phase $z \leq 1$ [153]) and the NFL state at higher temperatures. The former LFL piece is related to the peculiarities of the substrate on which the 2D ^3He film is placed. Namely, it is related to weak substrate heterogeneity (steps and edges on its surface) so that quasiparticles, being localized (pinned) on it, give rise to the LFL behavior [153]. The competition between thermal and pinning energies returns the system back to NFL state and hence

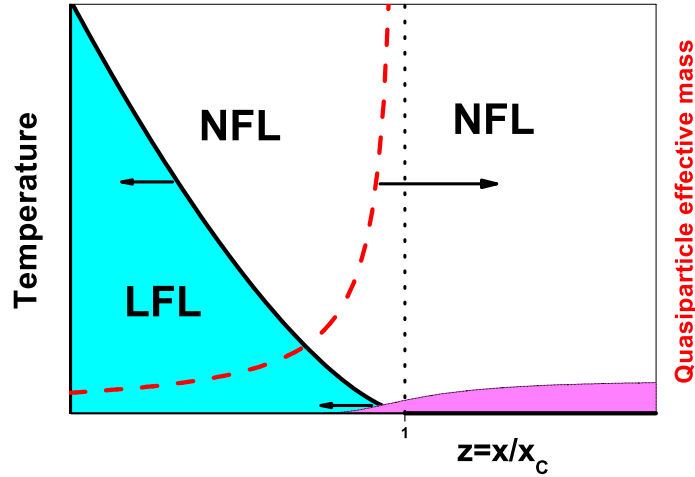


Figure 44: The phase diagram of the 2D ^3He system. The part for $z < 1$ corresponds to HF behavior divided into the LFL and NFL parts by the line $T_M(z) \propto (1-z)^{3/2}$, where T_M is the temperature at which the effective mass reaches its maximum. The exponent $3/2 = 1.5$ coming from Eq. (143) is in good agreement with the experimental value 1.7 ± 0.1 [153]. The dependence $M^*(z) \propto (1-z)^{-1}$ is shown by the dashed line. The regime for $z \geq 1$ consists of the LFL piece (the shadowed region, beginning in the intervening phase $z \leq 1$ [153], which is due to the substrate inhomogeneities, see text) and NFL regime at higher temperatures.

restores the NFL behavior. Note, that the presence of the substrate can be considered as the main difference between 2D ^3He and HF metals. Namely, the latter metals do not have a substrate, the above LFL piece would be absent or very thin if some 3D disorder (like point defects, dislocations etc) is present in a HF metals.

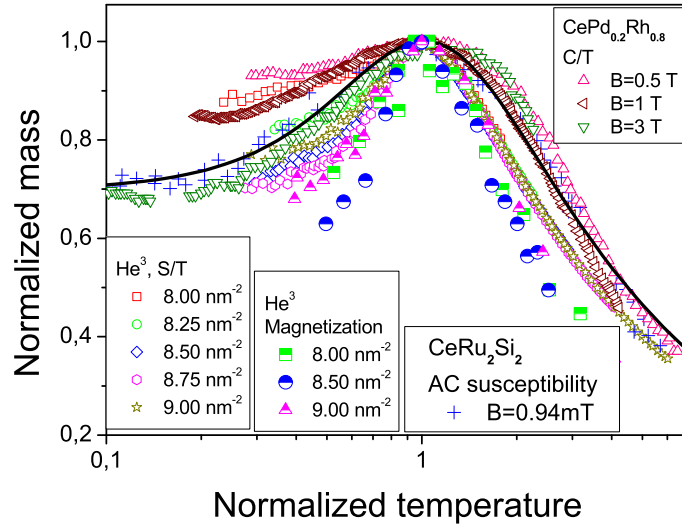


Figure 45: The normalized effective mass M_N^* as a function of the normalized temperature T/T_M at densities shown in the left lower corner. The behavior M_N^* is extracted from experimental data for the entropy in 2D ^3He [153] and 3D HF compounds with different magnetic ground states such as CeRu_2Si_2 and $\text{CePd}_{1-x}\text{Rh}_x$ [92, 174], fitted by the universal function (106).

In Fig. 13, we report the experimental values of the effective mass $M^*(z)$ obtained by the measurements on ^3He monolayer [72]. These measurements, in coincidence with those from Ref. [153], show the divergence of the effective mass at $x = x_c$. To show, that our FCQPT approach is able to describe the above data, we represent the fit of $M^*(z)$ by the fractional expression coming from Eq. (142) and the reciprocal effective mass by the linear fit $M/M^*(z) \propto a_1 z$.

We apply the universal dependence (106) to fit the experimental data not only in 2D ^3He but in 3D HF metals as well. $M_N^*(y)$ extracted from the entropy measurements on the ^3He film [153, 154] at different densities $x < x_c$ smaller than the critical point $x_c = 9.9 \pm 0.1 \text{ nm}^{-2}$ is reported in Fig. 45. In the same figure, the data extracted from the heat capacity of the ferromagnet $\text{CePd}_{0.2}\text{Rh}_{0.8}$ [174] and the AC magnetic susceptibility of the paramagnet CeRu_2Si_2 [92] are plotted for different magnetic fields. It is seen that the scaling behavior of the normalized effective mass given by Eq. (106) is in accord with the experimental facts. All substances are located at QCP, where the system progressively disrupts its LFL

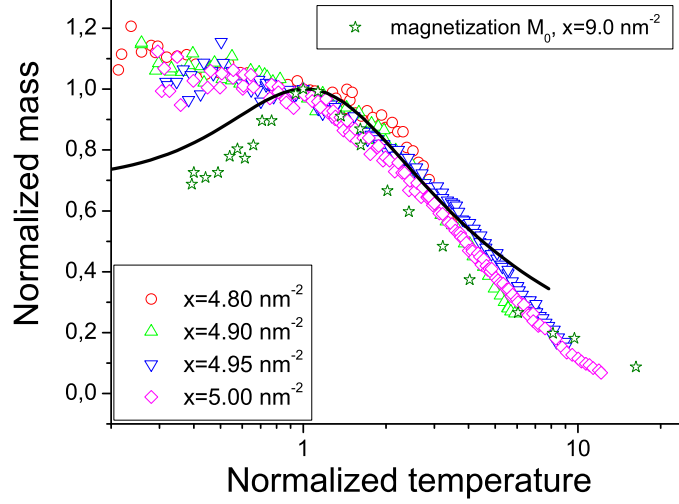


Figure 46: The dependence of $M_N^*(T/T_M)$ on T/T_M at densities shown in the left lower corner. The behavior M_N^* is extracted from experimental data for $C(T)/T$ in 2D ^3He [72] and for the magnetization M_0 in 2D ^3He [153]. The solid curve shows the universal function, see the caption to Fig. 45.

behavior at elevated temperatures. In that case the control parameter, which drives the system towards its QCP x_{FC} is represented merely by a number density x . It is seen that the behavior of the effective mass $M_N^*(y)$, extracted from $S(T)/T$ in 2D ^3He (the entropy $S(T)$ is reported in Fig. S8 A of Ref. [154]) looks very much like that in 3D HF compounds as was shown in Sections 9.

The attempt to fit the available experimental data for $C(T)/T$ in ^3He [72] by the universal function $M_N^*(y)$ is reported in Fig. 46. Here, the data extracted from heat capacity $C(T)/T$ for ^3He monolayer [72] and magnetization M_0 for bilayer [153, 154], are reported. It is seen that the normalized effective mass extracted from these thermodynamic quantities can be well described by Eq. (106). We note the qualitative similarity between the double layer [153] and monolayer [72] of ^3He seen from Fig. 46.

On the left panel of Fig. 47, we show the density dependence of T_{\max} , extracted from measurements of the magnetization $M_0(T)$ on ^3He bilayer [153, 154]. The peak temperature is fitted by Eq. (143). On the same figure, we have also reported the maximal magnetization M_{\max} . It is seen that M_{\max} is well described by the expression $M_{\max} \propto (S/T)_{\max} \propto (1-z)^{-1}$, see Eq. (142). The right panel of Fig. 47 reports the peak temperature T_{\max} and the maximal entropy $(S/T)_{\max}$ versus the number density x . They are extracted from the measurements of $S(T)/T$ on ^3He bilayer [153, 154]. The fact that both the left and right panels extracted from $M_0(T)$ and S/T demonstrate the same behavior shows once more that there are indeed the quasiparticles, which determine the thermodynamic behavior of 2D ^3He (and also 3D HF compounds [164]) near the point of their effective mass divergence.

As seen from Fig. 47, the amplitude and positions of the maxima of magnetization $M_0(T)$ and $S(T)/T$ in 2D ^3He follow well Eqs. (142) and (143), while Eq. (106) describes the scaling behavior of the normalized thermodynamic functions. We recall that we can calculate only relative values of the effective mass, that is the normalized effective mass, since the real values of T_M and M_M^* are determined by the specific properties of the system in question. Thus, with only two values defining both the real value, for example, of the entropy and the corresponding temperature, it is possible to calculate the thermodynamic or transport properties of HF metals or 2D ^3He . We conclude that Eq. (106) allows us to reduce a 4D function describing the normalized effective mass to a function of a single variable. Indeed, the normalized effective mass depends on magnetic field, temperature, number density and the composition of a strongly correlated Fermi

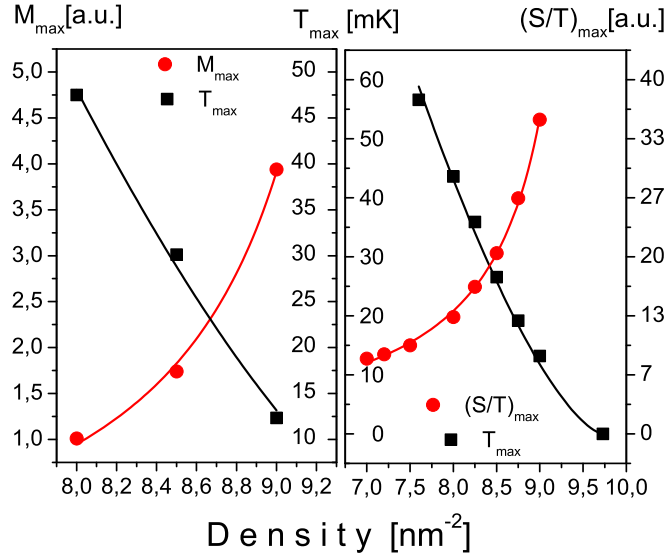


Figure 47: Left panel, the peak values M_{\max} and the peak temperatures T_{\max} extracted from measurements of the magnetization M_0 in ^3He [153, 154] are plotted versus density. Right panel shows T_{\max} and the peak values $(S/T)_{\max}$ extracted from measurements of $S(T)/T$ in ^3He [153, 154] also versus density. We approximate $T_{\max} = a_1(1-z)^{3/2}$, Eq. (143), and $(S/T)_{\max} \propto M_{\max} = a_2/(1-z)$, Eq. (142), with a_1 and a_2 fitting parameters.

system such as HF metals and 2D Fermi systems, and as we have seen above, all these parameters can be merged into the single variable by means of Eq. (106) [40]. We note that the validity of Eq. (106) is confirmed by numerical calculations as described in Subsection 9.3.1.

In conclusion of this Subsection, we have described the diverse experimental facts related to temperature and number density (2D number density) dependencies of different thermodynamic characteristics of 2D ^3He by the single universal function of one argument. The above universal behavior is also inherent to HF metals with different magnetic ground state properties. The amplitude and positions of the maxima of the magnetization $M_0(T)$ and $S(T)/T$ in 2D ^3He are also well described. We have shown that bringing the different experimental data collected on strongly correlated Fermi systems to the above form immediately reveals their universal scaling behavior.

11.2. Kinks in the thermodynamic functions

To illuminate kinks or energy scales observed in the thermodynamic functions measured on HF metals [17] and 2D ^3He , we present in Fig. 48 the normalized effective mass M_N^* extracted from the thermodynamic functions versus normalized temperature (the left panel) and the normalized thermodynamic functions proportional to $T_N M_N^*$ (the right panel) as a function of the normalized temperature T_N [166].

$M_N^*(y)$ extracted from the entropy $S(T)/T$ and magnetization M measurements on the ^3He film [153] at different densities x is reported in the left panel of Fig. 48. In the same panel, the data extracted from the heat capacity of the ferromagnet $\text{CePd}_{0.2}\text{Rh}_{0.8}$ [174], CeCoIn_5 [193] and the AC magnetic susceptibility of the paramagnet CeRu_2Si_2 [92] are plotted for different magnetic fields. It is seen that the universal behavior of the normalized effective mass given by Eq. (106) and shown by the solid curve is in accord with the experimental facts. It is seen that the behavior of $M_N^*(y)$, extracted from $S(T)/T$ and magnetization M of 2D ^3He looks very much like that of 3D HF compounds. In the right panel of Fig. 48, the normalized data on $C(y)$, $S(y)$, $y\chi(y)$ and $\underline{M} = M(y) + y\chi(y)$ extracted from data collected on $\text{CePd}_{1-x}\text{Rh}_x$ [174], ^3He [153], CeRu_2Si_2 [92], CeCoIn_5 [193] and YbRu_2Si_2 [17] respectively are presented. Note that in the case of YbRu_2Si_2 , the variable $y = (B - B_{c0})\mu_B/T_M$ can be viewed as effective normalized temperature. We remark that in Subsection 9.4.2 we calculate \underline{M} as a function of magnetic field.

It is seen from the right panel of Fig. 48 that all the data exhibit the kink (shown by arrow) at $y \geq 1$ taking place as soon as the system enters the transition region from the LFL state to the NFL one. This region corresponds to the temperatures where the vertical arrow in Fig. 15 a crosses the hatched area separating the LFL from NFL behavior. It is

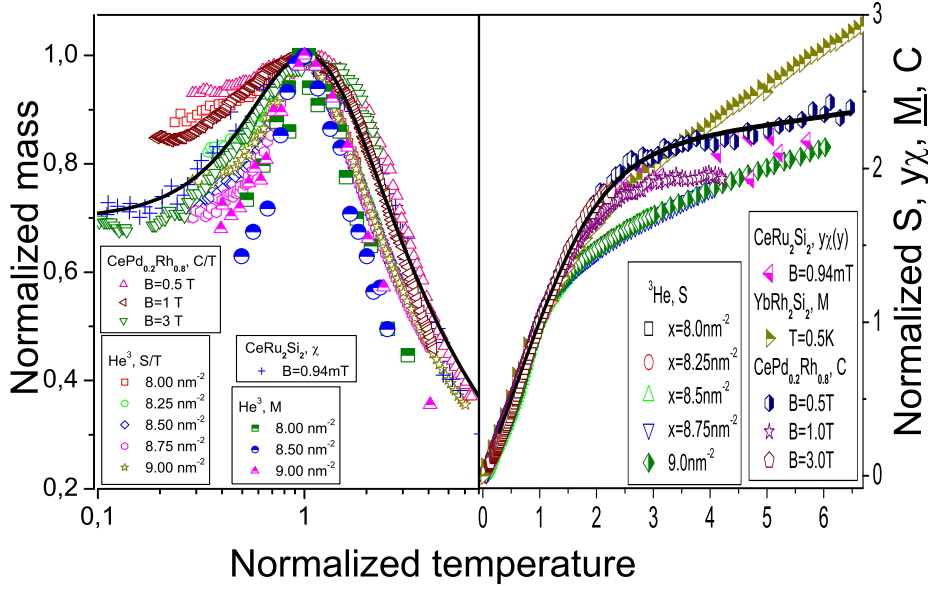


Figure 48: Energy scales in HF metals and 2D ^3He . The left panel. The normalized effective mass M_N^* versus the normalized temperature $y = T/T_M$. The dependence $M_N^*(y)$ is extracted from measurements of $S(T)/T$ and magnetization M on 2D ^3He [153]), from AC susceptibility $\chi(T)$ collected on CeRu_2Si_2 [92] and from $C(T)/T$ collected on both $\text{CePd}_{1-x}\text{Rh}_x$ [174] and CeCoIn_5 [193]. The data are collected for different densities and magnetic fields shown in the left bottom corner. The solid curve traces the universal behavior of the normalized effective mass determined by Eq. (106). Parameters c_1 and c_2 are adjusted for $\chi_N(T_N, B)$ at $B = 0.94$ mT. The right panel. The normalized specific heat $C(y)$ of $\text{CePd}_{1-x}\text{Rh}_x$ and CeCoIn_5 at different magnetic fields B , normalized entropy $S(y)$ of ^3He at different number densities x , and the normalized $y\chi(y)$ at $B = 0.94$ mT versus normalized temperature y are shown. The upright triangles depict the normalized "average" magnetization $\underline{M} = M + B\chi$ collected on YbRu_2Si_2 [17]. The kink (shown by the arrow) in all the data is clearly seen in the transition region $y \geq 1$. The solid curve represents $yM_N^*(y)$ with parameters c_1 and c_2 adjusted for the magnetic susceptibility of CeRu_2Si_2 at $B = 0.94$ mT.

also seen that the low temperature LFL scale of the thermodynamic functions (as a function of y) is characterized by the fast growth, and the high temperature scale related to the NFL behavior is characterized by the slow growth. As a result, we can identify the energy scales near QCP, discovered in Ref. [17]: the thermodynamic characteristics exhibit the kinks (crossover points from the fast to slow growth at elevated temperatures) which separate the low temperature LFL scale and high temperature one related to the NFL state.

11.3. Heavy-fermion metals at metamagnetic phase transitions

A Fermi system can be driven to FCQPT when narrow bands situated close to the Fermi surface are formed by the application of a high critical magnetic field B_m . The emergence of such state is known as metamagnetism that occurs when this transformation comes abruptly at B_m [194].

Let us assume that the magnetic field B_m is similar to that of B_{c0} driving a HF metal to its magnetic field tuned QCP. In our simple model both B_{c0} and B_m are taken as parameters. To apply equation (106) when the critical magnetic field is not zero, we have to replace B by $(B - B_m)$. Acting as above, we can extract the normalized effective mass $M_N^*(T_N)$ from data collected on HF metals at their metamagnetic QCP. In Fig. 49 the extracted normalized mass is displayed. $M_N^*(T_N)$ is extracted from measurements of C/T collected on $\text{URu}_{1.92}\text{Rh}_{0.08}\text{Si}_2$, CeRu_2Si_2 and $\text{CeRu}_2\text{Si}_{1.8}\text{Ge}_{0.2}$ at their metamagnetic QCP with $B_m \approx 35$ T, $B_m \approx 7$ T and $B_m \approx 1.2$ T respectively [195, 196]. As seen from Fig. 49, the effective mass $M_N^*(T_N)$ in different HF metals reveals the same form both in the high magnetic field and in low ones as soon as the corresponding bands become flat, that is the electronic system of HF metals is driven to FCQPT. This observation is extremely significant as it allows us to check the universal behavior in HF metals when these are under the application of essentially different magnetic fields. Namely, the magnitude of the applied field ($B \sim 10$ T) at the metamagnetic point is four orders of magnitude larger than that of the field applied to tune CeRu_2Si_2 to the LFL behavior ($B \sim 1$ mT). Relatively

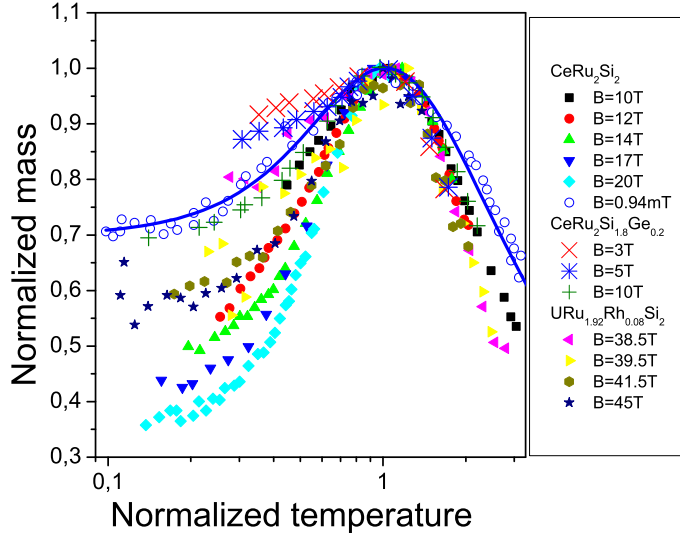


Figure 49: The normalized effective mass as a function of magnetic field versus the normalized temperature. $M_N^*(T_N)$ is extracted from measurements of C/T collected on $\text{URu}_{1.92}\text{Rh}_{0.08}\text{Si}_2$, CeRu_2Si_2 and $\text{CeRu}_2\text{Si}_{1.8}\text{Ge}_{0.2}$ at different magnetic fields [195, 196] shown in the right panel. The solid curve gives the universal behavior of M_N^* given by Eq. (106), see also the caption to Fig. 32.

small values of $M_N^*(T_N)$ observed in $\text{URu}_{1.92}\text{Rh}_{0.08}\text{Si}_2$ and CeRu_2Si_2 at the high fields and small temperatures can be explained by taking into account that the narrow band is completely polarized [195]. As a result, at low temperatures the summation over the spins "up" and "down" reduces to a single direction producing the coefficient 1/2 in front of the normalized effective mass. At high temperatures the summation is restored. As seen from Fig. 49, these observations are in accord with the experimental facts.

12. Asymmetric conductivity in HF metals and high- T_c superconductors

The main subjects of investigation in experiments on HF metals are the thermodynamic properties. Therefore, it seems reasonable to study the properties of HF liquids that are determined by the quasiparticle distribution function $n(\mathbf{p}, T)$ and not only by the density of states or by the behavior of the effective mass M^* [6, 172, 197, 198, 199]. As we shall see in this Section, the FC solutions $n_0(\mathbf{p})$ leads to the NFL behavior and violate the particle-hole symmetry inherent in LFL and generate dramatic changes in transport properties of HF metals, particularly, the differential conductivity becomes asymmetric. As was shown in Section 7, the LFL behavior is restored under the application of magnetic field. Thus, we expect that in magnetic fields the asymmetric part of the differential conductivity is suppressed. Scanning tunnel microscopy and point-contact spectroscopy closely related to the Andreev reflection are sensitive to both the density of states and the probability of the population of quasiparticle states determined by the function $n(\mathbf{p}, T)$ [200, 201]. Thus, scanning tunnel microscopy and point-contact spectroscopy are ideal tools for studying specific features of the NFL behavior of HF metals and high- T_c superconductors.

12.1. Normal state

The tunnel current I running through a point contact of two ordinary metals is proportional to the applied voltage V and to the square of the absolute value of the quantum mechanical transition amplitude t times the difference $N_1(0)N_2(0)(n_1(p, T) - n_2(p, T))$ [199], where $N_1(0) N_2(0)$ are the density of states of the respective metals and $n_1(p, T)$ and $n_2(p, T)$ are respectively the distribution functions of the respective metals. On the other hand, in the semiclassical approximation, the wave function that determines the amplitude t is proportional to $(N_1(0)N_2(0))^{-1/2}$. Therefore, the

density of states drops out from the final result and the tunnel current becomes independent of $N_1(0)N_2(0)$. Because the distribution $n(p, T \rightarrow 0) \rightarrow \theta(p_F - p)$ as $T \rightarrow 0$, where $\theta(p_F - p)$ is the step function, it can be verified that the differential tunnel conductivity $\sigma_d(V) = dI/dV$ is a symmetric or even function of V in the Landau Fermi-liquid theory. Actually, the symmetry of $\sigma_d(V)$ is obeyed if there is the hole-quasiparticle symmetry (which is present in the LFL theory). Hence, the fact that $\sigma_d(V)$ is symmetric is obvious and is natural in the case of metal-metal contacts for ordinary metals that are in the normal or superconducting state.

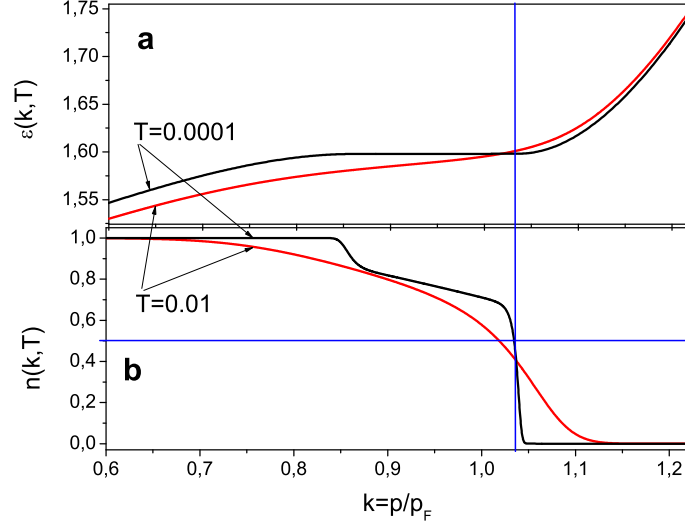


Figure 50: The single particle energy $\varepsilon(\mathbf{k}, T)$ (a) and the distribution function $n(\mathbf{k}, T)$ (b) at finite temperatures as functions of the dimensionless variable $k = p/p_F$. The arrows show temperature measured in T/E_F . At $T = 0.0001$ the vertical line shows the position of the Fermi level E_F at which $n(\mathbf{k}, T) = 0.5$ as depicted by the horizontal line. At diminishing temperatures $T \rightarrow 0$, the single particle energy $\varepsilon(\mathbf{k}, T)$ becomes more flat in the region $(p_f - p_i)$ and the distribution function $n(\mathbf{k}, T)$ in this region becomes more asymmetrical with respect to the Fermi level E_F producing the particle-hole asymmetry related to the NFL behavior.

We study the tunnel current at low temperatures, which for ordinary metals is given by the expression [199, 200]

$$I(V) = 2|t|^2 \int [n(\varepsilon - V) - n(\varepsilon)] d\varepsilon. \quad (144)$$

where we use the atomic system of units $e = m = \hbar = 1$ and normalize the transition amplitude to unity, $|t|^2 = 1$. Since the temperatures are low, we can approximate the distribution function $n(\varepsilon)$ by the step function $\theta(\mu - \varepsilon)$; Eq. (144) then yields $I(V) = a_1 V$, and hence the differential conductivity $\sigma_d(V) = dI/dV = a_1 = const$ is a symmetric function of the applied voltage V .

To quantitatively examine the behavior of the asymmetric part of the conductivity $\sigma_d(V)$, we find the derivatives of both sides of Eq. (144) with respect to V . The result is the following equation for $\sigma_d(V)$:

$$\sigma_d = \frac{1}{T} \int n(\varepsilon(z) - V, T) (1 - n(\varepsilon(z) - V, T)) \frac{\partial \varepsilon}{\partial z} dz, \quad (145)$$

In the integrand in Eq. (145), we used the dimensionless momentum $z = p/p_F$ instead of ε for the variable, because n is no longer a function of ε in the case of a strongly correlated electron liquid; it depends on the momentum as shown in Figs. 5 and 50. Indeed, the variable ε in the interval $(p_f - p_i)$ is equal to μ , and the quasiparticle distribution function varies within this interval. It is seen from Eq. (145) that the violation of the particle-hole symmetry makes $\sigma_d(V)$ asymmetric as a function of the applied voltage V [6, 172, 197, 198].

The single particle energy $\varepsilon(\mathbf{k}, T)$ shown in Fig. 50 (a) and the corresponding $n(\mathbf{k}, T)$ shown in the panel (b) evolve from the FC state characterized by $n_0(\mathbf{k}, T = 0)$ determined by Eq. (21). It is seen from Fig. 50 (a), that at elevated

temperatures the dispersion $\varepsilon(\mathbf{k}, T)$ becomes more inclined since the effective mass $M^*(T)$ diminishes as seen from Eq. (31). At the Fermi level $\varepsilon(p, T) = \mu$, then from Eq. (5) the distribution function $n(p, T) = 1/2$. The vertical line in Fig. 50 crossing the distribution function at the Fermi level illustrates the asymmetry of the distribution function with respect to the Fermi level at $T = 0.0001$. It is clearly seen that the FC state strongly violates the particle-hole symmetry at diminishing temperatures. As a result, at low temperatures the asymmetric part of the differential conductivity becomes larger. Under the application of magnetic fields the system transits to the LFL state that strongly supports the particle hole symmetry. Therefore, the application of magnetic fields restoring the symmetry suppresses the asymmetric part of the differential conductivity.

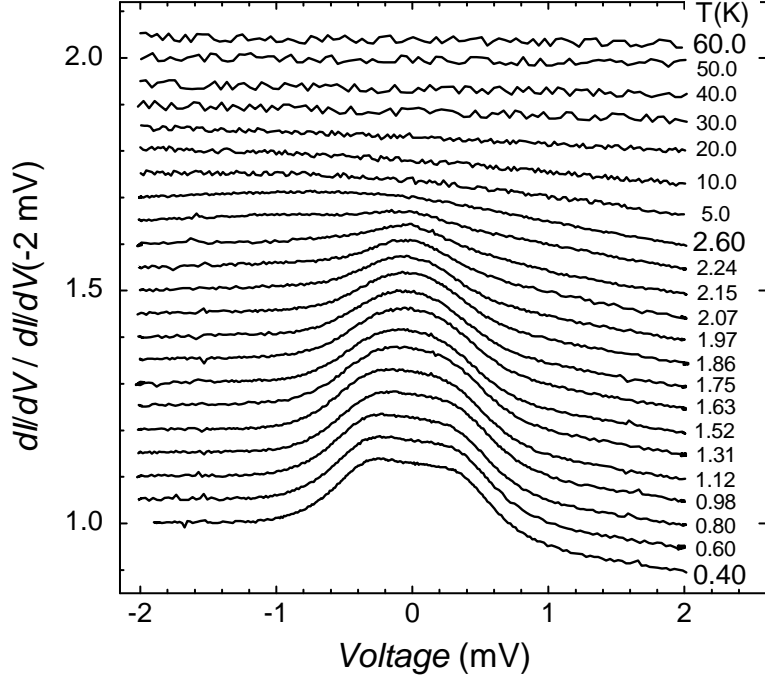


Figure 51: Differential conductivity $\sigma_d(V)$ measured in the case of point contacts Au/CeCoIn₅. The curves $\sigma_d(V)$ are displaced along the vertical axis by 0.05. The conductivity is normalized to its value at $V = -2$ mV. The asymmetry becomes noticeable at $T < 45$ K and increases as the temperature decreases [202].

After performing fairly simple transformations in Eq. (145), we find that the asymmetric part

$$\Delta\sigma_d(V) = (\sigma_d(V) - \sigma_d(-V))/2$$

of the differential conductivity can be expressed as

$$\begin{aligned} \Delta\sigma_d(V) &= \frac{1}{2} \int \frac{\alpha(1 - \alpha^2)}{[n(z, T) + \alpha[1 - n(z, T)]]^2} \\ &\times \frac{\partial n(z, T)}{\partial z} \frac{1 - 2n(z, T)}{[\alpha n(z, T) + [1 - n(z, T)]]^2} dz, \end{aligned} \quad (146)$$

where $\alpha = \exp(-V/T)$.

Asymmetric tunnel conductivity can be observed in measurements involving metals whose electron system is located near FCQPT or behind it. Among such metals are high- T_c superconductors and heavy-fermion metals, e.g., YbRh₂(Si_{0.95}Ge_{0.05})₂, CeCoIn₅, YbCu_{5-x}Al_x or YbRh₂Si₂. The measurements must be conducted when the heavy-fermion metal is in the superconducting or normal state. If the metal is in its normal state, measurements of $\Delta\sigma_d(V)$ can be done in a magnetic field $B > B_{c0}$ at temperatures $T^*(B) < T \leq T_f$ or in a zero magnetic field at temperatures

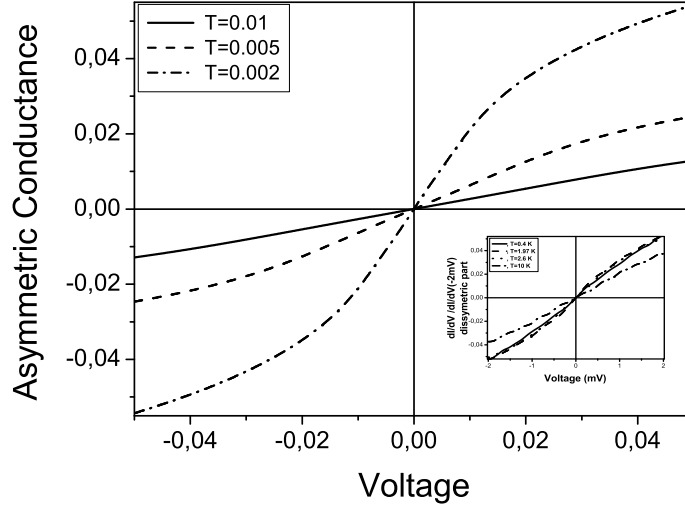


Figure 52: The asymmetric conductivity $\Delta\sigma_d(V)$ as a function of V/μ for three values of the temperature T/μ (normalized to μ). The inset shows the behavior of the asymmetric conductivity extracted from the data in Fig. 51.

higher than the corresponding critical temperature when the electron system is in the paramagnetic state and its behavior is determined by the entropy S_0 .

Recent measurements of the differential conductivity in CeCoIn_5 carried out using by the point-contact spectroscopy technique [202] have vividly revealed the asymmetry in the differential conductivity in the superconducting ($T_c = 2.3$ K) and normal states. Figure 51 shows the results of these measurements. Clearly, $\Delta\sigma_d(V)$ is nearly constant when the heavy-fermion metal is in the superconducting state, experiencing no substantial variation near T_c , see also Fig. 56 below. Then it monotonically decreases as the temperature increases [202].

Figure 52 shows the results of calculations of the asymmetric part $\Delta\sigma_d(V)$ of the conductivity $\sigma_d(V)$ obtained from Eq. (146) [172]. In calculating the distribution function $n(z, T)$, we used the functional (102) (with the parameters $\beta = 3$ and $g = 8$). In this case, $(p_f - p_i)/p_F \simeq 0.1$. Figure 52 also shows that the asymmetric part $\Delta\sigma_d(V)$ of the conductivity is a linear function of V for small voltages. Consistent with the Fig. 50 showing that the asymmetry of $n(\mathbf{k}, T)$ diminishes at elevated temperatures, the asymmetric part decreases with increasing temperature, which agrees with the behavior of the experimental curves in the inset in Fig. 52.

We now derive an estimate formula for analyzing the asymmetric part of the differential conductivity. It follows from Eq. (146) that for small values of V , the asymmetric part behaves as $\Delta\sigma_d(V) \propto V$. Here, it is appropriate to note that the asymmetric part of the tunnel conductivity is an odd function of V , and therefore $\Delta\sigma_d(V)$ must change sign when V changes sign. The natural unit for measuring voltage is $2T$, because this quantity determines the characteristic energy for FC, as shown by Eq. (33). Actually, the asymmetric part must be proportional to the size $(p_f - p_i)/p_F$ of the region occupied by FC:

$$\Delta\sigma_d(V) \simeq c \frac{V}{2T} \frac{p_f - p_i}{p_F} \simeq c \frac{V}{2T} \frac{S_0}{x_{FC}}. \quad (147)$$

where $S_0/x_{FC} \sim (p_f - p_i)/p_F$ is the temperature-independent part of the entropy [see Eq. (130)] and c is a constant of the order of unity. For instance, calculations of c using the distribution function displayed in Fig. 50 yield $c \sim 1$. From Eq. (147) we see that when $V \simeq 2T$ and FC occupies a sizable part of the Fermi volume, $(p_f - p_i)/p_F \simeq 1$, the asymmetric part becomes comparable to the differential tunnel conductivity $\Delta\sigma_d(V) \sim V_d(V)$.

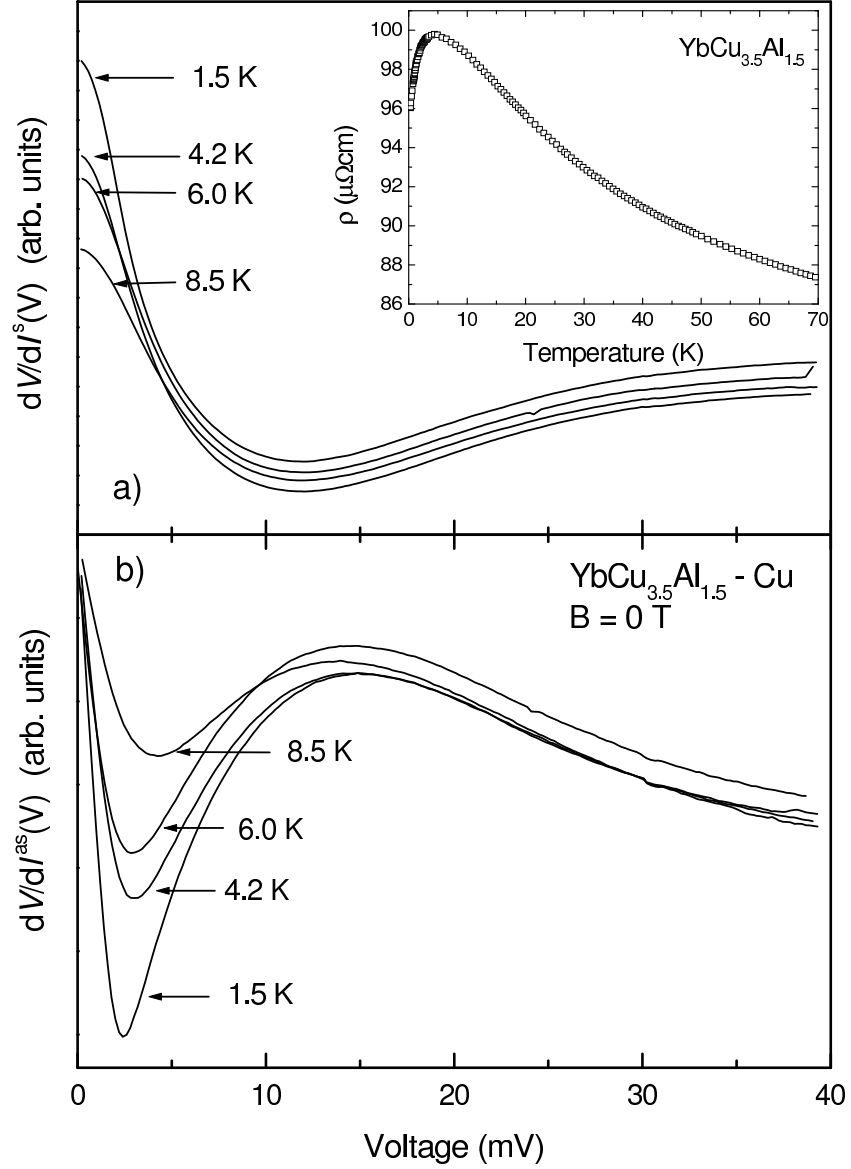


Figure 53: Characteristic temperature behavior of (a) symmetric $dV/dI^s(V)$ and (b) asymmetric $dV/dI^{as}(V)$ parts of $dV/dI(V)$ for heterocontact $\text{YbCu}_{3.5}\text{Al}_{1.5} - \text{Cu}$ at $B = 0$ T and different temperatures shown by the arrows. The inset shows the bulk resistivity $\rho(T)$ of $\text{YbCu}_{3.5}\text{Al}_{1.5}$ [203].

12.1.1. Suppression of the asymmetrical differential resistance in $\text{YbCu}_{5-x}\text{Al}_x$ in magnetic fields

Now consider the behavior of the asymmetric part of the differential conductivity $\Delta\sigma_d(V)$ under the application of a magnetic field B . Obviously, the differential conductivity being a scalar should not depend on the direction of current I . Thus, the non-zero value of $\Delta\sigma_d(V)$ manifests the violation of the particle-hole symmetry on a macroscopic scale. As we have seen in Section 7 and Subsection 9.1, at sufficiently low temperatures $T < T^*(B)$, the application of a magnetic field $B > B_{c0}$ leads to restoration of the LFL behavior eliminating the particle-hole asymmetry, and therefore the asymmetric part of the differential conductivity disappears [172, 197]. This prediction is in accord with the experimental facts collected in measurements on $\text{YbCu}_{5-x}\text{Al}_x$ of the differential resistance $dV/dI(V)$ under the application of magnetic fields [203]. Representing the differential resistance as the sum of its symmetrical $dV/dI^s(V)$ and the asymmetrical part $dV/dI^{as}(V)$,

$$dV/dI(V) = dV/dI^s(V) + dV/dI^{as}(V),$$

we obtain the equation

$$\Delta\sigma_d(V) \simeq -\frac{dV/dI^{as}(V)}{[dV/dI^s(V)]^2}. \quad (148)$$

Deriving Eq. (148), we assume that $dV/dI^s(V) \gg dV/dI^{as}(V)$. Figure 53 [203] shows the temperature evolution of (a) the symmetric $dV/dI^s(V)$ and (b) the asymmetric $dV/dI^{as}(V)$ parts at zero applied magnetic field. Also for the case of a heterocontact, the behavior of the symmetric part does not show a decrease in $\rho(T)$, while the asymmetric part decreases at elevated temperatures [203]. It seen from Fig. 53 that the behavior of the asymmetric part of the differential resistance given by Eqs. (147) and (148) is in accord with the experimental facts.

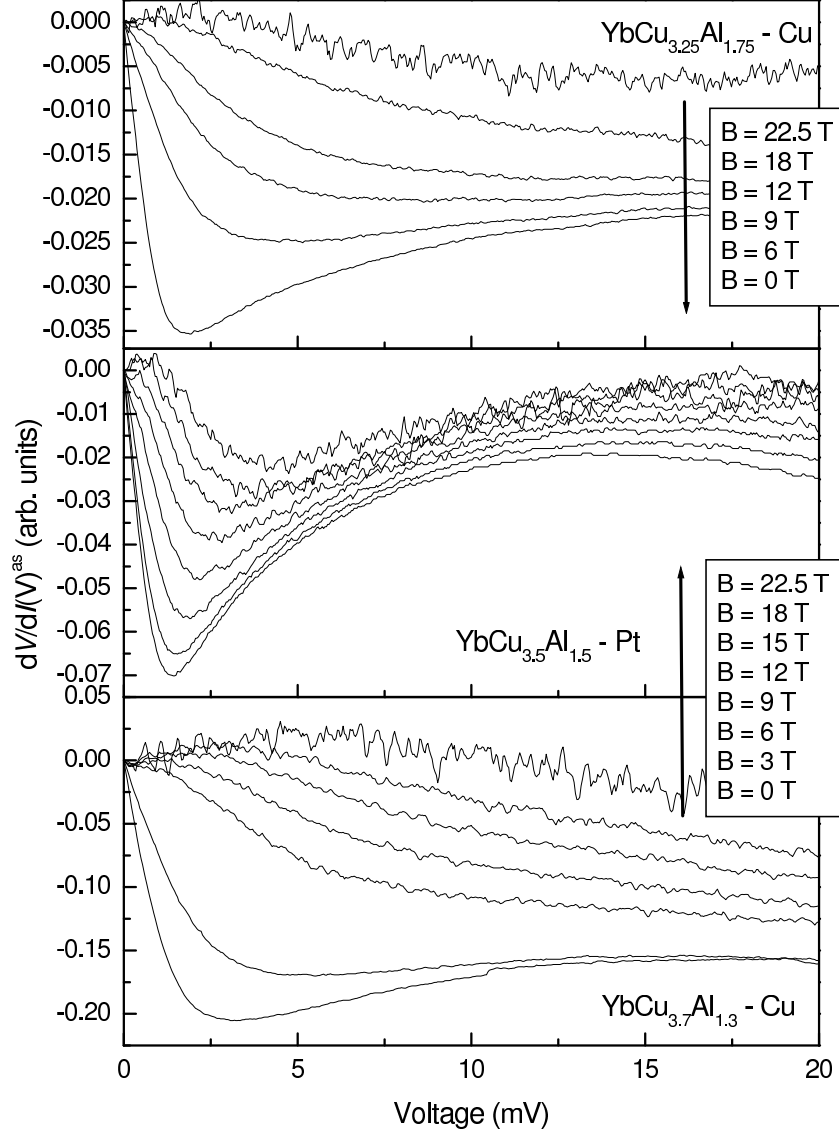


Figure 54: Characteristic magnetic-field behavior of the asymmetric part $dV/dI^{as}(V)$ of the differential conductivity is shown versus magnetic fields displayed in the legends for heterocontacts with different $x = 1.3, 1.5,$ and 1.75 at 1.5 K [203].

It is seen from Fig. 54 [203] that increasing magnetic fields suppress the asymmetric part. Thus, the application of magnetic fields destroys the NFL behavior and recovers both the LFL state and the particle-hole symmetry. Correspondingly, we conclude that the particle-hole symmetry is macroscopically broken in the absence of applied magnetic fields,

while the application of magnetic fields restores both the particle-hole symmetry and the LFL state. It is seen from Figs. 53 and 54 that the asymmetric part shows a linear behavior as function of the voltage below about 1 mV [203] as predicted [172].

12.2. Superconducting state

Tunnel conductivity may remain asymmetric as a high- T_c superconductor or a HF metal pass into the superconducting state from the normal state. The reason is that the function $n_0(\mathbf{p})$ again determines the differential conductivity. As we saw in Section 5, $n_0(\mathbf{p})$ is not noticeably distorted by the pairing interaction, which is relatively weak compared to the Landau interaction, which forms the distribution function $n_0(\mathbf{p})$. Hence, the asymmetric part of the conductivity remains practically unchanged for $T \leq T_c$, which agrees with the results of experiments (see Fig. 51). In calculating the conductivity using the results of measurements with a tunneling microscope, we must bear in mind that the density of states in the superconducting state

$$N_S(E) = N(\varepsilon - \mu) \frac{E}{\sqrt{E^2 - \Delta^2}}, \quad (149)$$

determines the conductivity, which is zero for $E \leq |\Delta|$. Here, E is the quasiparticle energy given by Eq. (38), and $\varepsilon - \mu = \sqrt{E^2 - \Delta^2}$. Equation (149) implies that the tunnel conductivity may be asymmetric if the density of states in the normal state $N(\varepsilon)$ is asymmetric with respect to the Fermi level [204], as is the case with strongly correlated Fermi systems with FC. Our calculations of the density of states based on model functional (102) with the same parameters as those used in calculating $\Delta\sigma_d(V)$ shown in Fig. 52 corroborate this conclusion.

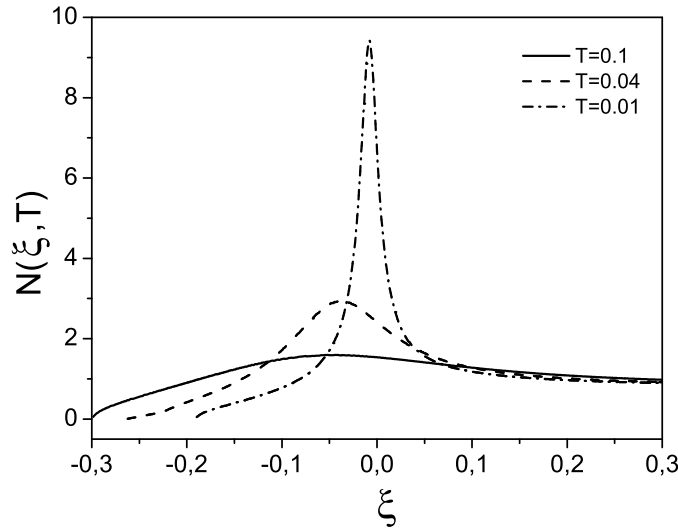


Figure 55: Density of states $N(\xi, T)$ as a function of $\xi = (\varepsilon - \mu)/\mu$, calculated for three values of the temperature T (normalized to μ).

Figure 55 shows the results of calculations of the density of states $N(\xi, T)$. Clearly, $N(\xi, T)$ is strongly asymmetric with respect to the Fermi level. If the system is in the superconducting state, the values of the normalized temperature given in the upper right corner of the diagram can be related to Δ_1 . With $\Delta_1 \simeq 2T_c$, we find that $2T/\mu \simeq \Delta_1/\mu$. Because $N(\xi, T)$ is asymmetric, the first derivative $\partial N(\xi, T)/\partial \xi$ is finite at the Fermi level, and the function $N(\xi, T)$ can be written as $N(\xi, T) \simeq a_0 + a_1 \xi$ for small values of ξ . The coefficient a_0 contributes nothing to the asymmetric part. Obviously, the value of $\Delta\sigma_d(V)$ is determined by the coefficient $a_1 \propto M^*(\xi = 0)$. In turn, $M^*(\xi = 0)$ is determined by Eq. (41). As a result, Eq. (149) yields

$$\Delta\sigma_d(V) \sim c_1 \frac{V}{80} \frac{S_0}{|\Delta| x_{FC}}, \quad (150)$$

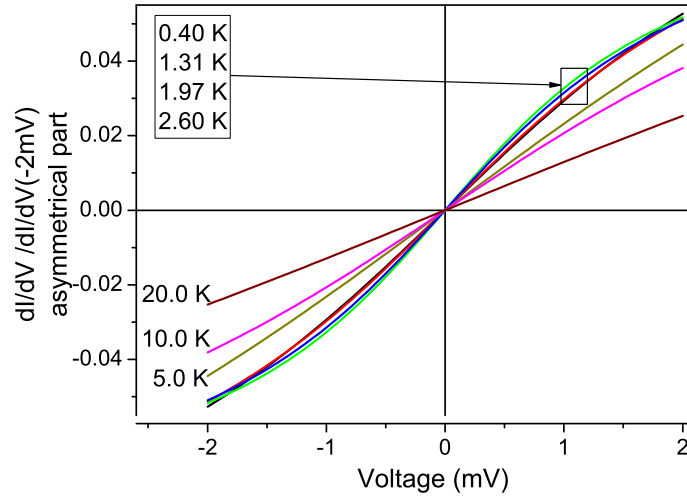


Figure 56: Temperature dependence of the asymmetric parts $\Delta\sigma_d(V)$ of the conductance spectra extracted from measurements on CeCoIn_5 [202]. The temperatures are boxed and shown by the arrow for $T \leq 2.60$ K, otherwise by numbers near the curves.

because $(p_f - p_i)/p_F \approx S_0/x_{FC}$, the energy E is replaced by the voltage V , and $\xi = \sqrt{V^2 - \Delta^2}$. The entropy S_0 here refers to the normal state of a heavy-fermion metal.

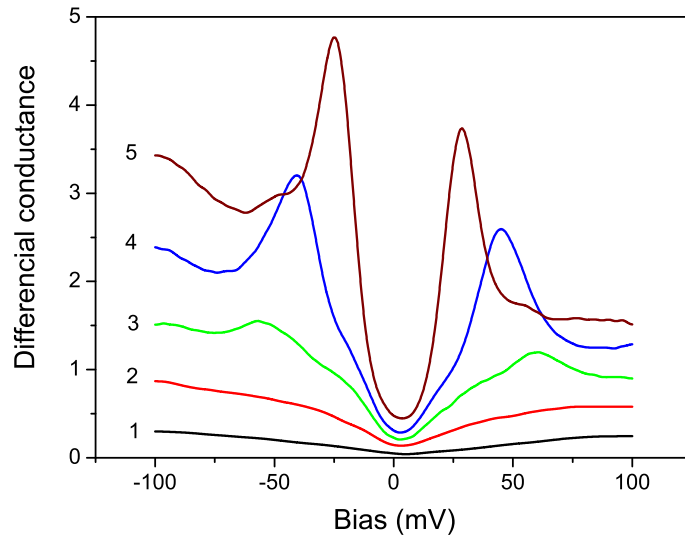


Figure 57: Spatial variation of the spectra of the differential tunnel conductivity measured in $\text{Bi}_2\text{Sr}_2\text{CaCu}_2\text{O}_{8+x}$. Lines 1 and 2 belong to regions in which the integrated local density of states is very low. Low differential conductivity and the absence of a gap are indications that we are dealing with an insulator. Line 3 corresponds to a large gap (65 meV) with mildly pronounced peaks. The integrated value of the local density of states for curve 3 is small, but is larger than that for lines 1 and 2. Line 4 corresponds to a gap of about 40 meV, which is close to the average value. Line 5 corresponds to the maximum integrated local density of states and the smallest gap about of 25 meV, and has two sharp coherent peaks [205].

Actually, Eq. (150) coincides with Eq. (147) if we use the fact that the characteristic energy of the superconducting state is determined by Eq. (42) and is temperature-independent. In studies of the universal behavior of the asymmetric conductivity, Eq. (150) has proved to be more convenient than (149). It follows from Eqs. (147) and (150) that measurements of the transport properties (the asymmetric part of the conductivity) allow the determination of the thermodynamic properties of the normal phase that are related to the entropy S_0 . Equation (150) clearly shows that the asymmetric part of the differential tunnel conductivity becomes comparable to the differential tunnel conductivity at $V \sim 2|\Delta|$ if FC occupies a substantial part of the Fermi volume, $(p_f - p_i)/p_F \simeq 1$. In the case of the d -wave symmetry of the gap, the right-hand side of Eq. (150) must be averaged over the gap distribution $\Delta(\phi)$, where ϕ is the angle. This simple procedure amounts to redefining the gap size or the constant c_1 . As a result, Eq. (150) can also be applied when $V < \Delta_1$, where Δ_1 is the maximum size of the d -wave gap [197]. For the Andreev reflection, where the current is finite for any small value of V , Eq. (150) also holds for $V < \Delta_1$ in the case of the s -wave gap.

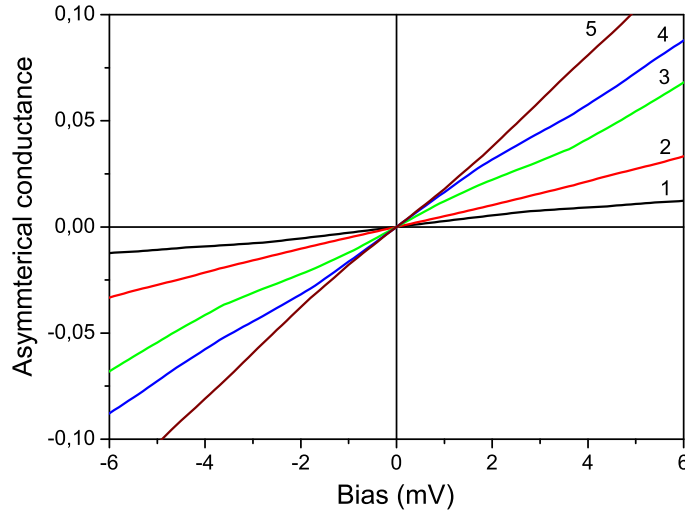


Figure 58: The asymmetric part $\Delta\sigma_d(V)$ of the differential tunnel conductivity in the high- T_c superconductor $\text{Bi}_2\text{Sr}_2\text{CaCu}_2\text{O}_{8+x}$, extracted from the data in Fig. 57, as a function of the voltage V (mV). The lines are numbered consistent with the numbers of the lines in Fig. 57.

It is seen from Fig. 56 that the asymmetrical part $\Delta\sigma_d(V)$ of the conductivity remains constant up to temperatures of about T_c and persists up to temperatures well above T_c . At small voltages the asymmetric part is a linear function of V and starts to diminish at $T \geq T_c$. It follows from Fig. 56 that the description of the asymmetric part given by Eqs. (147) and (150) coincides with the facts obtained in measurements on CeCoIn_5 .

Low-temperature measurements with tunneling microscopy and spectroscopy techniques were used in [205] to detect an inhomogeneity in the electron density distribution in $\text{Bi}_2\text{Sr}_2\text{CaCu}_2\text{O}_{8+x}$. This inhomogeneity manifests itself as spatial variations in the local density of states in the low-energy part of the spectrum and in the size of the superconducting gap. The inhomogeneity observed in the integrated local density of states is not caused by impurities but is inherent in the system. Observation facilitated relating the value of the integrated local density of states to the concentration x of local oxygen impurities.

Spatial variations in the differential tunnel conductivity spectrum are shown in Fig. 57. Clearly, the differential tunnel conductivity is highly asymmetric in the superconducting state of $\text{Bi}_2\text{Sr}_2\text{CaCu}_2\text{O}_{8+x}$. The differential tunnel conductivity shown in Fig. 57 may be interpreted as measured at different values of $\Delta_1(x)$ but at the same temperature, which allows studying the $\Delta\sigma_d(V)$ dependence on $\Delta_1(x)$. Figure 58 shows the asymmetric conductivity diagrams obtained from the data in Fig. 57. Clearly, for small values of V , $\Delta\sigma_d(V)$ is a linear function of voltage consistent with (150) and the slope of the respective straight lines $\Delta\sigma_d(V)$ is inversely proportional to the gap size Δ_1 .

Figure 59 shows the variation in the asymmetric part of the conductivity $\Delta\sigma_d(V)$ as the temperature increases. The

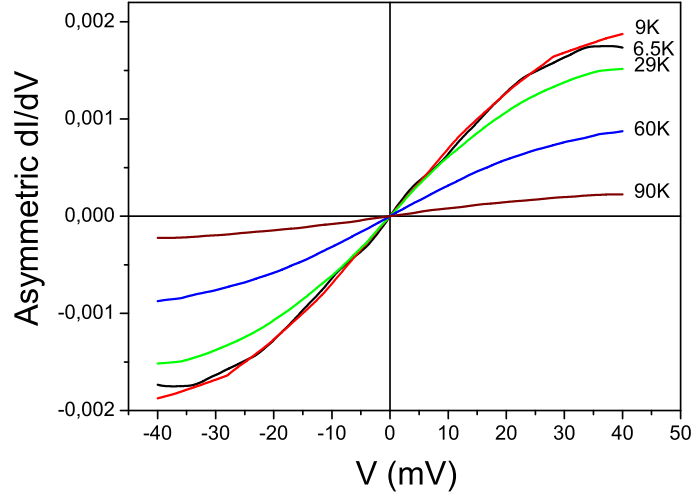


Figure 59: Temperature dependence of the asymmetric part $\Delta\sigma_d(V)$ of the conductivity spectra obtained in measurements for $\text{YBa}_2\text{Cu}_3\text{O}_{7-x}/\text{La}_{0.7}\text{Ca}_{0.3}\text{MnO}_3$ by the contact spectroscopy method; the critical temperature $T_c \approx 30$ K [206].

measurements were done on $\text{YBa}_2\text{Cu}_3\text{O}_{7-x}/\text{La}_{0.7}\text{Ca}_{0.3}\text{MnO}_3$ with $T_c \approx 30$ K [206]. Clearly, at $T < T_c$ in the region of the linear dependence on V , the asymmetric part $\Delta\sigma_d(V)$ of the conductivity depends only weakly on the temperature; such behavior agrees with (150). When $T > T_c$, the slope of the straight line sections of the $\Delta\sigma_d(V)$ diagrams decreases as the temperature increases; this behavior is described by Eq. (147). We conclude that the description of the universal behavior of $\Delta\sigma_d(V)$ based on the FCQPT is in good agreement with the results of the experiments presented in Figs. 52, 53, 54, 56, 58, and 59 and is valid for both high- T_c superconductors and heavy-fermion metals.

13. Violation of the Wiedemann-Franz law in HF metals

As early as in 1853, German physicists Gustav Wiedemann and Rudolph Franz [207] discovered the empirical law stating that for a metal at a constant temperature the ratio of its thermal conductivity $\kappa(T)$ to its electrical conductivity $\sigma(T)$ is a constant, $\kappa(T)/\sigma(T) = \text{const}$. Later on, the Danish physicist Ludvig Valentin Lorenz showed that the above ratio is proportional to the temperature T , $\kappa(T)/\sigma(T) = LT$, the proportionality constant L is known as the Lorenz number. What is called Wiedemann-Franz (WF) law is indeed an independence of the Lorenz number L on temperature. However, it was firmly established that the WF law is obeyed both at room temperatures and for low ones (several Kelvins); at the intermediate temperatures $L = L(T)$.

Strictly speaking, the Lorenz number is temperature-independent only at low temperatures; its theoretical value

$$L_0 = \lim_{T \rightarrow 0} \frac{\kappa(T)}{T\sigma(T)} = \frac{\pi^2 k_B}{3 e^2} \quad (151)$$

(k_B and e are Boltzmann constant and electron charge, respectively) had been calculated by Sommerfeld in 1927 [208] in the model of noninteracting electrons, obeying Fermi-Dirac statistics. The same result is obtained in LFL theory and reflects merely the fact that both thermal and electrical conductivities of a metal are determined by Landau quasiparticles. Due to this fact, possible deviations from the WF law can be regarded as a signature of NFL behavior in a sample.

Actually, Eq. (151) is usually referred to as the Wiedemann-Franz (WF) law. It was shown that at $T = 0$ Eq. (151) remains valid for arbitrarily strong scattering [209], disorder [210] and interactions [211]. This law holds for ordinary metals [212, 213, 214, 215] and does not hold for HF metals [31, 216, 217] CeNiSn and CeCoIn_3 , the electron-doped material [218] $\text{Pr}_{2-x}\text{Ce}_x\text{CuO}_{4-y}$, and the underdoped compound [219] $\text{YbBa}_2\text{Cu}_3\text{O}_y$. In CeNiSn , the experimental value

of the reduced Lorenz number $L(T)/L_0 \sim 1.5$ changes little at $T < 1$ K. This rules out the phonon contribution to the violation of the WF law. In the electron-doped compound $\text{Pr}_{2-x}\text{Ce}_x\text{CuO}_{4-y}$ the departure of $L(T)$ from L_0 at $T > 0.3$ K is also by more than unity and even larger [218] than that in CeNiSn . Other experimental tests of the WF law have been undertaken in the normal state of cuprate superconductors. The phase diagram of these compounds shows evolution from Mott insulator for undoped materials towards metallic Fermi liquid behavior for overdoped cases. Upward shift $L/L_0 \simeq 2 - 3$ was measured in underdoped cuprates at the lowest temperatures [218, 219, 220]. In strongly overdoped cuprates, the WF law was found to be obeyed perfectly [26].

The physical mechanism for the WF law violation is usually attributed to the NFL behavior like in Luttinger and Laughlin liquids [144, 145, 221, 222] or in the case of a marginal Fermi liquid [76]. Yet another possibility for the LFL theory and the WF law (151) violation occurs near QCPs where the effective mass M^* of a quasiparticle diverges. This is because at the QCP the Fermi liquid spectrum with finite Fermi velocity $v_F = p_F/M^*$ becomes meaningless as in this case $v_F \rightarrow 0$. In a standard scenario of the QCP [13, 18, 223] the divergence of the effective mass is attributed to the vanishing of the quasiparticle weight z in the single-particle states close to second-order phase transitions, implying that the quasiparticles disappear in this region. A conventional scenario of the WF law violation, associated with critical fluctuations in the vicinity of the second order phase transition, has recently been suggested in [224]. However, it has been shown in several works [6, 23, 24], that the standard scenario of the QCP is flawed so that to describe the deviations of L from the WF value L_0 , we apply a scenario of the QCP, where the NFL peculiarities are due to FCQPT. That is related to the rearrangement of the single-particle spectrum of strongly correlated electron liquid with the conservation of quasiparticle picture within the extended paradigm.

Therefore, to describe theoretically the violation of the WF law within the FCQPT formalism, it is sufficient to use the well-known LFL formulas for thermal and electrical conductivities with the substitution of the modified single particle spectrum into them. Such theory has been advanced in Refs. [225, 226]. The authors showed that close to the QCP the Lorenz number $L_{\text{QCP}}(T = 0) = 1.81 L_0$, i.e. almost two times larger than that from the LFL theory (151). This result agrees well with the experimental values [216, 218]. Furthermore, the dependence $L(T)/L_0$ has been calculated for two topologically distinct phases (see Section 15) - "iceberg" phase and FC phase [225, 226]. Theoretical calculations have shown that in both phases the largest departure from the WF law occurs near QCP [225, 226]. Deep in the "iceberg" phase we have the reentrance of the "classical" WF law in a sense that $L = L_0$ while in the deep FC phase the Lorenz number is temperature independent at low temperatures, but its value is slightly larger than L_0 . This is due to the particle-hole symmetry violation in FC phase [172, 197, 227].

Recently, the anisotropy of the WF law violation near the QCP has been experimentally observed in the HF metal CeCoIn_5 [217]. In that paper, the above HF compound has been studied experimentally in external magnetic fields, close to the critical value H_{c2} , suppressing the superconductivity. Under these conditions, the WF law was found to be violated. The violation is anisotropic and cannot be attributed to the standard scenario of quasiparticle collapse. At the same time, close to the QCP, sufficiently large external magnetic fields reveal the anisotropy of the electrical conductivities $\sigma_{ik} \propto \langle v_i v_k \rangle$ (v_i are the components of the group velocity vector) and thermal conductivities $\kappa_{ik} \propto \langle \varepsilon(\mathbf{p}) v_i v_k \rangle$ of a substance. This is because the magnetic field does not affect the z -components of the group velocity \mathbf{v} so that the QCP T -dependence of the transport coefficients holds, triggering the violation of the WF relation $L_{zz} = \sigma_{zz}/T\kappa_{zz} = \pi^2 k_B/3e^2$. On the other hand, the magnetic field \mathbf{B} alters substantially the electron motion in the perpendicular direction, yielding considerable increase of the x and y components of the group velocity so that the corresponding components L_{ik} do not depart from their WF value.

Therefore, the flattening of the single particle spectrum $\varepsilon(\mathbf{p})$ of strongly correlated electron systems considerably changes their transport properties, especially beyond the point of FCQPT due to breaking of the particle-hole symmetry. Also, in topologically different "iceberg" phases the WF law is also violated near its QCP. The results of theoretical [225] and experimental investigations demonstrate that the FCQPT scenario with further occurrence of both "iceberg" and FC phases give natural and universal explanation of the NFL changes of the transport properties of HF compounds and the WF law violation in particular.

14. The impact of FCQPT on ordinary continuous phase transitions in HF metals

The microscopic nature of quantum criticality determining the NFL behavior in strongly correlated fermion systems of different types is still unclear. Many puzzling and common experimental features of such seemingly different systems as two-dimensional (2D) electron systems and liquid ^3He as well as 3D heavy-fermion metals and high- T_c superconductors

suggest that there is a hidden fundamental law of nature, which remains to be recognized. To reveal this hidden law "the projection" of microscopic properties of the above materials on their observable, macroscopic characteristics is needed. One such "projections" is the impact of the FCQPT phenomenon on the ordinary phase transitions in HF metals. As we have seen in Subsection 10.3, the main peculiarity here is the continuous magnetic field evolution of the superconductive phase transition from the second order to the first one [171, 190, 192]. The same changing of the order is valid for magnetic phase transitions.

Exciting measurements on YbRh_2Si_2 at antiferromagnetic (AF) phase transition revealed a sharp peak in low-temperature specific heat, which is characterized by the critical exponent $\alpha = 0.38$ and therefore differs drastically from those of the conventional fluctuation theory of second order phase transitions [228], where $\alpha \simeq 0.1$ [156]. The obtained large value of α casts doubts on the applicability of the conventional theory and sends a real challenge for theories describing the second order phase transitions in HF metals [228], igniting strong theoretical effort to explain the violation of the critical universality in terms of the tricritical point [229, 230, 231, 232].

The striking feature of FCQPT is that it has profound influence on thermodynamically driven second order phase transitions provided that these take place in the NFL region formed by FCQPT. As a result, the curve of second order phase transitions passes into a curve of the first order ones at the tricritical point leading to a violation of the critical universality of the fluctuation theory. For example, as we have seen in Subsection 9.9 the second order superconducting phase transition in CeCoIn_5 changes to the first one in the NFL region. It is this feature that provides the key to resolve the challenge.

14.1. $T - B$ phase diagram for YbRh_2Si_2 versus one for CeCoIn_5

In Fig. 60, the T_{NL} line represents temperature $T_{NL}(B)/T_{N0}$ versus field B/B_{c0} in the schematic phase diagram for YbRh_2Si_2 , with $T_{N0} = T_{NL}(B = 0)$. There $T_{NL}(B)$ is the Néel temperature as a function of the magnetic field B . The solid and dashed curves indicate the boundary of the AF phase at $B/B_{c0} \leq 1$ [15]. For $B/B_{c0} \geq 1$, the dash-dot line marks the upper limit of the observed LFL behavior. This dash-dot line coming from Eq. (76) separates the NFL state and the weakly polarized LFL state, and in that case is represented by

$$\frac{T^*}{T_{NL}} = a_1 \sqrt{\frac{B}{B_{c0}} - 1}, \quad (152)$$

where a_1 is a parameter. We note that Eq. (152) is in good agreement with experimental facts [15]. Thus, YbRh_2Si_2 demonstrates two different LFL states, where the temperature-dependent electrical resistivity $\Delta\rho$ follows the LFL behavior $\Delta\rho \propto T^2$, one being weakly AF ordered ($B \leq B_{c0}$ and $T < T_{NL}(B)$) and the other being the weakly polarized ($B \geq B_{c0}$ and $T < T^*(B)$) [15]. At elevated temperatures and fixed magnetic field, during which the system moves along the vertical arrow shown in Fig. 60, the NFL state occurs which is separated from the AF phase by the curve T_{NL} of the phase transitions. Consistent with the experimental facts we assume that at relatively high temperatures $T/T_{NL}(B) \simeq 1$ the AF phase transition is of the second order [15, 228]. In that case, the entropy and the other thermodynamic functions are continuous functions at the line of the phase transitions T_{NL} shown in Fig. 60. This means that the entropy of the AF phase $S_{AF}(T)$ coincides with the entropy $S_{NFL}(T)$ of the NFL state. Since the AF phase demonstrates the LFL behavior, that is $S_{AF}(T \rightarrow 0) \rightarrow 0$, while $S_{NFL}(T)$ contains the temperature-independent term given by Eq. (27). Thus, in the NFL region formed by FCQPT Eq. (136) cannot be satisfied at diminishing temperatures and the second order AF phase transition inevitably becomes the first order one at the tricritical point with $T = T_{cr}$, as shown in Fig. 60. At $T = 0$, the heat of the transition $q = 0$ as was shown in Subsection 10.1, thus the critical field B_{c0} is determined by the condition that the ground state energy of the AF phase coincides with the ground state energy of the weakly polarized LFL, and the ground state of YbRh_2Si_2 becomes degenerate at $B = B_{c0}$. Therefore, the Néel temperature $T_{NL}(B \rightarrow B_{c0}) \rightarrow 0$. That means that at $T = 0$ the system moving along the horizontal arrow shown in Fig. 60 transits to its paramagnetic state when the applied magnetic field reaches its critical value $B = B_{c0}$, and becomes even higher $B = B_{c0} + \delta B$, where δB is an infinitesimal magnetic field increment, while the Hall coefficient experiences the jump as seen from Eq. (136) [233].

Upon comparing the phase diagram of YbRh_2Si_2 depicted in Fig. 60 with that of CeCoIn_5 shown in Fig. 31, it is possible to conclude that they are similar in many respects. Indeed, the line of the second order superconducting phase transitions changes to the line of the first ones at the tricritical point shown by the square in Fig. 31. This transition takes place under the application of magnetic fields $B > B_{c2} \geq B_{c0}$ (see Subsections 9.9 and 10.3), where B_{c2} is the critical field destroying the superconducting state, and B_{c0} is the critical field at which the magnetic field induced QCP takes place

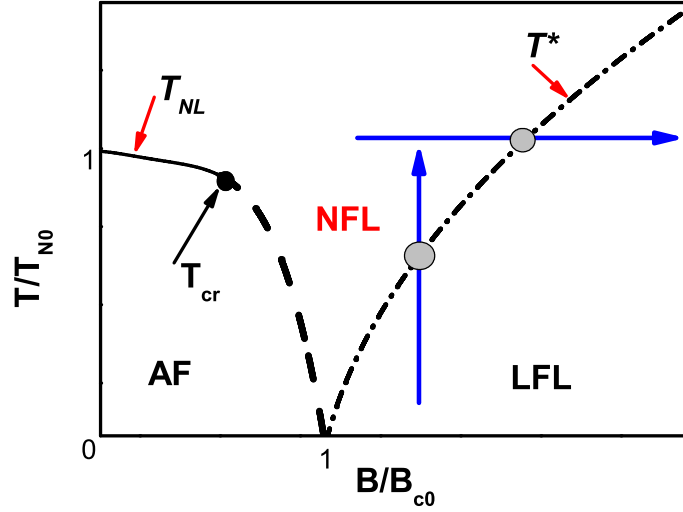


Figure 60: Schematic $T - B$ phase diagram for YbRh_2Si_2 . The solid and dashed T_{NL} curves separate the AF and NFL states representing the field dependence of the Néel temperature. The black dot at $T = T_{cr}$ shown by the arrow in the dashed curve is the tricritical point, at which the curve of second order AF phase transitions shown by the solid line passes into the curve of the first ones. At $T < T_{cr}$, the dashed line represents the field dependence of the Néel temperature when the AF phase transition is of the first order. The NFL state is characterized by the entropy S_0 given by Eq. (130). The dash-dot line separating the NFL state and the weakly polarized LFL state is represented by T^* given by Eq. (152). The horizontal solid arrow represents the direction along which the system transits from the NFL behavior to the LFL one at elevated magnetic field and fixed temperature. The vertical solid arrow represents the direction along which the system transits from the LFL behavior to the NFL one at elevated temperature and fixed magnetic field. The hatched circles depict the transition temperature T^* from the NFL to LFL behavior.

[171, 189]. We note that the superconducting boundary line $B_{c2}(T)$ at lower temperatures acquires the tricritical point due to Eq. (136) that cannot be satisfied at diminishing temperatures $T \leq T_{cr}$, i.e. the corresponding phase transition becomes first order [171]. This permits us to conclude that at lower temperatures, in the NFL region formed by FCQPT the curve of any second order phase transition passes into the curve of the first order one at the tricritical point.

14.2. The tricritical point in the $B - T$ phase diagram of YbRh_2Si_2

The Landau theory of the second order phase transitions is applicable as the tricritical point is approached, $T \simeq T_{cr}$, since the fluctuation theory can lead only to further logarithmic corrections to the values of the critical indices. Moreover, near the tricritical point, the difference $T_{NL}(B) - T_{cr}$ is a second order small quantity when entering the term defining the divergence of the specific heat [156]. As a result, upon using the Landau theory we obtain that the Sommerfeld coefficient $\gamma_0 = C/T$ varies as $\gamma_0 \propto |t-1|^{-\alpha}$ where $t = T/T_{NL}(B)$ with the exponent being $\alpha \simeq 0.5$ as the tricritical point is approached at fixed magnetic field [156]. We will see that $\alpha = 0.5$ gives a good description of the facts collected in measurements of the specific heat on YbRh_2Si_2 . Taking into account that the specific heat increases in going from the symmetrical to the asymmetrical AF phase [156], we obtain

$$\gamma_0(t) = A_1 + \frac{B_1}{\sqrt{|t-1|}}. \quad (153)$$

Here, $B_1 = B_{\pm}$ are the proportionality factors which are different for the two sides of the phase transition. The parameters $A_1 = A_{\pm}$, related to the corresponding specific heat $(C/T)_{\pm}$, are also different for the two sides, and “+” stands for $t > 1$, while “-” stands for $t < 1$.

The attempt to fit the available experimental data for $\gamma_0 = C(T)/T$ in YbRh_2Si_2 at the AF phase transition in zero magnetic fields [228] by the function (153) is reported in Fig. 61. We show there the normalized Sommerfeld coefficient γ_0/A_+ as a function of the normalized temperature $t = T/T_{N0}$. It is seen that the normalized Sommerfeld coefficient γ_0/A_+ extracted from C/T measurements on YbRh_2Si_2 [228] is well described in the entire temperature range around the AF phase transition by the formula (153) with $A_+ = 1$.

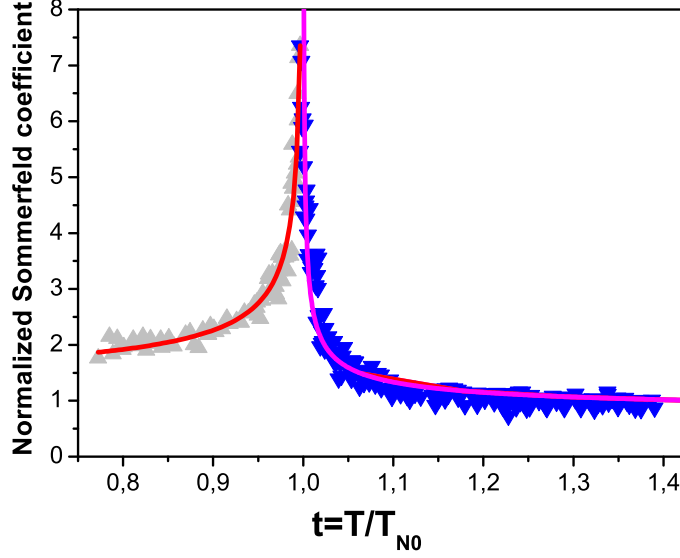


Figure 61: The normalized Sommerfeld coefficient γ_0/A_+ as a function of the normalized temperature $t = T/T_{N0}$ given by the formula (153) is shown by the solid curve. The normalized Sommerfeld coefficient is extracted from the facts obtained in measurements on YbRh_2Si_2 at the AF phase transition [228] and shown by the triangles.

Now transform Eq. (153) to the form

$$\frac{\gamma_0(t) - A_1}{B_1} = \frac{1}{\sqrt{|t-1|}}. \quad (154)$$

It follows from Eq. (154) that the ratios $(\gamma_0 - A_1)/B_1$ for $t < 1$ and $t > 1$ versus $|1 - t|$ collapse into a single line on logarithmic×logarithmic plot. The extracted from experimental facts [228] ratios are depicted in Fig. 62, the coefficients A_1 and B_1 are taken from fitting γ_0 shown in Fig. 61. It is seen from Fig. 62 that the ratios $(\gamma_0 - A_1)/B_1$ shown by the upward and downwards triangles for $t < 1$ and $t > 1$, respectively, do collapse into the single line shown by the solid straight line.

A few remarks are in order here. The good fitting shown in Figs. 61 and 62 of the experimental data by the functions (153) and (154) with the critical exponent $\alpha = 1/2$ allows us to conclude that the specific-heat measurements on YbRh_2Si_2 [228] are taken near the tricritical point and to predict that the second order AF phase transition in YbRh_2Si_2 changes to the first order under the application of magnetic field as it is shown by the arrow in Fig. 60 [184]. It is seen from Fig. 61 that at $t \simeq 1$ the peak is sharp, while one would expect that anomalies in the specific heat associated with the onset of magnetic order are broad [228, 234, 235]. Such a behavior represents fingerprints that the phase transition is to be changed to the first order one at the tricritical point, as it is shown in Fig. 60. As seen from Fig. 61, the Sommerfeld coefficient is larger below the phase transition than above it. This fact is in accord with the Landau theory that states that the specific heat increases when passing from $t > 1$ to $t < 1$ [156].

14.3. Entropy in YbRh_2Si_2 at low temperatures

It is instructive to analyze the evolution of magnetic entropy in YbRh_2Si_2 at low temperatures. We start with considering the derivative of magnetic entropy $dS(B, T)/dB$ as a function of magnetic field B at fixed temperature T_f when the system transits from the NFL behavior to the LFL one as shown by the horizontal solid arrow in Fig. 60. Such a behavior is of great importance since exciting experimental facts [161] on measurements of the magnetic entropy in YbRh_2Si_2 allow us to analyze the reliability of the theory employed and to study the scaling behavior of the entropy when the system is in its NFL, transition and LFL states, correspondingly.

The quantitative analysis of the scaling behavior of $dS(B, T)/dB$ is given in Subsection 9.4.4. Fig. 21 reports the normalized $(dS/dB)_N$ as a function of the normalized magnetic field. It is seen from Fig. 21 that our calculations shown by the solid line are in good agreement with the measurements and the scaled functions $(\Delta M/\Delta T)_N$ extracted from the experimental facts show the scaling behavior in a wide range variation of the normalized magnetic field B/B_M . The other

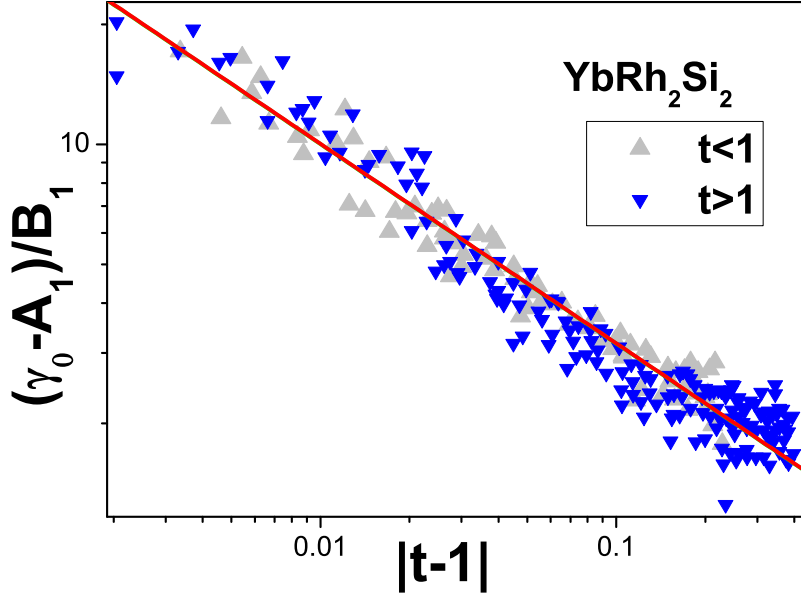


Figure 62: The temperature dependence of the ratios $(\gamma_0 - A_1)/B_1$ for $t < 1$ and $t > 1$ versus $|t - 1|$ given by the formula (154) is shown by the solid line. The ratios are extracted from the facts obtained in measurements of γ_0 on YbRh_2Si_2 at the AF phase transition [228] and depicted by the triangles as shown in the legend.

thermodynamic and transport properties of YbRh_2Si_2 analyzed in Subsection 9.4 are also in good agreement with the measurements. These developments make our analysis of the AF phase transition quite substantial.

Now we are in a position to evaluate the entropy S at temperatures $T \lesssim T^*$ in YbRh_2Si_2 . At $T < T^*$ the system is in its LFL state, the effective mass is independent of T , is a function of the magnetic field B . As a result, Eq. (73) reads

$$\frac{m}{M^*(B)} = a_2 \sqrt{\frac{B}{B_{c0}} - 1}, \quad (155)$$

where a_2 is a parameter. In the LFL state at $T < T^*$ when the system moves along the vertical arrow shown in Fig. 60, the entropy is given by the well-known relation, $S = M^* T \pi^2 / p_F^2 = \gamma_0 T$ [156]. Taking into account Eqs. (152) and (155) we obtain that at $T \approx T^*$ the entropy is independent of both the magnetic field and temperature, $S(T^*) \approx \gamma_0 T^* \approx S_0 \approx a_1 m T_{NL} \pi^2 / (a_2 p_F^2)$. Upon using the data [15], we obtain that for fields applied along the hard magnetic direction $S_0(B_{c0} \parallel c) \sim 0.03R \ln 2$, and for fields applied along the easy magnetic direction $S_0(B_{c0} \perp c) \sim 0.005R \ln 2$. Thus, as it follows from Fig. 42 and in accordance with the data collected on YbRh_2Si_2 [15] we conclude that the entropy contains the temperature-independent part S_0 [6, 79] which gives rise to the tricritical point.

To summarize this Section, we remark that a theory is an important tool in understanding what we observe; we have demonstrated that the obtained value of α is in good agreement with the specific-heat measurements on YbRh_2Si_2 and conclude that the critical universality of the fluctuation theory is violated at the AF phase transition since the second order phase transition is about to change to the first order one, making $\alpha \rightarrow 1/2$. We have also shown that in the NFL region formed by FCQPT the curve of any second order phase transitions passes into a curve of the first order ones at the tricritical point leading to the violation of the critical universality of the fluctuation theory. This change is generated by the temperature-independent entropy S_0 formed behind FCQPT.

15. Topological phase transitions related to FCQPT

We have now investigated the structure of the Fermi surface beyond QCP within the extended quasiparticle paradigm. We have shown that at $T = 0$ there is a scenario that entails the formation of FC, manifested by the emergence of a completely flat portion of the single-particle spectrum.

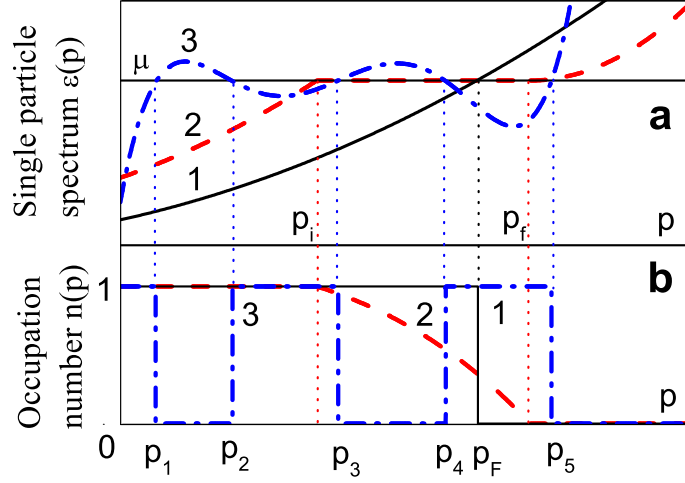


Figure 63: Schematic plot of the single particle spectrum $\varepsilon(p)$ (a) and occupation numbers $n(p)$ (b), corresponding to LFL (curves 1), FC (curves 2) and iceberg (curves 3) phases at $T = 0$. For LFL the equation, $\varepsilon(p) = \mu$, has a single root equal to Fermi momentum p_F . For iceberg phase, the above equation has countable set of the roots $p_1 \dots p_N \dots$, for FC phase the roots occupy the whole segment $(p_f - p_i)$. We note that $p_i < p_F < p_f$ and the states, where $\varepsilon(p) < \mu$ are occupied ($n=1$), while those with $\varepsilon(p) > \mu$ are empty ($n=0$).

In this Section we consider different kinds of instabilities of normal Fermi liquids relative to several perturbations of initial quasiparticle spectrum $\varepsilon(p)$ and occupation numbers $n(p)$ associated with the emergence of a multi-connected Fermi surface, see e.g. [23, 94, 95, 135, 137, 236]. Depending on the parameters and analytical properties of the Landau amplitude, such instabilities lead to several possible types of restructuring of initial Fermi liquid ground state. This restructuring generates topologically distinct phases. One of them is the FC discussed above, another one belongs to a class of topological transitions (TT) and will be called "iceberg" phase, where the sequence of rectangles ("icebergs") $n(p) = 0$ and $n(p) = 1$ is realized at $T = 0$.

In such considerations, we analyze stability of a fermion system with model repulsive Landau amplitude allowing us to carry out an analytical consideration of the emergence of a multi-connected Fermi surface [94, 95]. We show, in particular, that the Landau amplitude given by the screened Coulomb law does not generate FC phase, but rather iceberg TT phase. For this model, we plot a phase diagram in the variables "screening parameter - coupling constant" displaying two kinds of TT: a $5/2$ -kind similar to the known Lifshitz transitions in metals, and a 2-kind characteristic for a uniform strongly interacting system.

The common ground state of isotropic LFL with density ρ_x is described at zero temperature by the stepwise Fermi function $n_F(p) = \theta(p_F - p)$, dropping discontinuously from 1 to 0 at the Fermi momentum p_F . The LFL theory states that the quasiparticle distribution function $n(p)$ and its single particle spectrum $\varepsilon(p)$ are in all but name similar to those of an ideal Fermi gas with the substitution of real fermion mass m by the effective one M^* [19]. These $n_F(p)$ and $\varepsilon(p)$ can become unstable under several circumstances. The best known example is Cooper pairing at arbitrarily weak attractive interaction with subsequent formation of the pair condensate and gapped quasiparticle spectrum [78]. However, a sufficiently strong repulsive Landau amplitude can also generate non-trivial ground states. The first example of such restructuring for a Fermi system with model repulsive interaction is FC [41]. It reveals the existence of a critical value α_{cr} of the interaction constant α such that at $\alpha = \alpha_{cr}$ the stability criterion $s(p) = (\varepsilon(p) - E_F)/(p^2 - p_F^2) > 0$ fails at the Fermi surface $s(p_F) = 0$ (p_F -instability). We recall that in the case of this instability the single particle spectrum $\varepsilon(p)$ possesses the inflection point at the Fermi surface, see Subsection 9.3.1. Then at $\alpha > \alpha_{cr}$ an exact solution of a variational equation for $n(p)$ (following from the Landau functional $E(n(p))$) exists, exhibiting some finite interval $(p_f - p_i)$ around p_F where the distribution function $n(p)$ varies continuously taking intermediate values between 1 and 0, while the single-particle excitation spectrum $\varepsilon(p)$ has a flat plateau. Equation (21) means actually that the roots of the equation $\varepsilon(p) = \mu$ form an uncountable set in the range $p_i \leq p \leq p_f$, see Fig. 63. It is seen from Eq. (21) that the occupation numbers $n(p)$ become variational parameters, deviating from the Fermi step function to minimize the energy E .

The other type of phase transition the so-called iceberg phase occurs when the equation $\varepsilon(p) = \mu$ has discrete countable number of roots, either finite or infinite. This is reported on Fig. 63 and related to the situation when the Fermi surface becomes multi-connected. Note that the idea of multi-connected Fermi surface, with the production of new, interior segments, had already been considered [135, 136, 137].

Let us take the Landau functional $E(n(p))$ of the form

$$E(n(p)) = \int \frac{p^2}{2M} n(p) \frac{d\mathbf{p}}{(2\pi)^3} + \frac{1}{2} \int \int n(p) U(|\mathbf{p} - \mathbf{p}'|) n(p') \frac{d\mathbf{p}d\mathbf{p}'}{(2\pi)^6}, \quad (156)$$

which, by virtue of Eq. (3), leads to derivation of the quasiparticle dispersion law:

$$\varepsilon(p) = \frac{p^2}{2M} + \int U(|\mathbf{p} - \mathbf{p}'|) n(p') \frac{d\mathbf{p}'}{(2\pi)^3}. \quad (157)$$

The angular integration with subsequent change to the dimensionless variables $x = p/p_F$, $y = y(x) = 2M\varepsilon(p)/p_F^2$, $z = 2\pi^2 ME/p_F^5$, leads to simplification of the equations (156) and (157)

$$z[\nu(x)] = \int [x^4 + \frac{1}{2}x^2 V(x)] \nu(x) dx, \quad (158)$$

$$y(x) = x^2 + V(x), \quad (159)$$

where

$$V(x) = \frac{1}{x} \int x' \nu(x') u(x, x') dx',$$

$$u(x, x') = \frac{M}{\pi^2 p_F} \int_{|x-x'|}^{x+x'} u(t) dt. \quad (160)$$

Here $u(x) \equiv U(p_F x)$ and the distribution function $\nu(x) \equiv n(p_F x)$ is positive, obeys the normalization condition

$$\int x^2 \nu(x) dx = 1/3, \quad (161)$$

and the Pauli principle limitation $\nu(x) \leq 1$. The latter can be lifted using, e.g., the ansatz: $\nu(x) = [1 + \tanh \eta(x)]/2$. In the latter case the system ground state gives a minimum to the functional

$$f[\eta(x)] = \int [1 + \tanh \eta(x)] \{x^4 - \mu x^2 + x' [1 + \tanh \eta(x')] u(x, x')\} dx, \quad (162)$$

containing a Lagrange multiplier μ , with respect to an arbitrary variation of the auxiliary function $\eta(x)$. This allows us to represent the necessary condition of extremum $\delta f = 0$ in the form

$$x^2 \nu(x) [1 - \nu(x)] [y(x) - \mu] = 0. \quad (163)$$

This means that either $\nu(x)$ takes only the values 0 and 1 or the dispersion law is flat: $y(x) = \mu$ [41], in accordance with Eq. (21). The former possibility corresponds to iceberg phase, while the latter to FC. As it is seen from Eq. (21), the spectrum $\varepsilon(p)$ in this case cannot be an analytic function of complex p in any open domain, containing the FC interval $(p_f - p_i)$. In fact, all the derivatives of $\varepsilon(p)$ with respect to p along the strip $(p_f - p_i)$ should be zero, while this is not the case outside $(p_f - p_i)$. For instance, in the FC model with $U(p) = U_0/p$ [41] the kernel, Eq. (160), is non-analytic

$$u(x, x') = \frac{MU_0}{\pi^2 p_F} (x + x' + |x - x'|), \quad (164)$$

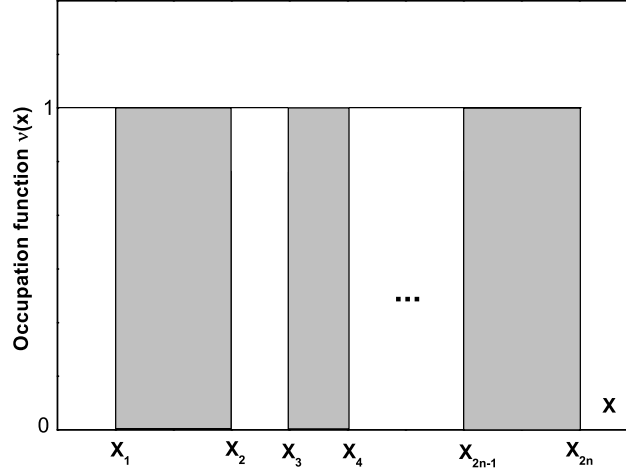


Figure 64: Occupation function for a multiconnected distribution.

which eventually causes non-analyticity of the potential $V(x)$. It follows from Eq. (159), that the single particle spectrum is an analytic function on the whole real axis if $V(x)$ is such a function. In this case FC is forbidden and the only alternative to the Fermi ground state (if the stability criterion gets broken) is iceberg phase corresponding to TT between the topologically unequal states with $\nu(x) = 0, 1$ [73].

On the other hand, applying the technique of Poincaré mapping, it is possible to analyze the sequence of iterative maps generated by Eq. (13) for the single-particle spectrum at zero temperature [23]. If the sequence of maps converges, the multi-connected Fermi surface is formed. If it fails to converge, the Fermi surface swells into a volume that provides a measure of entropy associated with the formation of an exceptional state of the system characterized by partial occupation of single-particle states and dispersion of their spectrum proportional to temperature as seen from Eq. (31).

Generally, all such states related to the formation of iceberg phases are classified by the indices of connectedness (known as Betti numbers in algebraic topology [237, 238]) for the support of $\nu(x)$. In fact, for an isotropic system, these numbers simply count the separate (concentric) segments of the Fermi surface. Then the system ground state corresponds to the following multi-connected distribution shown in Fig. 64

$$\nu(x) = \sum_{i=1}^n \theta(x - x_{2i-1})\theta(x_{2i} - x), \quad (165)$$

where the parameters $0 \leq x_1 < x_2 < \dots < x_{2n}$ obey the normalization condition

$$\sum_{i=1}^n (x_{2i}^3 - x_{2i-1}^3) = 1. \quad (166)$$

The function z , Eq. (158),

$$z = \frac{1}{2} \sum_{i=1}^n \int_{x_{2i-1}}^{x_{2i}} x^2 [x^2 + y(x)] dx, \quad (167)$$

has the absolute minimum with respect to x_1, \dots, x_{2n-1} and to $n \geq 1$. To obtain the necessary condition of extremum, we use the relations

$$\frac{\partial x_{2n}}{\partial x_k} = (-1)^{k-1} \left(\frac{x_k}{x_{2n}} \right)^2, \quad 1 \leq k \leq 2n - 1, \quad (168)$$

following from Eq. (166) and the dependence of the potential $V(x)$ in the dispersion law $y(x)$ on the parameters x_1, \dots, x_{2n-1}

$$V(x) = \frac{1}{x} \sum_{i=1}^n \int_{x_{2i-1}}^{x_{2i}} x' u(x, x') dx'. \quad (169)$$

Subsequent differentiation of Eq. (167) with respect to the parameters x_1, \dots, x_{2n-1} and the use of Eqs. (168) and (169) yield the necessary conditions of extremum in the following form

$$\frac{\partial z}{\partial x_k} = (-1)^k x_k^2 [y(x_k) - y(x_{2n})] = 0, \quad 1 \leq k \leq 2n - 1. \quad (170)$$

This means that a multi-connected ground state is controlled by the evident rule of unique Fermi level $y(x_k) = y(x_{2n})$ for all $1 \leq k \leq 2n - 1$ (except for $x_1 = 0$). In principle, given the dispersion law $y(x)$ all the $2n - 1$ unknown parameters x_k can be found from Eq. (170). Then, the sufficient stability conditions $\partial^2 z / \partial x_i \partial x_j = \gamma_i \delta_{ij}$, $\gamma_i > 0$ generate the generalized stability criterion. Namely, the dimensionless function

$$\sigma(x) = 2Ms(p) = \frac{y(x) - y(x_{2n})}{x^2 - x_{2n}^2}, \quad (171)$$

should be positive within filled and negative within empty intervals, turning to zero at their boundaries in accordance with Eq. (170). It can be proved rigorously that, for given analytic kernel $u(x, x')$, Eq. (171) uniquely defines the system ground state.

In what follows we shall label each multi-connected state, Eq. (165), by an entire number related to the binary sequence of empty and filled intervals read from x_{2n} to 0. Thus, the Fermi state with a single filled interval ($x_2 = 1, x_1 = 0$) reads as unity, the state with a void at the origin (filled $[x_2, x_1]$ and empty $[x_1, 0]$) reads as (10) = 2, the state with a single gap: (101) = 3, etc. Note that all even phases have a void at the origin and odd phases have not.

For free fermions $V(x) = 0$, $y(x) = x^2$, Eq. (170) only yields the trivial solution corresponding to the Fermi state 1. To obtain non-trivial realizations of TT, we choose $U(p)$ to correspond to the common screened Coulomb potential:

$$U(p) = \frac{4\pi e^2}{p^2 + p_0^2}. \quad (172)$$

The related explicit form of the kernel,

$$u(x, x') = \alpha \ln \frac{(x + x')^2 + x_0^2}{(x - x')^2 + x_0^2}, \quad (173)$$

with the dimensionless screening parameter $x_0 = p_0/p_F$ and the coupling constant $\alpha = 2Me^2/\pi p_F$, evidently displays the necessary analytical properties for existence of iceberg phase. Equations (169) and (173) permit to express the potential $V(x)$ in elementary functions [94]. Then, the straightforward analysis of Eq. (170) shows that their nontrivial solutions appear only when the coupling parameter α exceeds a certain critical value α^* . This corresponds to the situation when the stability criterion [41] $\sigma(x) = (y_F(1) - y_F(x))/(1 - x^2) > 0$ calculated with the Fermi distribution, $y_F(x) = x^2 + V(x; 0, 1)$, fails in a certain point $0 \leq x_i < 1$ within the Fermi sphere: $\sigma(x_i) \rightarrow 0$. There are two different types of such instabilities depending on the screening parameter x_0 (Fig. 65). For x_0 below a certain threshold value $x_{th} \approx 0.32365$ (weak screening regime, WSR) the instability point x_i sets rather close to the Fermi surface: $1 - x_i \ll 1$, while it drops abruptly to zero at $x_0 \rightarrow x_{th}$ and equals zero for all $x_0 > x_{th}$ (strong screening regime, SSR). The critical coupling $\alpha^*(x_0)$ results in a monotonously growing function of x_0 with the asymptotic $\alpha^* \approx (\ln 2/x_0 - 1)^{-1}$ at $x_0 \rightarrow 0$ and staying analytic at $\alpha_{th} = \alpha^*(x_{th}) \approx 0.91535$, where it only exhibits an inflection point.

These two types of instabilities give rise to different types of TT from the state 1 at $\alpha > \alpha^*$: at SSR a void appears around $x = 0$ (1 \rightarrow 2 transition), and at WSR a gap opens around x_i (1 \rightarrow 3 transition). Further analysis of Eq. (170) shows that the point x_{th}, α_{th} represents a triple point in the phase diagram in the variables x_0, α (Fig. 65) where the phases 1, 2, and 3 meet one another. Similarly to the onset of instability in the Fermi state 1, each evolution of TT to higher order phases with growing α is manifested by a zero of $\sigma(x)$, Eq. (171), at some point $0 \leq x_i < x_{2n}$ different from the existing interfaces. If this occurs at the very origin, $x_i = 0$, the phase number rises at TT by 1, corresponding

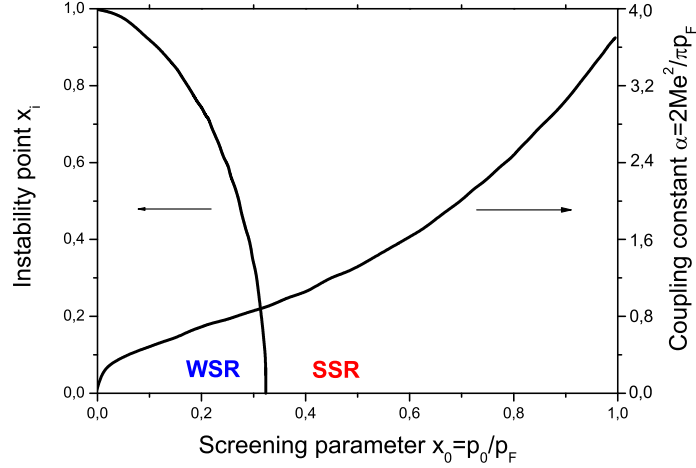


Figure 65: Instability point x_i and critical coupling α^* as functions of screening. The regions of weak screening (WSR) and strong screening (SSR) are separated by the threshold value x_{th} . Note that a x_{th} , α_{th} is the triple point between the phases 1, 2, 3 in Fig. 66.

to the opening of a void (passing from odd to even phase) or to emerging "island" (even \rightarrow odd). For $x_i > 0$, either a thin spherical gap opens within a filled region or a thin filled spherical sheet emerges within a gap, so that the phase number rises by 2, leaving the parity unaltered. A part of the whole diagram shown in Fig. 66 demonstrates that with decreasing of x_0 (screening weakening) all even phases terminate at certain triple points. This, in particular, agrees with numerical studies of the considered model along the line $x_0 = 0.07$ at growing α [137], where only the sequence of odd phases $1 \rightarrow 3 \rightarrow 5 \rightarrow \dots$ has been revealed (shown by the arrow in Fig. 65). The energy gain $\Delta(\tau)$ at TT as a function of small parameter $\tau = \alpha/\alpha^* - 1$ is evidently proportional to τ times the volume of a new emerging phase region (empty or filled). Introducing a void radius δ and expanding the energy gain $\Delta(\delta) = z[n(x, \delta)] - z[n_F(x)]$ in δ , one gets $\Delta = -\beta_1 \tau \delta^3 + \beta_2 \delta^5 + O(\delta^6)$, $\beta_1, \beta_2 > 0$. As a result, the optimum void radius is $\delta \sim \sqrt{\tau}$. Consequently we have $\Delta(\tau) \sim \tau^{5/2}$ indicating a resemblance to the known " $5/2$ -kind" phase transitions in the theory of metals [237]. The peculiar feature of our situation is that the new segment of the Fermi surface opens at very small momentum values, which can dramatically change the system response to, e.g., electron-phonon interaction. On the other hand, this segment may have a pronounced effect on the thermodynamical properties of ^3He at low temperatures, especially in the case of P -pairing, producing excitations with extremely small momenta.

For a TT with unchanged parity, the width of a gap (or a sheet) is found to be $\sim \tau$ so that the energy gain is $\Delta(\tau) \sim \tau^2$ and such TT can be related to the second kind. It follows from the above consideration that each triple point in the $x_0 - \alpha$ phase diagram is a point of confluence of two $5/2$ -kind TT lines into one 2-kind line. The latter type of TT has already been discussed in the literature [135, 137]. Here we only mention that its occurrence on a whole continuous surface in the momentum space is rather specific for systems with strong fermion-fermion interaction, while the known TT's in metals, under the effects of crystalline field, occur typically at separate points in the quasi-momentum space. It is interesting to note that in the limit $x_0 \rightarrow 0, \alpha \rightarrow 0$, reached along a line $\alpha = kx_0$, we attain the exactly solvable model: $U(p) \rightarrow (2\pi)^3 U_0 \delta(p)$ with $U_0 = k/(2Mp_F)$, which is known to display FC at all $U_0 > 0$ [41]. The analytic mechanism of this behavior is the disappearance of the poles of $U(p)$, Eq. (172), as $p_0 \rightarrow 0$, restoring the analytical properties necessary for FC. Otherwise, the FC regime corresponds to the phase order $\rightarrow \infty$, when the density of infinitely thin filled (separated by empty) regions approaches some continuous function $0 < \nu(x) < 1$ [137] and the dispersion law turns flat according to Eq. (170). A few remarks should be made at this point.

First, the considered model formally treats x_0 and α as independent parameters, though in fact a certain relation between them can be imposed. Under such restriction, the system ground state should depend on a single parameter, say the particle density ρ_x , along a certain trajectory $\alpha(x_0)$ in the above suggested phase diagram. For instance, with the

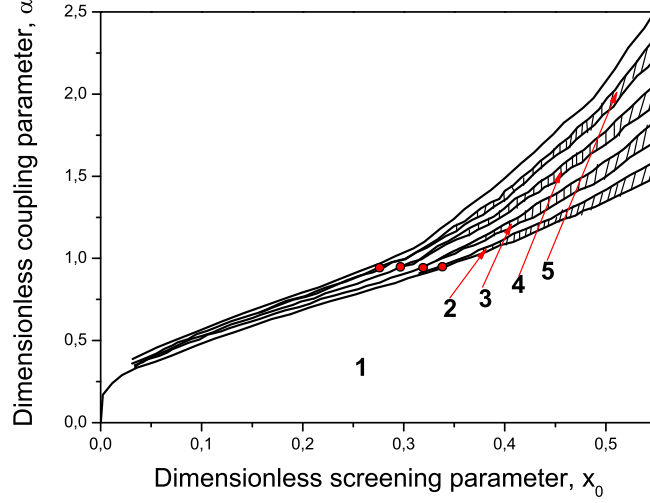


Figure 66: Phase diagram in variables “screening-coupling”. Each phase with certain topology is labeled by the total number of filled and empty regions (see Fig. 64). Even phases (shaded) are separated from odd ones by “ $5/2$ -kind” topological transition (TT) lines, while 2-kind TT lines separate odd phases. Triple points, where two $5/2$ -TT and one 2-TT meet, are shown by circles.

simplest Thomas-Fermi relation for a free electron gas $\alpha(x_0) = x_0^2/2$, this trajectory stays fully within the Fermi state 1 over all the physically reasonable range of densities. Hence a faster growth of $\alpha(x_0)$ is necessary for realization of TT in any fermionic system with the interaction, Eq. (172).

Second, at increasing temperatures, the stepwise form of the quasiparticle distribution is melting. Therefore, as temperature moves away from its zero value, the concentric Fermi spheres are taken up by FC. In fact, these arguments do not work in the case of a few icebergs. Thus, it is quite possible to observe the two separate Fermi sphere regimes related to the FC and iceberg states.

There is a good reason to mention that neither in the FC phase nor in the other TT phases, the standard Kohn-Sham scheme [239, 240] is no longer valid. This is because in the systems with FC or TT phase transitions the occupation numbers of quasiparticles are indeed variational parameters. Thus, to get a reasonable description of the system, one has to consider the ground state energy as a functional of the occupation numbers $E[(n(p))]$ rather than a functional of the density $E[\rho_x]$ [55, 56, 57].

16. Conclusions

In this review, we have described the effect of FCQPT on the properties of various Fermi systems and presented substantial evidence in favor of the existence of such a transition. We have demonstrated that FCQPT supporting the extended quasiparticle paradigm forms strongly correlated Fermi systems with their unique NFL behavior. Vast body of experimental facts gathered in studies of various materials, such as high- T_c superconductors, heavy-fermion metals, and correlated 2D Fermi liquids, can be explained by a theory based on the concept of FCQPT.

We have established that the physics of systems with heavy fermions is determined by the extended quasiparticle paradigm. In contrast to the stated Landau paradigm that the quasiparticle effective mass is a constant, within the extended quasiparticle paradigm the effective mass of new quasiparticles strongly depends on the temperature, magnetic field, pressure, and other parameters. The quasiparticles and the order parameter are well defined and can be used to describe the scaling behavior of the thermodynamic, relaxation and transport properties of high- T_c superconductors, HF metals, 2D electronic and ^3He systems and other correlated Fermi systems. The quasiparticle system determines the conservation of the Kadowaki-Woods relation and the restoration of the LFL behavior under the application of magnetic fields.

We have also shown both analytically and using arguments based entirely on the experimental grounds that the data collected on very different strongly correlated Fermi systems reveal their universal scaling behavior. This is because all above experimental quantities are indeed proportional to the normalized effective mass exhibiting the scaling behavior. Since the effective mass determines the thermodynamic, transport and relaxation properties, we conclude again that HF metals placed near their QCP demonstrate the same scaling behavior, independent of the details of HF metals such as their lattice structure, magnetic ground state, dimensionality etc. In other words, materials with strongly correlated fermions can unexpectedly be uniform despite their prominent diversity.

We have also shown that in finite magnetic fields, in the NFL region formed by FCQPT the curve of any second order phase transitions passes into a curve of the first order ones at the tricritical point leading to the violation of the critical universality of the fluctuation theory. This change is generated by the temperature-independent term of the entropy formed behind FCQPT. The quantum and thermal critical fluctuations corresponding to second-order phase transitions disappear and have no effect on the behavior of the system at low temperatures, and the low temperature thermodynamics of heavy-fermion metals is determined by quasiparticles.

We have found that the differential conductivity between a metal point contact and a HF metal or a high- T_c superconductor can be highly asymmetric as a function of the applied voltage. This asymmetry is observed when a strongly correlated metal is in its normal or superconducting state. We have shown that the application of magnetic field restoring the LFL behavior suppresses the asymmetry. Correspondingly, we conclude that the particle-hole symmetry is macroscopically broken in the absence of applied magnetic fields, while the application of magnetic fields restores both the LFL state and the particle-hole symmetry. The above features determine the universal behavior of strongly correlated Fermi systems and are related to the anomalous low-temperature behavior of the entropy, which contains the temperature independent term.

In the future, the realm of problems should be broadened and certain efforts should be made to describe the other macroscopic features of FCQPT, such as the propagation of zero-sound, sonic and shock waves. In addition to the already known materials whose properties not only provide information on the existence of FC but also almost cry aloud for such a condensate, there are other materials of enormous interest which could serve as possible objects for studying the phase transition in question. Among such objects are neutron stars, atomic clusters, ultra cold gases in traps, nuclei, and quark plasma. Another possible area of research is related to the structure of the nucleon, in which the entire "sea" of non-valence quarks may be in FCQPT. The combination of quarks and the gluons that hold them together is especially interesting because gluons, quite possibly, can be in the gluon-condensate phase, which could be qualitatively similar to the pion condensate proposed by A.B. Migdal long ago. We believe that FC can be observed in traps, where there is the possibility of controlling the emergence of a quantum phase transition accompanied by the formation of FCQPT by changing the particle number density.

Overall, the ideas associated with a new phase transition in one area of research stimulates intensive studies of the possible manifestation of such a transition in other areas. This has happened in the case of metal superconductivity, whose ideas were successfully used in describing atomic nuclei and in a possible explanation of the origin of the mass of elementary particles. This, quite possibly, could be the case with FCQPT.

Finally, our general discussion shows that FCQPT develops unexpectedly simple, yet completely good description of the NFL behavior of strongly correlated Fermi systems, while the extended quasiparticle paradigm constitute the properties inherent in strongly correlated fermion systems. Moreover, the extended paradigm can be considered as the universal reason for the NFL behavior observed in various HF metals, liquids, and other Fermi systems.

Acknowledgments

We grateful to V.A. Khodel and V.A. Stephanovich for valuable discussions. This work was partly supported by the RFBR # 09-02-00056 and U.S. DOE, Division of Chemical Sciences, Office of Basic Energy Sciences, Office of Energy Research.

References

- [1] G.R. Stewart, *Rev. Mod. Phys.* 73 (2001) 797-855.
- [2] C.M. Varma, Z. Nussionov, W. van Saarloos, *Phys. Rep.* 361 (2002) 267-417.
- [3] H. v. Löhneysen, A. Rosch, M. Vojta, P. Wölfle, *Rev. Mod. Phys.* 79 (2007) 1015-1076.

- [4] M. Vojta, Rep. Prog. Phys. 66 (2003) 2069-2110.
- [5] V.I. Belyavsky, Yu.K. Kopaev, Usp. Fiz. Nauk, 176 (2006) 457-485, [Phys. Usp. 49 (2006) 441-469].
- [6] V.R. Shaginyan, M.Ya. Amusia, K.G. Popov, Usp. Fiz. Nauk 177 (2007) 586-618, [Phys. Usp. 50 (2007) 563-595].
- [7] J. Custers, P. Gegenwart, H. Wilhelm, K. Neumaier, Y. Tokiwa, O. Trovarelli, C. Geibel, F. Steglich, C. Pépin, P. Coleman, Nature 424 (2003) 524-527.
- [8] T. Senthil, M.P.A. Fisher, Phys. Rev. B 62 (2000) 7850-7881.
- [9] T. Senthil, M. Vojta, S. Sachdev, Phys. Rev. B 69 (2004) 035111-035129.
- [10] T. Senthil, S. Sachdev, M. Vojta, Physica B 359-361 (2005) 9-14.
- [11] T. Senthil, A. Vishwanath, L. Balents, S. Sachdev, M.P.A. Fisher, Science 303 (2004) 1490-1513.
- [12] P. Coleman, Lectures on the Physics of Highly Correlated Electron Systems VI, in: F. Mancini (Ed.), American Institute of Physics, New York, 2002, pp. 79-160.
- [13] P. Coleman, A.J. Schofield, Nature 433 (2005) 226-229.
- [14] R. Küchler, N. Oeschler, P. Gegenwart, T. Cichorek, K. Neumaier, O. Tegus, C. Geibel, J. A. Mydosh, F. Steglich, L. Zhu, Q. Si, Phys. Rev. Lett. 91 (2003) 066405-066408.
- [15] P. Gegenwart, J. Custers, C. Geibel, K. Neumaier, T. Tayama, K. Tenya, O. Trovarelli, F. Steglich, Phys. Rev. Lett. 89 (2002) 056402-056405.
- [16] N.E. Hussey, Nature Phys. 3 (2007) 445-446.
- [17] P. Gegenwart, T. Westerkamp, C. Krellner, Y. Tokiwa, S. Paschen, C. Geibel, F. Steglich, E. Abrahams, Q. Si, Science 315 (2007) 969-971.
- [18] P. Coleman, C. Pépin, Q. Si, R. Ramazashvili, J. Phys. Condens. Matter 13 (2001) R723-R738.
- [19] L.D. Landau Zh. Eksp. Teor. Fiz. 30 (1956) 1058-1066; [Sov. Phys. JETP 3 (1956) 920-928].
- [20] E.M. Lifshitz, L.P. Pitaevskii, Statisticheskaya Fizika (Statistical Physics), Pt. 2, Nauka, Moscow, 1978; Translated into English, Pergamon Press, Oxford, 1980.
- [21] D. Pines, P. Nozières, Theory of Quantum Liquids, Benjamin, New York, 1966.
- [22] V.R. Shaginyan, J.G. Han, J. Lee, Phys. Lett. A 329 (2004) 108-115.
- [23] V.A. Khodel, J.W. Clark, and M.V. Zverev, Phys. Rev. B 78 (2008) 075120-075137.
- [24] V.A. Khodel, JETP Lett. 86 (2007) 721-726.
- [25] P. Coleman, <http://arxiv.org/abs/cond-mat/1001.0185v1> (2010) 1-9.
- [26] C. Proust, E. Boaknin, R. W. Hill, L. Taillefer, A. P. Mackenzie, Phys. Rev. Lett. 89 (2002) 147003-147006.
- [27] K. Kadowaki, S.B. Woods, Solid State Commun. 58 (1986) 507-509.
- [28] A.J. Millis, A.J. Schofield, G.G. Lonzarich, S.A. Grigera, Phys. Rev. Lett. 88 (2002) 217204-217207.
- [29] R. Bel, K. Behnia, Y. Nakajima, K. Izawa, Y. Matsuda, H. Shishido, R. Settai, Y. Onuki, Phys. Rev. Lett. 92 (2004) 217002-217005.
- [30] J. Paglione, M.A. Tanatar, D.G. Hawthorn, E. Boaknin, R.W. Hill, F. Ronning, M. Sutherland, L. Taillefer, C. Petrovic, P.C. Canfield, Phys. Rev. Lett. 91 (2003) 246405-246408.
- [31] J. Paglione, M.A. Tanatar, D.G. Hawthorn, F. Ronning, R.W. Hill, M. Sutherland, L. Taillefer, C. Petrovic, Phys. Rev. Lett. 97 (2006) 106606-106609.
- [32] F. Ronning, R.W. Hill, M. Sutherland, D.G. Hawthorn, M.A. Tanatar, J. Paglione, L. Taillefer, M.J. Graf, R. S. Perry, Y. Maeno, A.P. Mackenzie, Phys. Rev. Lett. 97 (2006) 067005-067008.
- [33] F. Ronning, C. Capan, E.D. Bauer, J.D. Thompson, J.L. Sarrao, R. Movshovich, Phys. Rev. B 73 (2006) 064519-064522.
- [34] J.D. Koralek, J.F. Douglas, N.C. Plumb, Z. Sun, A.V. Fedorov, M.M. Murnane, H.C. Kapteyn, S.T. Cundiff, Y. Aiura, K. Oka, H. Eisaki, D.S. Dessau, Phys. Rev. Lett. 96 (2006) 017005-017008.
- [35] S. Fujimori, A. Fujimori, K. Shimada, T. Narimura, K. Kobayashi, H. Namatame, M. Taniguchi, H. Harima, H. Shishido, S. Ikeda, D. Aoki, Y. Tokiwa, Y. Haga, Y. Onuki, Phys. Rev. B 73 (2006) 224517-224521.
- [36] N. Oeschler, S. Hartmann, A.P. Pikul, C. Krellner, C. Geibel, F. Steglich, Physica B 403 (2008) 1254-1256.
- [37] P. Gegenwart, T. Westerkamp, C. Krellner, M. Brandt, Y. Tokiwa, C. Geibel, F. Steglich, Physica B 403 (2008) 1184-1188.
- [38] V.R. Shaginyan, M.Ya. Amusia, K.G. Popov, Phys. Lett. A 373 (2009) 2281-2286.
- [39] V.R. Shaginyan, M.Ya. Amusia, K.G. Popov, S.A. Artamonov, JETP Lett. 90 (2009) 47-54.
- [40] V.R. Shaginyan, A.Z. Msezane, K.G. Popov, V.A. Stephanovich, Phys. Rev. Lett. 100 (2008) 096406-096409.
- [41] V.A. Khodel, V.A. Shaginyan, Pis'ma Zh. Eksp. Teor. Fiz. 51 (1990) 488-490 [JETP Lett. 51 (1990) 553-555].
- [42] V.A. Khodel, V.A. Shaginyan, V.V. Khodel, Phys. Rep. 249 (1994) 1-134.
- [43] V.A. Khodel, J.W. Clark, M.V. Zverev, Phys. Rev. Lett. 87 (2001) 031103-031106.
- [44] M.Ya. Amusia, A.Z. Msezane, V.R. Shaginyan, Physics of Atomic Nuclei 66 (2003) 1850-1875.
- [45] V.A. Khodel, J.W. Clark, Li. Hoachen, M.A. Zverev, Pisma v ZHETF 84 (2006) 703-707.
- [46] G.E. Volovik, Acta Phys. Slov. 56 (2006) 49-56.
- [47] G.E. Volovik, in Quantum Analogues: From Phase Transitions to Black Holes and Cosmology, eds. William G. Unruh and R. Schutzhold, Springer Lecture Notes in Physics, 718, 2007, pp. 31-73.
- [48] V.A. Khodel, J.W. Clark, H. Li, M.V. Zverev, Phys. Rev. Lett. 98 (2007) 216404-216407.
- [49] V.R. Shaginyan, Pis'ma Zh. Eksp. Teor. Fiz. 79 (2004) 344-350; [JETP Lett. 79 (2004) 286-292].
- [50] I.Yu. Pomeranchuk, Zh. Eksp. Teor. Fiz. 35 (1958) 524-526; [Sov. Phys. JETP 8 (1959) 361-363].
- [51] J. Dukelsky, V.A. Khodel, P. Schuck, V.R. Shaginyan, Z. Phys. 102 (1997) 245-254.
- [52] V.A. Khodel, V.R. Shaginyan, in: J. Clark, V.P. Plant (Eds.), Condensed Matter Theories 12, Nova Science Publishers Inc., NY, 1997, pp. 221-236.
- [53] J.W. Clark, V.A. Khodel, M.V. Zverev, Phys. Rev. B 71 (2005) 012401-012404.
- [54] L.N. Oliveira, E.K.U. Gross, W. Kohn, Phys. Rev. Lett. 60 (1988) 2430-2433.
- [55] V.R. Shaginyan, Phys. Lett. A 249 (1998) 237-241.
- [56] M.Ya. Amusia, V.R. Shaginyan, Phys. Lett. A 269 (2000) 337-342.
- [57] V.R. Shaginyan, Pis'ma Zh. Eksp. Teor. Fiz. 68 (1998) 491-496; [JETP Lett. 68 (1998) 527-532].

- [58] A.V. Chubukov, D.L. Maslov, A.J. Millis, *Phys. Rev. B* 73 (2006) 045128-045249.
- [59] D. Vollhardt, *Rev. Mod. Phys.* 56 (1984) 99-120.
- [60] M. Pfitzner, P. Wölfe, *Phys. Rev. B* 33 (1986) 2003-2006.
- [61] D. Vollhardt, P. Wölfe, P.W. Anderson, *Phys. Rev. B* 35 (1987) 6703-6715.
- [62] V.M. Yakovenko, V.A. Khodel, *JETP Lett.* 78 (2003) 850-853.
- [63] V.R. Shaginyan, *JETP Lett.* 77 (2003) 104-108.
- [64] A. Casey, H. Patel, J. Nyeki, B.P. Cowan, J. Saunders, *J. Low Temp. Phys.* 113 (1998) 293-298.
- [65] A.A. Shashkin, S.V. Kravchenko, V.T. Dolgoplov, T.M. Klapwijk, *Phys. Rev. B* 66 (2002) 073303-073306.
- [66] A.A. Shashkin, M. Rahimi, S. Anissimova, S.V. Kravchenko, V.T. Dolgoplov, T.M. Klapwijk, *Phys. Rev. Lett.* 91 (2003) 046403-046406.
- [67] J. Boronat, J. Casulleras, V. Grau, E. Krotscheck, J. Springer, *Phys. Rev. Lett.* 91 (2003) 085302-085305.
- [68] Y. Zhang, V.M. Yakovenko, S. Das Sarma, *Phys. Rev. B* 71 (2005) 115105-115114.
- [69] Y. Zhang, S. Das Sarma, *Phys. Rev. B* 70 (2004) 035104-035117.
- [70] V.A. Khodel, V.R. Shaginyan, M.V. Zverev, *JETP Lett.* 65 (1997) 242-247.
- [71] S.V. Kravchenko, M.P. Sarachik, *Rep. Prog. Phys.* 67 (2004) 1-44.
- [72] A. Casey, H. Patel, J. Cowan, B.P. Saunders, *Phys. Rev. Lett.* 90 (2003) 115301-115304.
- [73] G.E. Volovik, *Pis'ma Zh. Eksp. Teor. Fiz.* 53 (1991) 208-211; [*JETP Lett.* 53 (1991) 222-225]
- [74] M.Ya. Amusia, V.R. Shaginyan, *Pis'ma Zh. Eksp. Teor. Fiz.* 73 (2001) 268-273; [*JETP Lett.* 73 (2001) 232-237].
- [75] M.Ya. Amusia, V.R. Shaginyan, *Phys. Rev. B* 63 (2001) 224507-224512; V.R. Shaginyan, *Physica B* 312-313C (2002) 413-414.
- [76] C.M. Varma, P.B. Littlewood, S. Schmittrink, E. Abrahams, A.E. Ruckenstein, *Phys. Rev. Lett.* 63 (1989) 1996-1999.
- [77] C.M. Varma, P.B. Littlewood, S. Schmittrink, E. Abrahams, A.E. Ruckenstein, *Phys. Rev. Lett.* 64 (1990) 497.
- [78] J. Bardeen, L.N. Cooper, J.R. Schrieffer, *Phys. Rev.* 108 (1957) 1175-1204.
- [79] V.A. Khodel, M.V. Zverev, V.M. Yakovenko, *Phys. Rev. Lett.* 95 (2005) 236402-236405.
- [80] D.V. Khveshchenko, R. Hlubina, T.M. Rice, *Phys. Rev. B* 48 (1993) 10766-10776.
- [81] I.E. Dzyaloshinskii, *J. Phys. I (France)* 6 (1996) 119-135.
- [82] D. Lidsky, J. Shiraiishi, Y. Hatsugai, M. Kohmoto, *Phys. Rev. B* 57 (1996) 1340-1343.
- [83] V.Yu. Irkhin, A.A. Katanin, M.I. Katsnelson, *Phys. Rev. Lett.* 89 (2002) 076401-076404.
- [84] R.B. Laughlin, D. Pines, *Proc. Natl. Acad. Sci. USA* 97 (2000) 28-32.
- [85] P.W. Anderson, *Science* 288 (2000) 480-483.
- [86] V.A. Khodel, J.W. Clark, V.R. Shaginyan, *Solid Stat. Comm.* 96 (1995) 353-357.
- [87] S.A. Artamonov, V.R. Shaginyan, *Zh. Eksp. Teor. Fiz.* 119 (2001) 331-341, [*JETP* 92 (2001) 287-297].
- [88] P.V. Bogdanov, A. Lanzara, S.A. Kellar, X.J. Zhou, E.D. Lu, W.J. Zheng, G. Gu, J.-I. Shimoyama, K. Kishio, H. Ikeda, R. Yoshizaki, Z. Hussain, Z.X. Shen *Phys. Rev. Lett.* 85 (2000) 2581-2584.
- [89] A. Kaminski, M. Randeria, J.C. Campuzano, M.R. Norman, H. Fretwell, J. Mesot, T. Sato, T. Takahashi, K. Kadowaki, *Phys. Rev. Lett.* 86 (2001) 1070-1073.
- [90] T. Valla, A.V. Fedorov, P.D. Johnson, B.O. Wells, S.L. Hulbert, Q. Li, G.D. Gu, N. Koshizuka, *Science* 285 (1999) 2110-2113.
- [91] T. Valla, A.V. Fedorov, P.D. Johnson, Q. Li, G.D. Gu, N. Koshizuka, *Phys. Rev. Lett.* 85 (2000) 828-831.
- [92] D. Takahashi, S. Abe, H. Mizuno, D.A. Tayurskii, K. Matsumoto, H. Suzuki, Y. Onuki, *Phys. Rev. B* 67 (2003) 180407-180410.
- [93] D.R. Tilley, J. Tilley, *Superfluidity and Superconductivity*, Hilger, Bristol, 1985.
- [94] S.A. Artamonov, Yu.G. Pogorelov, V.R. Shaginyan, *Pis'ma Zh. Eksp. Teor. Fiz.* 68 (1998) 893-899; [*JETP Lett.* 68 (1998) 942-948].
- [95] Yu.G. Pogorelov, V.R. Shaginyan, *Condensed Matter Theories* 18 (2003) 191-200.
- [96] L.P. Gor'kov, *Zh. Eksp. Teor. Fiz.* 34 (1958) 735; [*Sov. Phys. JETP* 7 505 (1958)]
- [97] V.R. Shaginyan, A.Z. Msezane, V.A. Stephanovich, E.V. Kirichenko, *Europhys. Lett.* 76 (2006) 898-904.
- [98] N.N. Bogoliubov, *Nuovo Cimento* 7 (1958) 794.
- [99] M.Ya. Amusia, V.R. Shaginyan, *Pis'ma Zh. Eksp. Teor. Fiz.* 77 (2003) 803-810; [*JETP Lett.* 77 (2003) 671-678].
- [100] H. Matsui, T. Sato, T. Takahashi, S.-C. Wang, H.-B. Yang, H. Ding, T. Fujii, T. Watanabe, A. Matsuda, *Phys. Rev. Lett.* 90 (2003) 217002-217005.
- [101] M.Ya. Amusia, S.A. Artamonov, V.R. Shaginyan, *Pis'ma Zh. Eksp. Teor. Fiz.* 74 (2001) 435-439; [*JETP Lett.* 74 (2001) 396-400].
- [102] A. Paramekanti, M. Randeria, N. Trivedi, *Phys. Rev. Lett.* 87 (2001) 217002-217005.
- [103] P.W. Anderson, P.A. Lee, M. Randeria, T.M. Rice, N. Trivedi, F.C. Zhang, *J. Phys. Condens. Matter* 16 (2004) R755-R769.
- [104] M.Ya. Amusia, V.R. Shaginyan, *Phys. Lett. A* 298 (2002) 193-196.
- [105] M. Kugler, O. Fischer, Ch. Renner, S. Ono, Y. Ando, *Phys. Rev. Lett.* 86 (2001) 4911-4914.
- [106] A.A. Abrikosov, *Phys. Rev. B* 52 (1995) R15738-R15740.
- [107] N.-C. Yeh, C.-T. Chen, G. Hammerl, J. Mannhart, A. Schmehl, C. W. Schneider, R. R. Schulz, S. Tajima, K. Yoshida, D. Garrigus, M. Strasik, *Phys. Rev. Lett.* 87 (2001) 087003-087006.
- [108] A. Biswas, P. Fournier, M.M. Qazilbash, V.N. Smolyaninova, H. Balci, R.L. Greene, *Phys. Rev. Lett.* 88 (2002) 207004-207007.
- [109] J.A. Skinta, M.-S. Kim, T.R. Lemberger, T. Greibe, M. Naito, *Phys. Rev. Lett.* 88 (2002) 207005-207008.
- [110] J.A. Skinta, T.R. Lemberger, T. Greibe, M. Naito, *Phys. Rev. Lett.* 88 (2002) 207003-207006.
- [111] C.-T. Chen, P. Seneor, N.-C. Yeh, R.P. Vasquez, L.D. Bell, C.U. Jung, J.Y. Kim, M.-S. Park, H.-J. Kim, S.-I. Lee, *Phys. Rev. Lett.* 88 (2002) 227002-227005.
- [112] N. Metoki, Y. Haga, Y. Koike, Y. Onuki, *Phys. Rev. Lett.* 80 (1998) 5417-5420.
- [113] T. Honma, Y. Haga, E. Yamamoto, N. Metoki, Y. Koike, H. Ohkuni, N. Suzuki, Y. Onuki, *J. Phys. Soc. Jpn.* 68 (1999) 338-341.
- [114] V. Kresin, Yu.N. Ovchinnikov, S.A. Wolf, *Phys. Rep.* 431 (2006) 231-259.
- [115] T. Pereg-Barnea, H. Weber, G. Refael, M. Franz, *Nature Phys.* 6 (2010) 44-49.
- [116] M. Shi, J. Chang, S. Pailhes, M.R. Norman, J.C. Campuzano, M. Mansson, T. Claesson, O. Tjernberg, A. Bendounan, L. Patthey, N. Momono, M. Oda, M. Ido, C. Mudry, J. Mesot, *Phys. Rev. Lett.* 101 (2008) 047002-047005.
- [117] H.-B. Yang, J.D. Rameau, P.D. Johnson, T. Valla, A. Tsvetlik, G.D. Gu, *Nature* 456 (2008) 77-80.

- [118] A. Kanigel, U. Chatterjee, M. Randeria, M.R. Norman, G. Koren, K. Kadowaki, J.C. Campuzano, *Phys. Rev. Lett.* 101 (2008) 137002-137005.
- [119] J. Lee, K. Fujita, A.R. Schmidt, Ch.K. Kim, H. Eisaki, S. Uchida, J. C. Davis, *Science* 325 (2009) 1099-1103.
- [120] V.R. Shaginyan, M.Ya. Amusia, K.G. Popov, V.A. Stephanovich, *Phys. Lett. A* 373 (2009) 686-692.
- [121] M. Ya. Amusia, V.R. Shaginyan, *Pis'ma Zh. Eksp. Teor. Fiz.* 76 (2002) 774-778; [*JETP Lett.* 76 (2002) 651-655].
- [122] N. Miyakawa, J.F. Zasadzinski, L. Ozyuzer, P. Guptasarma, D.G. Hinks, C. Kendziora, K.E. Gray, *Phys. Rev. Lett.* 83 (1999) 1018-1021.
- [123] C. Petrovic, P.G. Pagliuso, M.F. Hundley, R. Movshovich, J.L. Sarrao, J.D. Thompson, Z. Fisk, P. Monthoux, *J. Phys. Condens. Matter* 13 (2001) L337-L342.
- [124] A. Ino, C. Kim, M. Nakamura, T. Yoshida, T. Mizokawa, A. Fujimori, Z.-X. Shen, T. Kakeshita, H. Eisaki, S. Uchida, *Phys. Rev. B* 65 (2002) 094504-094514.
- [125] X.J. Zhou, T. Yoshida, A. Lanzara, P.V. Bogdanov, S.A. Kellar, K.M. Shen, W.L. Yang, F. Ronning, T. Sasagawa, T. Kakeshita, T. Noda, H. Eisaki, S. Uchida, C.T. Lin, F. Zhou, J.W. Xiong, W.X. Ti, Z.X. Zhao, A. Fujimori, Z. Hussain, Z.-X. Shen, *Nature* 423 (2003) 398-398.
- [126] W.J. Padilla, Y.S. Lee, M. Dumm, G. Blumberg, S. Ono, K. Segawa, S. Komiya, Y. Ando, D.N. Basov, *Phys. Rev. B* 72 (2005) 060511-060514.
- [127] T. Valla, A.V. Fedorov, P.D. Johnson, S.L. Hulbert, *Phys. Rev. Lett.* 83 (1999) 2085-2088.
- [128] D.L. Feng, A. Damascelli, K.M. Shen, N. Motoyama, D.H. Lu, H. Eisaki, K. Shimizu, J.-i. Shimoyama, K. Kishio, N. Kaneko, M. Greven, G.D. Gu, X.J. Zhou, C. Kim, F. Ronning, N.P. Armitage, Z.-X. Shen, *Phys. Rev. Lett.* 88 (2002) 107001-107004.
- [129] D.S. Dessau, B.O. Wells, Z.-X. Shen, W.E. Spicer, A.J. Arko, R.S. List, D.B. Mitzi, A. Kapitulnik, *Phys. Rev. Lett.* 66 (1991) 2160-2163.
- [130] A.B. Migdal *Teoriya Konechnykh Fermi-Sistem i Svoistva Atomnykh Yader*, 2nd ed., Nauka, Moscow, 1983; [A.B. Migdal *Theory of Finite Fermi Systems, and Applications to Atomic Nuclei*, Interscience Publ., New York, 1967]
- [131] Z.M. Yusof, B.O. Wells, T. Valla, A.V. Fedorov, P.D. Johnson, Q. Li, C. Kendziora, S. Jian, D.G. Hinks, *Phys. Rev. Lett.* 88 (2002) 167006-167009.
- [132] S. Nakamae, K. Behnia, N. Mangkorntong, M. Nohara, H. Takagi, S.J.C. Yates, N. Hussey, *Phys. Rev. B* 68 (2003) 100502-100505.
- [133] N.E. Hussey, M. Abdel-Jawad, A. Carrington, A.P. Mackenzie, L. Balicas, *Nature* 425 (2003) 814-817.
- [134] Yu.G. Pogorelov, V.R. Shaginyan, *Pis'ma Zh. Eksp. Teor. Fiz.* 76 (2002) 614-618; [*JETP Lett.* 76 (2002) 532-536].
- [135] M. de Llano, J.P. Vary, *Phys. Rev. C* 19 (1979) 1083-1088.
- [136] M. de Llano, A. Plastino, J.P. Zabolitsky, *Phys. Rev. C* 20 (1979) 2418-2425.
- [137] M.V. Zverev, M. Baldo, *J. Phys. Condens. Matter* 11 (1999) 2059-2069.
- [138] V.R. Shaginyan, A.Z. Msezane, M.Ya. Amusia, *Phys. Lett. A* 338 (2005) 393-401.
- [139] A. Khodel, P. Schuck, *Z. Phys. B: Condens. Matter* 104 (1997) 505-508.
- [140] N. Tsujii, H. Kontani, K. Yoshimura, *Phys. Rev. Lett.* 94 (2005) 057201-057205.
- [141] A.C. Jacko, J.O. Fjærestad, B.J. Powell, *Nature Physics* 5 (2009) 422-425.
- [142] J. Koringa, *Physica (Utrecht)* 16 (1950) 601-610.
- [143] G.-Q. Zheng, T. Sato, Y. Kitaoka, M. Fujita, K. Yamada, *Phys. Rev. Lett.* 90 (2003) 197005-197008.
- [144] C.L. Kane, M.P.A. Fisher, *Phys. Rev. Lett.* 76 (1996) 3192-3195.
- [145] C.L. Kane, M.P.A. Fisher, *Phys. Rev. B* 55 (1997) 15832-15837.
- [146] A. Houghton, S. Lee, J.B. Marston, *Phys. Rev. B* 65 (2002) 220503-220506.
- [147] V.A. Khodel, M.V. Zverev, *JETP Lett.* 85 (2007) 404-409.
- [148] A.P. Mackenzie, S.R. Julian, D.C. Sinclair, C.T. Lin, *Phys. Rev. B* 53 (1996) 5848-5855.
- [149] M.Ya. Amusia, V.R. Shaginyan, *Phys. Lett. A* 315 (2003) 288-292.
- [150] T. Shibauchi, L. Krusin-Elbaum, M. Hasegawa, Y. Kasahara, R. Okazaki, Y. Matsuda, *Proc. Natl. Acad. Sci. USA* 105 (2008) 7120-7123.
- [151] V.R. Shaginyan, K.G. Popov, *JETP Lett.* 88 (2008) 183-188.
- [152] K.-D. Morhard, C. Bauerle, J. Bossy, Yu. Bunkov, S.N. Fisher, H. Godfrin, *Phys. Rev. B* 53 (1996) 2658-2661.
- [153] M. Neumann, J. Nyéki, B. Cowan, J. Saunders, *Science* 317 (2007) 1356-1359.
- [154] Supporting online material for Ref. [153].
- [155] A. Benlagra, C. Pépin, *Phys. Rev. Lett.* 100 (2008) 176401-176404.
- [156] E.M. Lifshitz, L.P. Pitaevskii, *Statistical Physics, Part 1*, Butterworth-Heinemann, Oxford, 1996.
- [157] V.R. Shaginyan, *Pis'ma Zh. Eksp. Teor. Fiz.* 80 (2004) 294-297; [*JETP Lett.* 80 (2004) 263-266].
- [158] V.A. Khodel, V.R. Shaginyan, *Nucl. Phys. A* 555 (1993) 33-58.
- [159] J.W. Clark, V.A. Khodel, M.V. Zverev, V.M. Yakovenko, *Phys. Rep.* 391 (2004) 123-156.
- [160] V.R. Shaginyan, *Pis'ma Zh. Eksp. Teor. Fiz.* 77 (2003) 208-211; [*JETP Lett.* 77 (2003) 178-181].
- [161] Y. Tokiwa, T. Radu, C. Geibel, F. Steglich, P. Gegenwart, *Phys. Rev. Lett.* 102 (2009) 066401-066404.
- [162] S.L. Budko, E. Morosan, P.C. Canfield, *Phys. Rev. B* 69 (2004) 014415-014422.
- [163] A. Bianchi, R. Movshovich, I. Vekhter, P.G. Pagliuso, J.L. Sarrao, *Phys. Rev. Lett.* 91 (2003) 257001-257004.
- [164] V.R. Shaginyan, K.G. Popov, V.A. Stephanovich, *Europhys. Lett.* 79 (2007) 47001-47006.
- [165] J.M. Ziman, *Electrons and Phonons*, Oxford University Press, Oxford, 1960.
- [166] V.R. Shaginyan, M.Ya. Amusia, A.Z. Msezane, K.G. Popov, V.A. Stephanovich, *Phys. Lett. A* 373 (2009) 986-991.
- [167] P. Carretta, R. Pasero, M. Giovannini, C. Baines, *Phys. Rev. B* 79 (2009) 020401-020404.
- [168] T. Moriya, *Spin Fluctuations in Itinerant Electron Magnetism*, Springer, Berlin, 1985.
- [169] V.R. Shaginyan, A.Z. Msezane, K.G. Popov, V.A. Stephanovich, *Phys. Lett. A* 373 (2009) 3783-3786.
- [170] P. Gegenwart, J. Custers, Y. Tokiwa, C. Geibel, F. Steglich, *Phys. Rev. Lett.* 94 (2005) 076402-076405.
- [171] A. Bianchi, R. Movshovich, N. Oeschler, P. Gegenwart, F. Steglich, J.D. Thompson, P.G. Pagliuso, J.L. Sarrao, *Phys. Rev. Lett.* 89 (2002) 137002-137005.
- [172] V.R. Shaginyan, K.G. Popov, *Phys. Lett. A* 361 (2007) 406-412.
- [173] J.G. Sereni, T. Westerkamp, R. Kuchler, N. Caroca-Canales, P. Gegenwart, C. Geibe, *Phys. Rev. B* 75 (2007) 024432-024439.
- [174] A.P. Pikul, N. Caroca-Canales, M. Deppe, P. Gegenwart, J.G. Sereni, C. Geibel, F. Steglich, *J. Phys. Condens. Matter* 18 (2006) L535-L542.
- [175] R. Kuchler, P. Gegenwart, K. Heuser, E.-W. Scheidt, G.R. Stewart, F. Steglich, *Phys. Rev. Lett.* 93 (2004) 096402-096405.

- [176] V.R. Shaginyan, E.V. Kirichenko, V.A. Stephanovich, *Physica B* 403 (2008) 755-757.
- [177] V.R. Shaginyan, K.G. Popov, *Physica B: Phys. Cond. Matt.* 404 (2009) 3179-3182.
- [178] T.R. Kirkpatrick, D. Belitz, *Phys. Rev. B* 67 (2003) 024419-024432.
- [179] N.P. Butch, M.B. Maple, *Phys. Rev. Lett.* 103 (2009) 076404.
- [180] P. Nozières, *J. Phys. I (Paris)* 2 (1992) 443-459.
- [181] M.Ya. Amusia, A.Z. Msezane, V.R. Shaginyan, *Phys. Lett. A* 320 (2004) 459-464.
- [182] M.V. Zverev, V.A. Khodel, V.R. Shaginyan, M. Baldo, *JETP Lett.* 65 (1997) 863-869.
- [183] V.R. Shaginyan, P.G. Popov, S.A. Artamonov, *JETP Lett.* 82 (2005) 215-219.
- [184] V.R. Shaginyan, M.Ya. Amusia, K.G. Popov, *Phys. Lett. A* 374 (2010) 659-664.
- [185] S. Paschen, T. Lühmann, S. Wirth, P. Gegenwart, O. Trovarelli, C. Geibel, F. Steglich, P. Coleman, Q. Si, *Nature* 432 (2004) 881-885.
- [186] C. Pépin, *Phys. Rev. Lett.* 94 (2005) 066402-066405.
- [187] E.D. Bauer, J.D. Thompson, J.L. Sarrao, L.A. Morales, F. Wastin, J. Rebizant, J.C. Griveau, P. Javorsky, P. Boulet, E. Colineau, G.H. Lander, G.R. Stewart, *Phys. Rev. Lett.* 93 (2004) 147005-147008.
- [188] F. Ronning, C. Capan, A. Bianchi, R. Movshovich, A. Lacerda, M.F. Hundley, J.D. Thompson, P.G. Pagliuso, J.L. Sarrao, *Phys. Rev. B* 71 (2005) 104528-104534.
- [189] N. Oeschler, P. Gegenwart, M. Lang, R. Movshovich, J. L. Sarrao, J.D. Thompson, F. Steglich, *Phys. Rev. Lett.* 91 (2003) 076402-076405.
- [190] K. Izawa, H. Yamaguchi, Y. Matsuda, H. Shishido, R. Settai, Y. Onuki *Phys. Rev. Lett.* 87 (2001) 057002-057005.
- [191] G.E. Volovik, *Pis'ma Zh. Eksp. Teor. Fiz.* 65 (1997) 465-469; [*JETP Lett.* 65 (1997) 491-495].
- [192] K. Maki, *Phys. Rev.* 148 (1966) 362-369.
- [193] R. Movshovich, M. Jaime, J. D. Thompson, C. Petrovic, Z. Fisk, P. G. Pagliuso, J. L. Sarrao, *Phys. Rev. Lett.* 91 (2001) 51525155.
- [194] R.A. Borzi, S.A. Grigera, J. Farrell, R.S. Perry, S.J.S. Lister, S.L. Lee, D.A. Tennant, Y. Maeno, A.P. Mackenzie *Science* 315 (2007) 214-217.
- [195] A.V. Silhanek, N. Harrison, C.D. Batista, M. Jaime, A. Lacerda, H. Amitsuka, J.A. Mydosh, *Phys. Rev. Lett.* 95 (2005) 026403-026406.
- [196] J.S. Kim, B. Andraka, G. Fraunberger, G.R. Stewart, *Phys. Rev. B* 41 (1990) 541-546.
- [197] V.R. Shaginyan, *Pis'ma Zh. Eksp. Teor. Fiz.* 81 (2005) 283-286; [*JETP Lett.* 81 (2005) 222-225].
- [198] V.R. Shaginyan, K.G. Popov, V.A. Stephanovich, E.V. Kirichenko, *Journal of Alloys and Compounds* 442 (2007) 29-33.
- [199] A.M. Zagoskin, *Quantum Theory of Many-Body Systems*, Springer-Verlag Inc., New York, 1998.
- [200] G. Deutscher, *Rev. Mod. Phys.* 77 (2005) 109-135.
- [201] A.F. Andreev, *Zh. Eksp. Teor. Fiz.* 46 (1964) 1823; [*Sov. Phys. JETP* 19 (1964) 1228]
- [202] W.K. Park, L.H. Greene, J.L. Sarrao, J.D. Thompson, *Phys. Rev. B* 72 (2005) 052509-052512.
- [203] G. Pristáš, M. Reiffers, E. Bauer, A.G.M. Jansen, D.K. Maude, *Phys. Rev. B* 78 (2008) 235108-235113.
- [204] P.W. Anderson, N.P. Ong, <http://arxiv.org/abs/cond-mat/0405518>, 1-5.
- [205] S.H. Pan, J.P. O'Neal, R.L. Badzey, C. Chamon, H. Ding, J.R. Engelbrecht, Z. Wang, H. Eisaki, S. Uchida, A.K. Gupta, K.-W. Ng, E.W. Hudson, K.M. Lang, J.C. Davis, *Nature* 413 (2001) 282-285.
- [206] S. Piano, F. Bobba, A. De Santis, F. Giubileo, A. Scarfato, A.M. Cucolo, *J. of Physics: Conference Series* 43 (2006) 1123-1126.
- [207] G. Wiedemann, R. Franz, *Ann. Phys.* 89 (1853) 497.
- [208] A. Sommerfeld, *Naturwissenschaften*, 15 (1927) 825.
- [209] G. V. Chester, A. Telling, *Proc. Phys. Soc.* 77 (1961) 1005.
- [210] M.J. Kearney, P.N. Butcher, *J. Phys. C.: Solid State Phys.* 21 (1988) L265-L270.
- [211] C. Castellani, C. DiCastro, G. Kotliar, P. A. Lee, G. Strinati, *Phys. Rev. Lett.* 59 (1987) 477-480.
- [212] H.R. Ott, O. Marti, F. Hulliger, *Solid St. Comm.* 49 (1984) 1129-1131.
- [213] A. Amato, D. Jaccard, E. Walker, J. Sierro, J. Flouquet, *J. Magn. Magn. Mater.* 63-64 (1987) 300-302.
- [214] S. Kambe, H. Suderow, T. Fukuhara, J. Flouquet, T. Takimoto, *J. Low Temp. Phys.* 117 (1999) 101-112.
- [215] R.T. Syme, M.J. Kelly, M. Pepper, *J. Phys.: Condens. Matter* 1 (1989) 3375-3380.
- [216] S. Paschen, B. Wand, G. Sparn, F. Steglich, Y. EchiZen, T. Takabatake, *Phys. Rev. B* 62 (2000) 14912-14919.
- [217] M.A. Tanatar, J. Paglione, L. Taillefer, C. Petrovich, *Science* 316 (2007) 1320-1322.
- [218] R.W. Hill, C. Proust, L. Taillefer, P. Fournier, R.L. Greene, *Nature* 414 (2001) 711-715.
- [219] N. Doiron-Leyrand, M. Sutherland, S.Y. Li, L. Taillefer, R. Liang, D.A. Bonn, W.N. Hardy, *Phys. Rev. Lett.* 97 (2006) 207001-207004.
- [220] C. Proust, K. Behnia, R. Bel, D. Maude, S.I. Vedenev, *Phys. Rev. B* 72 (2005) 214511-214519.
- [221] L.G.C. Rego, G. Kirczenow, *Phys. Rev. B* 59 (1999) 13080-13086.
- [222] M.R. Li, E. Orignac, *Europhys. Lett.* 60 (2002) 432-438.
- [223] P. Coleman, C. Pepin, *Physica B* 312-313 (2002) 383-389.
- [224] D. Podolsky, A. Vishvanath, J. Moore, S. Sachdev, *Phys. Rev. B* 75, 014520-014524 (2007).
- [225] V.A. Khodel, V.M. Yakovenko, M.V. Zverev, *Pis'ma Zh. Eksp. Teor. Fiz.* 86 (2007) 884-890; [*JETP Lett.* 86 (2007) 772-778].
- [226] V.A. Khodel, J.W. Clark, V.M. Yakovenko, M.V. Zverev, *Physica B* 403 (2008) 1227-1229.
- [227] V.R. Shaginyan, V.A. Stephanovich, *Physica B* 403 (2008) 739-741.
- [228] C. Krellner, S. Hartmann, A. Pikul, N. Oeschler, J.G. Donath, C. Geibel, F. Steglich, J. Wosnitzer, *Phys. Rev. Lett.* 102 (2009) 196402-196405.
- [229] V.R. Shaginyan, M.Ya. Amusia, K.G. Popov, <http://arxiv.org/abs/0905.1871v1>, 1-4.
- [230] T. Misawa, Y. Yamaji, M. Imada, *J. Phys. Soc. Jpn.* 78 (2009) 084707-084721.
- [231] M. Imada, T. Misawa, Y. Yamaji, <http://arxiv.org/abs/0909.0562v1>, 1-16.
- [232] C. Klingner, C. Krellner, C. Geibel, <http://arxiv.org/abs/0908.1299v1>, 1-5.
- [233] V.R. Shaginyan, *Physica B: Condensed Matter* 378-380 (2006) 127-128.
- [234] F. Steglich, B. Buschinger, P. Gegenwart, M. Lohmann, R. Helfrich, C. Langhammer, P. Hellmann, L. Donnevert, S. Thomas, A. Link, C. Geibel, M. Lang, G. Sparn, W. Assmus, *J. Phys. Cond. Mat.* 8 (1996) 9909-9921.
- [235] H.v. Löhneysen, *J. Phys. Condens. Matter* 8 (1996) 9689-9706.
- [236] M.V. Zverev, M. Baldo, *JETP* 87 (1998) 1129-1135.

- [237] I.M. Lifshitz, Sov. Phys. JETP 11 (1960) 1130.
- [238] M. Nakahara, Geometry, topology and physics, IOP Publ., Bristol (1990).
- [239] W. Kohn, L.J. Sham, Phys. Rev. 140 (1965) A1133-A1138.
- [240] W. Kohn, P. Vashishta, in Theory of the Inhomogeneous Electron Gas, ed. by S. Lundqvist, N.H. March, Plenum, New York, 1983.